DEVELOPMENT OF ^{13}C LIQUID STATE DYNAMIC NUCLEAR POLARIZATION AT 9.4 TESLA

Dissertation

for the award of the degree

Doctor rerum naturalium

of the Georg-August-Universität Göttingen

within the doctoral program

Physics of Biological and Complex Systems

of the Georg-August University School of Science (GAUSS)

MAX PLANCK INSTITUTE
FOR MULTIDISCIPLINARY SCIENCES

GEORG-AUGUST-UNIVERSITÄT
GÖTTINGEN

submitted by

Marcel Levien

from Kassel, Germany

Göttingen, 2022

PhD Examination Committee

Prof. Dr. Marina Bennati - *TAC member and 1st referee*
Research Group EPR Spectroscopy
Max Planck Intitute for Multidisciplinary Sciences, Göttingen
Institute for Organic and Biomolecular Chemistry
Georg-August-Universität Göttingen

Prof. Dr. Christian Griesinger - *TAC member and 2nd referee*
Department of NMR-based Structural Biology
Max Planck Intitute for Multidisciplinary Sciences, Göttingen

Dr. Aljaz Godec - *TAC member*
Research Group Mathematical Biophysics
Max Planck Intitute for Multidisciplinary Sciences, Göttingen

Dr. Stefan Glöggler
Research Group NMR Signal Enhancement
Center for Biostructural Imaging of Neurodegeneration, Göttingen

PhD Examination Committee

Dr. Michael John
Insitute for Organic and Biomolecular Chemistry
Georg-August-Universität Göttingen

Prof. Dr. Martin A. Suhm
Physical Chemistry II
Georg-August-Universität Göttingen

Date of Oral Examination: December 1, 2022

Abstract

Throughout the last decades, nuclear magnetic resonance (NMR) spectroscopy in liquids contributed to the structural elucidation of molecules of many types and sizes. Continuous improvements of the hardware and pulse sequences enabled the expansion of NMR applications from small molecules over large biological macromolecules to inorganic surfaces and battery research. However, the method is still hampered by the inherent low sensitivity arising from the small energy difference of the nuclear Zeeman states at magnetic fields employed in routine NMR experiments. One emerging approach to tackle the sensitivity issue is dynamic nuclear polarization (DNP), where spin polarization from highly polarized electron spins is transferred to nuclear spins.

In order to push liquid state DNP forward on its journey to a viable option in the toolbox of routine NMR, two different avenues were pursued during the course of this thesis. Firstly, the influence of the molecular structure of the polarizing agent (PA) as well as rotational diffusion and fast structural rearrangements of the PA were investigated at low magnetic field. The goal was to derive favorable experimental conditions for ^{13}C DNP at high magnetic field. The spin polarization transfer is favored, if the electron spin density of the PA is highly localized and readily accessible for the target molecule. Additionally, structural rearrangements of the PA that act on the picosecond to sub-picosecond timescale may amplify the DNP effect by modulating the hyperfine coupling on the correct timescale for DNP at high magnetic field.

Secondly, a new DNP instrument operating at 9.4 T with a frequency agile gyrotron as a microwave source and a sample volume of up to 40 µL was developed. Large ^{13}C NMR

signal enhancements of up to $\epsilon \approx 200$ on model systems (e.g. $CHCl_3$) and of up to $\epsilon \approx 37$ on a large variety of target molecules, including pharmaceutical drugs, were observed. The triple-resonance probehead was optimized to have an NMR resolution that is comparable with standard NMR experiments with linewidths in the range of $5 - 30$ Hz and in favorable cases reaching 2.3 Hz. The collected results led to new mechanistic insights such as the efficient hyperpolarization of iodine containing compounds ($\epsilon \approx 10 - 33$), possibly rooted in the halogen bond formation of the PA with iodine. The new DNP instrument also enabled DNP measurements in polar solvents, including water, with a sample volume of $\sim 15\,\mu L$ and an enhancement of up to $\epsilon \approx 6$.

Finally, 2D DNP NMR was tested on ^{13}C enriched and natural abundance target molecules and showed that the large signal enhancements of 1D NMR DNP are retained. This allowed for the transfer of the large hyperpolarization accumulated on favorable nuclear sites (e.g. iodinated carbons) to nuclei that cannot directly be polarized by DNP (e.g. fluorinated carbons or carbonyl groups) and therefore demonstrates the possibility to distribute the hyperpolarization over the target molecule.

Contents

PhD Examination Committee i

Abstract iii

Abbreviations and Symbols ix

List of Figures xv

List of Tables xxi

1 Introduction 1

2 Theoretical Background 7

2.1 The Overhauser Equation 8

2.2 The Coupling Factor 11

2.3 The Enhancement Factor 20

2.4 The Saturation Factor 20

2.5 The Leakage Factor 23

2.6 The Three-Spin Effect 24

2.7 Electron Spin-Lattice Relaxation 26

3 Materials and Methods **31**
3.1 Materials . . . 31
3.1.1 Sample Preparation . . . 34
3.2 Spectrometers . . . 34
3.2.1 Continuous Wave X-Band Spectrometer . . . 34
3.2.2 X- and Q-Band Spectrometer . . . 35
3.2.3 W-Band Spectrometer . . . 35
3.2.4 263 GHz EPR Spectrometer . . . 36
3.3 Methods . . . 36
3.3.1 Measurement of the Electron Spin Lattice Relaxation Time . . . 36
3.3.2 Saturation Measurements at X- and Q-Band . . . 36
3.3.3 Nuclear Relaxation Times . . . 37
3.3.4 ^{13}C DNP NMR Pulse Sequences . . . 38
3.3.5 Diffusion Measurements . . . 46
3.3.6 Theoretical Calculations . . . 46

4 The Influence of the Molecular Structure on Scalar Dynamic Nuclear Polarization **49**
4.1 Introduction . . . 49
4.2 Spin Density Localization and Accessibility of Organic Radicals Affect Liquid State DNP Efficiency . . . 50
4.3 Supplementary Information . . . 60
4.3.1 Sample Preparation . . . 60
4.3.2 Overhauser Experiments and Parameters . . . 61
4.3.3 ^{1}H-DNP at X-Band – 0.34 T . . . 61
4.3.4 ^{13}C-DNP at Q-Band – 1.2 T . . . 64
4.3.5 Heating Effects . . . 65
4.3.6 Quantum Chemistry Calculations . . . 67

5 The Influence of Molecular Dynamics on Scalar Dynamic Nuclear Polarization **73**
5.1 Introduction . . . 73

5.2 Nitroxide Derivatives for Dynamic Nuclear Polarization in Liquids: The Role of Rotational Diffusion . . . 74
5.3 Supplementary Information . . . 85
5.3.1 Sample Preparation . . . 85
5.3.2 Continuous Wave EPR Measurements . . . 85
5.3.3 Diffusion Coefficient . . . 87
5.3.4 Geometry Optimization for the TL/Toluene Complex . . . 90
5.3.5 ^{1}H-DNP Measurements at 0.34 T . . . 91
5.3.6 ^{1}H Coupling Factor . . . 94
5.3.7 ^{13}C DNP Measurements . . . 94
5.3.8 Simulation of the ^{1}H Coupling Factor . . . 98
5.3.9 Simulation of the ^{13}C Coupling Factor . . . 99
5.3.10 DFT and MD Simulations of TN and FN-2a . . . 102

6 Electron Spin Relaxation Times at 9.4 Tesla 111
6.1 Electron Spin Transversal Relaxation Time . . . 112
6.2 Electron Spin Longitudinal Relaxation Time . . . 115
6.2.1 Electron Spin Longitudinal Relaxation Time at 0.35 T, 1.2 T, and 3.4 T . . . 115
6.2.2 Electron Spin Lattice Relaxation Time at 9.4 T . . . 118

7 Dynamic Nuclear Polarization at 9.4 Tesla 125
7.1 Development of a 9.4 Tesla Liquid State DNP Setup . . . 129
7.1.1 The Gyrotron as a Microwave Source . . . 129
7.1.2 Gyrotron Output Power and Frequency Characterization . . . 131
7.1.3 The Quasi-Optical Table . . . 134
7.1.4 The Probehead . . . 136
7.1.5 Evaluation and Comparison of B_{1e} with the Literature . . . 144
7.1.6 Sample Volume and Geometrical Arrangement . . . 145
7.2 DNP in Non-Polar Solvents . . . 147
7.2.1 Evaluation of the Signal Enhancement of Model Systems . . . 148

7.2.2 Evaluation of the NMR Linewidth During DNP of Model Compounds and Comparison with the Literature . . . 155
7.2.3 DNP Efficiency of Various Substrates and Functional Groups . . 157
7.2.4 New Mechanistic Insights in the DNP Enhancement of Small Molecules . . . 160
7.2.5 DNP Results on Biologically Active Compounds . . . 168
7.3 DNP in Polar Solvents . . . 170
7.3.1 Temperature Calibration for DNP Experiments . . . 171
7.3.2 Magnetic Field Calibration . . . 174
7.3.3 Analysis of DNP Experiments in Polar Solvents . . . 175
7.4 2D Dynamic Nuclear Polarization in Liquids at 9.4 T . . . 179
7.4.1 Dynamic Nuclear Polarization Double Quantum Filtered Correlation Spectroscopy (DNP DQF COSY) . . . 181
7.4.2 Dynamic Nuclear Polarization Total Correlation Spectroscopy (DNP TOCSY) . . . 183
7.4.3 Dynamic Nuclear Polarization Incredible Natural Abundance Double Quantum Transfer Experiment (DNP INADEQUATE) . . . 187

8 Conclusion and Outlook **191**

Bibliography **199**

Appendix **225**
A Electron Spin Longitudinal Relaxation Time at 9.4 T . . . 226
B Continuous Wave EPR Measurements at 263 GHz of Different Radicals . 228
C ^{13}C NMR Signal Enhancements at 9.4 T . . . 230
D Nuclear Spin Longitudinal Relaxation Time . . . 249
E Temperature Calibration at 9.4 Tesla . . . 250

Acknowledgment **253**

Publications **255**

Abbreviations and Symbols

Abbreviations

1D	one-dimensional
2D	two-dimensional
BDPA	α,γ-bisdiphenylene-β-phenylallyl
COSY	correlation spectroscopy
CPI	Communications & Power Industries
cw	continuous wave
DABCO	1,4-diazabicyclo[2.2.2]octane
DDT	dichlorodiphenyltrichloroethane
DFT	density functional theory
DTBN	di-tert-butyl-nitroxide
DNP	dynamic nuclear polarization
DQF	double quantum filtered
DS	dummy scans
EDG	electron donating group
ELDOR	electron double resonance
EPR	electron paramagnetic resonance
ESR	electron spin resonance
EWG	electron withdrawing group

ffhs	force free hard spheres
FID	free induction decay
FN-*n*	fullerene-nitroxides
FT	fourier transform
FWHM	full width half maximum
HWHM	half width half maximum
hf	hyperfine
I.D.	inner diameter
IMPATT	impact ionization avalanche transit time diode
IMPRS-PBCS	international Max Planck research school - physics of biological and complex systems
INADEQUATE	incredible natural abundance double quantum transfer experiment
INEPT	insensitive nuclei enhancement by polarization transfer
LB	line broadening
LW	linewidth
MA	modulation amplitude
Me	methyl
MF	modulation frequency
M*n*	mirror *n*
MP	modulation phase
MPI-bpc	Max - Planck - institute for biophysical chemistry
MPI-NAT	Max - Planck - institute for multidisciplinary sciences
mw	microwave
MD	molecular dynamics
NMR	nuclear magnetic resonance
NOD	nitroxide derivative
NOE	nuclear Overhauser effect
NS	number of scans
O.D.	outer diameter
OE	Overhauser effect
PA	polarizing agent
PCCP	physical chemistry chemical physics

PFG	pulsed field gradient
PHEMT	pseudomorphic high electron mobility transistor
PTR	polarization transforming reflector
rf	radio-frequency
SI	supplementary information
RG	receiver gain
Ri	ring
SAS	solvent accessible surface
SCF	self-consistent field procedure
SES	solvent-exclusion surfaces
SPP	shots per point
SRT	shot repetition time
SW	sweep width
TL	4-hydroxy-2,2,6,6-tetramethylpiperidine 1-oxyl or tempol
TN	4-oxo-2,2,6,6-tetramethylpiperidine-d_{16},1-^{15}N-1-oxyl or tempone
TNH	tempone-H
TN-py	7-aza-3,11-dioxa-15-oxodispiro[5.1.5.3]hexadec-7-yl-7-oxyl
TP-CLST	3β-DOXYL-5α-cholestane
TOCSY	total correlation spectroscopy
TTL	transistor-transistor logic
TWT	travelling wave tube
VB	video bandwidth
VG	video gain
VNA	vectorial network analyzer
X-Band	$8 - 12$ GHz
Q-Band	$26 - 40$ GHz
W-Band	$75 - 110$ GHz
mm-Band	$110 - 300$ GHz

Symbols

A	hyperfine coupling constant
$A(\omega)$	real (absorptive) part of a lorentzian line
α	spin state "up"
B_0	main magnetic field
B_{1e}	microwave field strength
β	spin state "down"
c	concentration
C	constant
d	distance
D	diffusion constant
$D(\omega)$	imaginary (dispersive) part of the a lorentzian line
E_a	activation energy
E_{rt}	energy at room temperature ($T = 300\,\mathrm{K}$)
E_{rel}	relative energy
E	electric field
ϵ	enhancement factor
ϵ_r	relative dielectric constant
η	NOE NMR signal enhancement
f	leakage factor
f_M	molar fraction
$F\{\}$	fourier transformation
g	Landé factor
γ	gyromagnetic ratio
$\mathcal{H}$	Hamiltonian
h	filling height
$h(t)$	EPR signal in the time domain
$H(\omega)$	EPR signal in the frequency domain
H	magnetic field
$\hbar$	reduced Planck constant

$i_{1,2}$	signal intensity of the ELDOR and inversion recovery experiment
$I_{\mathrm{Bltz/DNP}}$	intensity or integrated signal intensity of the Boltzmann or DNP signal
I	nuclear spin
$\langle I_z \rangle$	expectation value of the nuclear spin magnetization
$\hat{I}_{x,y,z}$	nuclear spin operators
$\hat{I}_{+,-}$	nuclear shift operators
I_{main}	main magnetic field current
I_{gun}	gun current
I_0	collector current
$J_{\mathrm{trans/rot/con}}$	translational, rotational, and contact spectral density
${}^n J$	n bond J coupling between two nuclei
k	proportionality constant
$k_{\mathrm{rot/D/con}}$	pre-factor of the translational, rotational, and contact spectral density
k_{B}	Boltzmann constant
K_{Ox}	proportionality constant for oxygen content
K_X	Heisenberg exchange factor
m_S	electron spin state
m_I	nuclear spin state
μ	magnetic moment
μ_{B}	Bohr magneton
μ_0	vacuum permeability
μ_{r}	relative permeability of a medium
n	refraction index
N	population of a spin state
N_{A}	Avogadro constant
ω	angular resonance frequency
Ω	chemical shift
p	pressure
P_{pol}	polarization
P	power
r	distance
R	relaxation rate

ρ	spin density
s	saturation factor
S	electron spin
$\langle S_z \rangle$	expectation value of the electron spin magnetization
$\hat{S}_{x,y,z}$	electron spin operators
$\hat{S}_{+,-}$	electron shift operators
τ	delay of pulse sequences
$\tau_{D/C/con}$	correlation time of the translational, rotational, and contact interaction
τ_m	mixing time
T_{1e}	electron spin lattice relaxation time
T_{1n}	nuclear spin lattice relaxation time
T_{2e}	electron spin transversal relaxation time
t	time
t_p	pulse duration
T	temperature
$T_{Build\text{-}up}$	Build-up time
T_{cav}	cavity temperature
V	volume
$V_{gyr,H2O/gyr}$	voltage observed on the calorimeter of the gyrotron
V_0	cathode voltage
w_e	electron spin transition rate
w_n	nuclear spin transition rate
w_0	zero quantum transition rate
w_2	double quantum transition rate
w^0	relaxation rate excluding relaxation induced by the two spin system ($S = 1/2$ and $I = 1/2$)
ξ	coupling factor

List of Figures

2.1 Four level diagram of an electron spin $S = 1/2$ coupled to a nuclear spin $I = 1/2$. 8
2.2 Sketch of the different polarization transfer mechanisms in liquid state DNP. 11
2.3 A_{iso} as a function of t in the pulse model. 15
2.4 Spectral densities of the rotational diffusion, the translational diffusion, and the contact interaction. 16
2.5 Coupling factor as a function of the magnetic field. 19
2.6 Saturation factor as a function of the microwave field strength. 23
2.7 Schematic representation of the three-spin effect between an electron spin, a ^{13}C nucleus, and a ^{1}H nucleus. 24
2.8 T_{1e} and its components as a function of the electron spin resonance frequency. 28

3.1 Pulse sequences used for the determination of the electron spin longitudinal relaxation time. 36
3.2 ELDOR pulse sequence used for the determination of s during DNP. . . . 37
3.3 Pulse sequences used for the determination of the build-up time, the nuclear relaxation during DNP, and the nuclear relaxation time without mw irradiation. 37
3.4 1D NMR pulse sequences that were used for DNP measurements in this work. 39

3.5 Pulse sequence of the 2D double quantum filtered correlation spectroscopy experiment (DQF COSY). 40
3.6 Pulse sequence of the 2D experiment called total correlation spectroscopy (TOCSY). 42
3.7 Pulse sequence of the 2D incredible natural abundance double quantum transfer experiment (INADEQUATE). 44

4.1 Molecular structures of the organic radicals tested as PAs for DNP in the liquid state. 51
4.2 ^{13}C DNP coupling factors of $CHCl_3$, CCl_4, and ^{1}H DNP coupling factors of $CHCl_3$ and toluene at 1.2 T and 0.34 T, respectively. 53
4.3 Electron spin density maps of DFT optimized structures of BDPA and TN. 56
4.4 Hyperfine coupling of geometry optimized complexes of PA/$CHCl_3$. . . . 58
4.5 Signal enhancement, ELDOR curve, nuclear relaxation, and build-up measurement for DTBN in toluene. 63
4.6 Plots of the ^{1}H-DNP Overhauser parameters from tab. 4.2, tab. 4.3, and tab. 4.4. 64
4.7 Plots of the ^{13}C-DNP Overhauser parameters from tab. 4.5 and tab. 4.6. The inset displays the structure of the PAs used in ref. [83]. 66
4.8 Electron spin density calculated for TN-py and DTBN optimized structures. 67
4.9 Optimized structures of organic radicals and Löwdin spin density. 68
4.10 Conformations of the radical TN-py that are accessible at room temperature ($E_{rt} = 2.49\,kJ/mol$ at $T = 300\,K$). 70
4.11 Optimized structures for the complexes TN/$CHCl_3$ and BDPA/$CHCl_3$. . 70
4.12 Geometry optimized structures of the complex TN/$CHCl_3$. 71

5.1 ^{1}H coupling factor of $CHCl_3$ and toluene as a function of the temperature. 77
5.2 ^{1}H coupling factor of $CHCl_3$ and toluene as a function of the rotational correlation time. 78
5.3 Prediction of the ^{13}C coupling factor as a function of the magnetic field including the rotational correlation time. 81
5.4 $\xi_{13C}^{FN\text{-}2a}$ in CCl_4 and $CHCl_3$ as a function of the magnetic field. 84

5.5 Structures of the nitroxide derivatives used as polarizing agents and of the reduced form of TN, which was used for diffusion measurements (TNH). 85
5.6 Continuous wave EPR spectra obtained at 9.4 GHz of tempol in chloroform and toluene. 86
5.7 Continuous wave EPR spectra obtained at 9.4 GHz of different polarizing agents in chloroform at room temperature. 87
5.8 Correlation time of tempol in toluene and chloroform obtained from cw EPR measurements as a function of temperature. 87
5.9 Diffusion coefficient of chloroform (D_{CHCl3}) and TNH in chloroform ($D_{\mathrm{TL,CHCl3}}$) as a function of the temperature. 89
5.10 DFT optimized geometries for two orientations of the complex TL/toluene. 90
5.11 ELDOR curves for tempol in chloroform at room temperature. 92
5.12 $T_{1\mathrm{n}}$ and $T_{\text{Build-up}}$ measurements at two representative temperatures for a sample of toluene (aromatic ring protons) doped with tempol. 93
5.13 ^{1}H-DNP spectra at 0.34 T of toluene and chloroform doped with TL. . . 94
5.14 Experimental data and simulation of $\xi_{1\mathrm{H}}$ as a function of τ_{C} of of the PA in $CHCl_3$. 99
5.15 Coupling factor of FN-2a in CCl_4 as a function of the magnetic field. . . 101
5.16 DFT-optimized conformations and relative energies (excluding dispersion correction) for TN. 101
5.17 Atom numbering scheme for TN. 103
5.18 DFT-optimized conformations and relative energies (excluding dispersion correction) for the FN-2a model system. 104
5.19 DFT-optimized conformations and relative energies (excluding dispersion corrections) for the chain model system. 105
5.20 Model systems for investigations of fullerene charges. 106
5.21 Model system for the determination of the partial charges of the nitroxide group and linker. 106
5.22 FN-2a molecules with different positions for the two cyclopropyl substitutions and time traces of the C-C distance between the methyl groups on the nitroxide ring. 107

5.23 Atom numbering scheme for the side chain and the nitroxide group of the fullerene nitroxide. . . . 108

6.1 Continuous wave EPR spectra of ^{15}N-TN-d$_{16}$ in CCl_4 at 0.35 T (a-c) and 9.4 T (d-f). . . . 113
6.2 Electron spin longitudinal relaxation time measurements at X-, Q-, and W-band. . . . 116
6.3 Inversion recovery experiments to obtain T_{1e} of 10 mM ^{15}N-TN-d$_{16}$ in CCl_4 at 263 GHz at different time points t after removing the sample from N_2 atmosphere. . . . 118
6.4 Real and imaginary part of the inversion recovery experiment to obtain T_{1e} of 10 mM ^{15}N-TN-d$_{16}$ in CCl_4 at 263 GHz. . . . 120
6.5 Experimental values and theoretical calculation for T_{1e} as a function of the electron spin resonance frequency. . . . 121

7.1 263 GHz cw EPR spectra of ^{15}N-TN-d$_{16}$, BDPA, and galvinoxyl. . . . 126
7.2 Gyrotron sketch. . . . 128
7.3 Sketch of the vacuum tube of the gyrotron. . . . 130
7.4 Power dependence for defined gyrotron settings. . . . 131
7.5 Frequency and power characterization of the gyrotron. . . . 133
7.6 Quasi-optical table. . . . 135
7.7 Drawing of the DNP probehead. . . . 136
7.8 Microwave beam alignment tests. . . . 137
7.9 Microwave polarization at the sample position. . . . 139
7.10 CST calculation of the microwave field strength at the sample. . . . 141
7.11 Comparison of CST calculations of the microwave field strength at the sample for tetrachloromethane and water. . . . 143
7.12 Sample geometry of DNP at 9.4 T. . . . 146
7.16 Summary of the NMR signal enhancements at 9.4 T. . . . 158
7.17 ^{13}C NMR signal enhancement of p-IC_6H_4F and 1-fluoro-4-(trichloromethyl)-benzene in CCl_4. . . . 159
7.18 Demonstration of the NMR linewidth under DNP conditions. . . . 161

7.19 ^{13}C NMR signal enhancement of uniformly ^{13}C enriched halogenated aromatic compounds. 163
7.20 ^{13}C NMR signal enhancement of different functionalized aromatic compounds. 167
7.21 ^{13}C NMR signal enhancement of biological relevant compounds. 169
7.22 Temperature calibration for DNP measurements in the solvents CCl_4 and $CHCl_3$. 172
7.23 Temperature calibration for DNP measurements in water. 173
7.24 Magnetic field optimization for DNP in different solvents. 175
7.25 ^{13}C NMR signal enhancement of $^{13}CH_3CN$ in different polar solvents. . . 176
7.26 ^{13}C NMR signal enhancement of $^{13}C_3$ Na pyruvate and Na diatrizoate. . 178
7.27 ^{13}C DNP DQF COSY spectrum of ^{13}C enriched iodobenzene. 182
7.28 ^{13}C DNP TOCSY spectrum of ^{13}C enriched iodobenzene. 184
7.29 ^{13}C DNP INADEQUATE spectrum of natural abundant *p*-IC_6H_4F. 186

8.1 ^{13}C NMR signal enhancement times the amount of substance ($\epsilon \cdot n$) as a function of the magnetic field. 193

A.1 Real and imaginary part of the inversion recovery experiments of the samples $3-6$ of tab. 6.2. 226
B.1 Calibration of g_{iso} of N@C_{60} at 263 GHz using a carbon fiber according to the protocol from ref. [105]. 229
C.1 Boltzmann spectra and DNP spectra of ~ 500 mM $^{13}CHCl_3$ in CCl_4 doped with ~ 25 mM ^{15}N-TN-d_{16} with different sample heights *h*. 230
C.2 ^{13}C NMR spectra of $^{13}C_6$-C_6H_5Cl and $^{13}C_1$-C_2-indole with and without mw irradiation. 233
C.3 ^{13}C NMR spectra of a) $^{13}C_6$-C_6H_5Br (no ^{1}H pre-saturation) and b) $^{13}C_6$-C_6H_5Br (^{1}H pre-saturation) with and without mw irradiation. 234
C.4 ^{13}C NMR spectra of $^{13}C_6$-C_6H_5I (no ^{1}H pre-saturation) and $^{13}C_6$-C_6H_5I (^{1}H pre-saturation) with and without mw irradiation. 235
C.5 ^{13}C NMR spectra of a) $^{13}C_6$-GlcOMe and b) C_6H_5Br with and without mw irradiation. 236

C.6 ^{13}C NMR spectra of $C_6H_5NO_2$ and $C_6H_5COOCH_3$ with and without mw irradiation. . . . 237
C.7 ^{13}C NMR spectra of *p*-Cl-toluene and toluene with and without mw irradiation. . . . 238
C.8 ^{13}C NMR spectra of benzene and anisole with and without mw irradiation. 239
C.9 ^{13}C NMR spectra of 1,4-$Cl_2C_6H_{10}$ and diethylmalonate with and without mw irradiation. . . . 240
C.10 ^{13}C NMR spectra of $^{13}CBr_4$, neat CCl_4, and neat $CHCl_3$ with and without mw irradiation. . . . 241
C.11 ^{13}C NMR spectra of $CHCl_3$ (and CH_2Cl_2) in CH_2Cl_2 and CH_2Cl_2 in CCl_4 with and without mw irradiation. . . . 242
C.12 ^{13}C NMR spectra of DDT and *p*-I-C_6H_4-$COOCH_3$ with and without mw irradiation. . . . 243
C.13 ^{13}C NMR spectra of Na diatrizoate and *P*-I-C_6H_4F with and without mw irradiation. . . . 244
C.14 ^{13}C NMR spectra of $^{13}C_6$-C_6H_5Br in $^{13}CCl_4$ and $^{13}C_6$-C_6H_5Br in C_6H_6 with and without mw irradiation. . . . 245
C.15 ^{13}C NMR spectra of $^{13}C_6$-C_6H_5Br in C_6H_{12} with and without mw irradiation. 246
C.16 ^{13}C NMR spectra of $^{13}C_6$-C_6H_5I in C_6H_{12} and $^{13}C_6$-C_6H_5I in $CHCl_3$ with and without mw irradiation. . . . 247
C.17 ^{13}C NMR spectra of $^{13}CH_3CN$ in CH_2Cl_2 with and without mw irradiation. 248
C.18 ^{13}C NMR spectra of indole with and without mw irradiation. . . . 248
D.1 Inversion recovery experiments to obtain the nuclear spin-lattice relaxation time of 3-$^{13}C_1$-pyruvate in presence and absence of PA. . . . 249
D.2 Inversion recovery experiments to obtain the nuclear spin-lattice relaxation time of $^{13}C_6$-C_6-C_6H_5Br in presence and absence of PA. . . . 249
E.1 Temperature calibration of dichloromethane. . . . 250
E.2 Temperature calibration of acetonitrile. . . . 251
E.3 Calibration of T_{set} to obtain T_{sample} by comparison of the chemical shift of the ^1H signals of methanol. . . . 252

List of Tables

4.1 Overhauser parameters f, s, ϵ, and ξ for ^{13}C at 1.2 T and ^{1}H DNP at 0.34 T for different PAs in chloroform. 54

4.2 ^{1}H Overhauser parameters of the methyl group of toluene for different PAs at room temperature and at 0.34 T. 60

4.3 ^{1}H Overhauser parameters of the ring protons of toluene for different PAs at room temperature and at 0.34 T. 61

4.4 ^{1}H Overhauser parameters of chloroform for different PAs at room temperature and at 0.34 T. 62

4.5 ^{13}C Overhauser parameters of $^{13}CCl_4$ for different PAs at room temperature and at 1.2 T. 65

4.6 ^{13}C Overhauser parameters of $^{13}CHCl_3$ for different PAs at room temperature and at 1.2 T. 65

4.7 SAS and SES areas calculated for the radical site of the organic radical, i.e. the NO group for NODs and the allyl group for BDPA. 68

4.8 Hyperfine coupling on the C atom of $CHCl_3$ calculated for the complexes PA/$CHCl_3$. 69

5.1 Translational and rotational correlation times of different nitroxide radicals in $CHCl_3$ and toluene. 79

5.2 Correlation times and amplitudes of the contributions used for simulating the coupling factor ξ_{13C}^{TN} and $\xi_{13C}^{FN\text{-}2a}$ as a function of the magnetic field. . . 83

5.3 Rotational correlation times from cw EPR for different polarizing agents at room temperature. 88
5.4 Fit parameters for the calculation of $D(T)$ in toluene and chloroform. . . 90
5.5 Diffusion coefficients of TNH in toluene ($D_{TL,tol}$), TNH in chloroform ($D_{TL,CHCl3}$), and self-diffusion coefficient of chloroform (D_{CHCl3}) as a function of the temperature. 91
5.6 Nuclear relaxation times and Overhauser parameters for each measured temperature in toluene at 0.34 T. 95
5.7 Nuclear relaxation times and Overhauser parameters for each temperature measured in chloroform at 0.34 T. 96
5.8 Nuclear relaxation times and ^{1}H Overhauser parameters for chloroform doped with nitroxide derivatives at room temperature and 0.34 T. 97
5.9 Nuclear relaxation times and ^{1}H Overhauser parameters at 0.34 T for tempol and FN-2a in chloroform at room temperature. 97
5.10 Nuclear relaxation times and ^{13}C Overhauser parameters for nitroxide derivatives at room temperature ans 1.2 T. 97
5.11 Fit parameters used in eq. 5.2 to fit ξ_{1H} as a function of the correlation time τ_C. 99
5.12 Parameters used for simulating ξ_{13C} as a function of τ_C at 1.2 T for CCl_4 and $CHCl_3$. 100
5.13 Partial charges for chloroform. 102
5.14 Partial charges for TN. 103
5.15 Partial charges for FN-2a. 108

6.1 ΔB_{pp} and T_{2e} obtained from fig. 6.1 from the low field resonance of the spectrum. 115
6.2 T_{1e} at 263 GHz obtained from inversion recovery experiments on different samples. 119

7.1 A_{iso} and g_{iso} of different PAs at 9.4 T. 127
7.2 Output power of different gyrotron power settings. 132
7.3 Frequency stability of the gyrotron. 134
7.4 Power losses through the probehead at the sample position. 140

7.5 Calculated sample volume during DNP at 9.4 T. 147
7.6 Comparison of the ^{13}C NMR signal enhancement of $^{13}C_6$-BrC_6H_5, $^{13}C_6$-C_6H_5I, and diethylmalonate doped with ^{15}N-TN-d_{16} obtained with and without ^{1}H pre-saturation during mw irradiation. 150
7.7 Radiofrequency power and NMR linewidth comparison to a standard NMR probehead. 155
7.8 Radiofrequency power and NMR linewidth characterization under DNP conditions. 156
7.9 ^{13}C NMR signal enhancement of $^{13}C_6$-BrC_6H_5 and $^{13}C_6$-C_6H_5I doped with ^{15}N-TN-d16 in different solvents. 162
7.10 ^{13}C NMR signal enhancement and NMR linewidth of $^{13}CH_3CN$ in different polar solvents. 177

A.1 Experimental parameters of inversion recovery experiments on different samples (fig. 6.3, fig. 6.4, and fig. A.1). 227
B.2 Samples used for the determination of g_{iso} and A_{iso} of different PAs at 263 GHz. 228
B.3 Experimental parameters for cw EPR at 263 GHz of different PAs. 228
C.4 Experimental NMR parameters of the DNP enhancements presented in this thesis. 231
C.5 Experimental mw parameters of the DNP enhancements presented in this thesis. 232

1 Introduction

The discovery of nuclear magnetic resonance (NMR)[1,2] in 1946 marks the birth of a method that contributed to advancements of many scientific research areas ranging from biology[3,4] and medicine[5,6] to chemistry,[7] material sciences,[8,9] and far beyond. NMR detects small energy differences of nuclear Zeeman spin states in an external magnetic field.[10] Due to the required low frequency radiation, NMR is termed a non-invasive method that is harmless for the investigated target.[10] After the discovery of NMR, the method quickly matured and enabled the investigation of molecular structures in many forms and sizes. The advancements towards high resolution NMR and its application on biomolecular systems led to the award of two nobel prizes to Ernst (1991) and Wüthrich (2002).

Alongside with NMR, also magnetic resonance imaging (MRI)[11] quickly developed into a standard technique in hospitals all around the world, culminating in the award of another nobel prize for Lauterbur and Mayfield in 2003.

As of today, NMR is a routine tool for the characterization of synthetic products and almost every chemistry laboratory has access to an NMR spectrometer. Aside from day-to-day NMR, cutting edge spectroscopy is performed on a large variety of biological macromolecules such as proteins,[3] DNA and RNA[12] as well as disordered systems such as amyloid fibrils.[13] The advantage of NMR over other structure elucidation methods like X-ray and cryogenic electron microscopy is the capability to also investigate dynamics and interactions with other molecules in the liquid phase.

Despite the success of NMR, it still suffers from the inherent problem of low sensitivity

that arises from the aforementioned small energy difference of the nuclear Zeeman spin states.[10] As a result the spin polarization i.e. the difference of the population of the two spin states is such that at a magnetic field of 9.4 T only one out of 100 000 spins contributes to the signal.[14] Strategies to improve the sensitivity of standard NMR aim to increase the magnetic fields, optimize pulse sequences, and develop hardware.[15]
Another possibility to boost the sensitivity is the hyperpolarization of nuclei through interaction with highly polarized spin systems such as electron spins[15,16] or para-hydrogen.[17,18]
One subset of hyperpolarization methods is dynamic nuclear polarization (DNP), where spin polarization is transferred from electron spins that are, due to their increased magnetic moment, more polarized than nuclear spins.[16] Electron spins are usually added in the form of small stable organic radicals like nitroxide based radicals.[16,19]
With the introduction of high power microwave (mw) sources, such as gyrotrons, to magnetic resonance (MR), DNP in solids with signal enhancements of $\epsilon \geq 100$ was reported.[20–22] Due to the ability to perform DNP experiments at $\sim 100\,\mathrm{K}$, which compensated dielectric heating of the sample by mw irradiation, and a favorable polarization transfer mechanism in solids, solid-state NMR (ssNMR) DNP quickly developed into a viable tool to increase the NMR signal intensity of biological systems such as proteins.[23–25]
This was enabled by constant progress of the hardware but also by extensive investigations of the spin polarization mechanism and led to the discovery of new polarizing agents (PA), i.e. the electron spin carrying molecules. Early DNP measurements were performed with nitroxide radicals,[20] which were superseded by bi-nitroxide radicals.[26–28] Further optimization led to the discovery of even more efficient PAs such as mixed bi-radicals consisting of a nitroxide and either a trityl or a BDPA (α,γ-bisdiphenylene-β-phenylallyl) radical.[29,30]
Similar to the solid-state, DNP in liquids is also an active research area.[15,31–34] Significant signal enhancement above 10 000 were achieved by hyperpolarization in frozen solution at low temperature ($T \approx 1.2\,\mathrm{K}$) and medium magnetic field ($B_0 \approx 3.34\,\mathrm{T}$), rapid dissolution (dDNP) of the hyperpolarized substance, and subsequent detection at room-temperature.[31] After detection of the significantly enlarged signal, polarization is depleted and, because hyperpolarization is performed ex situ, cannot be quickly replenished. NMR acquisition is combined with ultra-fast NMR methods[35] and non-uniform sampling[32] but is limited by the nuclear spin relaxation time T_{1n} of the hyperpolarized

nucleus.[31,36] The situation is similar in para-hydrogen induced hyperpolarization (PHIP), where hyperpolarization is achieved by introduction of para-hydrogen into the target molecule.[17,18] Both techniques are therefore particularly well suited for MRI[5,6,17,18] but are also applied in NMR spectroscopy in special cases.[32,36,37]

Another technique in liquids is Overhauser DNP (ODNP). Predicted by Overhauser[38] and experimentally verified by Slichter,[39] it represents the earliest reported DNP mechanism. The advantage of ODNP over dDNP and PHIP is that it allows for signal averaging and easy integration in routine NMR pulse sequences, provided the necessary hardware is available.[34,40,41] In liquids, ODNP relies on cross-relaxation of an electron spin with a nuclear spin.[42] Cross-relaxation is driven by the modulation of the hyperfine coupling between the two interacting spins that in liquids is caused by molecular motions.[16,43]

The ODNP research of the last decades unravelled the spin polarization transfer mechanism and its performance at high magnetic field.[42,44,45] Unfortunately, the DNP efficiency decreases with increasing magnetic field.[46] This is particularly true, if the cross-relaxation is mainly caused by modulation of the electron nuclear dipolar hyperfine interaction through rotational and translational diffusion as it is the case for ^{1}H.[43,47–50] Due to hardware improvements,[51–54] a signal enhancement of $\epsilon \approx -83$ of H_2O at a sample temperature of 160 °C was obtained at 9.4 T.[55] Experimental observations at this magnetic field confirmed the theoretical predictions that large signal enhancements for ^{1}H DNP at high magnetic fields are a challenging task.[33,46,56]

Another target for ODNP are ^{13}C nuclei, because direct ^{13}C experiments deliver valuable insights in, for example, biomolecules, but are, due to the inherently low sensitivity of ^{13}C (low natural abundance of 1.1 % and small γ), currently challenging.[57] Initial ^{13}C ODNP experiments at low and medium field delivered surprisingly large signal enhancement of up to a factor of $\epsilon \approx 950$ on model systems.[58–60] Subsequent investigation of the magnetic field dependence demonstrated that large signal enhancements $\epsilon \geq 300$ are also accessible at magnetic fields as high as 9.4 T.[34] This was possible, because the spin polarization transfer is dominated by scalar cross-relaxation that is modulated by molecular collisions. This mechanism efficiently mediates spin polarization even at high magnetic fields and large ODNP enhancements were reported on ^{13}C at magnetic field up to 14 T with an enhancement of $\epsilon \approx 70$ on $^{13}CHCl_3$.[34,40,61]

Aside from mechanistic challenges, the development of ODNP at high magnetic field also

faced significant hardware limitations. Strong microwave absorption of the solvent at high magnetic field produced extensive sample heating and limited the sample volume to $V_{sample} \ll 1\,\mu L$.[55] As a counter-measure, mw irradiation and NMR detection were separated and electron spins were excited at low magnetic field, while NMR detection was performed at high magnetic field. This included a shuttle-spectrometer,[62] continuous flow setups,[59] and rapid-melt instruments.[63] Continuous flow setups were also combined with MRI detection,[64,65] supercritical CO_2,[66] and with benchtop NMR for industrial process monitoring.[67]

A combination of the favorable spin polarization transfer mechanism of ^{13}C and hardware optimizations led to the detection of sizable ^{13}C signal enhancements of up to $\epsilon(CBr_4) \approx 600$ in organic solvents and to $\epsilon \approx 50$ in water on imidazole with a sample volume of $V_{sample} \leq 100\,nL$.[33,34] Furthermore, liquid state DNP setups were reported at 9.4 T[68] as well as 14 T.[69]

These promising results of ^{13}C DNP at high magnetic field have sparked new interest in the development of dedicated liquid state DNP spectrometers at high magnetic field and in the further investigation of the spin polarization transfer mechanism of ^{13}C.[33,40,41,70]

In order to contribute to the advancement of liquid state DNP, this work follows two paths. First, mechanistic investigations of the PA and target molecule complex are performed to obtain information on structural and dynamical features of the PA that may boost DNP at high magnetic field ($B_0 \geq 9\,T$).

Second, the design, implementation, and characterization of a new high mw power ($P \leq 50\,W$), high magnetic field (9.4 T), and large sample volume ($V_{sample} \approx 20 - 40\,\mu L$) liquid state DNP spectrometer is presented. DNP experiments were performed on different organic compounds, which included pharmaceutical drugs. Furthermore, ODNP experiments were performed in water and other polar solvents. Finally, the integration of 2D NMR pulse sequences with DNP was demonstrated.

Chapter 2 summarizes the theoretical framework necessary to follow the presented results, while chapter 3 gives an overview on the materials and methods employed in this work. Chapter 4 discusses the influence of the molecular structure on the DNP efficiency and chapter 5 reveals dynamic processes that are important for liquid state DNP. Chapter 6 presents the experimental access to electron spin relaxation data at 9.4 T that are essential to evaluate DNP experiments at this magnetic field. Chapter 7 includes the implemen-

tation and characterization of a new DNP instrument operating at 9.4 T. It discusses the experimental results on a variety of target molecules in different solvents including water and compares with the recent literature. Furthermore, the implementation of 2D NMR pulse sequences in DNP is presented. Chapter 8 summarizes and draws conclusions from the presented data and highlights the mechanistic implications obtained from the results of the previous chapters 4–7. Finally, NMR signal enhancements and linewidths at 9.4 T are set into context of the current literature and an outlook for upcoming projects is presented, which includes projects immediately accessible with the current setup and also long term goals.

2 Theoretical Background

In this chapter, the theoretical framework, necessary to understand the results presented within this thesis, is established.

Albert Overhauser predicted the Overhauser effect in 1953.[38] He postulated the possibility to transfer spin polarization from electron spins to nuclear spins. Experimental proof was published shortly after by Carver and Slichter.[39] They demonstrated the polarization transfer in metallic lithium, however spin polarization transfer is also possible in liquids. Nowadays, many different DNP mechanisms were observed in the solid[22] as well as in the liquid state.[46] However, while in liquids different mechanisms were theoretically predicted,[71,72] only the Overhauser effect was demonstrated experimentally (excluding PHIP and chemically induced DNP (CIDNP)). Additionally, the solid-effect, thermal mixing, and the cross-effect are DNP mechanisms that are used in the solid state with great success.[22,25]

As this work only deals with the Overhauser effect in liquids, this chapter is limited to the Overhauser mechanism. This includes the discussion of all parameters of the Overhauser equation, their underlying physical principles, and the description of the molecular interactions and motions that are responsible for the polarization transfer. Experimental methods to access the Overhauser parameters are explained in chapter 3. Finally, the different contributions to electron spin lattice relaxation T_{1e} are reviewed. From this, the frequency dependence of T_{1e} is calculated. Knowledge of T_{1e} is essential to rationalize the saturation behaviour of DNP experiments at high magnetic field. As only a part of this thesis was dedicated to experimentally determine the electron spin-lattice

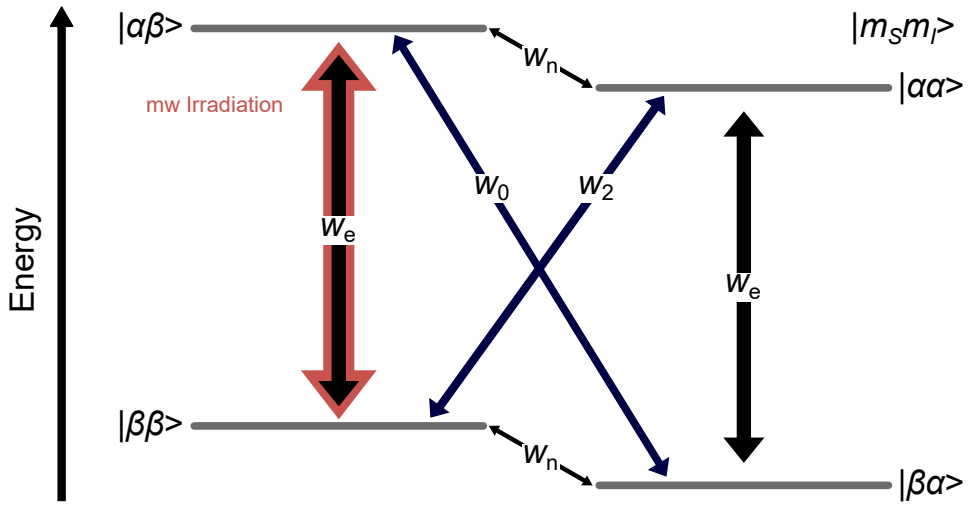

Figure 2.1: Four level diagram of an electron spin $S = 1/2$ coupled to a nuclear spin $I = 1/2$ with the spin states α and β. The first mentioned spin state belongs to the electron spin while the second belongs to the nuclear spin. Furthermore, w_e is the electron spin transition probability, w_n the nuclear transition probability, w_2 the double quantum, and w_0 the zero quantum transition probability.[42,76]

relaxation time at 9.4 T, the reader is for a more thorough description of electron spin resonance (EPR) in general referred to the literature.[73–75]

2.1 The Overhauser Equation

As soon as an electron spin S is placed in a magnetic field, the energetic degeneracy of its spin states m_S is lifted. This is called Zeeman effect and is observed for electron as well as for nuclear spins. For a spin S, $(2S + 1)$ m_S states exist that form the basis vectors of a $(2S + 1)$ dimensional Hilbert space. For the case of $S = 1/2$, the following notation is used[10]

$$m_S = \frac{1}{2} = |\alpha\rangle \equiv \begin{pmatrix} 1 \\ 0 \end{pmatrix}, \tag{2.1}$$

$$m_S = -\frac{1}{2} = |\beta\rangle \equiv \begin{pmatrix} 0 \\ 1 \end{pmatrix}. \tag{2.2}$$

The m_I states of a nuclear spin I are obtained in the same way. The basis vectors are normalized and orthogonal to each other. This can be expressed using the bra-ket notation[10]

$$\langle\alpha|\alpha\rangle = \langle\beta|\beta\rangle = 1, \tag{2.3}$$

$$\langle\alpha|\beta\rangle = \langle\beta|\alpha\rangle = 0. \tag{2.4}$$

The energy between the m_S (or m_I for nuclear) states is determined by the magnetic moment of the spin and is proportional to the gyromagnetic ratio γ. For an electron spin, γ_e is approximately 660 times larger than for ^{1}H atoms, the stable nucleus with the largest magnetic moment.

If two spins are in close proximity, they will interact with each other via dipolar or scalar hyperfine (hf) interaction. Figure 2.1 describes these two spin interactions in a four level energy diagram. To investigate the change of the population of the four states (due to spin-spin interaction), the rate equations for each energy level are written as[44,76]

$$\frac{\mathrm{d}N_{\alpha\beta}}{\mathrm{d}t} = w_\mathrm{e}N_{\beta\beta} + w_0N_{\beta\alpha} + w_\mathrm{n}N_{\alpha\alpha} - (w_\mathrm{e} + w_0 + w_\mathrm{n})\,N_{\alpha\beta} + C_1, \tag{2.5}$$

$$\frac{\mathrm{d}N_{\alpha\alpha}}{\mathrm{d}t} = w_\mathrm{e}N_{\beta\alpha} + w_2N_{\beta\beta} + w_\mathrm{n}N_{\alpha\beta} - (w_\mathrm{e} + w_2 + w_\mathrm{n})\,N_{\alpha\alpha} + C_2, \tag{2.6}$$

$$\frac{\mathrm{d}N_{\beta\beta}}{\mathrm{d}t} = w_\mathrm{e}N_{\alpha\beta} + w_2N_{\alpha\alpha} + w_\mathrm{n}N_{\beta\alpha} - (w_\mathrm{e} + w_2 + w_\mathrm{n})\,N_{\beta\beta} + C_3, \tag{2.7}$$

$$\frac{\mathrm{d}N_{\beta\alpha}}{\mathrm{d}t} = w_\mathrm{e}N_{\alpha\alpha} + w_0N_{\alpha\beta} + w_\mathrm{n}N_{\beta\beta} - (w_\mathrm{e} + w_0 + w_\mathrm{n})\,N_{\beta\alpha} + C_4, \tag{2.8}$$

with w_e being the electron spin transition probability, w_n the nuclear spin transition probability, and w_0 the zero and w_2 the double quantum transition probability, respectively. The populations are denoted with N and C_{1-4} are arbitrary constants. The expectation value of the nuclear $\langle I_\mathrm{z}\rangle$ and electron spin magnetization $\langle S_\mathrm{z}\rangle$ can be expressed in the form of population differences[42,44,76]

$$k_1\langle I_\mathrm{z}\rangle = (N_{\alpha\alpha} + N_{\beta\alpha}) - (N_{\alpha\beta} + N_{\beta\beta})\,, \tag{2.9}$$

$$k_2\langle S_\mathrm{z}\rangle = (N_{\beta\alpha} + N_{\beta\beta}) - (N_{\alpha\beta} + N_{\alpha\alpha})\,, \tag{2.10}$$

where $k_1 = k_2$ holds. With this at hand, the change of nuclear magnetization is calculated as[76]

$$\begin{aligned} k_1 \frac{\mathrm{d}\langle I_z\rangle}{\mathrm{d}t} &= \frac{\mathrm{d}\left(N_{\alpha\alpha} + N_{\beta\alpha}\right) - \left(N_{\alpha\beta} + N_{\beta\beta}\right)}{\mathrm{d}t}, \\ &= k_1 \left[-\langle I_z\rangle \left(2w_n + w_2 + w_0\right) + \langle S_z\rangle \left(w_2 - w_0\right) + \tilde{C}\right]. \end{aligned} \tag{2.11}$$

The constant $\tilde{C}$ is determined from the thermal equilibrium condition, i.e. $\frac{\mathrm{d}\langle I_z\rangle}{\mathrm{d}t} = 0$, $\langle S_z\rangle = S_0$ and $\langle I_z\rangle = I_0$:

$$\frac{\mathrm{d}\langle I_z\rangle}{\mathrm{d}t} = -I_0 \left(2w_n + w_2 + w_0\right) + S_0 \left(w_2 - w_0\right) + \tilde{C} = 0, \tag{2.12}$$

$$\tilde{C} = I_0 \left(2w_n + w_2 + w_0\right) - S_0 \left(w_2 - w_0\right). \tag{2.13}$$

Combining eq. 2.13 and eq. 2.11 yields the so-called Solomon equation[44]

$$\frac{\mathrm{d}\langle I_z\rangle}{\mathrm{d}t} = -\left(\langle I_z\rangle - I_0\right)\left(2w_n + w_2 + w_0\right) - \left(S_0 - \langle S_z\rangle\right)\left(w_2 - w_0\right). \tag{2.14}$$

The steady-state solution of the Solomon equation under constant microwave irradiation, i.e. $\frac{\mathrm{d}\langle I_z\rangle}{\mathrm{d}t} = 0$ and $\frac{\mathrm{d}\langle S_z\rangle}{\mathrm{d}t} = 0$ leads to the following expression[44,76]

$$\langle I_z\rangle = I_0 - \frac{\left(S_0 - \langle S_z\rangle\right)\left(w_2 - w_0\right)}{2w_n + w_2 + w_0}. \tag{2.15}$$

Finally, so far excluded relaxation pathways (i.e not induced by the two spins but rather by the lattice) are considered through the insertion of w^0. Furthermore, the ratio $\frac{S_0}{I_0}$ is equal to $\frac{\gamma_e}{\gamma_n}$. After some rearrangements, the famous Overhauser equation is obtained[42,44,76]

$$\underbrace{\frac{\langle I_z\rangle}{I_0}}_{\epsilon} = 1 - \underbrace{\frac{\left(w_2 - w_0\right)}{\left(2w_n + w_2 + w_0\right)}}_{\xi} \underbrace{\frac{\left(2w_n + w_2 + w_0\right)}{\left(2w_n + w_0 + w_2 + w^0\right)}}_{f} \underbrace{\frac{\left(S_0 - \langle S_z\rangle\right)}{S_0}}_{s} \underbrace{\frac{S_0}{I_0}}_{|\gamma_e|/\gamma_n}, \tag{2.16}$$

$$\epsilon = 1 - f\, s\, \xi \frac{|\gamma_e|}{\gamma_n}. \tag{2.17}$$

The Overhauser parameters are the NMR signal enhancement ϵ, the coupling factor ($\xi \in [-1.0; 0.5]$), the leakage factor ($f \in [0; 1]$), and the saturation factor ($s \in [0; 1]$).

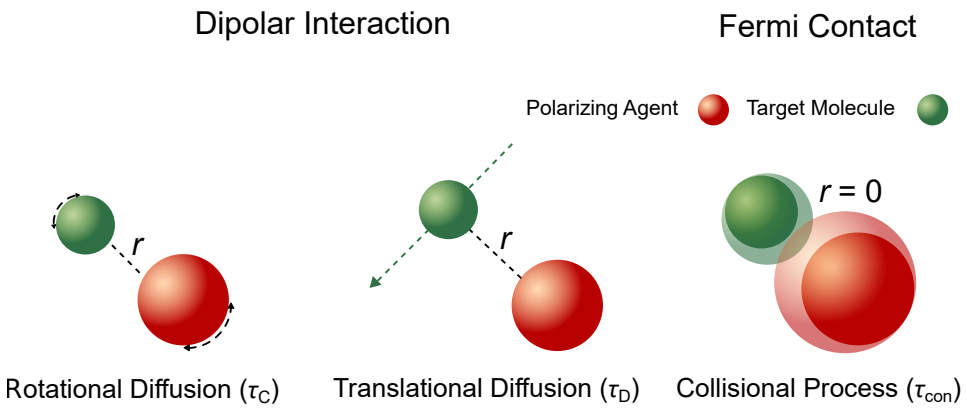

Figure 2.2: Sketch of the different polarization transfer mechanisms in liquid state DNP.

2.2 The Coupling Factor

To understand the physical mechanisms driving dynamic nuclear polarization in liquids, the coupling factor ξ is the relevant parameter. Recalling eq. 2.16, the coupling factor describes the ratio between the difference of zero- and double quantum transition probabilities and the sum of all nuclear spin transition probabilities that are induced by the electron spin[42]

$$\xi = \frac{w_2 - w_0}{2w_n + w_2 + w_0}. \tag{2.18}$$

It is particularly important to understand, which molecular interactions induce cross-relaxation (w_0 and w_2). In general, dipolar and scalar (isotropic) interactions are considered. Dipolar interactions are distance- as well as orientation dependent.[77] Therefore, it is rather straightforward to picture translational- and rotational diffusion of the two coupled molecules to induce a fluctuating dipolar magnetic field, that in turn causes cross-relaxation.[16,46] Scalar hyperfine coupling is modulated by molecular collisions, which is described by the pulse model.[78,79]

The timescale of the interactions is quantified by their correlation time τ. In order to efficiently mediate cross-relaxation, the motion has to modulate the hyperfine coupling (dipolar or scalar) with a frequency that is comparable to the resonance frequency of the electron spin. This is the case, if the condition $\omega\tau \approx 1$ is fulfilled (with ω being the angular resonance frequency). A sketch of these interactions is depicted in fig. 2.2.

Furthermore, while dipolar relaxation can induce all transitions depicted in fig. 2.1, scalar relaxation can only induce zero quantum transitions. This statement needs further explanation and can be understood by first considering the general expression for the spin Hamiltonians describing the dipolar and the scalar (isotropic) hf interaction[77]

$$\mathcal{H}_{\mathrm{D}} = \frac{\mu_0}{4\pi} g_e \mu_{\mathrm{B}} g_{\mathrm{n}} \mu_{\mathrm{n}} \left[\frac{3\left(\hat{\boldsymbol{S}} \cdot \boldsymbol{r}\right)\left(\boldsymbol{r} \cdot \hat{\boldsymbol{I}}\right)}{r^5} - \frac{\hat{\boldsymbol{S}} \cdot \hat{\boldsymbol{I}}}{r^3} \right], \tag{2.19}$$

$$\mathcal{H}_{\mathrm{con}} = \frac{2\mu_0}{3} g_{\mathrm{e}} \mu_{\mathrm{B}} g_{\mathrm{n}} \mu_{\mathrm{n}} \rho(0) \hat{\boldsymbol{I}} \cdot \hat{\boldsymbol{S}}. \tag{2.20}$$

Here, $\mu_{\mathrm{e/n}}$ are the magnetic moments of the electron and nuclear spin, r the distance between them, μ_{B} the Bohr magneton, μ_0 the vacuum permeability, g_{e} the g value of the free electron, g_{n} the nuclear g value, and $\rho(0)$ the spin density at the position of the nucleus. $\hat{\boldsymbol{S}}$ and $\hat{\boldsymbol{I}}$ are the spin operators. Bold symbols indicate a vector. Furthermore, the transition probabilities w_{ji} are calculated as[44]

$$w_{ij} = \frac{1}{t\hbar^2} \left| \int_0^t \langle j | \, \mathcal{H}'(t') \, | i \rangle \, e^{-i\omega_{ij} t} \mathrm{d}t' \right|^2, \tag{2.21}$$

where $\hbar$ is the reduced Planck constant, t the time, m_{ij} the eigenstates of i and j, $\mathcal{H}'(t')$ the time dependent Hamiltonian, perturbing the system and ω_{ij} the transition frequency between the states i and j. For a finite transition probability, the matrix element $\langle j | \, \mathcal{H}'(t') \, | i \rangle$ (i and j are of the form $m_S m_I$) needs to differ from zero. Subsequently, the matrix elements for each transition probability w_{ij} are evaluated. For the scalar case, the matrix elements of the form $\langle j | \, \hat{\boldsymbol{I}} \cdot \hat{\boldsymbol{S}} \, | i \rangle$ are calculated. The product $\hat{\boldsymbol{I}} \cdot \hat{\boldsymbol{S}}$ is equal to[76]

$$\hat{\boldsymbol{I}} \cdot \hat{\boldsymbol{S}} = \hat{I}_{\mathrm{x}} \hat{S}_{\mathrm{x}} + \hat{I}_{\mathrm{y}} \hat{S}_{\mathrm{y}} + \hat{I}_{\mathrm{z}} \hat{S}_{\mathrm{z}} = \frac{1}{2}\left(\hat{S}_- \hat{I}_+ + \hat{S}_+ \hat{I}_-\right) + \hat{I}_{\mathrm{z}} \hat{S}_{\mathrm{z}}, \tag{2.22}$$

where $\hat{I}_{x,y,z}$ and $\hat{S}_{x,y,z}$ are spin operators and $\hat{I}_{+,-}$ and $\hat{S}_{+,-}$ are the raising and lowering operators (or ladder/shift operators). The effect of the shift operators on the $|m_S m_I\rangle$ states is given by[76]

$$\hat{S}_+ |m_S m_I\rangle = |m_S + 1, m_I\rangle , \tag{2.23}$$

$$\hat{I}_+ |m_S m_I\rangle = |m_S, m_I + 1\rangle , \tag{2.24}$$

$$\hat{S}_- |m_S m_I\rangle = |m_S - 1, m_I\rangle , \tag{2.25}$$

$$\hat{I}_- |m_S m_I\rangle = |m_S, m_I - 1\rangle . \tag{2.26}$$

With this, the normalization relation (eq. 2.3), the orthogonality relation (eq. 2.4), and eq. 2.22, the transition matrix element for the w_0 transition induced by scalar coupling is given by ($|m_S m_I\rangle$ holds here)[76]

$$\langle\alpha\beta| \hat{\boldsymbol{I}} \cdot \hat{\boldsymbol{S}} |\beta\alpha\rangle = \langle\alpha\beta| \frac{1}{2} \left(\hat{S}_- \hat{I}_+ + \hat{S}_+ \hat{I}_- \right) + \hat{I}_z \hat{S}_z |\beta\alpha\rangle , \tag{2.27}$$

$$= \frac{1}{2} \langle\alpha\beta| I_+ S_- |\beta\alpha\rangle + \frac{1}{2} \langle\alpha\beta| \hat{I}_- \hat{S}_+ |\beta\alpha\rangle + \langle\alpha\beta| \hat{I}_z \hat{S}_z |\beta\alpha\rangle , \tag{2.28}$$

$$= \frac{1}{2} \underbrace{\langle\alpha\beta|\beta\alpha\rangle}_{=0} + \frac{1}{2} \underbrace{\langle\alpha\beta|\alpha\beta\rangle}_{\neq 0} + \underbrace{\langle\alpha\beta|\beta\alpha\rangle}_{=0} . \tag{2.29}$$

Notably, α refers to the $+\frac{1}{2}$ spin state, β refers to the $-\frac{1}{2}$ spin state, and the first named spin state in the ket notation is the m_S state ($|m_S m_I\rangle$).

As shown, the second term of eq. 2.29 does not vanish and therefore the transition probability is not zero. Evaluation of the other transitions reveals that only w_0 has a non vanishing transition matrix element for scalar relaxation. For the dipolar interaction, it was shown in a comparable way that all possible transitions depicted in fig. 2.1 can be induced.[76]

In order to gain a better understanding of the spin polarization transfer mechanism, the different contributions to nuclear relaxation are disentangled. Conveniently, rotational, translational, and collisional processes are described by spectral densities J. Rotational diffusion is described with a Lorentzian spectral density[80]

$$J_{\text{rot}}(\omega, \tau_C) = \frac{\tau_C}{1 + \omega^2 \tau_C^2}, \tag{2.30}$$

where ω is the angular resonance frequency and τ_C the rotational correlation time. Assuming $\omega_e \pm \omega_n \approx \omega_e$, the overall contribution of dipolar rotational diffusion to the nuclear relaxation rate R_1 is[43]

$$R_{1,\mathrm{rot}} = k_{\mathrm{rot}} \left[7J_{\mathrm{rot}}(\omega_e,\tau_C) + 3J_{\mathrm{rot}}(\omega_n,\tau_C)\right], \tag{2.31}$$

with k_{rot} being[43]

$$k_{\mathrm{rot}} = f_M \frac{2}{15}\left(\frac{\mu_0}{4\pi}\right)^2 \frac{\gamma_e^2 g_e^2 \mu_B^2 S(S+1)}{r^6}. \tag{2.32}$$

Here, f_M is the molar fraction of the bound state between target molecule and the radical, r the distance of closest approach between the two spins. Because an experimental determination of f_M and r is challenging, they may be accessed via molecular dynamic simulations.[56]

For the description of the translational diffusion, the force-free hard-spheres (ffhs) model by Freed is employed. It assumes the interacting spins to be in the center of undeformable spherical molecules.[81,82] The spectral density of the ffhs model is given by[81,82]

$$J_D(\omega_i,\tau_D) = \frac{1 + 5z/8 + z^2/8}{1 + z + z^2/2 + z^3/6 + 4z^4/81 + z^5/81 + z^6/648}, \tag{2.33}$$

where $z = \sqrt{2\omega\tau_D}$. The translational correlation time is

$$\tau_D = \frac{r_D^2}{D_{r,s} + D_s}, \tag{2.34}$$

with r_D being the distance of closest approach between electron spin and nuclear spin and D the diffusion coefficient of the polarizing agent ($D_{r,s}$) in the respective solvent and the target molecule containing the nuclear spin of interest (D_s, in the specific solvent). Similar to the rotational diffusion, the relaxation rate for translational diffusion is[43,80]

$$R_{1,D} = k_D \left[7J_D(\omega_e,\tau_D) + 3J_D(\omega_n,\tau_D)\right], \tag{2.35}$$

with[81,82]

$$k_D = \frac{32000\pi}{405}\left(\frac{\mu_0}{4\pi}\right)^2 \frac{N_A c \gamma_n^2 g_e^2 \mu_B^2 S(S+1)}{r_D(D_s + D_{r,s})}. \tag{2.36}$$

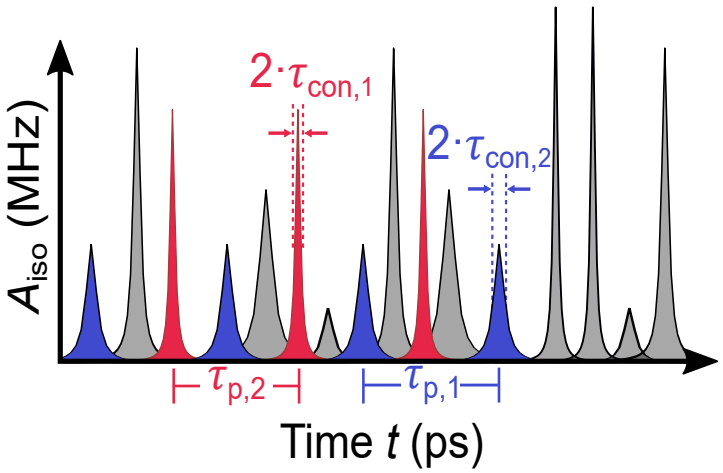

Figure 2.3: A_{iso} as a function of t in the pulse model. The graph highlights two different types of collision. Their correlation times $\tau_{con,1}$ and $\tau_{con,2}$ as well as $\tau_{p,1}$ and $\tau_{p,2}$ are indicated in the graph for clarity. Figure adapted from ref. [70].

Here, N_A is the Avogadro constant and c the concentration of the polarizing agent. Finally, the scalar interaction is described by the pulse model from Müller-Warmuth.[78,79] Within this model, the isotropic hf coupling A_{iso} between electron spin and nuclear spin is considered negligible unless the two molecules collide. Each type of collision is characterized by a duration $2\tau_{con,i}$ and the time between two similar encounters $\tau_{p,i}$ (with i being the type of encounter). The hf coupling as a function of the time t is depicted in fig. 2.3 for two different collisions.
The pulse model employs the following spectral density to describe the scalar interaction[78,79,83]

$$J_{con}(\omega_e, \tau_{con,i}) = \sum_{i=1}^{n} \frac{\langle A_i \rangle^2}{\hbar^2 \tau_{p,i}} \left[\tau_{con,i} \cdot \exp\{(-\tau_{con,i}\omega_e)\}\right]^2 . \tag{2.37}$$

This spectral density differs slightly from the original $J_{con}(\omega_e, \tau_{con,i})$ by Müller-Warmuth,[79] because here, each encounter is associated with a corresponding isotropic hyperfine coupling as well as the frequency of this particular encounter $\tau_{p,i}^{-1}$. In contrast, in the initial form $\tau_{p,i}^{-1}$ and $\langle A \rangle$ were not part of the sum and therefore not specific for each kind of encounter, which was compensated by a scaling factor x_i.[79] Finally, the nuclear relaxation rate of the Fermi contact interaction is given by[16,79]

$$R_{1,con} = k_{con} J_{con}(\omega_e, \tau_{con,i}), \tag{2.38}$$

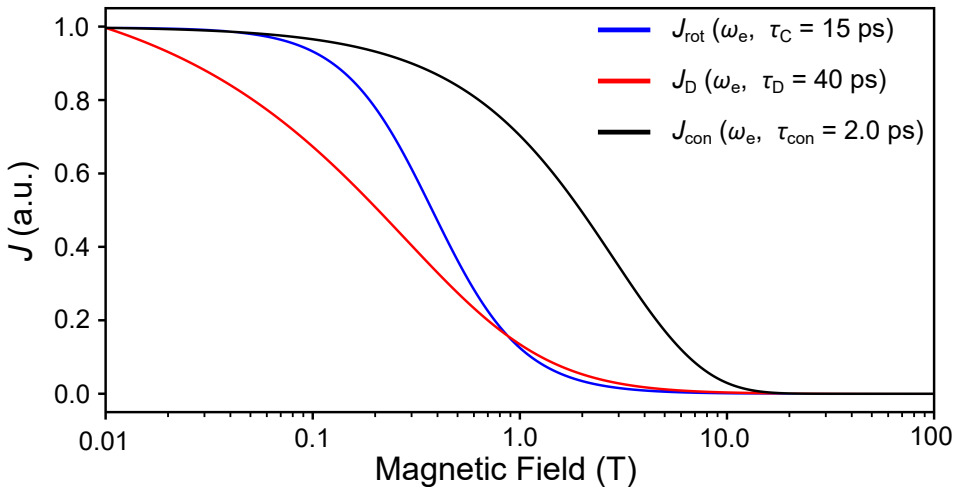

Figure 2.4: Spectral densities of the rotational diffusion (eq. 2.30, $\tau_C = 15\,\text{ps}$), translational diffusion (eq. 2.33, $\tau_D = 40\,\text{ps}$) and contact interaction (eq. 2.37, $\tau_{con} = 2.0\,\text{ps}$). For illustration, the spectral densities were scaled to $J \approx 1.0$ at $B_0 \approx 0\,\text{T}$. For J_{con}, a single correlation time was used.

with

$$k_{con} = \frac{2}{3} S(S+1). \tag{2.39}$$

So far, the description of scalar coupling deals with short encounters i.e. $^1/_{\tau_{con}} \gg A_{iso}$ (A_{iso} in MHz), which is called scalar relaxation of the first kind. Additionally, scalar relaxation of the second kind may occur, if the conditions $^1/_{T_{1e}} \gg A$ and $^1/_{T_{1e}} \gg {}^1/_{\tau_{con}}$ are met. However, for the interacting nucleus the result is the same: it experiences a fluctuating magnetic field, which may induce relaxation.[45]

Figure 2.4 compares the three spectral densities with realistic τ values for the representative case of a nitroxide radical interacting with a small molecule (e.g. CCl_4 or $CHCl_3$). The scalar interaction will induce cross-relaxation at much higher magnetic field than the dipolar mechanisms. This is the reason, why at high magnetic field scalar dominated cross-relaxation is targeted for Overhauser DNP.

Finally, eq. 2.18 is expressed in terms of spectral densities of dipolar (neglecting for now the translational diffusion and assuming $\omega_e \pm \omega_n \approx \omega_e$) and scalar relaxation[43,80]

$$w_0 = k_{rot} J_{rot}(\omega_e, \tau_C) + k_{con} J_{con}(\omega_e, \tau_{con}), \tag{2.40}$$

$$w_n = \frac{3}{2} k_{rot} J_{rot}(\omega_n, \tau_C), \tag{2.41}$$

$$w_2 = 6 k_{rot} J_{rot}(\omega_e, \tau_C). \tag{2.42}$$

Inserting eq. 2.40-2.42 into eq. 2.18 leads to[43,80]

$$\xi = \frac{6 k_{rot} J_{rot}(\omega_e, \tau_C) - k_{rot} J_{rot}(\omega_e, \tau_C) - k_{con} J_{con}(\omega_e, \tau_{con})}{6 k_{rot} J_{rot}(\omega_e, \tau_C) + k_{rot} J_{rot}(\omega_e, \tau_C) + k_{con} J_{con}(\omega_e, \tau_{con}) + 3 k_{rot} J_{rot}(\omega_n, \tau_C)}. \tag{2.43}$$

Summation of the paramagnetic contributions to nuclear relaxation leads to $R_{1,para} = R_{1,rot} + R_{1,con}$. This relation and eq. 2.38 are employed to rearrange eq. 2.43[43,80]

$$\xi = \frac{5 k_{rot} J_{rot}(\omega_e, \tau_C) - R_{1,con}}{R_{1,para}}, \tag{2.44}$$

$$\xi = \frac{5}{7} \left(1 - \frac{3 k_{rot} J_{rot}(\omega_n, \tau_C) - R_{1,con}}{R_{1,para}} \right) - \frac{12}{7} \frac{R_{1,con}}{R_{1,para}}. \tag{2.45}$$

For the limiting case of low magnetic field ($J_{rot}(\omega_e, \tau_C) \approx \tau_C$ and $J_{rot}(\omega_n, \tau_C) \approx \tau_C$) and pure dipolar relaxation ($R_{1,con} = 0$), eq. 2.45 reduces to[80]

$$\xi = \frac{5}{7} \left(1 - \frac{3\tau_C}{10\tau_C} \right) = 0.5. \tag{2.46}$$

Therefore, $\xi = 0.5$ is the theoretical limit for purely dipolar cross-relaxation. As scalar relaxation can only induce w_0, it can be easily seen from eq. 2.18 that the theoretical limit for exclusive scalar relaxation is $\xi = -1$.[80]
In order to include the contribution of translational diffusion to the paramagnetic relaxation rate, $R_{1,para}$ expands to

$$R_{1,para} = R_{1,rot} + R_{1,D} + R_{1,con}. \tag{2.47}$$

With this and with the inclusion of the translational spectral density, the final expression for the coupling factor is derived as[43,80]

$$\xi = \frac{5}{7}\left(1 - \frac{3k_{\mathrm{D}}J_{\mathrm{D}}(\omega_{\mathrm{n}},\tau_{\mathrm{D}}) + 3k_{\mathrm{rot}}J_{\mathrm{rot}}(\omega_{\mathrm{n}},\tau_{\mathrm{C}})}{R_{1,\mathrm{para}}}\right) - \frac{12}{7}\left(\frac{R_{1,\mathrm{con}}}{R_{1,\mathrm{para}}}\right). \tag{2.48}$$

This equation (eq. 2.48) is used to calculate the dependence of the coupling factor on the magnetic field. Figure 2.5a shows the magnetic field dependence of ξ using only Lorentzian spectral densities and only employing the contact interaction and rotational diffusion with $\tau_{\mathrm{C}} = \tau_{\mathrm{con}} = 20\,\mathrm{ps}$. For the different curves, the ratio between the contact interaction at low field and the overall relaxation (contact and rotational diffusion) was varied between 0 % (only dipolar relaxation) and 100 % (only scalar relaxation).[43] For dominant dipolar relaxation, ξ decays rapidly with increasing magnetic field, ($\xi(B \approx 10\,\mathrm{T}) \approx 0$), while scalar relaxation is still efficient at large magnetic field. In the limiting case of no dipolar relaxation ξ becomes independent of the magnetic field.

However, recent results show that the picture of a monotone decrease of the coupling factor, as shown in fig. 2.5a, is incomplete. If $\tau_{\mathrm{con}} \neq \tau_{\mathrm{C}}$, the magnetic field dependence of the coupling factor shows a distinct maximum and decays towards high magnetic field. Additionally, a shorter τ_{con} leads to a slower decay of ξ at high magnetic field. This is depicted in fig. 2.5b. In this case, the translational diffusion is calculated with the ffhs model (eq. 2.35 with $\tau_{\mathrm{D}} = 114\,\mathrm{ps}$), while the pulse model (eq. 2.38) is used for the scalar coupling (no contribution from rotational diffusion was used). The field dependence of ξ is shown for different τ_{con} and the case of $\tau_{\mathrm{con}} = 0.5\,\mathrm{ps}$ resembles the case of CCl_4 doped with nitroxide radical, which was observed experimentally.[34] This plot demonstrates the complex interplay between scalar and dipolar coupling, which may differ significantly for each target nucleus. In fact, it may also be possible that the coupling factor of a specific nucleus changes sign with increasing magnetic field. This could be the case, when the efficiency of dipolar relaxation decays faster than scalar relaxation.

Furthermore, recent molecular dynamics simulations revealed that even for longer lived bound states (e.g. hydrogen bond states) of two molecules, A_{iso} can, on top of this long lived state, still be modulated on shorter timescales. This indicates that the scalar mechanism might still be efficient, if intermolecular interactions lead to long lived states, which is the case in, for example, protein-drug complexes.[70]

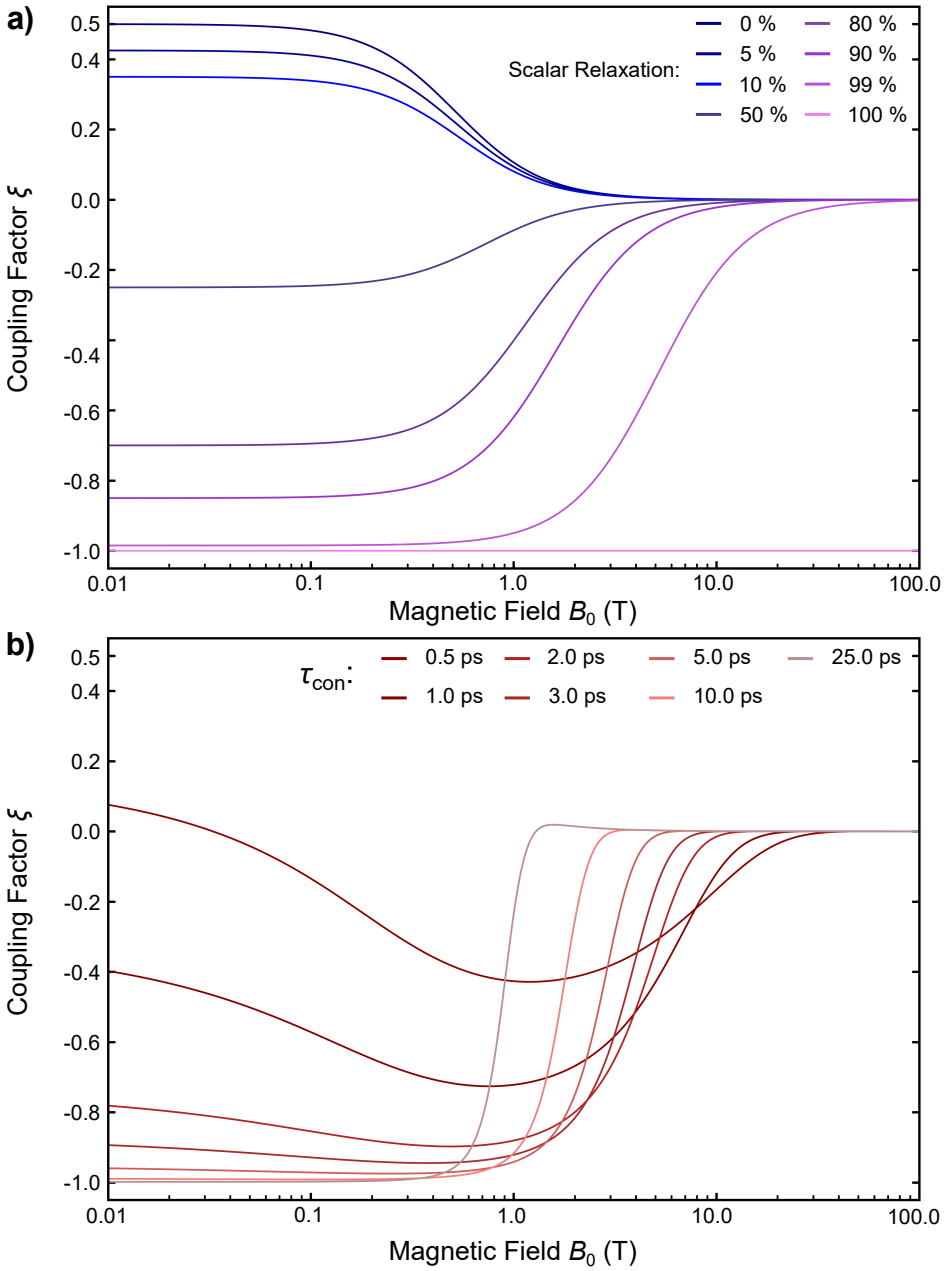

Figure 2.5: a) Coupling factor ξ as a function of the magnetic field B_0 with different ratios ($0 - 100\,\%$) of scalar relaxation at low magnetic field with respect to the overall relaxation rate (considering rotational diffusion and contact interaction). A Lorentzian spectral density was utilized (with $\tau_C = \tau_{con} = 20\,\text{ps}$) for the dipolar as well as for the contact interaction. Translational diffusion was neglected. b) Coupling factor as a function of the magnetic field for different τ_{con}. Here, the ffhs model (eq. 2.33) and the pulse model (eq. 2.37) were used. A $\tau_D = 114\,\text{ps}$ was used for the translational diffusion, while rotational diffusion was neglected.

2.3 The Enhancement Factor

The enhancement factor ϵ is defined as the ratio between the expectation value of the nuclear magnetization under mw irradiation $\langle I_z \rangle$ and at thermal equilibrium I_0 (Boltzmann magnetization)

$$\epsilon = \frac{\langle I_z \rangle}{I_0}. \tag{2.49}$$

The enhancement factor is measured from the comparison of the integrated NMR signal with (I_{DNP}) and without (I_{Bltz}) microwave irradiation, scaled by the number of scans of the two experiments (NS_{DNP} and NS_{Bltz})

$$\epsilon = \frac{I_{DNP}}{I_{Bltz}} \cdot \frac{NS_{Bltz}}{NS_{DNP}}. \tag{2.50}$$

In general, the most important goal of the development of DNP methods is the maximization of ϵ. Even though the understanding of the remaining Overhauser parameters is important to improve DNP, the results are always judged by the achieved ϵ. Therefore, the evaluation of the enhancement factor is of particular importance. For this, it is essential to acquire enhanced and Boltzmann spectra under the same experimental conditions. This is a non trivial task, because microwave irradiation may cause significant sample heating, even when using a microwave resonator.[55,83] Furthermore, if the sample is irradiated inhomogeneously or incompletely, the enhancement factor may be underestimated.

2.4 The Saturation Factor

The saturation factor indicates to what extend the electron spin transitions are saturated, i.e. driven out of equilibrium, during microwave irradiation:

$$s = \frac{S_0 - \langle S_z \rangle}{S_0}. \tag{2.51}$$

Here, $\langle S_z \rangle$ is the expectation value of the electron spin magnetization under mw irradiation and S_0 at thermal equilibrium.

The saturation factor is exclusively determined by electron spin properties and the microwave field strength. Therefore, s is an indicator for the microwave performance of an

experimental setup.

For the case of one electron spin transition, s can be derived directly from the Bloch equations[2,45]

$$s = 1 - \frac{1}{1 + \gamma_e^2 T_{1e} T_{2e} B_{1e}^2}. \tag{2.52}$$

Here, T_{1e} is the longitudinal electron spin relaxation time, T_{2e} the transverse relaxation time of the electron spin and B_{1e} the microwave field strength.

If a hf splitting of the EPR transitions is observed that is caused by an interaction between the electron spin with nearby nuclei, an effective saturation factor is defined as

$$s_{\text{eff}} = \frac{1}{n} \sum_{i=1}^{n} s_i, \tag{2.53}$$

where n is the number of hf transitions and s_i the saturation factor of each hf transition.[84,85] This thesis deals mostly with cases, where $n = 1 - 3$. BDPA at high concentration (at $c(\text{BDPA} \approx 10\,\text{mM})$[1] is an example for $n = 1$, while for nitroxide based radicals with ^{15}N and ^{14}N two and three hyperfine transitions are observed, respectively. The structures of the radicals are displayed in fig. 4.1 and fig. 4.3.

Microwave bandwidths are usually limited and therefore only allow for excitation of one transition. Assuming one hf transition fully saturated ($s_1 = 1$) and the second hf transition fully unperturbed ($s_2 = 0$), the expected effective saturation factor of a radical with two hf transitions should be $s_{\text{eff}} = 0.5$. However, the two transitions are interacting and thus exchanging polarization with each other.[84] Due to this, saturation factors close to unity are possible under optimized conditions.[86–88] The two main interactions responsible are intermolecular Heisenberg exchange and intramolecular nuclear relaxation of the hyperfine coupled nuclei.[85,88] If these contributions are considered for $n = 2$, the saturation factor of the first resonance s_1 is expressed as[85]

$$s_1(B_{1e}) = 1 - \frac{w_e \left[2(w_e + w_n) + c K_X\right]}{{}^1\!/_4 \gamma_e^2 B_{1e}^2 T_{2e} (4w_e + 2w_n + c K_X) + w_e \left[2(w_e + w_n) + c K_X\right]}, \tag{2.54}$$

[1] The hyperfine coupling between electron spin and protons is at this concentration not resolved anymore.

with the second hf transition s_2 being

$$s_2(B_{1e}) = \frac{{}^1\!/_4\gamma_e^2 B_{1e}^2 T_{2e}(2w_n + cK_X)}{{}^1\!/_4\gamma_e^2 B_{1e}^2 T_{2e}(4w_e + 2w_n + cK_X) + w_e\left[2(w_e + w_n) + cK_X\right]}. \tag{2.55}$$

Here, w_e is the electron transition probability, w_n the nuclear transition probability, K_X the Heisenberg exchange factor$\left[\frac{\mathrm{GHz}}{\mathrm{mol\,L^{-1}}} = \frac{\mathrm{GHz}}{\mathrm{M}}\right]$, and c [M] the concentration of the PA. If both of them are combined, the effective saturation factor s_{eff} results in

$$s_{\mathrm{eff}}(B_{1e}) = \frac{{}^1\!/_4\gamma_e^2 B_{1e}^2 T_{2e}\left[2(w_e + w_n) + cK_X\right]}{{}^1\!/_4\gamma_e^2 B_{1e}^2 T_{2e}(4w_e + 2w_n + cK_X) + w_e(2\left[w_e + w_n\right) + cK_X]}. \tag{2.56}$$

Because of the intermolecular nature of the Heisenberg exchange, its influence increases with increasing radical concentration. At high PA concentration ($c \geq 10\,\mathrm{mM}$), $K_X c$ is dominant and w_n can be neglected.[60] However, at low concentrations and for the case of low radical mobility (nitroxides functionalized with fullerenes), w_n plays a key role and leads to high saturation factors independent of PA concentration.[88]

Furthermore, the theoretical treatment can be extended to the $n = 3$ case. Assuming that the irradiated hf transition is fully saturated, an analytical expression for each hf transition s_i can be obtained. If s_1 is fully saturated, s_2 and s_3 are[88]

$$s_2 = 1 - \frac{1}{1 + \frac{w_n + \frac{1}{3}K_X c + \frac{1}{6w_e}(3w_n + K_X c)(w_n + K_X c)}{2w_e + 2w_n + K_X c}} \tag{2.57}$$

and

$$s_3 = 1 - \frac{1}{1 + \frac{\frac{1}{3}K_X c + \frac{1}{6w_e}(3w_n + K_X c)(w_n + K_X c)}{2w_e + 3w_n + K_X c}}. \tag{2.58}$$

Similar expressions may be obtained, if s_2 or s_3 are fully saturated.

Figure 2.6 shows the dependence of the effective saturation factor on B_{1e} (for $n = 1,2$). In figure 2.6 $n = 3$ is not shown, because the starting assumption $s_{\mathrm{irradiated}} = 1$ makes the effective saturation factor independent on the effective microwave field. The comparison between the cases of one and two hf transitions shows, that for $n = 2$ only slightly larger B_{1e} values are required to achieve a similar saturation factor. This demonstrates that effective saturation factors close to unity are readily accessible for polarizing agents with significant hyperfine coupling.

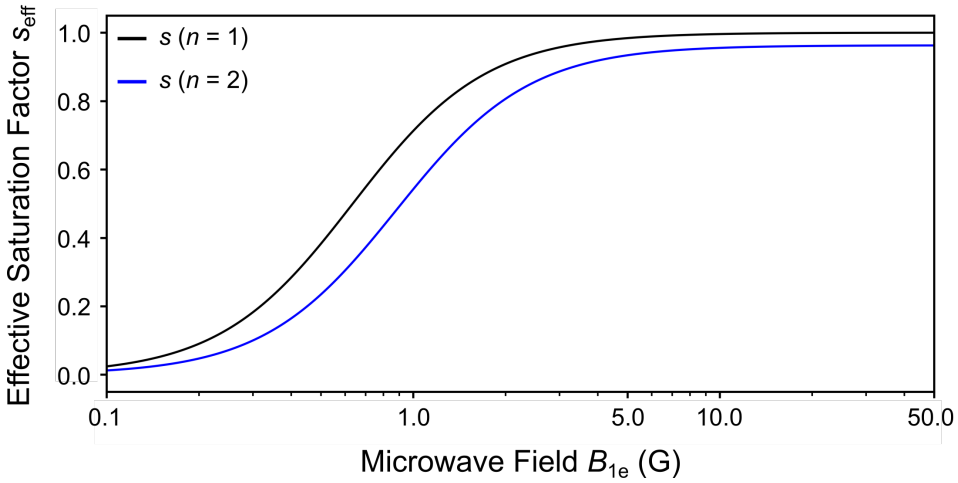

Figure 2.6: Effective saturation factor s_{eff} as a function of the microwave field B_{1e} for the one (eq. 2.52, blue line) and two (eq. 2.56, black line) line case ($n = 1{,}2$). Parameters used for the calculation: $T_{1e} = 400$ ns, $T_{2e} = 20$ ns, $K_X = 2.5\,\mathrm{GHz\,M^{-1}}$, $c = 25$ mM and $w_n = 0$. The display of s_{eff} for $n = 3$ is omitted, because of the starting assumption of $s_{irradiated} = 1$ that makes the calculation in that case independent of B_{1e}.[85]

Finally, the linewidth of the EPR transition needs to be considered. If the EPR linewidth becomes large, mw irradiation will leave some spins unaffected, because they are out of resonance. Therefore, they will not participate in the polarization transfer. Reasons for EPR line broadening are for example, high PA concentration, reduced mobility of the PA (e.g. fullerene nitroxides[34,83]), and in general a short T_{2e}. Even though a large c(PA) may favor s mechanistically, there is a point at which it will cause incomplete irradiation of the hf transition and therefore limit the saturation factor.

2.5 The Leakage Factor

The leakage factor f quantifies the paramagnetic contribution to the overall nuclear relaxation. It is determined by the comparison of the nuclear relaxation time with (T_{1n}) and without radical (T_{1n}^0)[42]

$$f = \frac{(2w_n + w_2 + w_0)}{(2w_n + w_0 + w_2 + w^0)} = 1 - \frac{T_{1n}}{T_{1n}^0}. \tag{2.59}$$

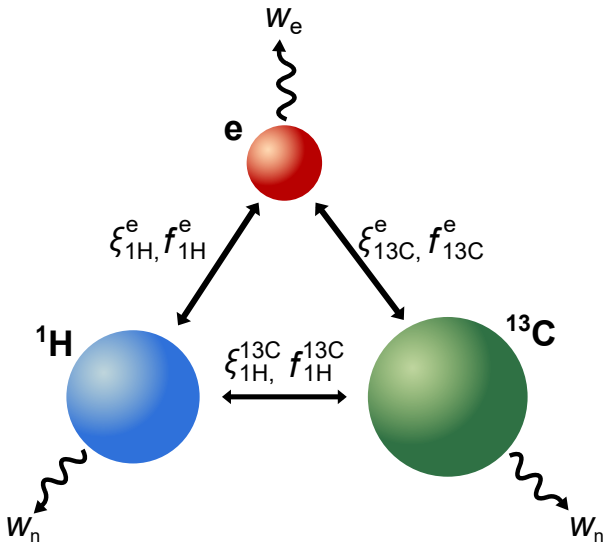

Figure 2.7: Schematic representation of the three-spin effect between an electron spin, a ^{13}C nucleus, and a ^{1}H nucleus. The arrows indicate different relaxation pathways and the Overhauser parameters that describe them. The sub- and superscript indicate which spins are interacting.[89–91]

In general, leakage factors approaching unity are accessible for large PA concentration (c(PA) $\geq$ 10 mM). Consequently, in order to obtain the largest signal, a balance between leakage and saturation factor is necessary.

2.6 The Three-Spin Effect

The Overhauser equation (eq. 2.17) was derived for an isolated spin pair (one electron spin and one nuclear spin). However, in reality almost all molecules are composed of more than one kind of nuclear spins. For example, if carbon (^{13}C) is the target nucleus, usually also hydrogen (^{1}H) will be present and often directly bound to the target ^{13}C. To increase the ^{13}C signal intensity, continuous radiofrequency (rf) irradiation on resonance with ^{1}H can be applied. This transfers spin polarization from ^{1}H to ^{13}C and is called nuclear Overhauser effect (NOE).[10,92] Its analytical treatment is completely analogous to the Overhauser effect between an electron spin and a nuclear spin. However, in this case the ^{1}H nucleus serves as the source of hyperpolarization for the less polarized nucleus (usually ^{13}C). The NOE effect is used in routine ^{13}C NMR experiments. More generally,

this method is always applicable if a nucleus with low magnetic moment is detected, while also a nucleus with large magnetic moment is present (e.g. ^{1}H or ^{19}F).[10]
In order to account for this additional cross-relaxation between nearby nuclei in DNP, eq. 2.17 is expanded by an NOE term that considers the interaction between the two nuclei. This is called three-spin effect:[89–91]

$$\epsilon = 1 - f s \xi \frac{|\gamma_e|}{\gamma_n} + \text{NOE term.} \tag{2.60}$$

Figure 2.7 shows the situation for the three-spin case. Here, the example of one electron, one ^{1}H, and one ^{13}C spin is used for simplicity. Both nuclei are coupled to the electron spin (via hyperfine coupling) as well as to each other (via J coupling). Therefore, the NOE term in eq. 2.60 must depend on the coupling between the two nuclei and on the polarization level of the nucleus that is not detected. When detecting ^{13}C, the enhancement is

$$\epsilon_{13C} = 1 - f^{e}_{13C} s \xi^{e}_{13C} \frac{|\gamma_e|}{\gamma_{13C}} - \xi^{1H}_{13C} f^{1H}_{13C} \frac{\gamma_{1H}}{\gamma_{13C}} P_{\text{pol, }1H}. \tag{2.61}$$

Here, the superscript refers to the spin that is coupled to the spin indicated in the subscript. $P_{\text{pol, }1H} = 1 - \epsilon_{1H} = -f^{e}_{1H} s \xi^{e}_{1H} \frac{\gamma_e}{\gamma_{1H}}$ refers to the polarization of the proton and is expressed through the signal enhancement ϵ_{1H} of ^{1}H caused by the coupling to the electron spin[89]

$$\epsilon_{13C} = 1 + \frac{|\gamma_e|}{\gamma_{13C}} \left(-f^{e}_{13C} s \xi^{e}_{13C} + \xi^{1H}_{13C} f^{1H}_{13C} f^{e}_{1H} s \xi^{e}_{1H} \right). \tag{2.62}$$

In order to understand whether the three-spin effect increases or decreases the expected signal enhancement of the ^{13}C nucleus, it is important to consider the sign of the NOE term. Because of their dipolar nature, the coupling factors of ^{1}H with the electron spin (ξ^{e}_{1H}) and with ^{13}C $\left(\xi^{13C}_{1H}\right)$ are usually positive.[89] The coupling factor (ξ^{e}_{13C}) is, for most carbon moieties, scalar dominated and therefore negative.[33,59,60] For eq. 2.62, this leads to

$$\epsilon_{13C} = 1 + \frac{|\gamma_e|}{\gamma_{13C}} \left(\left|\xi^{1H}_{13C}\right| f^{1H}_{13C} f^{e}_{1H} s |\xi^{e}_{1H}| + f^{e}_{13C} s |\xi^{e}_{13C}| \right). \tag{2.63}$$

From this equation it is evident that the three-spin effect increases the signal enhancement for ^{13}C nuclei, if the third spin is a proton. The influence of the three-spin effect can be suppressed, when the third spin is saturated during the DNP measurement (i.e. via

rf irradiation on resonance with ^{1}H) or if a high PA concentration (c(PA) $\geq$ 10 mM) is used.[89] The reason for the latter is that the leakage factor between ^{1}H and ^{13}C becomes negligible as

$$f_{13C}^{e} + f_{13C}^{1H} \approx f_{13C}^{e} \approx 1 \tag{2.64}$$

holds and the paramagnetic center is the primary relaxation pathway of ^{13}C.[91]

2.7 Electron Spin-Lattice Relaxation

General theories on relaxation have been formulated, for example, by Redfield[93,94] and Abragam.[45] Within this thesis, the spin-lattice or longitudinal relaxation time (for $S = 1/2$) of nitroxides in organic solvents at room temperature and 9.4 Tesla was experimentally investigated. Due to this, only the contributions to relaxation in the fast tumbling regime (small organic radicals in non-viscous solutions) are discussed and the description remains phenomenological.

The relaxation mechanisms described here are independent of each other, therefore the overall spin-lattice relaxation time is written as the sum of all contributions[95]

$$\frac{1}{T_{1e}} = \sum_{i=1}^{n} \frac{1}{T_{1e}^{i}}. \tag{2.65}$$

Here, T_{1e} is the electron spin-lattice relaxation time and T_{1e}^{i} the contribution of the respective relaxation mechanism i. In order to be an efficient relaxation pathway, an interaction needs to induce a fluctuating magnetic field with a frequency on the order of the resonance frequency of the electron spin transition. Therefore, if strong interactions are not time dependent, they might not have a large contribution to relaxation. On the other hand, anisotropic interactions that are averaged in a liquid sample and are therefore invisible in the spectrum, may still deliver a significant contribution to T_{1e}.

The first relaxation mechanism discussed here is caused by spin rotation, which depends on the g-anisotropy[95,96]

$$\frac{1}{T_{1e}^{SR}} = \frac{\sum_{i=1}^{3} (g_i - g_e)^2}{9\tau_C}, \tag{2.66}$$

where T_{1e}^{SR} is the contribution of spin rotation to the overall T_{1e}, τ_C is the rotational correlation time, g_i is the g-value of the different principal axis of the g-tensor with i =x,y,z and g_e is the g-factor of the free electron. This mechanism is particularly important, because it only depends on the rotational correlation time and not on ω_e.
Secondly, the g-anisotropy itself is also a relaxation pathway. While negligible at low magnetic field its contribution to relaxation becomes significant at 34 GHz (see fig. 2.8)[96]

$$\frac{1}{T_{1e}^{g}} = \frac{2}{5}\left(\frac{\mu_B B_0}{\hbar}\right)^2 \left(\frac{(\Delta g)^2}{3} + (\delta g)\right)^2 J(\omega_e), \tag{2.67}$$

with B_0 being the external magnetic field. Additionally, Δg and δg are defined as[96]

$$\Delta g = g_z - \frac{1}{2}\left(g_x + g_y\right), \tag{2.68}$$

$$\delta g = \frac{1}{2}\left(g_x - g_y\right). \tag{2.69}$$

The spectral density $J(\omega_e)$ is a Lorentzian and contains the electron spin resonance frequency ω_e and the rotational correlation time τ_C:

$$J(\omega_e) = \frac{\tau_C}{1 + (\omega_e \tau_C)^2}. \tag{2.70}$$

Furthermore, the hyperfine anisotropy may induce relaxation[95–97]

$$\frac{1}{T_{1e}^{A}} = \frac{2}{9} I(I+1) \sum_i^3 \left[(A_i - \bar{A})^2\right] J(\omega_e), \tag{2.71}$$

where I is the nuclear spin quantum number of the coupled spin, A_i is the principal axis value of the hyperfine tensor with i =x,y,z and $\bar{A}$ the average of the three principal axis values.
Another electron spin relaxation pathway is spin diffusion, where relaxation is induced by, for example, solvent protons which are diffusing around the electron spin[95,97]

$$\frac{1}{T_{1e}^{SD}} = R_{1e,max}^{SD} \left(\frac{2\omega_e \tau_C}{1 + (\omega_e \tau_C)^{3/2}}\right)^{1/4}. \tag{2.72}$$

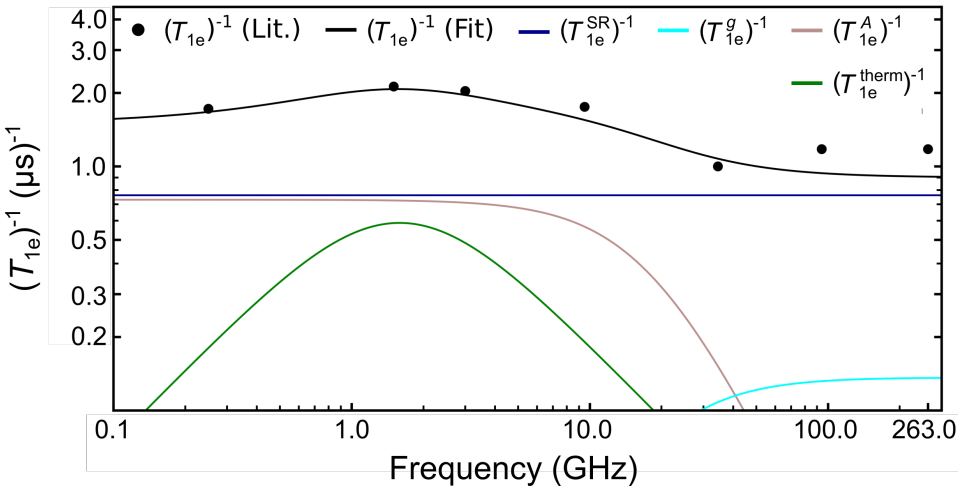

Figure 2.8: Simulation of the frequency dependence of the different electron spin relaxation mechanisms for the TN radical in water: Spin rotation $(T_{1e}^{SR})^{-1}$ (dark blue line), hyperfine anisotropy $(T_{1e}^{A})^{-1}$ (brown line), g anisotropy $(T_{1e}^{g})^{-1}$ (turquoise line), and the thermal contribution $(T_{1e}^{therm})^{-1}$ (green line). Their sum $(T_{1e})^{-1}$ is depicted as a black line. Equations 2.66, 2.67, 2.71, 2.73 and 2.75 were used for the simulation. For eq. 2.75 the contributions from spin diffusion and oxygen content were omitted. Simulation parameters:[96] $g_x = 2.0092$, $g_y = 2.0061$, $g_z = 2.0022$, $A_x = 5.5\,\mathrm{G}$, $A_y = 6.3\,\mathrm{G}$, $A_z = 35.6\,\mathrm{G}$, $I = 1$, $\tau_C = 9.0\,\mathrm{ps}$, $C_{therm} = 7.0 \times 10^{16}$, $\tau_{therm} = 100\,\mathrm{ps}$ and $\omega_{ref} = 9.5\,\mathrm{GHz}$. Experimental values from the literature (black dots) from 0.2 GHz – 34.0 GHz are from ref. [96] and at 94 GHz from ref. [100]. The point at 263 GHz is a theoretical prediction that was reported in ref. [101]. Figure adapted from ref. [96]. Errors for the literature data were reported to be $\sim 3\,\%$, which lie within the symbol.

Here, $R_{1e,max}^{SD}$ is the maximum spin diffusion relaxation rate that is usually used as a fitting parameter.[95] While eq. 2.72 considers spin diffusion in general, it may be beneficial to account for specific molecular dynamics. In the particular case of nitroxides, the methyl rotation was identified as a source of relaxation. This process goes under the name "thermal process"[96–99]

$$\frac{1}{T_{1e}^{therm}} = C_{therm}\left(\frac{\omega_e}{\omega_{ref}}\right)\frac{\tau_{therm}}{1+(\omega_e\tau_{therm})^2}, \tag{2.73}$$

with C_{therm} being a coefficient for the thermal contribution, $\omega_{ref} = 9.5\,\mathrm{GHz}$, and $\tau_{therm} = \tau_{therm}^0 \exp\left(\frac{E_a}{N_A k_B T}\right)$. Here, τ_{therm}^0 is the pre-exponential factor of the Arrhenius-law, E_a is the activation energy, N_A Avogadro constant, k_B the Boltzmann factor, and T the temperature.[96]

Finally, also paramagnetic impurities in solution serve as a source of relaxation. Specifically, oxygen is abundantly present in solutions that are not prepared under oxygen exclusion. The contribution of O_2 to electron spin relaxation is[95]

$$\frac{1}{T_{1e}^{Ox}} = \frac{K_{Ox}}{\tau_C}, \tag{2.74}$$

where K_{Ox} is the difference of $\frac{1}{T_{1e}^{Ox}}$ with and without oxygen. In general, $\frac{1}{T_{1e}^{Ox}}$ is proportional to the concentration of oxygen in the solution and the relative translational diffusion coefficient.[95]

Considering all the different contributions, T_{1e} is finally expressed as[95,96]

$$\frac{1}{T_{1e}} = \frac{1}{T_{1e}^{SR}} + \frac{1}{T_{1e}^{A}} + \frac{1}{T_{1e}^{g}} + \frac{1}{T_{1e}^{therm}} + \frac{1}{T_{1e}^{SD}} + \frac{1}{T_{1e}^{Ox}}. \tag{2.75}$$

Figure 2.8 shows the frequency dependence of the electron longitudinal relaxation time as a function of the resonance frequency. While at low magnetic field, hyperfine anisotropy and the methyl rotation contribute significantly to the relaxation, their influence becomes negligible at high magnetic field ($\omega_e \geq 34\,\text{GHz}$). At high field $\frac{1}{T_{1e}}$ is dominated by spin rotation with a small contribution from g anisotropy.

Experimental access to T_{1e} is possible through power saturation curves with continuous wave (cw) EPR or by pulsed EPR with pulsed EPR being the far more often used method nowadays.[102–104] These experiments will be discussed in chapter 3.

3 Materials and Methods

In this chapter, the materials and methods of this thesis are listed and explained. This includes all instruments, chemicals, and sample tubes. The NMR pulse sequences of this thesis are explained with the product operator formalism. However, a general description of the fundamental principles of NMR is omitted. For this, the reader is referred to text books.[10,45,92] Furthermore, the newly developed liquid state DNP spectrometer is excluded in this chapter, because it is discussed in detail in chapter 7.

3.1 Materials

All substances except for $^{13}CHCl_3$ were used as received, For $^{13}CHCl_3$, K_2CO_3 was added to neutralize the solvent. The following materials were used:

Solvents

1. Tetrachloromethane (CCl_4, Sigma-Aldrich)
2. Chloroform ($CHCl_3$, Merck)
3. Benzene (C_6H_6, Roth)
4. Cyclohexane (C_6H_{12}, Merck)
5. Dichloromethane (CH_2Cl_2, Merck)

6. Acetonitrile (CH_3CN, Merck)
7. Toluene ($PhCH_3$, Merck)
8. *n*-Hexane (C_6H_{14}, Merck)
9. Dimethylsulfoxide (DMSO, Merck)

Polarizing agents

1. α,γ-Bisdiphenylene-β-phenylallyl (BDPA, 1:1 complex with benzene, Sigma-Aldrich)
2. α,γ-Bisdiphenylene-β-phenylallyl-d_{27} (BDPA-d_{27})
3. Di-*tert*-butylnitroxide (DTBN, Sigma-Aldrich)
4. 4-Hydroxy-2,2,6,6-tetramethylpiperidine-1-oxyl or tempol (TL, Sigma-Aldrich)
5. 4-Oxo-2,2,6,6-tetramethylpiperidine-d_{16},1-^{15}N-1-oxyl or tempone (^{15}N-TN-d_{16}, Sigma-Aldrich)
6. 3β-DOXYL-5α-cholestane (TP-CLST, Sigma-Aldrich)
7. 7-Aza-3,11-dioxa-15-oxodispiro[5.1.5.3]hexadec-7-yl-7-oxyl (TN-py)
8. Fullerene-nitroxides (FN-*n*)
9. 2,6-Di-tert-butyl-α-(3,5-di-tert-butyl-4-oxo-2,5-cyclohexadien-1-ylidene)-*p*-tolyloxy (galvinoxyl, Sigma-Aldrich)
10. Carbon fiber (private communication with the author of ref. [105].
11. N@C_{60} (private communication with Dr. A. Schnegg, Max Planck Institute for Chemical Energy Conversion)

TN-py and FN-*n* were synthesized by the chemical facility of the Max Planck Institute for Multidisciplinary Sciences following protocols from the literature.[88,106] Additionally, BDPA-d_{27} was also synthesized by the chemical facility according to protocols from the literature.[107,108]

Target molecules

ST034307 (Sigma-Aldrich), Na Diatrizoate (Fisher Scientific), Fluorobenzene, (EGA), Chlorobenzene (Sigma-Aldrich), Bromobenzene (Sigma-Aldrich), Iodobenzene (Merck), Acetophenone (Sigma-Aldrich), Nitrobenzene (Fluka), Anisole (Sigma-Aldrich), 1,4-Dichlorocyclohexane (TCI), Diethylmalonate (Sigma-Aldrich), Etylacetoacetate (Sigma-Aldrich), Mitotane (Fisher Scientific), Amiodarone (Fisher Scientific), Dichlorodiphenyltrichloroethane (Sigma-Aldrich), Indole (Sigma-Aldrich) 1-Fluoro-4-iodobenzene (Fluka), 1-Chloro-4-methylbenzene (Sigma-Aldrich), 1-Fluoro-4-(trichloromethyl)benzene (Lancaster) and Methyl 4-iodobenzoate (Eastman).

^{13}C enriched compounds

1. ^{13}C Tetrachloromethane ($^{13}CCl_4$, Eurisotop)
2. ^{13}C Chloroform ($^{13}CHCl_3$, Sigma-Aldrich)
3. ^{13}C Dichloromethane ($^{13}CH_2Cl_2$, Sigma-Aldrich)
4. ^{13}C Tetrabromomethan ($^{13}CBr_4$, Sigma-Aldrich)
5. $^{13}C_6$ Fluorobenzene (C_6H_5F, CIL)
6. $^{13}C_6$ Chlorobenzene (C_6H_5Cl, Sigma-Aldrich)
7. $^{13}C_6$ Bromobenzene (C_6H_5Br, Sigma-Aldrich)
8. $^{13}C_6$ Iodobenzene (C_6H_5I, Sigma-Aldrich)
9. ^{13}C Methanol (CH_3OH, Sigma-Aldrich)
10. 3-$^{13}C_1$ Na Pyruvate (Sigma-Aldrich)
11. 2-$^{13}C_1$ Indole (CIL)
12. $^{13}C_6$ 2-(chloromethyl)-3,4,5,6-tetramethoxytetrahydro-*2H*-pyran (GlcOMe)

GlcOMe was synthesized by the chemical facility of the Max Planck Institute for multidisciplinary sciences following protocols from the literature.[109,110]

Sample tubes

1. 9.4 T, NMR tubes Outer diameter O.D. = 4.936 ± 0.0065 mm, inner diameter I.D. = 4.2065 ± 0.0065 mm (Wilmad Labglass 528(or 535)-PP-7QTZ)
2. Q-band tubes, O.D. = 1.6 mm, I.D. = 1.1 mm (Wilmad Labglass WG-221T-RB)
3. W-band tubes, O.D. = 0.9 mm, I.D. = 0.5 mm (Wilmad Labglass Suprasil WG-213ST9S)
4. EPR tubes at 263 GHz, O.D. = 0.33 mm, I.D. = 0.3 mm (Vitrocom CV1017)

Inner tubes for DNP measurements at 9.4 T were provided by Hilgenberg and are listed in tab. 7.5.

3.1.1 Sample Preparation

Before each measurement, dissolved oxygen was removed from the solution. Generally, a solution containing the target molecules and the PA was degassed by freeze-pump-thaw cycles (5× with $p \approx 5 \times 10^{-5}$ mbar). For this, a turbo pumping station (HiCUbe 80 Eco), which consists of a DCU display control unit, a diaphragm pump (MVP 015-2), and a turbo pump (HiPace 80), was employed. Afterwards, the sample was either sealed with an O_2/H_2 torch ($T \approx 1200 - 2200$ K) or transferred to the glove box operating with N_2 atmosphere (MBraun-Unilab Plus, O_2 and H_2O content ≤ 0.1 ppm). There, sample preparation was finalized and the tube was sealed with a homemade gas tight cap. Samples prepared for 263 GHz EPR measurements, were filled in the glove box and sealed with sealing rubber (Critoseal). From the sample preparation protocol, the experimental error of the radical and target molecule concentration was estimated to be $10 - 20$ %.

3.2 Spectrometers

3.2.1 Continuous Wave X-Band Spectrometer

To ensure the stability of the radical, cw measurements at X-band were performed prior to all DNP measurements. For this, a Bruker Elexsys E500T X-band spectrometer was

used. The resonator was an Elexsys High Sensitivity probehead (Bruker), which can host up to O.D. = 10 mm sample tubes. The magnetic field was provided by a water-cooled 0.35 T electromagnet. A representative spectrum of 10 mM ^{15}N-TN-d^{16} in CCl_4 is shown in fig. 3.2b.

3.2.2 X- and Q-Band Spectrometer

Pulsed EPR experiments at X- and Q-band were performed with a Bruker ElexSys E580 EPR spectrometer and for DNP measurements an AVANCE III ^{1}H 300MHz NMR console was used. Resonance frequencies were $\sim$ 9.5 GHz and $\sim$ 34 GHz for X- and Q-band, respectively. The magnetic field was provided by a water-cooled electromagnet that operates in a range of $B_0 = 0 - 1.5$ T.
At X-band, an EN4118X-MD-4 EPR resonator (Bruker), which is also equipped with an Electron Double Resonance (ENDOR) coil, was used for pulsed EPR as well as for DNP experiments. Pulsed EPR experiments were performed with a mw TWT amplifier ($P = 1$ kW), while for DNP measurements a cw mw AmpX amplifier ($P = 5 W$) was used. A previous reported study demonstrated the comparability of the two setups.[87]
At Q-band, a Bruker ER-5106QT/W cw resonator (Bruker) was used for pulsed EPR and DNP experiments. For pulsed EPR and DNP experiments, two mw TWT amplifier (cw amplifier $P = 40$ W and a gated amplifier $P = 100$ W) were used. For DNP measurements, only the 40 W cw amplifier was employed and to enable radiofrequency (rf) irradiation a copper coil was inserted into the resonator and wrapped around the EPR tube.

3.2.3 W-Band Spectrometer

Pulsed W-band (94 GHz) EPR experiments were performed on a Bruker E680 pulsed W-band spectrometer. The magnetic field was provided by a superconducting magnet operating at $\sim$ 3.4 T. An additional sweep coil ensured magnetic field flexibility. The EN600-1021H resonator (Bruker) was used for pulsed EPR measurements.

3.2.4 263 GHz EPR Spectrometer

The EPR measurements at 263 GHz were performed on a Bruker E780 spectrometer that produces microwave radiation with $P = 100$ mW with a mw amplifier chain (AMC, Virginia Diodes). Pulsed experiments were conducted with a Model E9501510 (Bruker) resonator and cw measurements were carried out with a Bruker 263 GHz large sample volume non-resonant probehead.

3.3 Methods

3.3.1 Measurement of the Electron Spin Lattice Relaxation Time

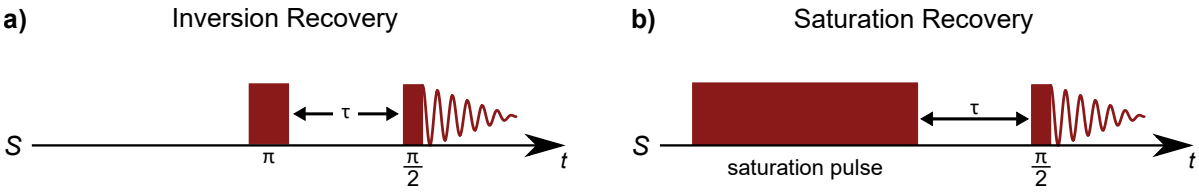

Figure 3.1: Pulse sequences used for the determination of the electron spin longitudinal relaxation time called: a) inversion recovery and b) saturation recovery.

Inversion- and saturation recovery experiments were performed to determine the electron spin-lattice relaxation time (fig. 3.1). The inversion recovery experiment inverts the electron spin magnetization with a 180 ° pulse. This is followed by free induction decay (FID) detection after a $\pi/2$ pulse. The time between the two pulses was incremented. The only difference in the pulse sequence between inversion and saturation recovery is that for the saturation recovery pulse sequence, the π-pulse is replaced by a long saturation pulse. This equalizes the population of the electron spin levels. The integrated EPR signal intensity can be plotted as a function of the incremented time τ and fit to an exponential function $y = A[1 - \exp(\tau/T_i)]$, from which T_{1e} is obtained.

3.3.2 Saturation Measurements at X- and Q-Band

Figure 3.2a displays the ELDOR sequence.[84] FID detection is performed after a $\pi/2$ pulse on resonance with the low field resonance and remains fixed throughout the experiment.

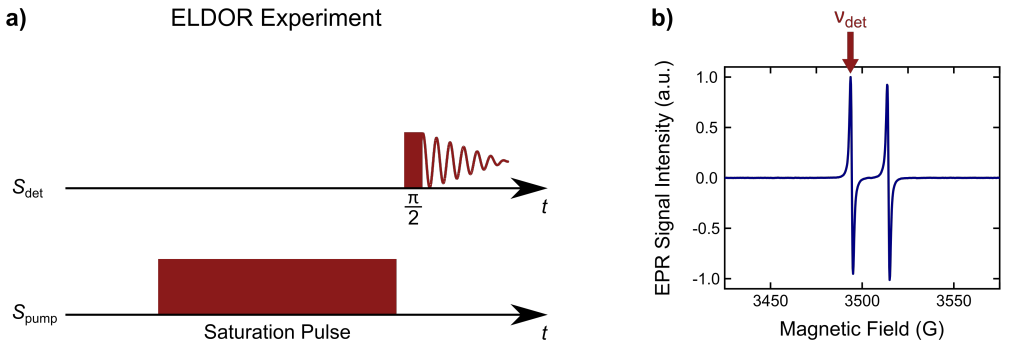

Figure 3.2: a) ELDOR pulse sequence used for the determination of s during DNP. b) Continuous wave EPR measurement at 0.34 T. The red arrow indicates the position of the detection frequency in a cw EPR spectrum of ^{15}N-TN-d$_{16}$ ($c \approx 10$ mM) in CCl_4 during an ELDOR experiment.

During this, a long saturation pulse is swept through the EPR spectrum. As soon as the saturation pulse is on resonance with the EPR signal, the signal intensity drops. Due to Heisenberg exchange, a drop in intensity is also observed when the ELDOR pulse is on resonance with the second EPR hf resonance.[84] Figure 3.2b depicts a representative cw spectrum. The detection frequency during an ELDOR measurement is indicated with a red arrow, while the saturation pulse is swept through the whole spectrum.

3.3.3 Nuclear Relaxation Times

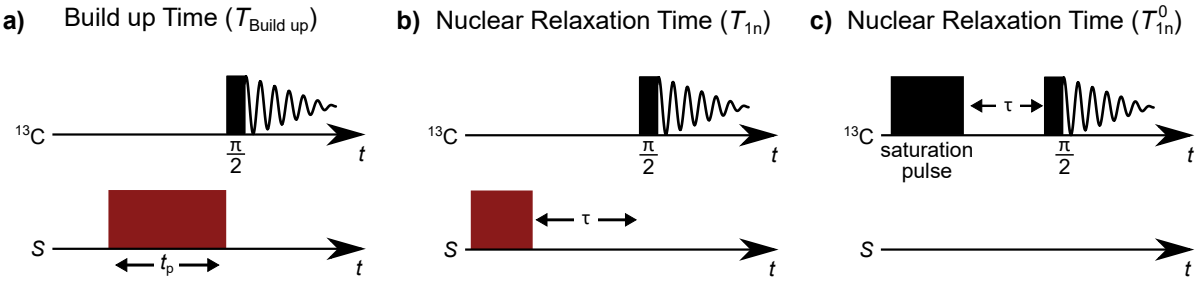

Figure 3.3: Pulse sequences used for the determination of a) the build up time $T_{\text{Build-up}}$ during DNP, b) the nuclear relaxation rate T_{1n} during DNP, and c) the nuclear relaxation time without mw and/or PA.

Figure 3.3a shows the pulse sequence used to measure the build up time during a DNP

experiment. The mw irradiation time is incremented and NMR detection is performed after a $\pi/2$ rf pulse. The pulse sequence depicted in fig. 3.3b shows the determination of T_{1n} during DNP at 0.34 T and 1.2 T. The time between a mw pulse of fixed length and the NMR detection is incremented. In fig. 3.3c, the pulse sequence for the measurement of the nuclear relaxation time with a saturation recovery experiment is depicted. The time between rf saturation pulse and detection is incremented. From these measurements, the NMR signal intensity is plotted as a function of the incremented time (or mw pulse length) τ. From an exponential fit of the experimental data to $y = A[1 - \exp(\tau/T_i)]$, the time constants $T_{\text{Build-up}}$, T_{1n} and T_{1n}^0 are obtained. As the nuclear relaxation times are temperature sensitive, a comparison between $T_{\text{Build-up}}$ and T_{1n} reveals mw induced sample heating. Indeed, if no mw heating is observed during a DNP measurement, $T_{\text{Build-up}}$ and T_{1n} have similar values.[42,83] These sequences were used at 0.34 T and 1.2 T. At 9.4 T, saturation- or inversion recovery experiments (fig. 3.3c) were executed under cw mw irradiation to obtain T_{1n}.

3.3.4 ^{13}C DNP NMR Pulse Sequences

The description of the pulse sequences presented herein is based on ref.[92] and ref.[10]. Coherence selection is achieved through phase cycling, which is explained in the literature.[10,92]

3.3.4.1 1D DNP NMR Pulse Sequences

Figure 3.4 depicts five different DNP pulse sequences. Black bars indicate a $\pi/2$ pulse. If not noted otherwise, pulses are applied along the x axis. The sequences concern pulse acquire experiments, in which a ^{13}C FID is detected immediately following a $\pi/2$ pulse While in fig. 3.4a-c, mw is applied continuously, microwave irradiation is gated in fig. 3.4d. To reduce sample heating induced by mw absorption of the mw irradiation, the latter is the pulse sequence used in polar solvents (see sec. 7.3). Furthermore, a strong ^{1}H pulse (or train of pulses) during acquisition removes the coupling between ^{1}H and ^{13}C. Consequently, instead of a mulitplet, a single line for each ^{13}C signal is observed. This line combines the intensity of all lines of the multiplet, which substantially improves the sensitivity of ^{13}C NMR and is used in the sequences fig. 3.4b-d.

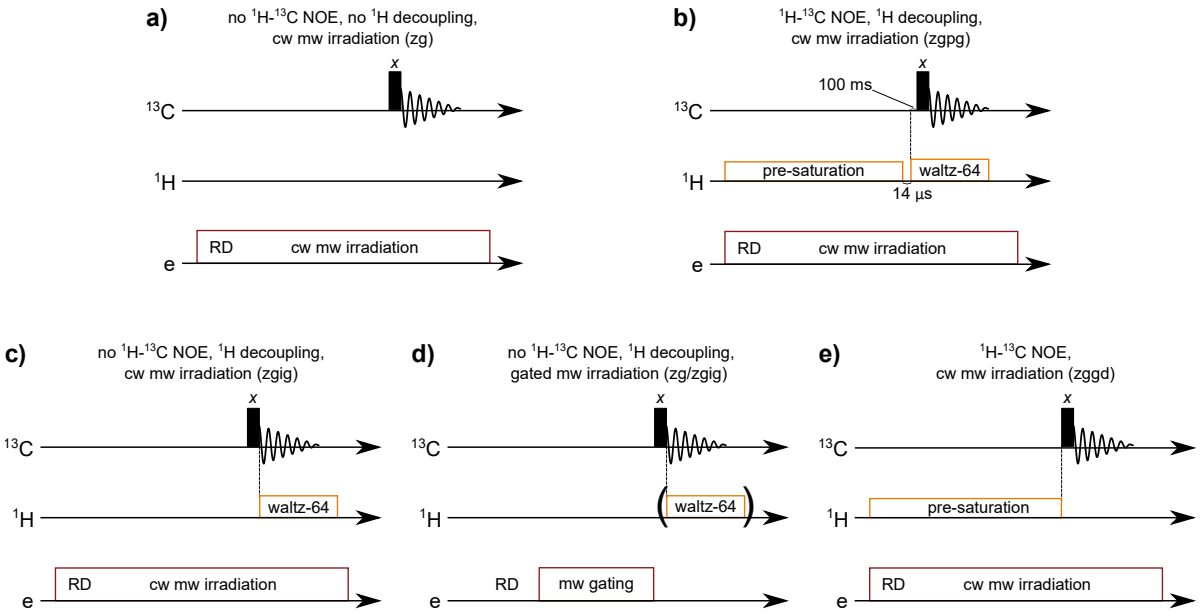

Figure 3.4: 1D NMR pulse sequences that were used for DNP measurements in this work. Black bars represent a $\pi/2$ pulse. Pre-saturation of ^{1}H results in a spin polarization transfer from proton to carbon. A strong ^{1}H pulse (or pulse train) during ^{13}C acquisition removes the coupling between ^{1}H and ^{13}C and therefore simplifies the spectra. Pulse acquire (a), pulse acquire power gated (b), pulse acquire inverse gated (c), and pulse acquire gated decoupling (e) experiments are abbreviated by zg, zgpg, zgig, and zggd throughout this work. Continuous mw irradiation is applied during the recycle delay (RD). waltz-64 is used for ^{1}H decoupling.[111]

Additionally, in traditional ^{13}C NMR experiments, ^{1}H irradiation (cw or a pulse train) is applied during the recycle delay (RD).[92] This further improves the ^{13}C Boltzmann signal via polarization transfer from proton to carbon. This is called nuclear Overhauser effect (NOE) and the maximum ^{13}C NMR signal enhancement is determined by $\eta = 1 + \gamma_{1H}/2\gamma_{13C} \approx 3$ (η being the NOE induced NMR signal enhancement) for small molecules in the fast motion regime.[10] However, measurements with ^{1}H pre-saturation lack comparability with the literature, because ^{1}H decoupling has only been reported in two studies[41,112] and is otherwise not reported in the literature under mw irradiation. This is in contrast to the pulse sequences fig. 3.4a, c, and d, that allow for comparison with the literature. Therefore, if not noted otherwise, enhancements reported in this thesis were obtained without ^{1}H pre-saturation. Pulse acquire, pulse acquire power gated, and pulse acquire inverse gated experiments are abbreviated by zg, zgpg, and zgig throughout this work.

The pulse acquire gated decoupling experiment is used for the comparison of the DNP enhancement with and without ^{1}H pre-saturation and is abbreviated with zggd.

3.3.4.2 Double Quantum Filtered Correlation Spectroscopy (DQF COSY)

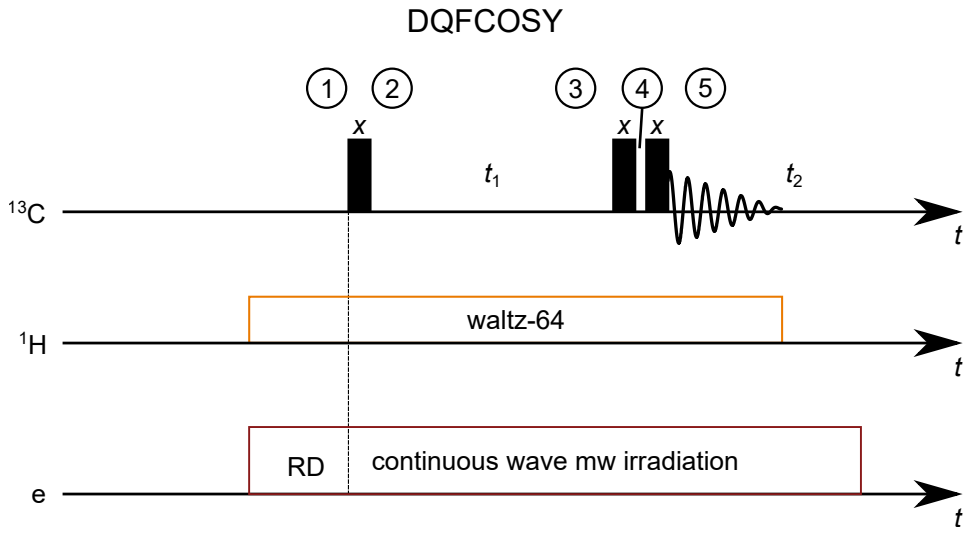

Figure 3.5: Pulse sequence of the 2D double quantum filtered correlation spectroscopy experiment (DQF COSY).[92] Black bars represent a $\pi/2$ pulse. Waltz64 is used for ^{1}H pre-saturation and decoupling.[111] Continuous mw irradiation is applied during the recycle delay (RD).

Double quantum filtered correlation spectroscopy (DQF COSY) is a standard NMR pulse sequence. It correlates spins, which are scalar coupled to each other. The pulse sequence is depicted in fig. 3.5. During DNP, cw mw irradiation is applied and the ^{1}H nuclei are decoupled during acquisition. The product operator formalism is used to describe the evolution of the ^{13}C magnetization. The desired coherence pathways are selected by phase cycling.[10,92] Only the product operators ($\hat{I}_{x,y,z}$) that evolve into observable magnetization are carried through the calculations. Figure 3.5 shows the positions of the pulse sequence, where the product operators are evaluated. First, z magnetization is turned into $\hat{I}_{1y}$ by a $\left(\frac{\pi}{2}\right)_x$ pulse[10,92]

$$① \; \hat{I}_{1z} \xrightarrow{\left(\frac{\pi}{2}\right)_x} -\hat{I}_{1y} = ②. \tag{3.1}$$

Chemical shift evolution leads to

$$\textcircled{2} \xrightarrow{\Omega_1 t_1} -\cos(\Omega_1 t_1)\,\hat{I}_{1y} + \sin(\Omega_1 t_1)\,\hat{I}_{1x} \tag{3.2}$$

and concomitant evolution of the J coupling

$$\begin{aligned} &-\cos(\Omega_1 t_1)\,\hat{I}_{1y} + \sin(\Omega_1 t_1)\,\hat{I}_{1x} \xrightarrow{2\pi J_{12}\hat{I}_{1z}\hat{I}_{2z}t_1} \\ &-\cos(\pi J_{12} t_1)\cos(\Omega_1 t_1)\,\hat{I}_{1y} + \sin(\pi J_{12} t_1)\cos(\Omega_1 t_1)\,2\hat{I}_{1x}\hat{I}_{2z} \\ &+\cos(\pi J_{12} t_1)\sin(\Omega_1 t_1)\,\hat{I}_{1x} + \sin(\pi J_{12} t_1)\sin(\Omega_1 t_1)\,2\hat{I}_{1y}\hat{I}_{2z} = \textcircled{3}. \end{aligned} \tag{3.3}$$

The second $\pi/2$ pulse is applied along the x direction

$$\begin{aligned} &-\cos(\pi J_{12} t_1)\cos(\Omega_1 t_1)\,\hat{I}_{1z} - \sin(\pi J_{12} t_1)\cos(\Omega_1 t_1)\,2\hat{I}_{1x}\hat{I}_{2y} \\ &+\cos(\pi J_{12} t_1)\sin(\Omega_1 t_1)\,\hat{I}_{1x} - \sin(\pi J_{12} t_1)\sin(\Omega_1 t_1)\,2\hat{I}_{1z}\hat{I}_{2y} = \textcircled{4}. \end{aligned} \tag{3.4}$$

Only the second term contains double quantum coherences, which can be decomposed into an equal mixture of double- and zero- quantum coherences[92]

$$2(2\hat{I}_{1x}\hat{I}_{2y}) = \frac{1}{2}\left((2\hat{I}_{1x}\hat{I}_{2y} + 2\hat{I}_{1y}\hat{I}_{2x}) - (2\hat{I}_{1y}\hat{I}_{2x} - 2\hat{I}_{1x}\hat{I}_{2y})\right). \tag{3.5}$$

As the name of the pulse sequence suggests, only the double quantum part is of interest. Therefore, only its evolution during the pulse sequence is described further. The third $\pi/2$ pulse turns the double quantum part into antiphase magnetization that is observable

$$\begin{aligned} &-\frac{1}{2}\sin(\pi J_{12} t_1)\cos(\Omega_1 t_1)\left(2\hat{I}_{1x}\hat{I}_{2y} + 2\hat{I}_{1y}\hat{I}_{2x}\right) \xrightarrow{\left(\frac{\pi}{2}\right)_x} \\ &-\frac{1}{2}\sin(\pi J_{12} t_1)\cos(\Omega_1 t_1)\left(2\hat{I}_{1x}\hat{I}_{2z} + 2\hat{I}_{1z}\hat{I}_{2x}\right) = \textcircled{5}. \end{aligned} \tag{3.6}$$

3.3.4.3 Total Correlation Spectroscopy (TOCSY)

The total correlation spectroscopy (TOCSY) experiment, also known as homonuclear Hartmann-Hahn spectroscopy (HOHAHA), is a 2D pulse sequence that allows for the observation of all spins that belong to the same spin system.[92] That means, cross peaks may still be observed even if there is no direct coupling between two nuclei, as long as

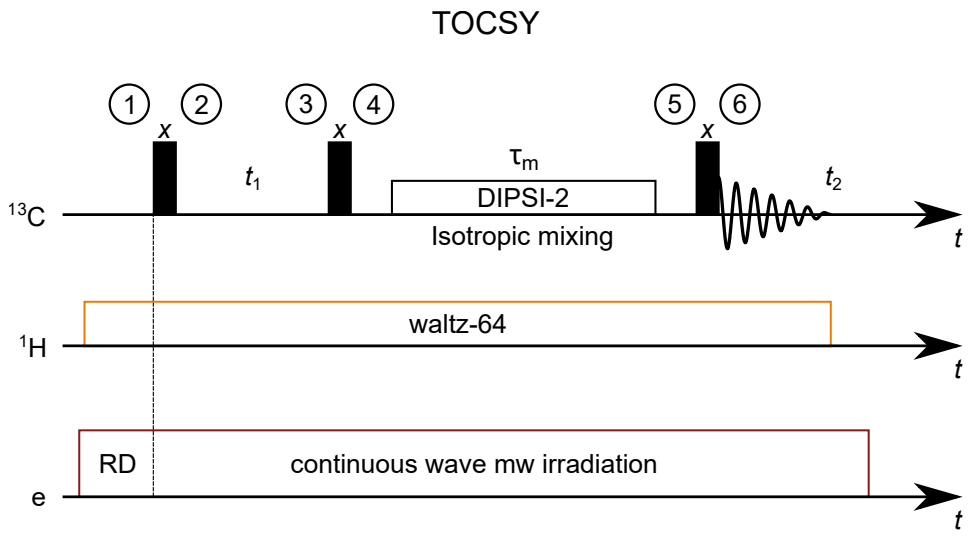

Figure 3.6: Pulse sequence of the 2D experiment called total correlation spectroscopy (TOCSY).[10,92] Black bars represent a $\pi/2$ pulse. Waltz64 is used for ^{1}H pre-saturation and decoupling.[111] Continuous mw irradiation is applied during the recycle delay (RD).

these two nuclei mutually couple to a third spin that is coupled to the other two.
Up to (4) the pulse sequence is identical with the DQF COSY sequence. Therefore, the descriptions with the product operator formalism continues from[92]

$$\begin{aligned} &-\cos(\pi J_{12} t_1)\cos(\Omega_1 t_1)\,\hat{I}_{1z} - \sin(\pi J_{12} t_1)\cos(\Omega_1 t_1)\,2\hat{I}_{1x}\hat{I}_{2y} \\ &+\cos(\pi J_{12} t_1)\sin(\Omega_1 t_1)\,\hat{I}_{1x} - \sin(\pi J_{12} t_1)\sin(\Omega_1 t_1)\,2\hat{I}_{1z}\hat{I}_{2y} = (4). \end{aligned} \tag{3.7}$$

The next part is called isotropic mixing phase. during isotropic mixing, spins are locked along either the x, y or z direction and chemical shift evolution is prevented by continuous rf irradiation or the application of a series of pulses.[10] The spacing between each pulse during the pulse train needs to satisfy the condition $|(\Omega_1 - \Omega_2)\tau_{\text{spacing}}| \ll 1$.[10] During this period, the spin system is in the "strong coupling regime", i.e. the chemical shift difference of the two coupled spins is much smaller than their J coupling constant with each other.[10,92] Because chemical shift evolution is prevented, only $\mathcal{H}_J$ is active during

this period.[10] The Hamiltonian for J coupling for the two limiting cases of weak and strong coupling is given by[10,92]

$$\mathcal{H}_J^{\text{weak}} = \sum_{j<k} 2\pi J_{jk} \hat{I}_{jz} \hat{I}_{kz} \quad \text{and} \quad \mathcal{H}_J^{\text{strong}} = \sum_{j<k} 2\pi J_{jk} \hat{\boldsymbol{I}}_{\boldsymbol{j}} \hat{\boldsymbol{I}}_{\boldsymbol{k}}, \tag{3.8}$$

where bold symbols indicate vectors of the form $\hat{\boldsymbol{I}}_{\boldsymbol{j}} = \left(\hat{I}_{j\text{x}}, \hat{I}_{j\text{y}}, \hat{I}_{j\text{z}}\right)^{\mathsf{T}}$. This complicates the calculation of the coupling during the isotropic mixing. However, as TOCSY experiments performed in this thesis (topspin sequence: dipsi2phdc) utilize spin polarization transfer of z magnetization, only the first term of eq. 3.7 needs to be considered[10,92]

$$\begin{aligned}
&- \cos(\pi J_{12} t_1) \cos(\Omega_1 t_1)\, \hat{I}_{1\text{z}} \xrightarrow{2\pi J_{12} \hat{\boldsymbol{I}}_{\boldsymbol{1}} \hat{\boldsymbol{I}}_{\boldsymbol{2}} \tau_{\text{m}}} \\
&- \frac{1}{2} \cos(\pi J_{12} t_1) \cos(\Omega_1 t_1) \left[1 + \cos(2\pi J_{12} \tau_{\text{m}})\right] \hat{I}_{1\text{z}} \\
&- \frac{1}{2} \cos(\pi J_{12} t_1) \cos(\Omega_1 t_1) \left[1 - \cos(2\pi J_{12} \tau_{\text{m}})\right] \hat{I}_{2\text{z}} \\
&+ \frac{1}{2} \cos(\pi J_{12} t_1) \cos(\Omega_1 t_1) \sin(2\pi J_{12} \tau_{\text{m}}) \left[2\hat{I}_{1\text{y}} \hat{I}_{2\text{x}} - 2\hat{I}_{1\text{x}} \hat{I}_{2\text{y}}\right] = \textcircled{5}.
\end{aligned} \tag{3.9}$$

The last expression does not evolve to observable magnetization and is therefore in the remaining treatment neglected. The concept can be extended to three spins and more.[10] Note that even if $J_{jk} = 0$, magnetization may still be transferred. The maximum peak intensity is observed for $\tau_{\text{m}} = {}^1/_{(2J_{jk})}$, i.e. when $\cos(2\pi J_{jk} \tau_{\text{m}}) = -1$.[10]
However, as J_{jk} is different for each spin pair, maximum transfer for all spins in a single experiment is impossible. For ^{1}H, a good compromise is $\tau_{\text{m}} \approx 100\,\text{ms}$, while in this thesis TOCSY measurements were only performed on ^{13}C with a mixing time of $\tau_{\text{m}} \approx 20\,\text{ms}$.[10] The difference in τ_{m} originates from much stronger J couplings ($^{2-3}J_{\text{HH}} \sim 2 - 15\,\text{Hz}$ and $^1J_{\text{CC}} \sim 10 - 150\,\text{Hz}$).[10]

Finally, the last $\pi/2$ pulse of the sequence rotates the magnetization back into the xy plane (the zero quantum term is dropped)[92]

$$\begin{aligned} ⑤ \xrightarrow{\left(\frac{\pi}{2}\right)_x} &+ \frac{1}{2}\cos\left(\pi J_{12} t_1\right)\cos\left(\Omega_1 t_1\right)\left[1+\cos\left(2\pi J_{12}\tau_m\right)\right]\hat{I}_{1y} \\ &+ \frac{1}{2}\cos\left(\pi J_{12} t_1\right)\cos\left(\Omega_1 t_1\right)\left[1-\cos(2\pi J_{12}\tau_m)\right]\hat{I}_{2y} \\ &= ⑥. \end{aligned} \tag{3.10}$$

There are multiple isotropic mixing schemes. The one employed within this thesis is called DIPSI-2.[113–116]

3.3.4.4 Incredible Natural Abundance Double Quantum Transfer (INADEQUATE)

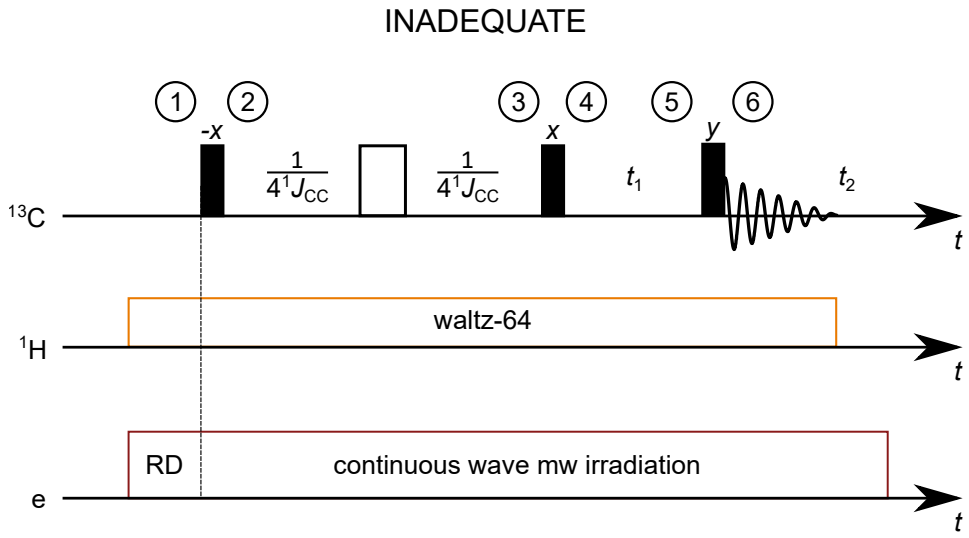

Figure 3.7: Pulse sequence of the 2D incredible natural abundance double quantum transfer experiment (INADEQUATE).[92] Black bars represent a $\pi/2$ pulse and empty bars are π pulses. Waltz64 is used for ^{1}H pre-saturation and decoupling.[111] Continuous mw irradiation is applied during the recycle delay (RD).

The incredible natural abundance double quantum transfer experiment (INADEQUATE) is an experiment to detect ^{13}C-^{13}C correlations and was designed to work with natural abundance samples.[117] Proton decoupling is applied throughout the sequence and under DNP conditions also cw mw irradiation is performed (see fig. 3.7). The description of the INADEQUATE pulse sequence starts with $\hat{I}_{1z} + \hat{I}_{2z}$, because it selects the signal of two

coupled nuclei and suppresses the signal of isolated spins ($\hat{I}_{1z}$ and $\hat{I}_{2z}$).[10,92] Therefore, the first $\pi/2$ pulse leads to[10]

$$\textcircled{1}\ \hat{I}_{1z} + \hat{I}_{2z} \xrightarrow{-\left(\frac{\pi}{2}\right)_x} \hat{I}_{1y} + \hat{I}_{2y} = \textcircled{2}. \tag{3.11}$$

This is followed by J coupling evolution, while chemical shift evolution is refocused

$$\hat{I}_{1y} + \hat{I}_{2y} \xrightarrow{2\pi J_{12}\hat{I}_{1z}\hat{I}_{2z}} -2\hat{I}_{1x}\hat{I}_{2z} - 2\hat{I}_{1z}\hat{I}_{2x} = \textcircled{3}. \tag{3.12}$$

The next $\pi/2$ pulse generates

$$-2\hat{I}_{1x}\hat{I}_{2z} - 2\hat{I}_{1z}\hat{I}_{2x} \xrightarrow{\left(\frac{\pi}{2}\right)_x} 2\hat{I}_{1x}\hat{I}_{2y} + 2\hat{I}_{1y}\hat{I}_{2x} = \textcircled{4}. \tag{3.13}$$

At this point in the pulse sequence, magnetization stemming from isolated spins is rejected, because only double quantum coherences are allowed to proceed.[10] Coherence selection is achieved via phase cycling.[10,92] Next, the chemical shift evolves as a sum

$$\begin{aligned} &2\hat{I}_{1x}\hat{I}_{2y} + 2\hat{I}_{1y}\hat{I}_{2x} \xrightarrow{([\Omega_1+\Omega_2]t_1)} \\ &\left(2\hat{I}_{1x}\hat{I}_{2y} + 2\hat{I}_{1y}\hat{I}_{2x}\right)\cos\left[(\Omega_1+\Omega_2)t_1\right] - \left(2\hat{I}_{1x}\hat{I}_{2x} - 2\hat{I}_{1y}\hat{I}_{2y}\right)\sin\left[(\Omega_1+\Omega_2)t_1\right] \\ &= \textcircled{5}. \end{aligned} \tag{3.14}$$

The final $\pi/2$ generates observable magnetization

$$\begin{aligned} &\left(2\hat{I}_{1x}\hat{I}_{2y} + 2\hat{I}_{1y}\hat{I}_{2x}\right)\cos\left[(\Omega_1+\Omega_2)t_1\right] - \left(2\hat{I}_{1x}\hat{I}_{2x} - 2\hat{I}_{1y}\hat{I}_{2y}\right)\sin\left[(\Omega_1+\Omega_2)t_1\right] \\ &\xrightarrow{\left(\frac{\pi}{2}\right)_y} -\left(2\hat{I}_{1z}\hat{I}_{2y} + 2\hat{I}_{1y}\hat{I}_{2z}\right)\cos\left[(\Omega_1+\Omega_2)t_1\right] \\ &-\left(2\hat{I}_{1z}\hat{I}_{2z} - 2\hat{I}_{1y}\hat{I}_{2y}\right)\sin\left[(\Omega_1+\Omega_2)t_1\right] = \textcircled{6} \end{aligned} \tag{3.15}$$

The first part of $\textcircled{6}$ contains observable antiphase single quantum coherences. Phase cycling was used for coherence selection.[10,118]

3.3.5 Diffusion Measurements

Measurements were executed on a 400 MHz Bruker UltraShield Avance III HD spectrometer using a 5 mm PAQXI 1H/31P-13C/15N Z-GRD 1832842/0001 probehead. The diffusion coefficient D was accessed by pulsed field gradients experiments with the standard Bruker sequence dstebpgp3s.[119] Detailed information on the gradient strength and temperature is provided in sec. 5.3.3.

3.3.6 Theoretical Calculations

3.3.6.1 Numerical Finite Element Microwave Propagation Simulations

Calculations were executed by Dr. I. Tkach, however interpretation was performed in conjunction with the author of this thesis. For the calculations, CST Microwave Studio (Dassault Systemes/CST Studio Suite^{TM} 2019) was used. The Transmission Line Matrix (TLM) time domain solver, which is based on a hexahedral mesh was applied. Usually, $(5-12)\times10^8$ cells were simulated. For excitation, a gaussian beam near field source was used. Simulations were performed on a Dell Precision T7820 workstation (Intel Xeon Gold 6242R processor/20 cores), equipped with the NVIDIA Quadro GV100 GPU (5120/640 CUDA/Tensor cores) with a computing time of $\sim 4.5-6$ h depending on the sample volume and dielectric properties.

3.3.6.2 Chemical Structure and Dynamic Simulations

Density functional theory (DFT) and molecular dynamic (MD) calculations included in this thesis were performed by Dr. Tomas Orlando and Dr. Markus Hiller. Yet, analysis and interpretation was performed by the author.

DFT calculations Geometry optimizations were performed with Orca 4.2.1 (or 4.0.1) at B3LYP level with the def2-TZVPP (or 6-311++G**/G) basis set.[120,121] The resolution-of-the-identity and chains-of-spheres approximations (RIJCOSX with def2/J auxiliary basis set) as well as the dispersion correction D3BJ[122,123] was used. The optimization criteria

TIGHTOPT and tight convergence criteria (TIGHTSCF) for the self-consistent field procedure SCF were chosen. The Löwdin population analysis delivered spin populations and spin density maps were displayed with UCSF Chimera.[124] Solvent-accessible-surfaces were calculated with Jmol and UCSF Chimera. Calculation of the hyperfine coupling at $CHCl_3$ was performed with the EPR-III basis set for H, C, N, and O and IGLO-II for Cl. More specific computational details on the particular molecular structure are given in ch.4 and ch.5.

MD calculations MD simulations were performed with Gromacs 2018.4.[125–128] A box of $CHCl_3$ with $1348 - 2485$ molecules was pre-equilibrated. The PA was positioned in the box, equilibrated, and energy minimized for 500 ps. Details on the determination of the partial charges, bond lengths, bond angles, and non bonding parameters as well as on the density and isothermal compressibility are given in sec. 5.3.10.2.

The Influence of the Molecular Structure on Scalar Dynamic Nuclear Polarization

4

4.1 Introduction

The goal of this chapter was to understand the role of the molecular structure of the polarizing agent in scalar dominated ^{13}C liquid state DNP with the prospect to identify molecular motifs that boost the DNP efficiency. To this end, a comparative study of the DNP efficiency of model compounds was performed with a variety of different nitroxide radicals and BDPA. The measurements revealed a up to a factor of five change in the DNP efficiency upon PA variation. Complementary DFT calculations indicated that a localized spin density favors an efficient spin polarization transfer. Moreover, the DNP efficiency was further increased for PAs, where the moiety containing the highest spin density is easily accessible for the target molecule. Both parameters are static parameters that contribute to the field independent part (hyperfine coupling and collision frequency) of the scalar cross-relaxation and are therefore relevant for DNP at high magnetic field. The herein identified static (or structural) contributions to the spin polarization transfer are discussed together with dynamic contributions (chapter 5) in chapter 8.

Section 4.2-4.3.6 are published as a communication in the journal Physical Chemistry Chemical Physics. They are reproduced from ref. [86] with permission from the PCCP Owner Societies. The article is available as: M. Levien, M. Reinhard, M. Hiller, I. Tkach, M. Bennati, and T. Orlando, "Spin density localization and accessibility of organic radicals affect liquid-state DNP efficiency", *Phys. Chem. Chem. Phys.* **2021**, *23*, 4480 – 4485

[86]. The ^{1}H experiments in this chapter were performed by M. Reinhard during his master thesis[129] and by the author. The master thesis was supervised by the author. M. Reinhard also contributed to preliminary experiments at 1.2 T, which were finalized and experimentally verified by the author. I. Tkach contributed to the hardware optimization during the experiments. DFT calculations were performed by M. Hiller. Data analysis and interpretation was performed by the author and T. Orlando. The manuscript was conceptualized and written by T. Orlando, M. Bennati, and the author.

Abstract We report a large variation in liquid DNP performance of up to a factor of about five in coupling factors among organic radicals commonly used as polarizing agents. A comparative study of ^{1}H and ^{13}C DNP in model systems shows the impact of the spin density distribution and accessibility of the radical site by the target molecule.

Acknowledgment Financial support has been provided by the Max Planck Society. M. Levien acknowledges IMPRS-PBCS of the Max Planck Society for funding for a fellowship. The Synthetic Chemistry facility of MPI-bpc is acknowledged for the synthesis of the radical TN-py.

4.2 Spin Density Localization and Accessibility of Organic Radicals Affect Liquid State DNP Efficiency

In the past two decades, dynamic nuclear polarization (DNP) has become one of the most important tools to tackle the long-standing sensitivity issue in modern nuclear magnetic resonance (NMR).[15,130] In a DNP experiment, polarization is transferred from higher polarized electron spins by resonant microwave (mw) irradiation to the target nuclei. Electron spins are often added to the investigated sample in the form of exogenous polarizing agents (PAs), usually organic radicals.

DNP has been successful in the solid-state, where it is routinely applied to various systems in biology and material science, and enables an extraordinary saving of experimental time.[131,132] Part of these achievements were possible thanks to the optimization of bi-radicals as excellent PAs for the polarization transfer via the cross-effect.[26,27,133]

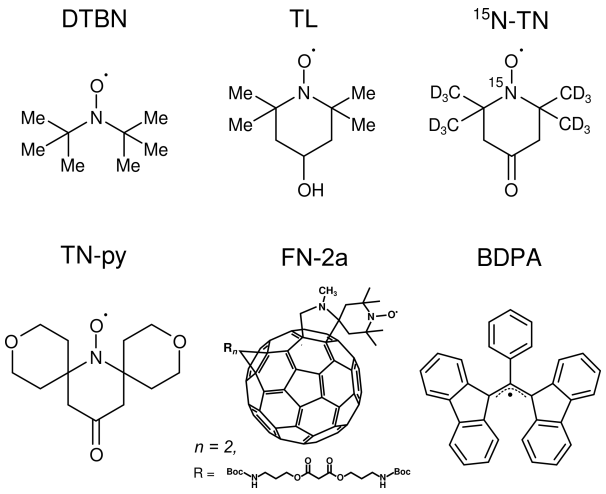

Figure 4.1: Molecular structures of the organic radicals tested as PAs for DNP in the liquid state. **DTBN** (di-*tert*-butyl-nitroxide); **TL** (tempol - 4-Hydroxy-2,2,6,6-tetramethylpiperidine 1-oxyl); ^{15}**N-TN** (^{15}N-TN-d$_{16}$ - 4-Oxo-2,2,6,6-tetramethylpiperidine-d$_{16}$,1-^{15}N-1-oxyl); **TN-py** (7-Aza-3,11-dioxa-15oxodispiro[5.1.5.3]hexadec-7-yl-7-oxyl); **FN-2a**, fullerene-nitroxide derivative with 2 adducts (see inset); **BDPA** (α,γ-Bisdiphenylene-β-phenylallyl). Reproduced from ref. [86] with permission from the PCCP Owner Societies.

The polarization transfer in liquids is dominated by the Overhauser effect (OE)[42] and strongly depends on the chosen target molecule/PA system as well as on the external magnetic field strength.[16,134] Increasing the efficiency of OE-DNP is of particular importance. At high magnetic fields, the choice of an optimal PA would help the application of the method in analytics and high resolution NMR spectroscopy.[48,53,68,69,135] Furthermore, higher NMR enhancements could boost the applications of OE-DNP at low fields (<2 T), which include in-flow hyperpolarization for magnetic resonance imaging[64,65] or chromatography,[136,137] NMR relaxometry of low-γ nuclei,[138] hydration dynamic studies,[139,140] and DNP-NMR spectroscopy.[34,141,142]

In the experimental practice, nitroxide derivatives (NODs) have been established as optimal PAs for OE-DNP in the liquid state at room temperature and ambient pressure.[46,143] In water, they perform better than trityl radicals at various fields (from 0.34 T to 3.4 T),[144,145] and they are the benchmark for ^{1}H-DNP at low fields (enhancements $\epsilon = -178 \pm 13$ for water doped with TN).[84,85]

An improvement of nitroxide derivatives performance was realized by linking a C_{60}

(fullerene) moiety to a TEMPO based radical, which increased the saturation factor of the electron spin transition.[88]

Also BDPA has been employed in numerous DNP studies in solid and in liquids, the latter particularly at high fields ($\geq 5\,\mathrm{T}$).[58,69,146] However, despite its favourable saturation behaviour, the performance of BDPA in liquids as compared to NODs appeared moderate, but a systematic study has been missing.

Despite the available data, it is difficult to compare the PA's performance independently of the experimental conditions, such as mw power and resonant cavity, magnetic field, radical concentration, and target nuclei. Although several mechanistic studies on ^{1}H[43,46,49] and ^{13}C[34,59,89] have been reported, the detailed role of the PA remains unclear. Very recently, we investigated the case of fullerene nitroxides in comparison to TN,[34,83] and found that small structural reorientations can impact the DNP efficiency at both low and high magnetic fields.[83] Therefore, we proposed that the chemical structure of the PA molecule must play an essential role within the OE-DNP mechanism.

To examine this hypothesis, in this work we systematically investigate and compare the performance of several PAs in OE-DNP in the liquid state and show that NODs, with subtle differences in their chemical structure, behave differently from each other. To ensure comparability of the results, we utilized model solvents in which the polarization transfer mechanisms are known. DNP was performed at low fields (0.34 T and 1.2 T), where an independent determination of all OE parameters was feasible with our available instrumentation. The trend that we observe in DNP performance is interpreted in terms of radical mobility, solvent accessibility, and spin density distributions, with the support of DFT calculations. Our investigation allows to recognize specific characteristics of the PA structure which are a prerequisite for effective OE-DNP in liquids.

Overhauser DNP is based on a cross-relaxation process between an electron spin system and a nuclear spin system mediated by molecular motions.[42,43,80] The hyperfine coupling driving the relaxation consists of two contributions: *i*) dipolar coupling, modulated by diffusion;[43,79] *ii*) scalar coupling, due to Fermi contact interactions, usually mediated by molecular collisions.[60,79] The complex interplay of these two mechanisms is reflected in

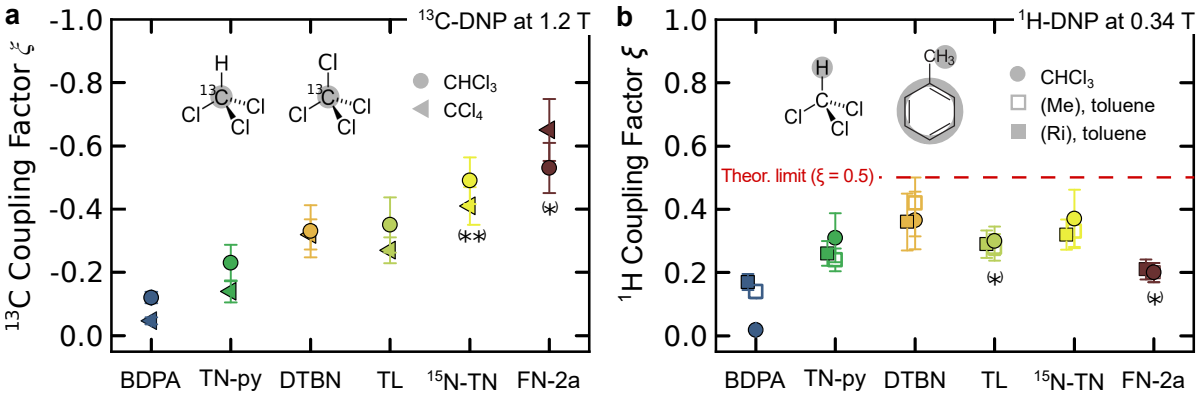

Figure 4.2: (a) ^{13}C-DNP coupling factors ξ obtained at 1.2 T for chloroform (circle) and tetrachloromethane (triangle) doped with the organic radicals from fig. 4.1. (b) ^{1}H-DNP coupling factors ξ measured at 0.34 T for chloroform and toluene doped with the organic radicals from fig. 4.2. Ring (Ri) and methyl (Me) protons of toluene are distinguished. $^{(*)}$Data from previous reports.[34,83,88] $^{(**)}$Data reproduced from previous reports.[34] Reproduced from ref. [86] with permission from the PCCP Owner Societies.

a single parameter, the coupling factor ξ, which varies between $\xi = 0.5$ (pure dipolar) and $\xi = -1$ (pure scalar). ξ is defined by the Overhauser equation[42]

$$\epsilon = \frac{\langle I_z \rangle}{I_0} = 1 - \xi s f \frac{|\gamma_e|}{\gamma_n}, \tag{4.1}$$

where ϵ is the NMR signal enhancement, which is defined as the ratio between the expectation value of the nuclear magnetization under mw irradiation $\langle I_z \rangle$ and the one at thermal equilibrium I_0. γ_e and γ_n are the gyromagnetic ratios of the electron spin (e) and the nuclear spin (n), respectively. The saturation factor s ($0 \leq s \leq 1$) is a measure of how far the electron spin is driven out of equilibrium by the applied mw irradiation.[84] The leakage factor f ($0 \leq f \leq 1$) accounts for the paramagnetic relaxation contribution to the nuclear relaxation term, and depends on the PA concentration. Since s and f can be tuned by the mw power and the radical concentration, respectively, the coupling factor ξ defines the net efficiency of a specific PA in a given system, and can be calculated with eq. 4.1 once s, f, and ϵ are independently determined.

In this study, we compare the DNP efficiency, represented by ξ, of six organic radicals that differ in their chemical structure (fig. 4.1). Within the NODs, TL and TN have both a six-membered ring but a different backbone. DTBN lacks the piperidine backbone

Table 4.1: Overhauser parameters f, s, ϵ, and ξ for ^{13}C at 1.2 T and ^{1}H DNP at 0.34 T for different PAs in chloroform. Uncertainties for f and s are 10% while errors for ϵ and ξ are up to 15% and 25%, respectively (see sec. 4.3.5). Radical concentration is 0.5−16 mM (see tab. 4.2, tab. 4.3, tab. **??**, tab. 4.5, and tab. 4.6).(*) Uncertainty of this measurement is ∼15 %. Reproduced from ref. [86] with permission from the PCCP Owner Societies.

	^{13}C DNP at 1.2 T				^{1}H DNP at 0.34 T			
Radical	$f(^{13}C)$	$s(^{13}C)$	$\epsilon(^{13}C)$	$\xi(^{13}C)$	$f(^{1}H)$	$s(^{1}H)$	$\epsilon(^{1}H)$	$\xi(^{1}H)$
DTBN	0.88	0.04	31	−0.33	0.99	0.76	−181	0.37
^{15}N-TN	0.85	0.18	200	−0.49	0.99	0.92	−224	0.37
TL	0.92	0.07	59	−0.35	0.97[83]	0.45[83]	−85[83]	0.30[83]
TN-py	0.89	0.10	55	−0.23	0.99	0.78	−156	0.31
FN-2a[88]	0.89	0.30	370	−0.53	0.99	0.87	−116	0.20
BDPA	0.40	1.0*	122	−0.12	0.99	1.0	−11	0.018

and is therefore very mobile, a feature that, in principle, makes this radical ideal for DNP modulated by fast diffusion processes. In contrast, TN-py has the same backbone structure of TN but has two hydropyrane rings in the direct vicinity of the NO group. We also consider the fullerene-nitroxide FN-2a, which has been already reported as a PA in the context of ^{1}H and ^{13}C DNP.[34,83,88] Finally, we compared NODs with BDPA. The organic radicals were dissolved in toluene (C_7H_8), chloroform ($CHCl_3$) and tetrachloromethane (CCl_4), with concentrations in the range 1.5-10 mM. All samples were degassed and sealed in quartz tubes.

^{1}H-DNP measurements were performed in toluene and chloroform at 0.34 T. ^{13}C-DNP was performed at 1.2 T in $^{13}CCl_4$ and $^{13}CHCl_3$ samples, and, in order to limit the temperature raise, we worked under low power condition (< 3 W). The polarization build-up time was monitored to exclude severe heating effects (see sec. 4.3.5). The saturation factor s and f were measured independently with electron-nuclear double resonance (ELDOR) experiments and nuclear relaxation measurements, respectively (tab. 4.1 and sec. 4.3.3). NMR enhancements ϵ were obtained with a mw pumping pulse up to 80 s, depending on the sample. The coupling factor ξ was then calculated with eq. 4.1.

Figure 4.2a and fig. 4.2b display ξ for ^{13}C and ^{1}H, respectively, in different solvent/PA systems. ^{13}C-DNP coupling factors ξ (fig 4.2a) are negative, a fact which indicates a scalar-dominated polarization transfer,[42,80] and shows an interesting, quite unexpected

behaviour. Indeed, in CCl_4, ξ is strongly dependent on the PA, and goes from the least efficient BDPA ($|\xi| < 0.12$) to the most efficient fullerene nitroxide (FN-2a),[34,88] with $|\xi| = 0.65 \pm 0.1$. This indicates a factor of ~ 5 variation in DNP efficiency. Besides these large differences, also variations among structurally similar small NODs (TL, DTBN and TN) are observed. In $CHCl_3$, the total variation of ξ (from BDPA to FN-2a) is a factor of ~ 4 (tab. 4.1), whereas it is a factor of 1.5 among the small NODs ($|\xi|$(DTBN) = 0.33 and $|\xi|$(^{15}N-TN) = 0.49, tab. 4.1).

^{1}H-DNP coupling factors show a different trend. Firstly, ξ is positive, consistent with a mechanism dominated by dipolar relaxation. Specifically, ξ varies from $\xi = 0.24 \pm 0.04$ for TN-py up to a maximum $\xi = 0.42 \pm 0.1$ for DTBN in toluene, which is close to the theoretical limit of $\xi = 0.5$.[42,80] Among the NODs, ξ decreases with larger molecular sizes and the smallest radical, DTBN, displays the largest ξ. This behaviour is consistent with the prediction by the force-free hard-sphere (ffhs) model,[81,82] according to which the polarization transfer mediated by dipolar relaxation is modulated by diffusion. Indeed, the efficiency decreases with increasing translational and rotational diffusion time of the PA/target molecule complex. Finally, BDPA performs worse than NODs, and shows a solvent dependency for ξ, possibly due to secondary interactions (e.g. π-stacking in toluene).

The main question is how to rationalize the trend of the ^{13}C coupling factors shown in fig. 4.2a. Indeed, we reported in previous studies,[34,60] and it is predicted[42] by the theory that coupling factor in ^{13}C-DNP arises from an interplay of dipolar and scalar relaxations mechanisms.[16,80] First, our results show that, a poor performance of dipolar dominated DNP (such as ^{1}H-DNP) does not necessarily correlate with an efficient scalar mechanism (fig. 4.2). This means that the observed trend reflects a property of the scalar mechanism. Scalar relaxation via contact interaction can be described by the Pulse model for random molecular collisions[79] with the spectral density for a single type of collision

$$J_{\text{Pulse}}(\omega_e, A_{\text{iso}}, \tau_{\text{con}}, \tau_p) = \frac{\langle A_{\text{iso}} \rangle^2 \cdot \pi^2}{\tau_p} \cdot J_{\text{con}}(\omega_e, \tau_{\text{con}}), \tag{4.2}$$

where ω_e is the Larmor angular frequency of the electron spin, A_{iso} is the isotropic (Fermi Contact, in Hz) hyperfine coupling modulated by collisions of a duration τ_{con} and the

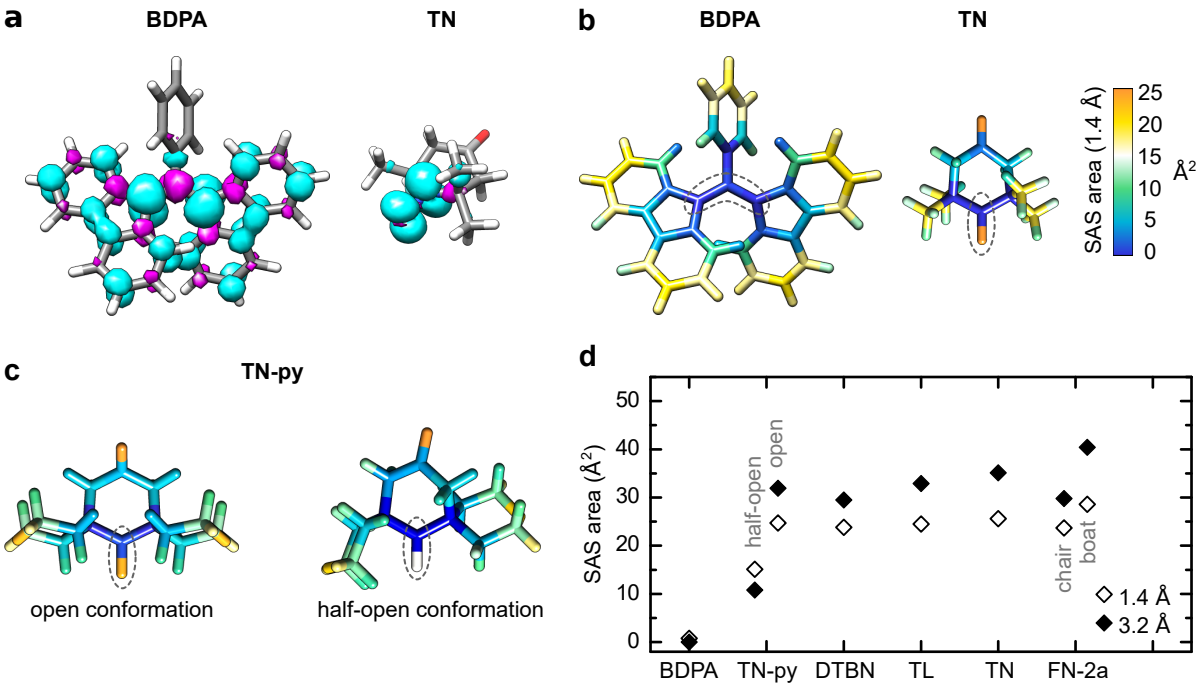

Figure 4.3: Geometry optimization and DFT calculations were performed with Orca,[120] using def2-TZVPP as basis set and B3LYP as functional (see sec. 4.3.6). (a) Electron spin density distribution (isosurface threshold $\pm 0.002\ e/\text{Å}^{-3}$) calculated for DFT optimized structures of BDPA and TN. Spin density colour code: cyan: positive, magenta: negative. Atoms colour code: H white, C grey, N blue, O red. (b) Colour map of the SAS area for each atom in BDPA and TN calculated with a spherical probe of radius 1.4 Å corresponding to the Van der Waals sphere of a water molecule. Blue: least accessible; orange: most accessible. Dash lines show the sites with the largest spin density. (c) Colour maps of the SAS areas for TN-py in the open conformation ($E_{\text{rel}} = 0.0$ kJ/mol) and in the half-open conformation ($E_{\text{rel}} = 0.46$ kJ/mol). The piperidine ring is arranged in a chair for the open conformation and in a twist for the half-open. Graphics and SAS calculations were obtained with UCSF Chimera[124] and jmol. (d) SAS areas of the radical sites, where the largest spin density is localized. Two stable conformations were considered also for FN-2a, the most stable one (chair) and the closest in energy (boat), although the latter is not accessible at room temperature.[83] Reproduced from ref. [86] with permission from the PCCP Owner Societies.

frequency of this collisions τ_{p}^{-1}. Accordingly, the scalar mechanism requires that the radical spin density is accessible and transferred to the target nucleus during an encounter. Hereby, we examined whether the observed trend in ξ could depend on the accessibility of the radical site or on the achievable hyperfine coupling constant or both. For this

goal, we analyzed the radical structure as well as the structure of the static complex PA/target molecule using DFT calculations. In the first step, we computed the spin density distribution for each radical optimized structure to identify the radical sites in each PA. In NODs, the electron spin density is almost completely localized on the NO group[59,147] (∼90% of the Löwdin spin population, fig. 4.3a). In contrast, the majority of the spin population of BDPA is localized on the allyl group (∼40%), while the remaining spin density is widely distributed over the fluenyl systems (fig. 4.3a).[148] It becomes clear that, in the case of BDPA, the ffhs model, which defines a single value for the distance of closest approach between the electron spin density and the solvent molecules, is an insufficient approximation.

The spin density distribution was used to identify the radical sites and then calculate their accessibility. We computed the solvent-accessibility surface (SAS) area, a parameter that tracks the center of a spherical probe (the solvent) rolling on the Van der Waals surface of the radical. As solvent probes, we considered water ($r_{H2O} = 1.4$ Å), for comparison with literature data,[149] and chloroform $CHCl_3$ ($r_{CHCl3} = 3.2$ Å). Due to the geometrical nature of SAS areas, the conclusions hold for both solvent probes. Figure 4.3b shows that the allyl group in BDPA is deeply buried and almost inaccessible, with SAS < 1 Å^2 for both probes. On the contrary, the SAS area of the NO group in the NODs is larger, ranging from a $SAS_{3.2Å} = 29.5$ Å^2 for DTBN to $SAS_{3.2Å} = 35.1$ Å^2 for TN (fig. 4.3b and 4.3d). These large SAS areas are mainly due to the accessibility of the O atom, while the N atom remains buried. For TN-py, a conformational analysis shows four energetically accessible conformers at room temperature, which differ in the orientation of their hydropyrane rings, i.e. open and half-open (see sec. 4.3.6).[149] While the $SAS_{3.2Å}$ is ∼32 Å^2 for the open conformation, the accessibility of the radical site is hampered in the half-open ones ($SAS_{3.2Å} \sim 11$ Å^2) (fig. 4.3c).

Overall, the trend of the SAS depicted in fig. 4.3d correlates with our observations of $\xi(^{13}C)$ (fig. 4.2a) with the exception of the very large ξ of FN-2a. This can be interpreted phenomenologically with the Pulse model for molecular collisions (eq. 4.2), which describes $|\xi| \propto J_{Pulse}$. Intuition suggests that the accessibility of the radical site should mainly impact the rate of collision τ_p^{-1}, i.e. the likelihood of a given encounter. Since τ_p^{-1} is a prefactor in J_{Pulse}, this could explain the observed correlation. To support this, we note that the field dependent term J_{con} (τ_{con},ω_e) in eq. 4.2 is determined by the duration

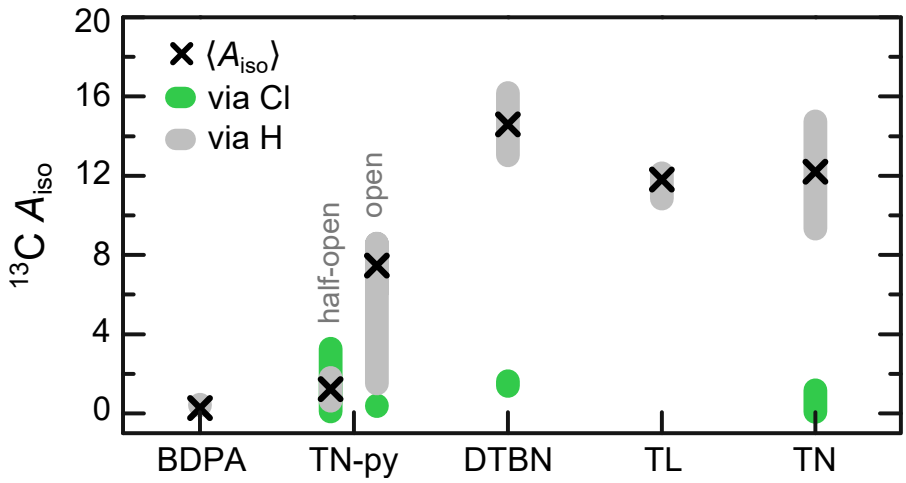

Figure 4.4: Hyperfine coupling computed for geometry optimized complexes of PA/$CHCl_3$. The calculations were performed with Orca[120] using the basis set EPR-III for H, C, N, and O, and IGLO-II for Cl.[150] Two orientations of the $CHCl_3$ are considered ("via H" and "via Cl"). $\langle A_{iso} \rangle$ is the weighed average with respect to the relative energy of each configuration. Reproduced from ref. [86] with permission from the PCCP Owner Societies.

of each encounter. In previous studies[34,60] we showed that, in CCl_4 and $CHCl_3$ doped with TN, the main contribution comes from $\tau_{con} \approx 0.5 - 2\,ps$. The same could be reasonably assumed for other NODs (DTBN, TL) in the same solvent and at the same temperature. Nonetheless, structural reorientations on the PA molecule can introduce additional contributions to $J_{con}(\tau_{con},\omega_e)$. This is particularly relevant for the specific case of FN-2a, whose outstanding performance is likely caused by a particularly favourable collision time scale ($\tau_{con} \approx 4 - 12\,ps$), which maximizes $J_{con}(\tau_{con},\omega_e)$ at this magnetic field (1.2 T). In our previous report,[83] this was attributed to the transition of the six-membered ring from a chair to an unstable half-chair conformation, enabled by the asymmetry of the backbone linker.[83] Similar dynamics are not expected in TL, TN, and DTBN but cannot be excluded for TN-py.

In a second step, we considered the static complex PA/target molecule and used DFT calculations to compute the hyperfine coupling constant A_{iso} to the target nucleus.[59,60] A_{iso} of the C nucleus in $CHCl_3$ was calculated for at least four optimized geometries i for each complex PA/$CHCl_3$ (see tab. 4.8). Due to the tendency of the H atom of $CHCl_3$ to form hydrogen bonds, we distinguish an energetically favoured complex where the H

is pointing towards the radical ("via H"), and a less favoured one, where the Cl atom is the closest to the radical ("via Cl"). The hyperfine coupling $\langle A_{\text{iso}} \rangle$ was calculated as the weighted average of $A_{\text{FC},i}$ over the relative free energy $E_{\text{rel},i}$ of each configuration i, i.e. $\langle A_{\text{iso}} \rangle = \sum_i A_{\text{iso},i} \cdot P_i / \sum_i P_i$ where $P_i = e^{E_{\text{rel},i}/k_{\text{B}}T}$, with $T = 300\,\text{K}$. $\langle A_{\text{iso}} \rangle$ calculated for DTBN, TL, and TN are similar and between 11.8 MHz and 14.6 MHz. The lack of the piperidine backbone structure in DTBN seems to slightly affect the hyperfine coupling to the C nucleus. Notably, the $\langle A_{\text{iso}} \rangle$ of TN-py calculated for both the open and the half-open conformations are smaller than the other NODs (fig. 4.4), which agrees with our experimental observation of a lower $\xi(^{13}\text{C})$. This is justified within the Pulse model, where the spectral density J_{Pulse} scales with $\langle A_{\text{iso}} \rangle$ (eq. 4.2).
Finally, the $\langle A_{\text{iso}} \rangle$ calculated for the complex BDPA/$CHCl_3$ is 0.26 MHz, significantly lower than $\langle A_{\text{iso}} \rangle$ calculated for NODs (fig. 4.4 and tab. 4.8). This reveals the weak ability of BDPA to transfer spin density on the C nucleus, despite more than 50% of the spin density is readily accessible on the phenylene rings. Therefore, the lack of an accessible site where a large spin density is localized seems to be detrimental for scalar-driven DNP.

In conclusion, our study revealed that differences in the chemical structure of organic PAs commonly used in DNP can influence the performance of OE-DNP, up to a factor of five when the mechanism is scalar-dominated. We identified features that should be considered for designing an optimal PA. Specifically, a localized spin density is preferred over a distributed one, because it increases the hyperfine coupling with the target nuclei. Secondly, the accessibility of the radical site, which affects the collision rate with the target molecule, should not be compromised by structural design (BDPA) or conformational rearrangements (TN-py). We note that these characteristics, which can be inferred a priori from the structure of the PA, affect the field independent term of the scalar relaxation and should therefore be taken into account also for OE-DNP at high magnetic fields.

Table 4.2: ^{1}H Overhauser parameters of the methyl group of toluene for different PAs at room temperature and at 0.34 T. The leakage factor f was calculated using $T_{1n}^{0} = 8.1\,s$ (ref. [83]). Errors of the concentration are $10-15\,\%$, for T_{1n}, $T_{Build\text{-}up}$, s, ϵ and f 10 % and for ξ 15 %. As $T_{1n} \neq T_{Build\text{-}up}$ for DTBN, errors for ϵ and ξ are increased to 15 and 25 %, respectively (see error discussion in sec. 4.3.5). (*) Data from ref. [83]. Reproduced from ref. [86] with permission from the PCCP Owner Societies.

	^{1}H-DNP in toluene - methyl protons						
	c (mM)	T_{1n} (s)	$T_{Build\text{-}up}$ (s)	f	s_{eff}	ϵ	ξ
DTBN	2	4.9	3.8	0.40	0.58	−62	0.42
^{15}N-TN	2	3.8	3.4	0.53	0.78	−88	0.33
TL*	1.5	4.7	4.7	0.42	0.58	−45	0.28
TN-py	2	2.6	2.6	0.68	0.80	−86	0.24
BDPA	2	4.2	4.8	0.48	1.00	−45	0.14

4.3 Supplementary Information

4.3.1 Sample Preparation

Organic radicals α,γ-Bisdiphenylene-β-phenylallyl (BDPA, 1:1 complex with benzene), Di-*tert*-butyl-nitroxide (DTBN), 4-Hydroxy-2,2,6,6-tetramethylpiperidine 1-oxyl or tempol (TL) and 4-Oxo-2,2,6,6-tetramethylpiperidine-d_{16},1-^{15}N-1-oxyl or tempone (TN) were purchased from Sigma-Aldrich and used as received. 7-Aza-3,11-dioxa-15-oxodispiro-[5.1.5.3]hexadec-7-yl-7-oxyl (TN-py) was prepared in house according to a protocol from ref. [106].

$^{13}CCl_4$ and $^{13}CHCl_3$ were purchased from Eurisotop and Sigma-Aldrich, respectively. As the pH value of $^{13}CHCl_3$ was ~ 1 upon delivery, K_2CO_3 was added until a pH of $6-7$ was reached. Roughly 1% ethanol (of the absolute volume of $^{13}CHCl_3$) was added for stabilization. Unlabelled tetrachloromethane, chloroform, and toluene were purchased from Merck KGaA and Sigma-Aldrich.

PA concentrations range between 1 mM and 16 mM and were verified by continuous wave (cw) measurements. Approximately 7 µL per sample were inserted in a quartz tube with an outer diameter of 1.6 mm and an inner diameter of 1.1 mm. All samples were degassed by freeze-pump-thaw cycles (from two to four) to remove dissolved oxygen. Degassing small amounts of sample results in an error of up to 15% for the concentration.

4.3.2 Overhauser Experiments and Parameters

4.3.3 ^{1}H-DNP at X-Band – 0.34 T

Measurements were performed using a Bruker ElexSys E580 EPR spectrometer combined with an AVANCE III ^{1}H 300 MHz NMR console. We utilized an EN 4118X-MD-4 EPR resonator with Electron Nuclear Double Resonance (ENDOR) capabilities. The ENDOR coil was used to excite and detect the NMR transitions. EPR and ELDOR measurements (see below) were performed employing a 1 kW TWT microwave amplifier, while for DNP measurements we utilized an AmpX 5 W cw mw amplifier. Comparability of the results was demonstrated before.[87]

^{1}H NMR signal enhancements were obtained from comparison of the integrated NMR signal with and without microwave. Boltzmann signals were typically acquired using up to 64 scans, while 1 or 2 scans were recorded under DNP conditions. The used recycle delay was $\sim 5 \times T_{1n}$. The signal enhancement can be calculated

$$\epsilon = \frac{I_{DNP}}{I_{Bltz}} \cdot \frac{NS_{Bltz}}{NS_{DNP}}, \tag{4.3}$$

where $I_{DNP/Bltz}$ is the integral of the NMR signal with and without mw irradiation and $NS_{DNP/Bltz}$ is the number of scans with and without mw irradiation. Figure 4.5a shows the enhanced NMR signal and the Boltzmann signal of toluene doped with DTBN.

Table 4.3: ^{1}H Overhauser parameters of the ring protons of toluene for different PAs at room temperature and at 0.34 T. The leakage factor f was calculated using $T_{1n}^0 = 12.5$ s (ref. [83]). Errors of the concentration are 10 – 15 %, for T_{1n}, $T_{Build\text{-}up}$, s, ϵ and f 10 % and for ξ 15 %. As $T_{1n} \neq T_{Build\text{-}up}$ for DTBN, errors for ϵ and ξ are increased to 15 and 25 %, respectively (see error discussion in sec. 4.3.5). (*) Data from ref. [83]. Reproduced from ref. [86] with permission from the PCCP Owner Societies.

	^{1}H-DNP in toluene - aromatic protons						
	c (mM)	T_{1n} (s)	$T_{Build\text{-}up}$ (s)	f	s_{eff}	ϵ	ξ
DTBN	2	5.5	4.2	0.56	0.58	−77	0.36
^{15}N-TN	2	4.2	3.6	0.67	0.78	−108	0.32
TL*	1.5	5.5	5.5	0.56	0.58	−61	0.29
TN-py	2	2.6	2.7	0.79	0.80	−109	0.26
BDPA	2	5.2	6.3	0.58	1.00	−63	0.17

Table 4.4: ^{1}H Overhauser parameters of chloroform for different PAs at room temperature and at 0.34 T. The leakage factor f was calculated using $T_{1n}^0 = 82.5\,\text{s}$ (ref. [83]). Errors of the concentration are $10-15\,\%$, for T_{1n}, $T_{\text{Build-up}}$, s, ϵ and f 10 % and for ξ 15 %. As $T_{1n} \neq T_{\text{Build-up}}$ for DTBN, TN-py and TN errors for ϵ and ξ are increased to 15 and 25 %, respectively (see error discussion in sec. 4.3.5). (*) Data from ref. [83]. Reproduced from ref. [86] with permission from the PCCP Owner Societies.

	^{1}**H-DNP in $CHCl_3$**						
	c (mM)	T_{1n} (s)	$T_{\text{Build-up}}$ (s)	f	s_{eff}	ϵ	ξ
DTBN	10	0.73	0.51	0.99	0.72	−163	0.35
DTBN	16	0.12	0.10	0.99	0.79	−199	0.38
^{15}N-TN	10	0.32	0.21	0.99	0.92	−224	0.37
TL*	0.5	2.8	2.9	0.97	0.45	−85	0.30
TN-py	10	0.42	0.24	0.99	0.78	−156	0.31
BDPA	10	0.56	0.69	0.99	1.00	−11	0.018

Saturation factors were determined using an ELDOR (Electron Nuclear Double Resonance) sequence. During this experiments, EPR detection is performed on one of the EPR lines while a long saturation pulse ($3-5\,\mu$s) is swept through the EPR spectrum. At positions where the ELDOR pulse is on resonance with either one of the lines, a signal drop is detected. From these intensity drops the saturation factor of each line can be obtained. The effective saturation factor s_{eff} for a n-line systems is calculated as follows[84,85]

$$s_{\text{eff}} = \frac{1}{n} \cdot \sum_{i=1}^{n} s_i. \tag{4.4}$$

Figure 4.5b shows the ELDOR curve for DTBN in toluene and, in the inset, the ELDOR pulse sequence.

The leakage factor f can be calculated with the formula

$$f = 1 - \frac{T_{1n}}{T_{1n}^0}, \tag{4.5}$$

where T_{1n} and T_{1n}^0 are the nuclear relaxation times in presence and absence of paramagnetic substance.

T_{1n} was measured with a saturation recovery experiment (8 saturation pulses with a duration of 6 μs each, $(\pi/2)_{\text{RF}} = 6\,\mu\text{s}$, $P_{\text{RF}} = 60\,\text{W}$). Build-up times $T_{\text{Build-up}}$ were measured

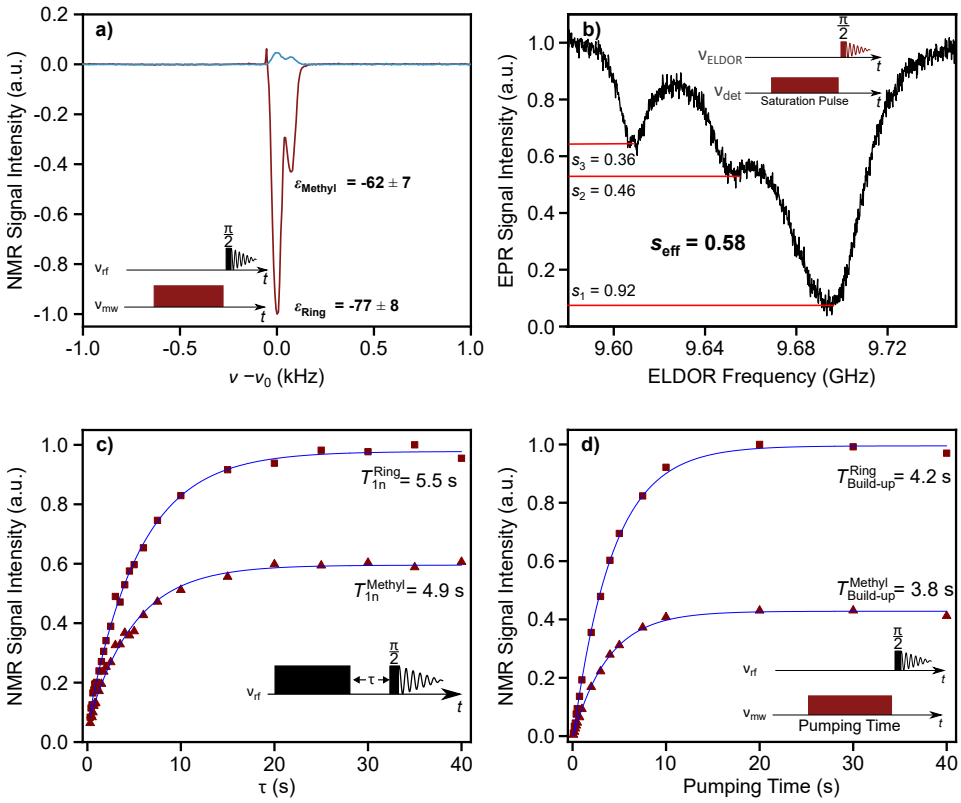

Figure 4.5: a) ^{1}H NMR signal with (red) and without (blue) mw irradiation of toluene using DTBN as a PA. b) saturation curve (black) of DTBN in toluene, s_{eff} results as the average of s_1, s_2 and s_3. c) T_{1n} determination via saturation recovery measurements; d) measurement of $T_{Build\text{-}up}$ by increasing the mw pumping time (red squares for the ring protons and red triangles for the methyl group of toluene) at 0.34 T. Blue curves are the mono exponential fits used to obtain T_{1n} and $T_{Build\text{-}up}$. Reproduced from ref. [86] with permission from the PCCP Owner Societies.

by increasing the mw irradiation time. Both T_{1n} and $T_{Build\text{-}up}$ were obtained from fitting the experimental data to a mono exponential function i.e. $y = A(1 - \exp(-t/T_i))$. Examples of T_{1n} and $T_{Build\text{-}up}$ recovery experiments are shown in fig. 4.5c and fig. 4.5d, together with the respective pulse sequences.

The experimental results of ^{1}H-DNP measurements at 0.34 T for different PAs and solvents are summarised in tab. 4.2-4.4, fig. 4.7, and fig. 4.6.

4.3.4 ^{13}C-DNP at Q-Band – 1.2 T

^{13}C-DNP at 1.2 T was performed on an Bruker ElexSys E580 EPR spectrometer combined with an AVANCE III ^{1}H 300 MHz NMR console. We used a Bruker ER-5106QT/W cw resonator. For NMR detection, a copper coil was wrapped around the tube, thereby reducing the Q-value of the resonator. In order to limit sample heating during mw irradiation, we operated at low mw power (< 3 W).

The parameters s, f, and ϵ were measured as described in the previous section. However, due to the low NMR sensitivity, T_{1n} was measured with a pre-polarization sequence, where a short mw pulse (< 3 s) is introduced before the $\pi/2$ NMR detection. The time t between the two pulses is incremented, and the signal decay is fitted to the exponential function $A \cdot \exp\{(-t/T_{1n})\}$. During the measurement of the saturation factor of BDPA in $^{13}CHCl_3$ we observed an artefact which led to a distorted shape of the spectrum. Due to this, we assign an increased uncertainty of 15 % to this measurement.

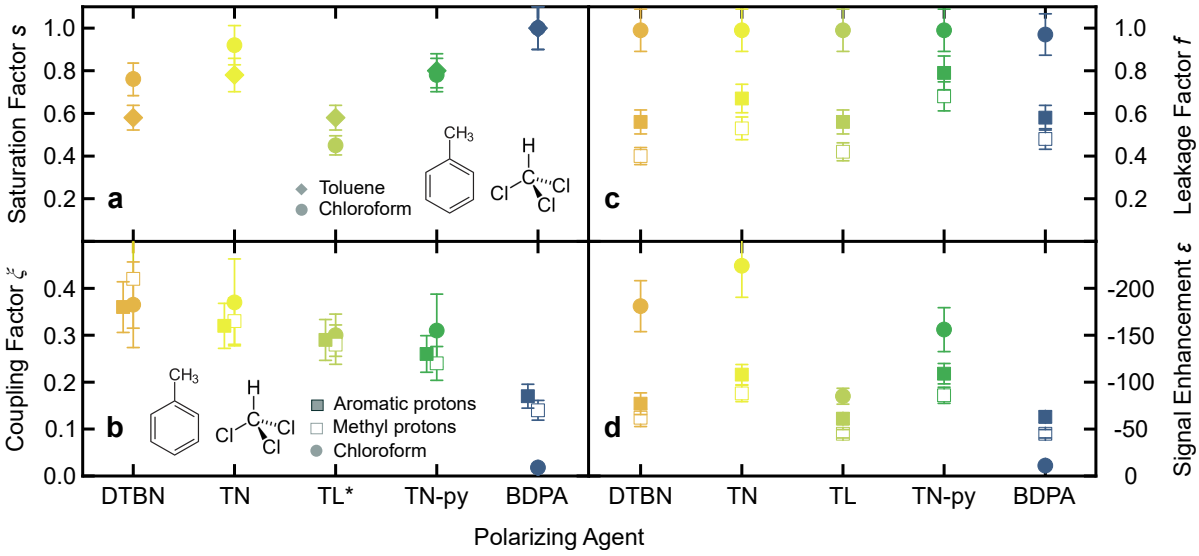

Figure 4.6: Plots of the ^{1}H-DNP Overhauser parameters from tab. 4.2, tab. 4.3, and tab. 4.4. Reproduced from ref. [86] with permission from the PCCP Owner Societies.

4.3.5 Heating Effects

The longitudinal nuclear relaxation times are sensitive to the temperature. Therefore, a comparison between between $T_{\text{Build-up}}$ and T_{1n} can reveal heating effects during mw irradiation. We observed differences on the order of 9% – 20% for all the investigated samples, suggesting that a temperature deviation of a few K may be present. In the

Table 4.5: ^{13}C Overhauser parameters of $^{13}CCl_4$ for different PAs at room temperature and at 1.2 T. The leakage factor f was calculated using $T_{1n}^0 = 200$ s.[60] Errors of the concentration are 10 – 15 %, for T_{1n}, $T_{\text{Build-up}}$, s, ϵ and f 10 % and for ξ 15 %. As $T_{1n} \neq T_{\text{Build-up}}$ for TN-py and BDPA errors for ϵ and ξ are increased to 15 and 25 %, respectively (see error discussion in sec. 4.3.5). (*) Data from ref. [83]. Reproduced from ref. [86] with permission from the PCCP Owner Societies.

^{13}C-DNP in CCl_4	c (mM)	T_{1n} (s)	$T_{\text{Build-up}}$ (s)	f	s_{eff}	ϵ	ξ
BDPA	10	47.0	33.0	0.84	0.95	98	−0.047
TN-py	10	9.3	6.7	0.95	0.06	22	−0.14
DTBN	10	6.7	6.1	0.97	0.05	41	−0.32
TL	10	7.7	6.8	0.96	0.11	75	−0.27
^{15}N-TN*	10	18.5	16.6	0.93	0.25	250	−0.41
TP-CLST*	10	2.9	3.4	0.99	0.12	150	−0.48
FN-2a*	10	3.8	3.8	0.98	0.33	550	−0.65

Table 4.6: ^{13}C Overhauser parameters of $^{13}CHCl_3$ for different PAs at room temperature and at 1.2 T. The leakage factor f was calculated using $T_{1n}^0 = 30$ s.[60] Errors of the concentration are 10 – 15 %, for T_{1n}, $T_{\text{Build-up}}$, s, ϵ and f 10 % and for ξ 15 %. As $T_{1n} \neq T_{\text{Build-up}}$ for DTBN, TN-py and TL errors for ϵ and ξ are increased to 15 and 25 %, respectively (see error discussion in sec. 4.3.5). (*) Data from ref. [83].(**) Uncertainty for this value is 15 %. Reproduced from ref. [86] with permission from the PCCP Owner Societies.

^{13}C-DNP in $CHCl_3$	c (mM)	T_{1n} (s)	$T_{\text{Build-up}}$ (s)	f	s_{eff}	ϵ	ξ
BDPA	10	18.1	15.4	0.40	1.00**	122	−0.12
TN-py	10	4.8	3.3	0.89	0.10	55	−0.23
DTBN	10	3.7	2.0	0.88	0.04	31	−0.33
TL	10	2.5	1.6	0.92	0.07	59	−0.35
^{15}N-TN*	10	3.9	2.9	0.85	0.18	200	−0.49
TP-CLST*	10	2.8	2.9	0.90	0.29	350	−0.51
FN-2a*	4	3.5	3.1	0.89	0.30	370	−0.53

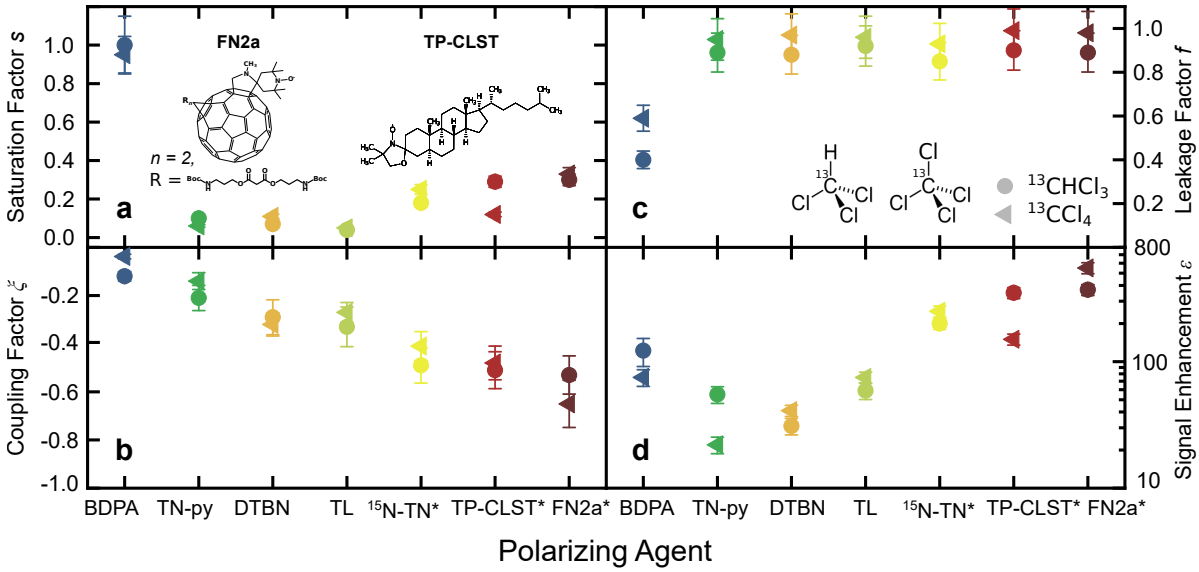

Figure 4.7: Plots of the ^{13}C-DNP Overhauser parameters from tab. 4.5 and tab. 4.6. The inset displays the structure of the PAs used in ref. [83]. Reproduced from ref. [86] with permission from the PCCP Owner Societies.

case of $CHCl_3$ measured at 1.2 T, where the NMR coil spoils the homogeneity of the induced electromagnetic field, we observed deviations up to 46% between $T_{\text{Build-up}}$ and T_{1n}, especially for the cases of DTBN, TL, and TN-py. Although a precise estimation of the temperature deviation is difficult without an *ad-hoc* designed study, a comparison with previous data[83] allowed us to estimate a maximum temperature deviation of ∼30 K under mw irradiation.

In terms of DNP parameters, the direct impact of a deviation in relaxation time on f is negligible, since it is mainly determined by the radical concentration. However, we expect an error on the estimation of the NMR signal enhancement.

Following these considerations, we assign an uncertainty of up to 15% for the enhancement ϵ and 25% for the coupling factor ξ for cases where $T_{\text{Build-up}}$ deviates more than 15% from T_{1n}. PA/solvent pairs, for which sample heating was observed are indicated in tab. 4.2-4.6.

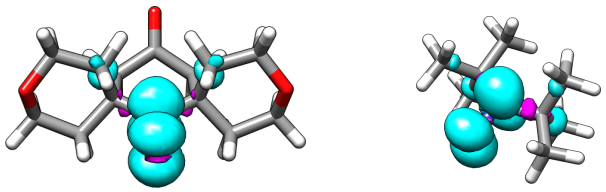

Figure 4.8: Electron spin density calculated for TN-py and DTBN optimized structures and represented with isosurfaces with threshold $\pm 0.002\ e/\text{Å}^3$. Color code: positive lobes in cyan, negative lobes in magenta, H white, C grey, N blue, O red. Reproduced from ref. [86] with permission from the PCCP Owner Societies.

4.3.6 Quantum Chemistry Calculations

Geometry optimizations of the radical structures (DTBN, TL, TN, TN-py) have been performed with the Orca software ver. 4.2.1.[120,121] The calculations were performed at B3LYP level of theory employing the def2-TZVPP basis set. Additionally, we employed the resolution-of-the-identity and chains-of-spheres approximations (RIJCOSX with def2/J auxiliary basis set) as well as the dispersion correction (D3BJ). Tight convergence criteria for the SCF (TIGHTSCF) and the optimization procedure (TIGHTOPT) were chosen. Spin density maps were calculated with Orca and represented with UCSF Chimera[124]: They are shown in the fig. 4.3 and in fig. 4.8. Spin populations for each atom position were obtained from the Löwdin population analysis (fig. 4.9).
A conformation analysis was performed for the radical TN-py (fig. 4.10). For estimating the relative energies of different conformers, dispersion correction energies were disregarded, as they only consider interaction within the molecule excluding the surroundings.
Solvent-accessible surfaces (SASs) were calculated on the optimized structures of the radicals with the softwares UCSF Chimera[124] and Jmol. We considered a spherical probe with a radius of 1.4 Å representing a water molecule and one with radius 3.2 Å representing $CHCl_3$. For comparison, solvent-exclusion surfaces (SESs), corresponding to the contact point between the probe sphere and the Van der Waals surface of the radical, were also calculated. The results are summarised in tab. 4.7.
Geometry optimizations of the PA/$CHCl_3$ complexes were performed with the same functional and basis as for the radicals. In the case of BDPA and TN-py in the half-open

conformation, we used geometry constrains on the radical molecule, while $CHCl_3$ was left free. The hyperfine coupling of the C atom of the $CHCl_3$ molecule was calculated with the EPR-III basis set for H, C, N, and O and IGLO-II for Cl[150]. The results for each complex are reported in tab. 4.8, while some representative geometry optimized complexes with the approach "via H" and "via Cl" are shown in fig. 4.11. The energy-weighted hyperfine coupling $\langle A_{iso} \rangle$ is listed in tab. 4.8.

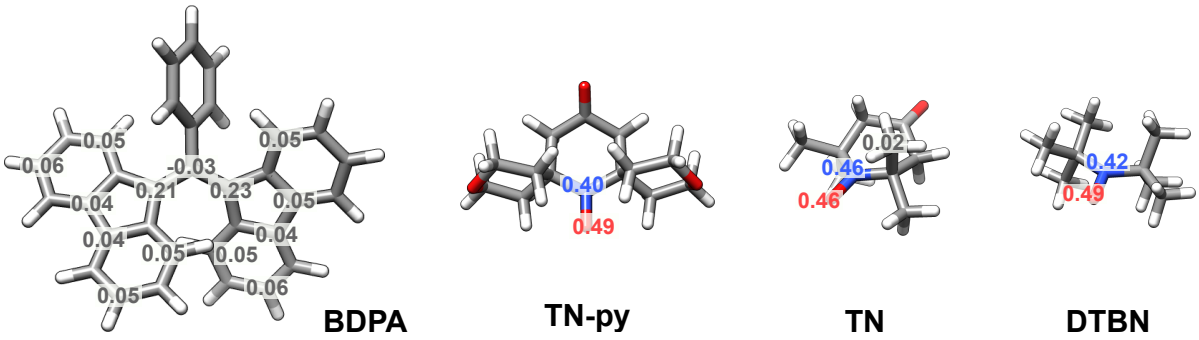

Figure 4.9: Optimized structures of organic radicals and Löwdin spin density shown for some of the atoms. Reproduced from ref. [86] with permission from the PCCP Owner Societies.

Table 4.7: SAS and SES areas calculated for the radical site of the organic radical, i.e. the NO group for NODs and the allyl group for BDPA. Values in brackets have been computed with the software Jmol, while the other calculations have been performed with UCSF Chimera. Reproduced from ref. [86] with permission from the PCCP Owner Societies.

Radical	SAS (Å^2) $r_{H2O} = 1.4$ Å	SAS (Å^2) $r_{CHCl3} = 3.2$ Å	SES (Å^2) $r_{H2O} = 1.4$ Å	SES (Å^2) $r_{CHCl3} = 3.2$ Å
DTBN	23.8 [19.1]	[29.5]	13.2	11.3
TL	24.5 [20.1]	[32.9]	14.2	11.8
TN	25.6 [21.4]	[35.1]	13.4	12.0
TN-py (open)	24.7 [19.6]	[31.9]	14.2	11.5
TN-py (half-open)	15.1 [10.2]	[10.8]	11.2	8.1
FN-2a (chair)	23.7 [19.0]	[29.8]	14.1	11.5
FN-2a (boat)	28.6 [23.9]	[40.4]	14.7	13.5
BDPA	0.78 [0.07]	[0.0]	5.2	0.0

Table 4.8: Hyperfine coupling on the C atom of $CHCl_3$ calculated for the complexes PA/$CHCl_3$. The relative energy of each geometry was calculated including the dispersion correction. Reproduced from ref. [86] with permission from the PCCP Owner Societies.

			DTBN/$CHCl_3$		
complex	**1**	**2**	**3**	**4**	**5**
approach via	H	H	Cl	Cl	Cl
A_{iso} (MHz)	13.0	16.2	1.61	1.55	1.39
E_{rel} (kJ/mol)	0.08	0.0	20.9	158	19.9
				$\langle A_{FC} \rangle$ = 14.6 MHz	

			TN/$CHCl_3$		
complex	**1**	**2**	**3**	**4**	**5**
approach via	H	H	Cl	Cl	
A_{iso} (MHz)	9.3	14.7	1.17	0.07	7.2
E_{rel} (kJ/mol)	2.52	0.0	15.7	8.24	4.01
				$\langle A_{FC} \rangle$ = 12.2 MHz	

	TL/$CHCl_3$	
complex	**1**	**2**
approach via	H	H
A_{iso} (MHz)	10.8	12.1
E_{rel} (kJ/mol)	2.26	0.0
		$\langle A_{FC} \rangle$ = 11.8 MHz

			TN-py (open)/$CHCl_3$	
complex	**1**	**2**	**3**	**4**
approach via	H	H	H	Cl
A_{iso} (MHz)	6.18	8.57	1.52	0.39
E_{rel} (kJ/mol)	0.78	0.0	9.94	13.4
				$\langle A_{FC} \rangle$ = 7.47 MHz

			BDPA/$CHCl_3$		
complex	**1**	**2**	**3**	**4**	**5**
approach via	H	Cl	H/Cl	H	Cl
A_{iso} (MHz)	0.43	0.067	0.063	0.46	0.22
E_{rel} (kJ/mol)	1.89	10.6	0.0	1.31	4.85
				$\langle A_{FC} \rangle$ = 0.26 MHz	

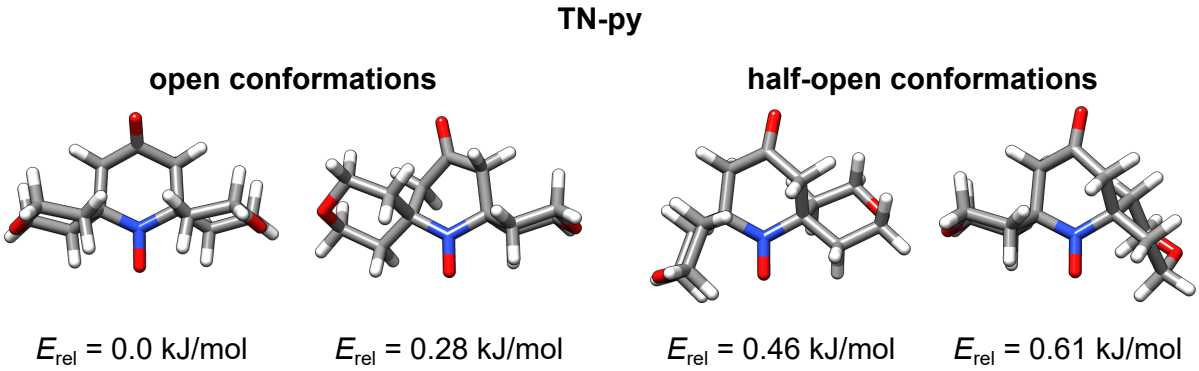

Figure 4.10: Conformations of the radical TN-py that are accessible at room temperature (E_{rt} = 2.49 kJ/mol at T = 300 K). An additional conformation with the piperidine arranged as a chair and the tetrahydropyrane rings in a closed conformation was calculated but it is not accessible at room temperature (E_{rel} = 6.25 kJ/mol). Reproduced from ref. [86] with permission from the PCCP Owner Societies.

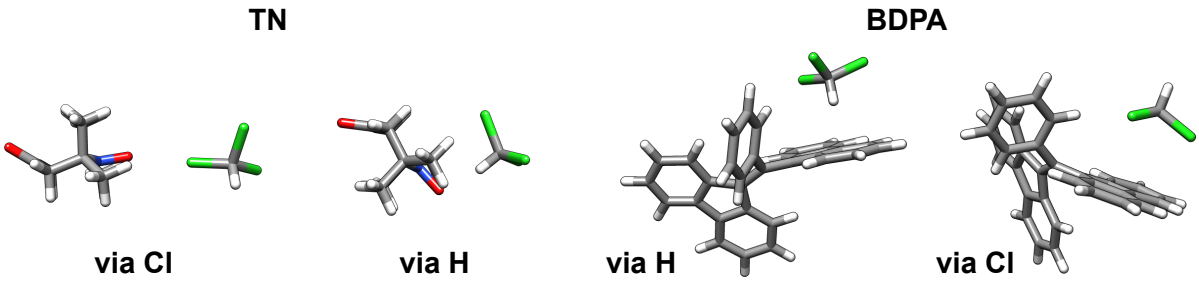

Figure 4.11: Optimized structures for the complexes TN/$CHCl_3$ and BDPA/$CHCl_3$. The approach "via H" and "via Cl" is shown for both radicals. Reproduced from ref. [86] with permission from the PCCP Owner Societies.

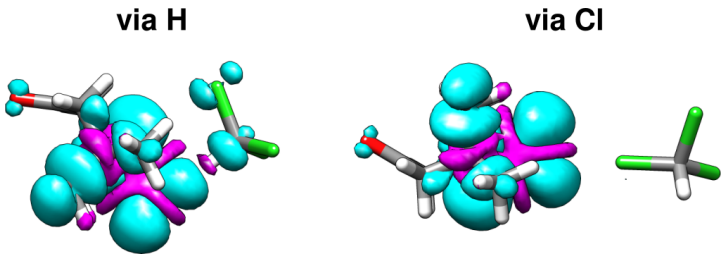

Figure 4.12: Geometry optimized structures of the complex TN/$CHCl_3$ for the two approaches that were considered, "via H" and "via Cl". The spin density is represented with an isosurface of 0.0002 $e/Å^3$ to highlight the spin density transfer to the C atom of the $CHCl_3$ molecule. Reproduced from ref. [86] with permission from the PCCP Owner Societies.

The Influence of Molecular Dynamics on Scalar Dynamic Nuclear Polarization

5

5.1 Introduction

Initiated by the puzzling difference in the DNP efficiency of tempone (TN) and a fullerene nitroxide (FN-2a) at different magnetic fields, the influence of the PA mobility on scalar DNP was analyzed. The goal was again the optimization of polarizing agents for DNP at high magnetic field. For this, the different dipolar contributions to the spin polarization transfer mechanism, i.e. translational and rotational diffusion were experimentally disentangled. Building on this and previously obtained insights in the scalar DNP mechanism,[34,60] rotational diffusion and rapid structural reorientation of the PA were identified as possible molecular motions that may modulate scalar cross relaxation. The influence of the radical mobility on the DNP efficiency was discussed in the context of possible implications for high field DNP together with results for structural influences (chapter 4) on the DNP efficiency in chapter 8.

Sections 5.2-5.3 are published as a letter in the Journal of Physical Chemistry Letters. They are reprinted with the permission of M. Levien, M. Hiller, I. Tkach, M. Bennati, and T. Orlando, "Nitroxide Derivatives for Dynamic Nuclear Polarization in Liquids: The Role of Rotational Diffusion", *J. Phys. Chem. Lett* **2020**, *11*, 1629-1635;[86] Copyright 2020 American Chemical Society. The experiments in this chapter were performed by the author. I. Tkach contributed to the hardware optimization during the experiments. DFT and MD calculations were performed by M. Hiller. Data analysis and interpretation

was performed by the author and T. Orlando. The manuscript was conceptualized and written by T. Orlando, M. Bennati and the author.

Abstract Polarization transfer efficiency in liquid-state dynamic nuclear polarization (DNP) depends on the interaction between polarizing agents (PAs) and target nuclei modulated by molecular motions. Hereby, we show how translational and rotational diffusion differently affect the DNP efficiency. These contributions were disentangled by measuring ^{1}H-DNP enhancements of toluene and chloroform doped with nitroxide derivatives at 0.34 T as a function of either the temperature or the size of the PA. The results were employed to analyze ^{13}C-DNP data at higher fields, where the polarization transfer is also driven by the Fermi contact interaction. In this case, bulky nitroxide PAs perform better than the small TN radical due to structural fluctuations of the ring conformation. These findings will help in designing PAs with features specifically optimized for liquid state DNP at various fields.

Acknowledgement Financial support has been provided by the Max Planck Society. ML acknowledges IMPRS-PBCS of the Max Planck Society for funding. We acknowledge Maik Reinhard for conducting ^{1}H-DNP experiments. Daniel Sieme and Niels Karschin are acknowledged for the assistance in PFG-NMR measurements. We thank Aljaz Godec for fruitful discussions and the Synthetic Chemistry facility at MPI-BPC for the synthesis of FN samples.

5.2 Nitroxide Derivatives for Dynamic Nuclear Polarization in Liquids: The Role of Rotational Diffusion

Dynamic nuclear polarization (DNP) is a class of methods developed to overcome the low sensitivity issue affecting nuclear magnetic resonance (NMR) measurements. They rely on the transfer of the high spin polarization of a polarizing agent (PA) to coupled target nuclei via microwave irradiation.[15] DNP in liquids at room temperature, often known as Overhauser DNP,[38,42] is a spin relaxation mechanism driven by the time modulation of the hyperfine coupling between an unpaired electron and a target nuclear spin through

molecular motions. This technique allows for direct polarization of target nuclei and therefore has the potential to become a precious tool for routine NMR spectroscopy.[16,134] In the last decade, DNP in liquids on ^{1}H nuclei has been extensively studied at various magnetic fields.[14,46,151,152] In this case, dipolar relaxation modulated by molecular diffusion provides the main mechanism for the polarization transfer.[43,153–155] However, the efficiency of such process decreases with rising magnetic field strength, and limits the enhancements to $\epsilon \lesssim 10^2$ at 9.4 T on DNP optimized instruments.[55]

More recently, larger enhancements have been observed for ^{13}C nuclei,[34,60,61] reaching $\epsilon > 400$ at 9.4 T and $\epsilon > 20$ at 14.1 T. For ^{13}C, the polarization transfer is driven by a mixture of dipolar relaxation and the counteracting scalar relaxation, based on Fermi contact interaction. The latter is modulated by fast molecular collisions[34,60] (from subpicoseconds to picoseconds) and has been predicted to be the most efficient contribution.[60]

Small nitroxide radicals have often been chosen as PAs for liquid DNP thanks to their efficiency, which is usually attributed to fast diffusion rates and to the localized electron spin density. Other PAs have not been systematically tested and only a few studies report on them,[58,88,144,156,157] whereas PA optimization is a thriving field in solid-state DNP.[133,158] Recently, we reported 50% larger ^{13}C scalar enhancements when fullerene-nitroxides are used as PAs in comparison to the TN radical.[34] This unexpected observation still lacks a satisfactory explanation, and shows how the current understanding of the scalar relaxation is limited. Therefore, it is still difficult to design a PA whose features are specifically tuned for boosting the DNP efficiency in liquids.

We aim at elucidating the mechanisms contributing to the polarization transfer when the mobility of the PA changes. DNP enhancements on ^{1}H nuclei were measured at low field as a function of the temperature and the size of the PA. In this way, we targeted separately translational diffusion and rotational diffusion, disentangling their impact on the polarization transfer mechanism. DNP enhancements were then measured on ^{13}C nuclei at higher fields. In this case, the polarization transfer is driven by a complex interplay of translational diffusion, rotational diffusion, and Fermi contact. Semi-classical theory and atomistic simulations were used to investigate how the peculiar differences in the structural dynamics of fullerene nitroxide and nitroxide radicals affect the DNP efficiency. To analyze the DNP mechanism, it is essential to access the DNP coupling factor ξ, which

describes the efficiency of the relaxation processes driving the polarization transfer.[80] ξ can be calculated from the NMR enhancement ϵ with the Overhauser equation[42]

$$\epsilon = 1 - f\, s_{\text{eff}}\, \xi\, \frac{|\gamma_{\text{e}}|}{\gamma_{\text{n}}}, \tag{5.1}$$

where γ_{e} and γ_{n} are the electron and the nuclear gyromagnetic ratio, respectively. The leakage factor f and the effective saturation factor s_{eff} were determined independently via nuclear $T_{1\text{n}}$ relaxation measurements and ELDOR experiments,[84] respectively (see sec. 5.3.5.1 and sec. 5.3.5.2).

^{1}H-DNP experiments were performed at 0.34 T in the temperature range of 200−295 K for toluene and 220−295 K for chloroform, both doped with $\sim$ 1 mM of tempol radical (TL). The coupling factor $\xi_{1\text{H}}$ calculated from eq. 5.1 decreases monotonically for decreasing temperatures for both toluene and chloroform, and it is positive over the whole temperature range (fig. 5.1a and fig. 5.1b). Since $\xi_{1\text{H}} > 0$, the polarization transfer is dominated by dipolar relaxation, which is diffusion controlled, while the scalar contribution for ^{1}H-DNP is negligible.[43,88] Employing semi-classical relaxation theory,[43] the coupling factor for dipolar relaxation can be calculated considering both translational diffusion and molecular rotations[43]

$$\xi = \frac{5}{7}\left(1 - \frac{3k_{\text{D}}J_{\text{D}}(\omega_{\text{n}},\tau_{\text{D}}) + 3k_{\text{rot}}J_{\text{rot}}(\omega_{\text{n}},\tau_{\text{C}})}{R_{1,\text{D}} + R_{1,\text{rot}}}\right), \tag{5.2}$$

where ω_{n} is the proton Larmor frequency. $R_{1,i}$ is the nuclear relaxation rate, k_i is the amplitude and J_i is the spectral density of translational diffusion ("D") and rotational contribution ("rot"), respectively (sec. 2.2 and sec. 5.3.8). The spectral density $J_{\text{D}}(\omega_{\text{n}}, \tau_{\text{D}})$, where τ_{D} is the correlation time, is described by the force-free hard-sphere model (ffhs) for translational diffusion.[81,82] The rotational component can be included phenomenologically with a Lorentzian spectral density $J_{\text{rot}}(\omega_{\text{n}},\tau_{\text{C}})$ with τ_{C} as rotational correlation time.[155,159] As previously predicted for water[43,47] and observed in organic solvents,[135] the coupling factor $\xi_{1\text{H}}$ at room temperature for small organic radicals is mainly dependent on translational diffusion, and including a rotational contribution introduces an over parameterization.[66,85] Therefore, as a first approximation we assume $k_{\text{rot}} = 0$ for TL, leaving only the translational diffusion component in eq. 5.2. The correlation time is defined as $\tau_{\text{D}} = r_{\text{D}}^2/(D_{\text{s}} + D_{\text{r,s}})$, where r_{D} is the distance of closest approach, while D_{s}

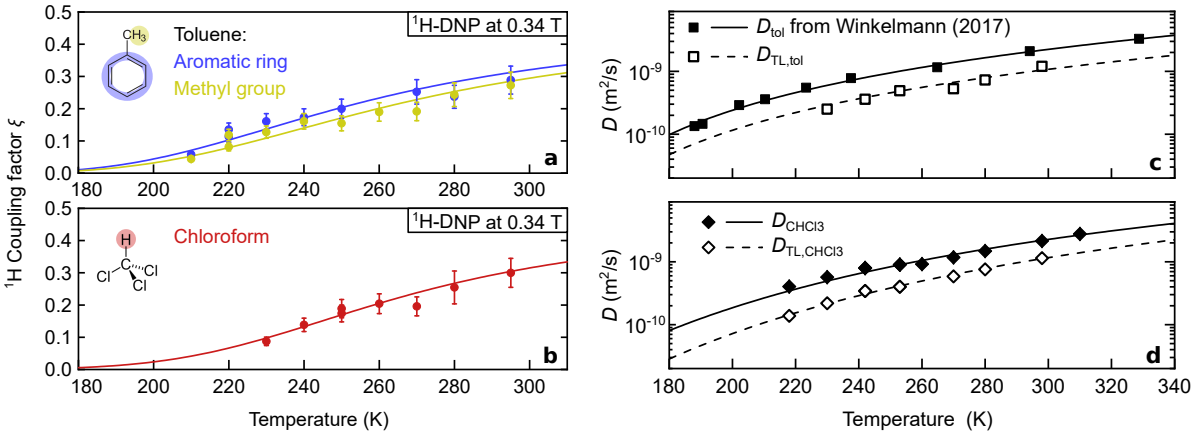

Figure 5.1: (a-b) ^{1}H coupling factor ξ for toluene and chloroform doped with TL as a function of temperature. The values at room temperature agree with the predictions from molecular dynamics calculations.[153,160] Fits (solid lines) were performed with eq. 5.2, where $k_{rot} \approx 0$. (c-d) Self-diffusion coefficient of solvent (D_s) and TL in the solvent ($D_{TL,s}$) as a function of temperature for toluene and chloroform. Lines are fits performed with a Speedy-Angell power law (toluene) and Arrhenius function (chloroform) (see sec. 5.3.3).

and $D_{r,s}$ are the self diffusion coefficients of the solvent and of the radical in the solvent, respectively. Therefore, it is necessary to determine D_s and $D_{r,s}$ over a wide range of temperatures.

Figure 5.1c and fig. 5.1d show D_s and $D_{r,s}$ of the investigated solvents as a function of temperature. $D_{TL,tol}$, D_{CHCl3}, and $D_{TL,CHCl3}$ were measured with pulsed field gradient NMR (see sec. 5.3.3), while D_{tol} is reproduced from the literature.[161]

With D_s and $D_{r,s}$, the fit of the coupling factor ξ_{1H} to eq. 5.2 requires only one free parameter, which is the distance of closest approach r_D, i.e. the average distance over the different directions of approach between the PA and the target molecule.[43] The fits are in good agreement with the experimental data (fig. 5.1), and confirm that a slower translational diffusion reduces the coupling factor ξ_{1H}. The best fit parameters are $r_D^{ring} = 3.5$ Å and $r_D^{methyl} = 3.9$ Å for toluene, and $r_D = 3.65$ Å for chloroform, respectively. The trend $\xi_{1H}^{ring} > \xi_{1H}^{methyl}$ that is experimentally observed for toluene over the whole temperature range implies $r_D^{ring} < r_D^{methyl}$. Interestingly, the geometries of the TL-toluene complexes optimized via DFT calculations reflect the same relation (see sec. 5.3.4).

Besides the translational diffusion, we aimed to selectively target the influence of molecular

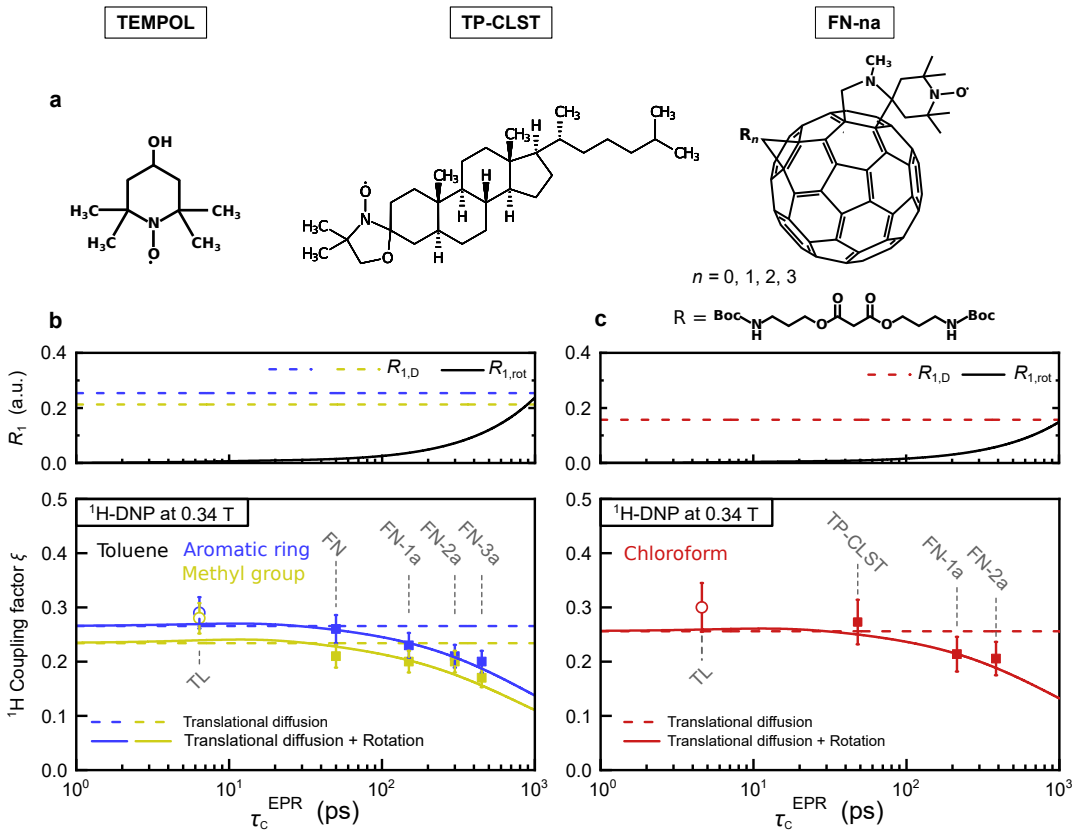

Figure 5.2: (a) Structure of nitroxide radical and nitroxide derivatives used as PAs. (b-c, bottom) Coupling factor ξ_{1H} of toluene[88] and chloroform doped with nitroxide derivatives plotted as a function of the rotational correlation time τ_C^{EPR} of the PA. Radical concentration was $c \sim 1.5\,\text{mM}$ for toluene and $c \sim 1\,\text{mM}$ for chloroform. ξ was simulated with eq. 5.2 without (dashed lines) and with the rotational contribution (solid lines). (b-c, top) Relaxation rates for translational diffusion ($R_{1,D}$) and rotation ($R_{1,rot}$) as a function of τ_C.

rotation by testing a series of bulkier nitroxide derivatives as PAs in both chloroform and toluene. They consist of 3β-DOXYL-5α-cholestane (TP-CLST), and fullerene nitroxides (FN), i.e. nitroxide radicals functionalized with fullerene C_{60}, having additional side chains (up to three) that improve the solubility and increase the rotational correlation time[88] (fig. 5.2a). All selected nitroxide derivatives have the spin density localised on the NO group. Therefore, the hyperfine coupling which drives the polarization transfer is not different from the TL radical. However, their increasing molecular size affects the rotational correlation time of the PA in the solvent, which ranges from $\tau_C^{EPR} \approx 6$ ps for

Table 5.1: Correlation times (in ps) for translational diffusion (τ_D) and rotation (τ_C^{EPR}) in toluene and chloroform doped with TL and nitroxide derivatives.

Toluene					Chloroform			
T (K)	τ_D^{ring}	τ_D^{methyl}	τ_C^{EPR}	τ_D/τ_C^{EPR}	T (K)	τ_D	τ_C^{EPR}	τ_D/τ_C^{EPR}
200	344	427	16.2	> 21	220	256	30	8.5
240	108	134	10.4	> 10	240	142	14	10
270	59	74	7.4	> 7.9	270	69	7.3	9.5
297	38	47	6.4	> 5.9	297	40	4.6	8.7
Nitroxide derivatives					Nitroxide derivatives			
Sample	τ_D^{ring}	τ_D^{methyl}	τ_C^{EPR} [(a)]	τ_D/τ_C^{EPR}	Sample	τ_D	τ_C^{EPR}	τ_D/τ_C^{EPR}
FN	57	71	50	< 1.4	TP-CLST	61	19	3.2
FN-1a	57	71	150	< 0.5	FN-1a	61	214	0.3
FN-2a	57	71	300	< 0.24	FN-2a	61	385	0.16
FN-3a	57	71	450	< 0.16				

[(a)] Data from Enkin et al., 2015.[88]

the TL radical to $\tau_C^{EPR} \approx 450$ ps for larger fullerene nitroxides, as obtained from cw EPR measurements at 9 GHz (tab. 5.1 and sec. 5.3.2).

The coupling factor ξ_{1H} of chloroform doped with nitroxide derivatives ($c \sim 1$ mM) was measured at 0.34 T at room temperature, while the values for toluene at the same field were previously reported.[88] As shown in fig. 5.2, ξ_{1H} decreases for larger τ_C^{EPR}, and so does the DNP efficiency. The rationale for describing the polarization transfer requires an interplay of translational diffusion, governed by τ_D, and rotational motion, characterized by the rotational correlation time τ_C. The translational diffusion of solvent molecules nearby the NO group of the PA remains almost unchanged compared to free TL, because the accessibility to the radical is not hampered.[157] Therefore, the distance of closest approach r_D in the ffhs model is considered to be independent of the particular derivative under study. However, due to the larger molecular size, the diffusion coefficient of nitroxide derivatives in the solvent ($D_{r,s}$) is expected to be much smaller than $D_{TL,s}$. A reasonable approximation consists in choosing $D_{r,s} \approx 0$ for nitroxide derivatives, which leads to $\tau_D \approx r_D^2/D_s$ (tab. 5.1). The rotational component of the dipolar relaxation becomes larger for slower rotations, as previously observed in high viscosity liquids.[159,162] This is the

case in fullerene nitroxides FN-*n*a (where *n* is the number of adducts), with rotational correlation times τ_C^{EPR} larger than τ_D (tab. 5.1). The rotational dynamics of the solvent molecules are much faster, being $\tau_C < 2$ ps for both toluene[163] and chloroform,[164] meaning that their contribution can be neglected at this field ($\tau_C\omega_n \ll 1$). Therefore, the spectral density $J_{rot}(\omega_i,\tau_C) = 2\tau_C/(1+\tau_C^2\omega_i^2)$ can be calculated assuming $\tau_C \approx \tau_C^{EPR}$.
The data in fig.5.2 were fitted to eq. 5.2, where the sole free parameter is the amplitude of the rotational contribution k_{rot}, while k_D is determined by τ_D and the radical concentration c (see sec. 2.2). The model fits the experimental data (fig. 5.2) when $k_{rot} = 0.8 \times 10^8$ for toluene and $k_{rot} = 0.5 \times 10^8$ for chloroform. k_{rot} is similar for the two investigated solvents, thus a bound state due to secondary interactions, such as $\pi-$stacking or halogen bond-like interactions between PA and target molecule, is unlikely. Therefore, the rotational contribution is determined mainly by the choice of the PA. Particularly, we note that in the limit of either fast rotating PAs ($\tau_C < 20 \times 10^{-12}$ s) or immobilized PAs ($\tau_C > 10^{-5}$ s) this contribution is ineffective (see fig. 5.14).
The effect of bulkier nitroxide derivatives used as PAs in liquid DNP was also investigated for ^{13}C as target nuclei. In this case, the scalar relaxation effectively contributes to the polarization transfer. Nitroxide derivatives TP-CLST, FN-1a and FN-2a were tested as PAs in $^{13}CCl_4$ and $^{13}CHCl_3$ ($c \sim 10-20$ mM), while FN and FN-3a showed instability in those solvents. DNP on ^{13}C nuclei was performed at 1.2 T rather than at 0.34 T, due to better NMR sensitivity. The experimental ξ_{13C} values are reported in fig. 5.3 and show an increase in absolute value with the molecular size. This translates into higher DNP efficiency for larger PAs: specifically, up to 50% larger ^{13}C enhancements were observed for FN-2a in comparison to the nitroxide radical tempone (TN).[34] However, the dependency of the dipolar contribution on τ_C^{EPR} does not account for such an effect, as discussed in the following paragraph.
The coupling factor ξ_{13C} for TN in CCl_4 and $CHCl_3$ were modelled using a combination of relaxation rates driven by translational diffusion ($R_{1,D}$ from ffhs model) and scalar relaxation arising from Fermi contact ($R_{1,con}$), as reported in previous studies.[34,60] $R_{1,con}$ is described by the Pulse model for random molecular collisions,[78] which comprises

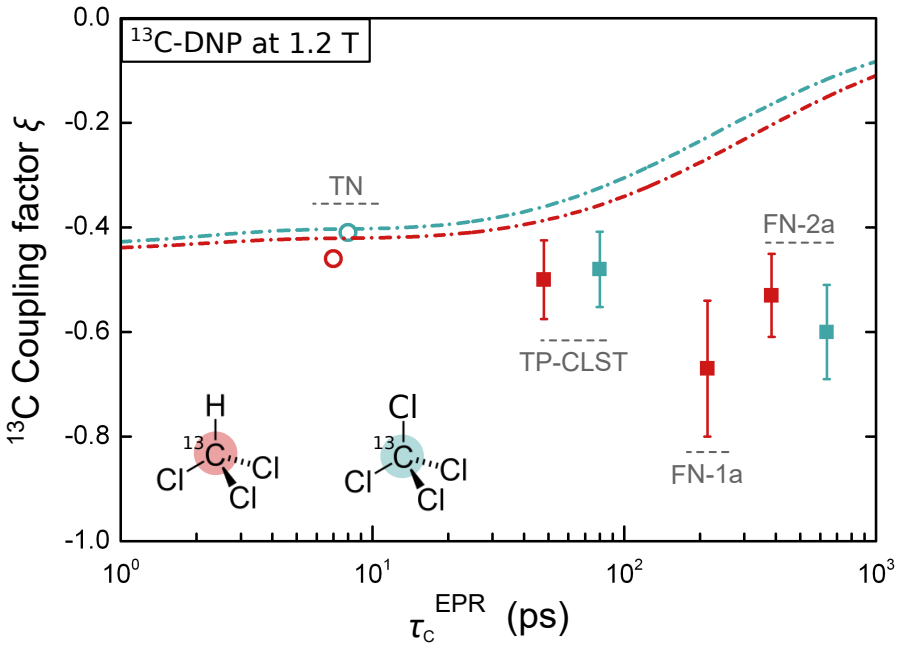

Figure 5.3: ξ_{13C} from ^{13}C-DNP at 1.2 T on $^{13}CCl_4$ and $^{13}CHCl_3$ doped with nitroxide derivatives. The prediction (dash-dot line) has been calculated considering the contributions to the relaxation rates from the translational diffusion ($R_{1,D}$), the contact scalar interaction ($R_{1,con1}$), and the rotation ($R_{1,rot}$).

different types i of contact, each one characterized by a duration $2\tau_{con,i}$ and a collision frequency $1/\tau_{p,i}$

$$R_{1,con} = \sum_i R_{1,con(i)} = \frac{2}{3} S(S+1) \sum_i F_i \left(\tau_{con,i} \cdot \exp\{(-\tau_{con,i}\,\omega_e)\}\right)^2 , \qquad (5.3)$$

where $F_i = \langle A_{iso,i}\rangle^2/(\hbar^2\tau_{p,i})$ and $\langle A_{iso,i}\rangle$ is the mean square amplitude over time of the scalar hyperfine interaction. For CCl_4 and $CHCl_3$, the scalar coupling is modulated mainly by fast molecular collisions with a duration $\tau_{con,1} \approx 0.5$ ps.[34,60] The scalar contribution is included in eq. 5.2 as follows[43]

$$\xi = \frac{5}{7}\left(1 - \frac{3k_D J_D(\omega_n,\tau_D) + 3k_{rot} J_{rot}(\omega_n,\tau_C)}{R_1}\right) - \frac{12}{7}\left(\frac{R_{1,con}}{R_1}\right), \qquad (5.4)$$

where $R_1 = R_{1,D} + R_{1,rot} + R_{1,con}$. Equation 5.4 can be used to predict ξ_{13C} for nitroxide derivatives at 1.2 T. The component $R_{1,D}$ was previously parameterized for the TN

radical[34] and has now been rescaled for the diffusion of larger PAs (tab. 5.2). $R_{1,\mathrm{con}}$ was modelled as in ref. [34]. The amplitude of the rotational component was fixed to $k_{\mathrm{rot}} = 5 \cdot 10^8$ for both solvents, as determined from the low field analysis of chloroform and rescaled for $c \sim 10$ mM. However, the prediction of $\xi_{13\mathrm{C}}$ calculated with eq. 5.4 does not fit the experimental data, as shown in fig. 5.3. This implies that for nitroxide derivatives the Fermi contact hyperfine coupling between the NO group and the target molecule could be subject to additional modulations with timescales different from the one of random molecular collisions.

To access quantitatively the timescales at which the hyperfine coupling is modulated, we also analyzed $\xi_{13\mathrm{C}}$ values reported in a previous study[34] for different magnetic fields (1.2 T, 9.4 T, and 14.1 T). FN-2a in CCl_4 was chosen as a study system due to its good DNP performance at low fields. While the efficiency of FN-2a as a PA is higher than TN at low field ($|\xi_{13\mathrm{C}}^{\text{FN-2a}}| > |\xi_{13\mathrm{C}}^{\mathrm{TN}}|$), the situation is reversed at high fields ($|\xi_{13\mathrm{C}}^{\text{FN-2a}}| \ll |\xi_{13\mathrm{C}}^{\mathrm{TN}}|$), where the enhancements in $^{13}CCl_4$ at 9.4 T are $\epsilon \approx 10$ and $\epsilon \approx 430$ for FN-2a and TN,[34] respectively. $\xi_{13\mathrm{C}}^{\text{FN-2a}}$ was simulated with eq. 5.4 with the components $R_{1,\mathrm{D}}$, $R_{1,\mathrm{rot}}$ and $R_{1,\mathrm{con}}$ (tab. 5.2), where now the scalar part considers not only one but rather two types of collisions ($R_{1,\mathrm{con}} = R_{1,\mathrm{con1}} + R_{1,\mathrm{con2}}$). Despite the few experimental data points, the correlation time $\tau_{\mathrm{con},2}$ of the additional contribution $R_{1,\mathrm{con2}}$ can be reasonably estimated due to its large impact on the shape of ξ as a function of the magnetic field (fig. 5.15 and ref. [34]), while the amplitude F_2 acts as a scaling factor. From this analysis, we obtained $\tau_{\mathrm{con},2} = 2.0 - 6.0$ ps, being $\overline{\tau}_{\mathrm{con},2} = 3.0$ ps the best fit parameter, with an amplitude F_2 accounting for $\sim$ 40% of the total scalar contribution (tab. 5.2 and fig. 5.4a).

To shine light onto the origin of this collision on a longer timescale, the behaviour of nitroxide derivatives was explored by a computational approach combining DFT calculations and MD simulations. Specifically, we focused on possible structural rearrangements of the nitroxide groups capable of modulating the hyperfine interaction. The conformational space of TN and FN-2a was explored by DFT calculations to identify structures corresponding to true energetic minima (see sec. 5.3.10.1). As already known for TN, a chair-like conformation constitutes the energetic minimum, while a twist structure is higher in energy (2.86 kJ/mol), yet still accessible at T = 300 K. For FN-2a the asymmetry of the linker increases the number of possible conformations but only one chair-like conformation

Table 5.2: Correlation times and amplitudes of the contributions used for simulating the coupling factor ξ_{13C}^{TN} (from ref. [34]) and $\xi_{13C}^{FN\text{-}2a}$ as a function of the magnetic field. For $CHCl_3$, an additional Fermi contact component $R_{1,con1,H}$ arises from hydrogen bond-like collisions mediated by H atom: the parameter $\sqrt{F_{1,H}} = 0.5 \cdot 10^{12}$ rad/s, $\tau_{1,H}$ = 12 ps, as reported in ref. [34]. $\overline{\tau_{con,2}}$ is the best fit value within the range $\tau_{con,2} = 2.0 - 6.0$ ps (fig. 5.15).

		Rotation		Contact 1		Contact 2	
Solvent	Radical	k_{rot}	τ_C	$\sqrt{F_1}$	$\tau_{con,1}$	$\sqrt{F_2}$	$\overline{\tau_{con,2}}$
CCl_4	TN	–	7.7 ps [(a)]	$1.25 \cdot 10^{12}$	0.5 ps	–	–
CCl_4	FN-2a	$5{\cdot}10^8$	637 ps	$1.25 \cdot 10^{12}$	0.5 ps	$1.2 \cdot 10^{12}$	3.0 ps
$CHCl_3$	TN	–	4.8 ps	$1.25 \cdot 10^{12}$	0.5 ps	–	–
$CHCl_3$	FN-2a	$5{\cdot}10^8$	385 ps	$1.25 \cdot 10^{12}$	0.5 ps	$0.8 \cdot 10^{12}$	3.0 ps

[(a)] Data from Liu et al., 2017.[60]

was identified as the most favourable. In contrast with TN, other arrangements, such as the boat and, higher in energy, the twist, are inaccessible for FN-2a at room temperature. The dynamics of both polarizing agents were probed by molecular dynamics (MD) simulations in $CHCl_3$ using GROMACS 2018.4[128] and a set of previously reported parameters for the nitroxide radicals.[165] The results are summarized in fig. 5.4b, where the C-C distance of the methyl groups on one side of the nitroxide ring is used as a descriptor of the corresponding ring conformation. For TN, the expected interchange of chair conformations via twist intermediates is observed (fig. 5.4b). In contrast, FN-2a shows a stable chair conformation that remains unchanged at the simulation temperature in the investigated timeframe, in agreement with DFT predictions. However, a different type of structural variation is observable for FN-2a, best described as the transformation of a chair to a half-chair conformation of the six-membered ring (fig. 5.4c). With respect to the DFT results, this corresponds to a transition state between the two conformers of lowest energy, i.e. a chair and a boat (see sec. 5.3.10). Notably, this structural fluctuation happens on a timescale of few picoseconds (fig. 5.4b), which correlates well with the one extracted from the ξ_{13C} experimental data (collision duration $2 \cdot \tau_{con,2} = 4.0 - 12.0$ ps). This suggests that the rearrangement of the methyl groups could effectively contribute to the modulation of the Fermi contact between the NO group and the target molecule, thus affecting the DNP efficiency.

In conclusion, we have explored how the mobility of the PA affects the efficiency of DNP in

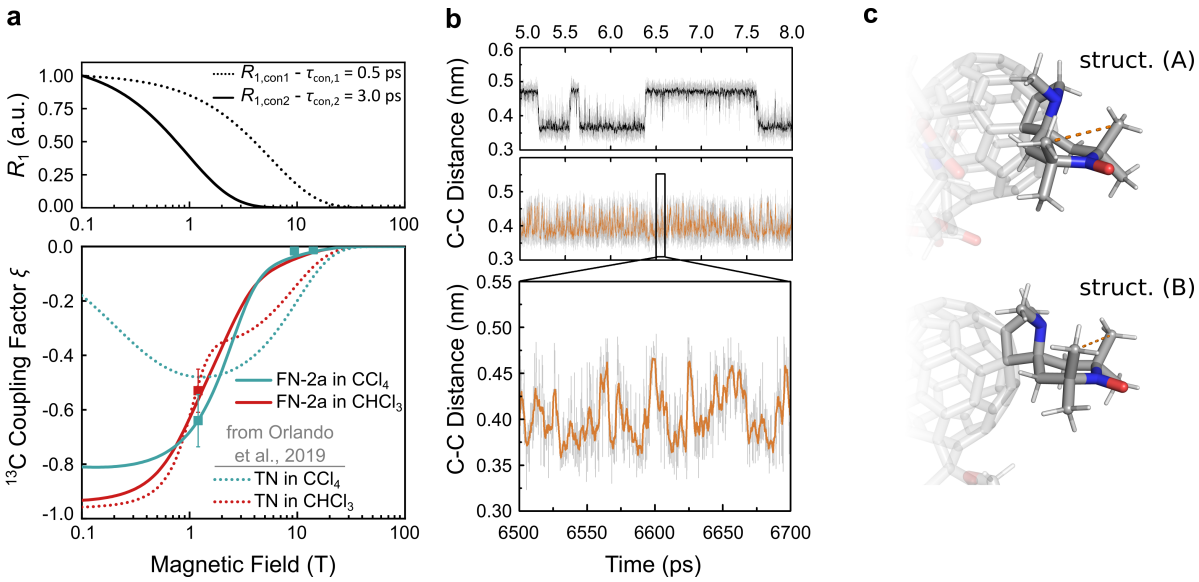

Figure 5.4: (a) $\xi_{13C}^{FN\text{-}2a}$ in CCl_4 and $CHCl_3$ as a function of the magnetic field: experimental data (squares) and fits with eq. 5.4 (solid lines). The relaxation contributions calculated with the values in tab. 5.2 and normalized are shown in the top panel. Calculation for ξ_{13C}^{TN} (dotted lines) are shown for comparison.[34] (b) Time trace of the C-C distance of the methyl groups on one side of the nitroxide ring obtained from MD runs for TN and FN-2a in chloroform (total time = 10 ns, T = 300 K, integration step = 2 fs). Dark lines are smoothed data (11 pt moving average). (c) Structural variation observed with the measured distance indicated in orange in FN-2a as extracted from MD simulation.

liquids. Translational diffusion and rotational diffusion can be disentangled by manipulating independently the temperature and the molecular size of the PA, respectively. In the case of ^{1}H-DNP, where the polarization transfer is mainly driven by dipolar relaxation, fast rotating small molecules or immobilized radicals are the best choices as PAs. The situation is more complex for DNP on ^{13}C nuclei when fullerene-nitroxides are used as PAs. The Fermi contact interaction between target molecule and PA is modulated on two different timescales ($2\tau_{con,1} \sim 1$ ps and $2\tau_{con,2\cdot} \sim 6$ ps), which are determined by molecular collision and, as suggested here, by conformational changes of the PA. Our findings show how rotational diffusion and structural reorientations affect the DNP performances at specific magnetic fields. We foresee that these results will help in designing optimal PAs/target systems for efficient DNP in liquids, and eventually boost new applications of NMR spectroscopy.

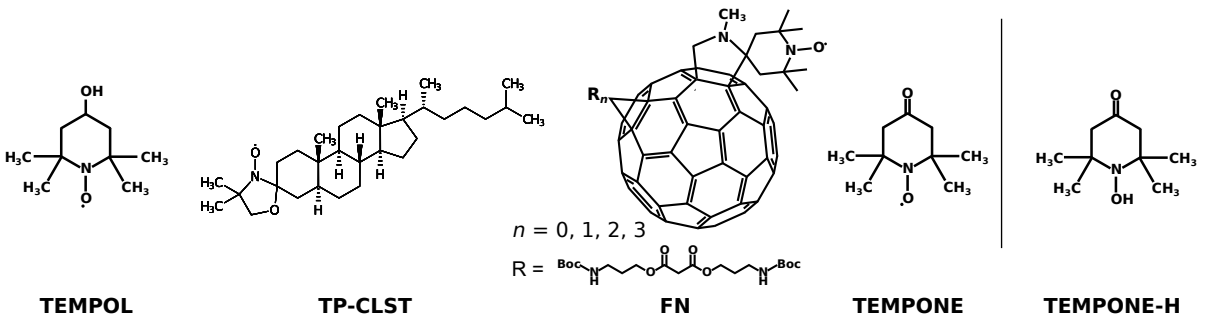

Figure 5.5: Structures of the nitroxide derivatives used as polarizing agents and the reduced form of TN used for diffusion measurements (TNH).

5.3 Supplementary Information

5.3.1 Sample Preparation

Nitroxide radical 4-Hydroxy-2,2,6,6-tetramethylpiperidine 1-oxyl, known as tempol, was purchased from Sigma-Aldrich, as well as 3β-DOXYL-5α-cholestane (TP-CLST). 4-Oxo-2,2,6,6-tetramethylpiperidine-$d_1$6,1-^{15}N-1-oxyl (^{15}N-TN-d_{16}) was purchased from Sigma-Aldrich. ^{13}C-labelled chloroform and tetrachlormethane were purchased from Eurisotop and Sigma-Aldrich, respectively. Toluene and chloroform were purchased from Merck KGaA. Fullerene-nitroxides (FN) were synthesized in house as described in ref. [88]. Radical concentration ranges from 0.5 mM to 1.5 mM and from 3 mM to 20 mM (tab. 5.3) for ^{1}H DNP measurements at 0.34 T and ^{13}C DNP measurements at 1.2 T, respectively and was calibrated by cw EPR spin counting. About 7 μL of sample was inserted in a quartz tube with outer diameter of 1.6 mm and inner diameter of 0.8 mm. Samples were then degassed by freeze-pump-thaw cycles (from one to three) to remove the oxygen dissolved inside. Due to the degassing procedure, the error of the concentration of the PA used is around 15 %.

5.3.2 Continuous Wave EPR Measurements

EPR spectra are acquired at 9.4 GHz/0.34 T (modulation amplitude 0.1 mT, modulation frequency 100 kHz) on degassed samples (fig. 5.6 and 5.7). The molecular rotational correlation time τ_C^{EPR} was obtained by fitting the data with Easyspin,[166] using the routine

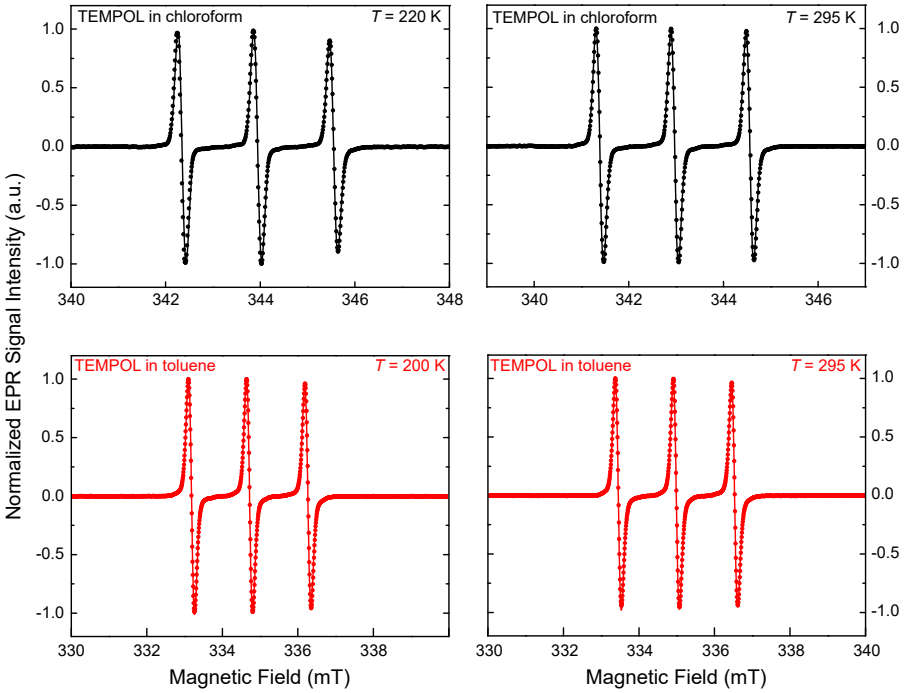

Figure 5.6: Continuous wave EPR spectra obtained at 9.4 GHz of tempol in chloroform (black) and toluene (red) at two characteristic temperatures. Fit (solid lines) were performed with *garlic* (fast motions regime) routine in Easyspin.[166]

garlic (for tempol and TP-CLST) and *chili* (for FNs samples), corresponding to the fast motion and the slow motions regime, respectively. In the case of FN samples, the rigid linker restricts the motion of the nitroxide radical and assure that the FN molecule rotates as a whole. As simulation parameters we assumed $g = [2.0090, 2.0065, 2.0022]$ and $A = [16.9, 19.1, 93.7]$, the latter with a 10% deviation allowed to improve the fit quality for different solvent and polarizing agents, whereas the adjusted fit parameters were kept unchanged within the whole temperature range. τ_C^{EPR} shows a clear trend as a function of the temperature in both toluene and chloroform, which can be fitted with an exponential decay, i.e. $\tau_C^{EPR} = \tau_0^{EPR} + A \cdot \exp(-E/T)$ (fig. 5.8). The rotational correlation times of nitroxide derivatives at room temperature are listed in tab. 5.3, while some of the spectra are shown in fig.5.7.

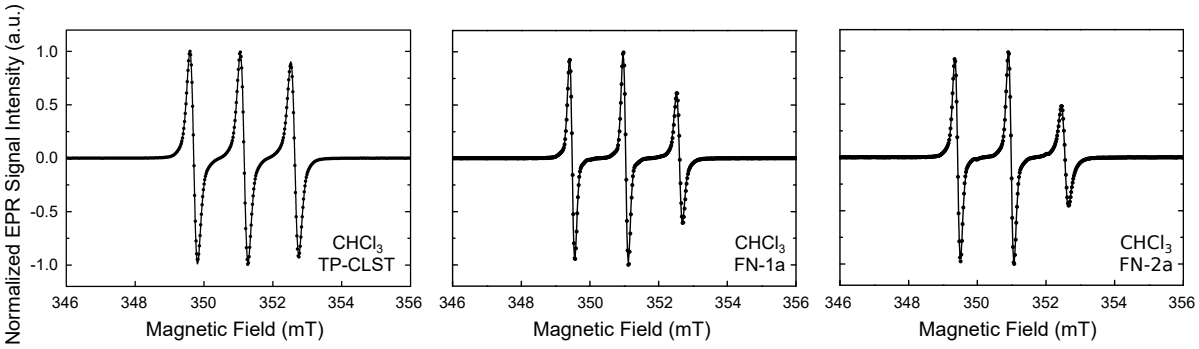

Figure 5.7: Continuous wave EPR spectra obtained at 9.4 GHz of different polarizing agents in chloroform at room temperature. Fit (solid lines) were performed in Easyspin[166] with *garlic* routine (fast motions regime) for TP-CLST radical and with *chili* routine (slow motions regime) for FN samples.

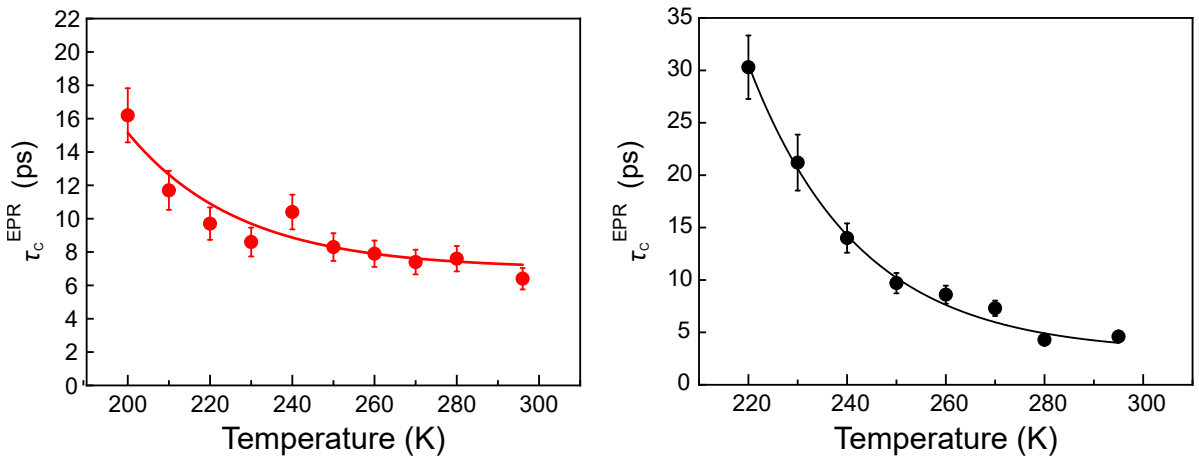

Figure 5.8: Correlation time of tempol in (a) toluene and (b) chloroform obtained from cw EPR measurements as a function of temperature (error bar 10%). The solid lines are the fit with the exponential function $\tau_C^{EPR} = \tau_0^{EPR} + A \cdot \exp(-T/E)$, where A, τ_0^{EPR}, and E are fit parameters.

5.3.3 Diffusion Coefficient

Diffusion coefficients of the solvents and the radical in the solvent were measured by PFG (pulsed field gradient) NMR.[119] Measurements were performed on a 400 MHz Bruker UltraShield Avance III HD spectrometer using a 5 mm PAQXI 1H/31P-13C/15N Z-GRD 1832842/0001 probehead. The maximum gradient duration was 2.7 ms using a maximum gradient strength of 0.385 T/ m. Experiments were carried out utilizing the standard

Table 5.3: Rotational correlation times from cw EPR for different polarizing agents at room temperature (295 K). Data of fullerene-nitroxides in toluene are from ref. [88] Error on τ_C^{EPR} values is ∼10%.

Toluene			Chloroform		
Radical	c (mM)	τ_C^{EPR} (ps)	Radical	c (mM)	τ_C^{EPR} (ps)
tempol	1	6.4	tempol	0.5	4.6
TP-CLST	1.4	31.0	TP-CLST	0.7	48
FN	1.5	60	FN-1a	1.2	214
FN-1a	1.5	150	FN-2a	1.1	385
FN-2a	1.5	300	TN	10	4.5
FN-3a	1.5	450			

Bruker pulse sequence dstebpgp3s introduced by Jerschow and Müller.[119] A gradient recovery delay of 0.5 ms was used and the diffusion time was up to 50 ms. Samples were measured in a 5 mm tube. Measurements were performed in the temperature range 190 − 310 K, using a liquid nitrogen cooling cabinet for T < 260 K and a dry nitrogen gas flow for T > 260 K.

The diffusion constant of TN in the solvent was accessed by measuring the diffusion coefficient of its reduced species tempone-H (TNH, see scheme 5.5). We noted that TNH is not stable under ambient conditions and slowly oxidizes to its radical form, as observed via cw EPR. However, the residual ^{1}H NMR signal of the reduced form was still readily detectable. Stability throughout the measurements of the diffusion coefficient was ensured via ^{1}H NMR measurements. Minor impurities were detected with NMR but, as verified by cross check comparisons, they are not affecting the determination of $D_{TL,s}$.

5.3.3.1 Toluene

The self diffusion coefficient of toluene D_{tol} as a function of the temperature has been previously reported by Winkelmann et al. in ref. [161] Those values were reproduced via PFG-NMR measurements in toluene. The temperature dependency of D_{tol} over the range 160-320 K was fitted with the Speedy-Angell function, $D = a \cdot (T/T_0 - 1)^{\gamma}$.[48]

$D_{TL,tol}$ was measured via PFG-NMR for TNH in deuterated toluene. Gradient strength calibration was performed by measurement of the self diffusion coefficient of D_2O (residual ^{1}H-

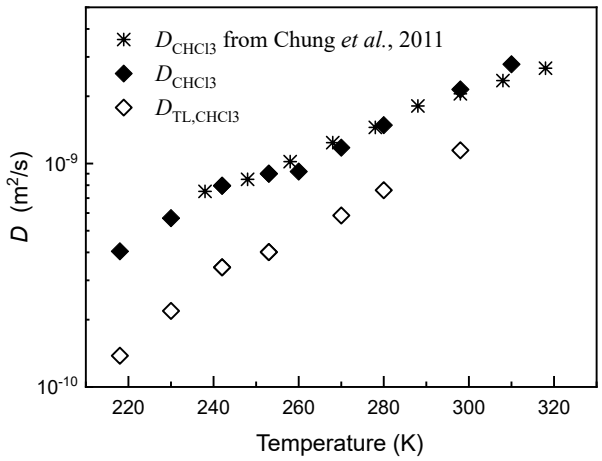

Figure 5.9: Diffusion coefficient of chloroform (D_{CHCl3}) and TNH in chloroform ($D_{TL,CHCl3}$) as a function of the temperature.

signal of HDO was detected) adjusting the obtained value to be $D = 1.90 \cdot 10^{-9}\,m^2/s$.[167] Data analysis was performed as discussed in ref. [119]. The temperature dependence of $D_{TL,tol}$ over the range $190 - 320\,K$ was fitted using a Speedy-Angell function $D = a \cdot (T/T_0 - 1)^{\gamma}$, where, due to the limited temperature range, the parameters T_0 and γ were obtained from D_{tol} curve.

5.3.3.2 Chloroform

Measurements of D_{CHCl_3} and $D_{TL,CHCl_3}$ were performed over the temperature range $218 - 310\,K$. Deuterated chloroform was used as solvent and the self-diffusion coefficient of $CHCl_3$ was determined via detecting the residual ^1H NMR signal. Experimental data obtained in the range $218 - 260$ K shows a systematic error in the absolute value of D, probably due to convection effects.[168] Therefore, the low temperature data of D_{CHCl3} were rescaled according to literature values at 250 K (fig. 5.9). The same scaling was used for $D_{TL,CHCl3}$. The data are reported in tab. 5.5. Experimental data were fitted assuming an Arrhenius like behaviour[169] (i.e. $D(T) = a\exp(-T/T_0)$). The fit parameters are displayed in tab. 5.4.

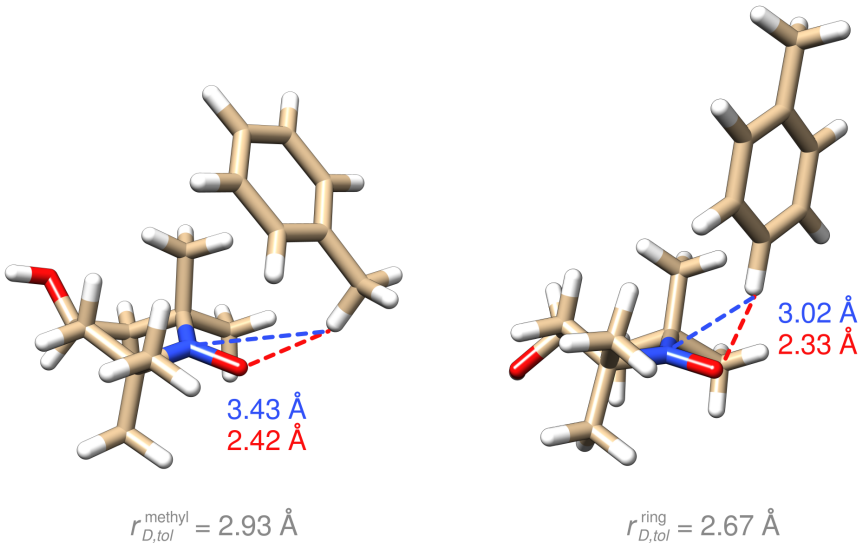

Figure 5.10: DFT optimized geometries for two orientations of the complex TL/toluene. Distances between the closest H atom of toluene and the two atoms on which the electron spin density is localized are marked. Color code for the structure: H - white; C - beige; N - blue; O - red.

5.3.4 Geometry Optimization for the TL/Toluene Complex

The simulation package Orca 4.0[120] was used for geometry optimization. DFT calculations were performed at the B3LYP level of theory using the 6-311++G**/G basis set. A dispersion correction as well as a continuum model accounting for dielectric properties of the solvent was used. The optimized geometries for different orientations of tempol/toluene are displayed in fig.5.10.

Since the electron spin density of the nitroxide is localized on the NO group (about 50%

Table 5.4: Parameters of the Speedy-Angell function $D(T) = a \cdot (T/T_0 - 1)^{\gamma}$ used to fit $D(T)$ of toluene in fig. 5.1. For chloroform experimental data were fitted to an Arrhenius function $D(T) = a \cdot \exp(-T_0/T)$

	a	T_0	γ
D_{tol}	1.49×10^{-9}	137.4	2.35
$D_{TL,tol}$	0.72×10^{-9}	137.4	2.35
D_{CHCl_3}	3.40×10^{-7}	1503	–
$D_{TL,CHCl_3}$	3.06×10^{-7}	1671	–

Table 5.5: Diffusion coefficients of TNH in toluene ($D_{TL,tol}$), TNH in chloroform ($D_{TL,CHCl3}$) and self-diffusion coefficient of chloroform (D_{CHCl3}) as a function of the temperature. Errors are estimated to be 10% of the determined value.

Temperature (K)	$D_{TL,tol}$ ($\times 10^{-9}$ m^2/s)	$D_{TL,CHCl_3}$ ($\times 10^{-9}$ m^2/ s)	D_{CHCl_3} ($\times 10^{-9}$ m^2/s)
310	–	–	2.78
298	1.20	1.15	2.14
280	0.73	0.76	1.48
270	0.53	0.59	1.18
260	–	–	0.92
253	0.49	0.40	0.91
242	0.36	0.34	0.79
230	0.25	0.22	0.57
218	–	0.14	0.40

on each atom), the distances between the nearest proton of toluene and the two atoms were measured (fig. 5.10). The resulting average r_D was taken as the inter-spin distance. It is worth noticing that d is slightly shorter for protons of the aromatic ring ($d = 2.7$ Å) then for the ones of the methyl group ($d = 2.9$ Å).

5.3.5 ^{1}H-DNP Measurements at 0.34 T

5.3.5.1 Saturation Factor

The saturation factor s was obtained via ELDOR experiment.[84] In such experiments, the detection is performed on one of the EPR lines, while an ELDOR pulse ($3-5\,\mu$s) is swept in frequency through the EPR spectrum (see inset of Fig.5.11). Whenever the ELDOR pulse is on resonance with an EPR line, a drop in signal intensity is observed Fig.(5.11). The intensity s_i (with i= 1, 2, 3) of these peaks depends on Heisenberg exchange and internal relaxation. The effective saturation factor is calculated by $s_{eff} = (s_1 + s_2 + s_3)/3$.

5.3.5.2 Leakage Factor and Build-up Time

The leakage factor f is defined by $f = 1 - \frac{T_{1n}}{T_{1n}^0}$, where T_{1n} and T_{1n}^0 are the nuclear relaxation times with and without polarizing agent. Nuclear relaxation times were measured using

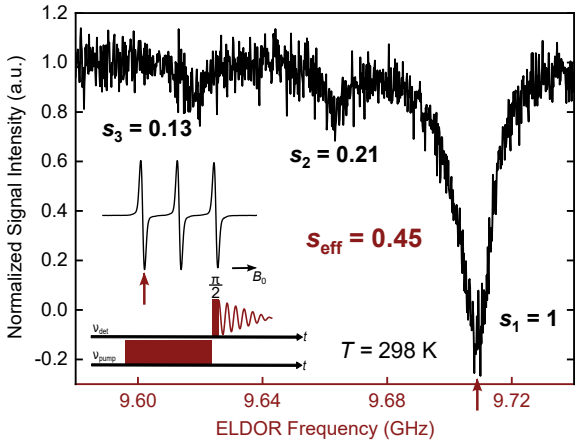

Figure 5.11: ELDOR curves for tempol in chloroform at room temperature. The pulse sequence is displayed in the inset. Blue arrows indicate the position of the detection pulse whereas the frequency of the ELDOR pulse was swept through the EPR spectrum (red).

a saturation recovery experiment with FID detection (8 saturation pulses, $\tau_{sat} = 6\,\mu s$, $\pi/2 = 6\,\mu s$, 60 W). Data were fitted with a single exponential function.

Additionally, the DNP build-up time $T_{\text{Build-up}}$ was measured for each sample and temperature. The pulse sequence consists of a mw irradiation pulse followed by an NMR detection (see fig. 5.12). The mw pulse duration was increased step-by-step until a steady state in signal intensity was reached.

As the relaxation time is sensitive to the temperature, the comparison of $T_{\text{Build-up}}$ measured under mw irradiation with $T_{1,n}$ measured without mw irradiation allows the evaluation of heating effects on the sample during microwave irradiation. If $T_{\text{Build-up}} \sim T_{1,n}$ holds, heating effects are negligible. Sample heating is negligible for toluene except for the two lowest temperatures (tab. 5.6), while it is not for chloroform (tab. 5.7). Consequently, the build-up time has been used as a calibration for the local temperature of the sample under mw irradiation. According to this, the obtained coupling factors have been adjusted to their respective local sample temperature.

5.3.5.3 NMR Enhancement

DNP enhancements were evaluated by comparing the NMR intensities recorded with (DNP) and without (Boltzmann) microwave irradiation. Boltzmann signals were acquired

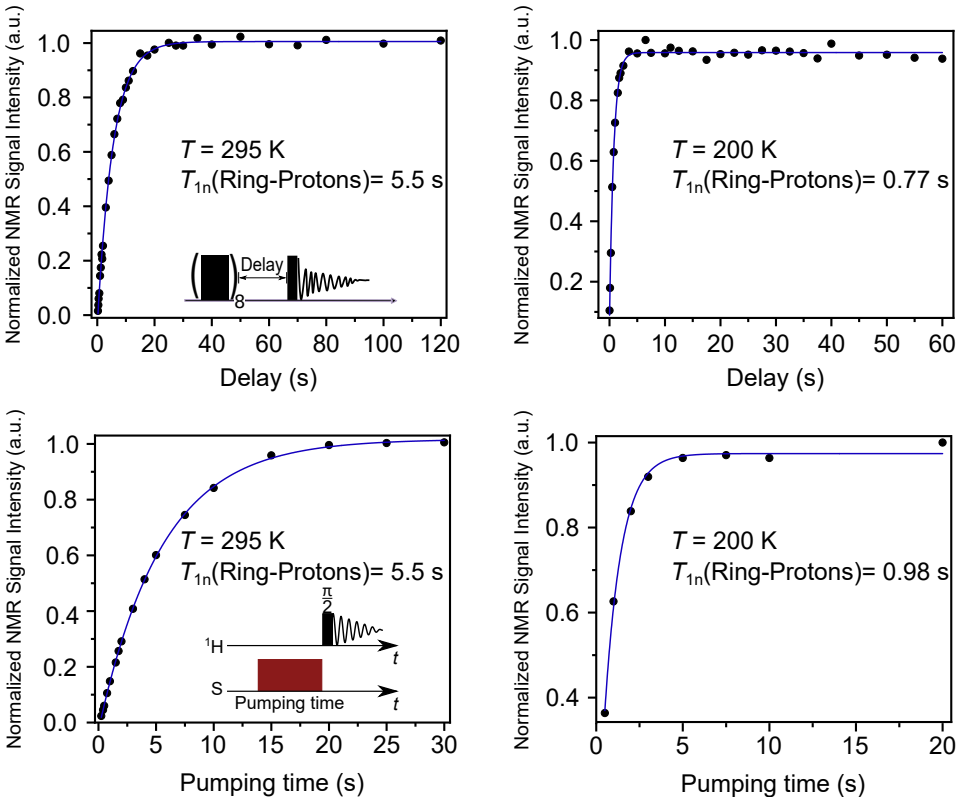

Figure 5.12: T_{1n} measurement (top) and $T_{\text{Build-up}}$ measurement (bottom) obtained at two representative temperatures for a sample of toluene (aromatic ring protons) doped with tempol. Red curves represent exponential fits.

with a number of scans $NS_{Bltz} = 4 - 128$ and a recycle delay of $5 \cdot T_{1,n}$. DNP signals were obtained after a mw pulse lasting several seconds. Two example spectra are shown in fig. 5.13. The maximum enhancement was obtained by irradiating with mw for a pumping time $\sim 5 \cdot T_{\text{Build-up}}$. The enhancements ϵ were then evaluated considering the signal integrals I

$$\epsilon = \frac{I_{DNP}}{I_{Bltz}} \cdot \frac{NS_{Bltz}}{NS_{DNP}}. \tag{5.5}$$

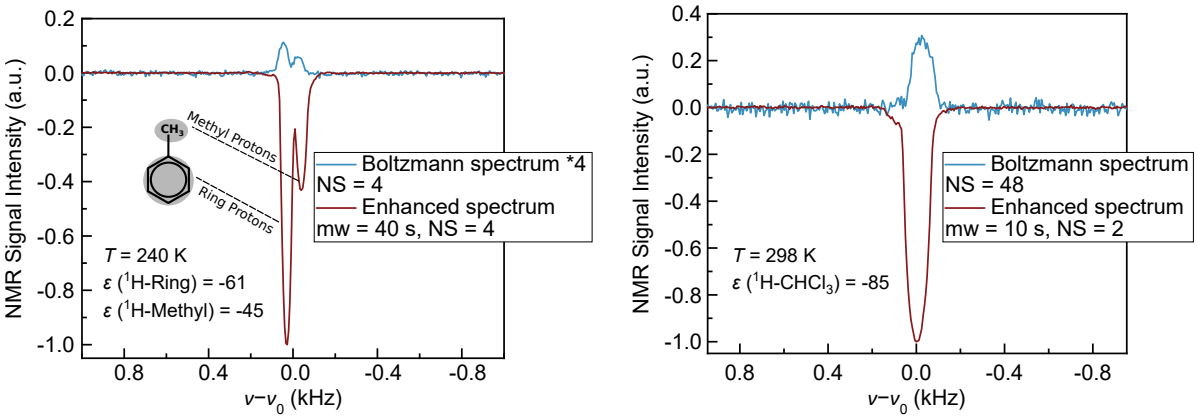

Figure 5.13: ^{1}H-DNP spectra at 0.34 T of toluene (left) and chloroform (right) doped with TL. The chemical shift difference between enhanced and thermal equilibrium spectra is due to field instabilities during the measurements time, since the magnet was not equipped with locking.

5.3.6 ^{1}H Coupling Factor

5.3.6.1 Experimental Data

The coupling factor ξ was obtained with the Overhauser equation $\xi = (\epsilon - 1)/\left(s_{\text{eff}} f \frac{\gamma_e}{\gamma_n}\right)$, where s_{eff}, f, and ϵ were experimentally measured as described in the previous sections. Table 5.6 and 5.7 summarize the Overhauser parameters for tempol in toluene and chloroform, respectively, obtained at 0.34 T. Table 5.8 reports the coupling factor measured at 0.34 T and room temperature for nitroxide derivatives. The nitroxide derivative TP-CLST was not tested in toluene due to an anomalous broadening of the NMR line, which was ascribed to radical/solvent aggregation. The influence of radical concentration c was tested in chloroform doped with 10 mM of tempol and FN-2a, revealing that, within this range, c does not affect ξ. These results are summarized in tab. 5.9.

5.3.7 ^{13}C DNP Measurements

^{13}C-DNP experiments at 1.2 T were performed on an instrument having both EPR and NMR capabilities, and whose technical details have been described elsewhere.[34] A custom made copper coil was inserted in a Bruker cylindrical resonator (ER-5106QT/W) to enable NMR detection. Samples (5-8 μL) were filled in quartz tube with a 1.6 mm outer

Table 5.6: Nuclear relaxation times and Overhauser parameters for each temperature measured in toluene at 0.34 T. The sample was doped with $\sim 1-1.5$ mM of tempol. Protons belonging to the aromatic ring and the methyl group are distinguished. Error on f and s_{eff} is $\sim 5\%$, while for ϵ is $\sim 10\%$. Error on ξ has been quantified as 15%.

Aromatic ring protons

Temperature (K)	$T_{1,\text{n}}$ (s)	$T_{\text{Build-up}}$ (s)	$T_{1,\text{n}}^{\text{dia}}$ (s) [a]	f	s_{eff}	ϵ	ξ
210[b]	1.1	1.0	1.9	0.52	0.63	-13.3	0.057
220[b]	1.5	1.55	2.3	0.52	0.60	-22.4	0.11
220	1.5	1.63	3.3	0.54	0.60	-28.2	0.14
230	1.9	2.0	4.5	0.57	0.57	-33.5	0.16
240	2.6	2.4	5.3	0.52	0.59	-33.8	0.17
250	2.8	2.8	7.1	0.61	0.55	-43.3	0.20
260	3.2	3.4	8.2	0.60	0.57	-59.5	0.26
270	4.0	3.9	10.5	0.62	0.59	-59.8	0.25
280	4.5	4.1	11.4	0.61	0.51	-55.8	0.28
297	5.5	5.5	12.5	0.56	0.58	-61.1	0.29

Methyl group protons

Temperature (K)	$T_{1,\text{n}}$ (s)	$T_{\text{Build-up}}$ (s)	$T_{1,\text{n}}^{\text{dia}}$ (s)	f	s_{eff}	ϵ	ξ
210[b]	1.1	1.1	1.5	0.45	0.63	-8.8	0.052
220[b]	1.8	1.8	2.0	0.38	0.60	-15.5	0.11
220	1.8	1.7	2.9	0.38	0.60	-18.8	0.12
230	1.9	2.0	3.7	0.49	0.57	-24.3	0.13
240	2.2	2.2	4.3	0.49	0.59	-31.6	0.16
250	2.4	2.6	5.3	0.55	0.55	-31.7	0.15
260	3.3	3.1	6.3	0.48	0.57	-35.0	0.19
270	3.7	3.8	7.1	0.48	0.59	-36.7	0.25
280	4.1	3.6	7.5	0.45	0.51	-44.7	0.29
297	4.7	4.7	8.1	0.42	0.58	-44.8	0.28

[a] $T_{1,\text{n}}$ of toluene without radical. [b] Temperature calibrated with $T_{\text{Build-up}}$.

diameter, and then degassed with freeze-pump-thaw cycles. The effective saturation factor s_{eff} was measured with ELDOR sequence, as described in section 5.3.5. Due to the lack of NMR sensitivity, the nuclear relaxation time $T_{1,\text{n}}$ was measured recording the signal intensity as a function of the delay time after a mw pump pulse. The latter was calibrated

Table 5.7: Nuclear relaxation times and Overhauser parameters for each temperature measured in chloroform at 0.34 T. The sample was doped with $\sim 0.5-1$ mM of tempol. For repeated measurements, the average of the coupling factor values has been reported in the text. Errors on f is $\sim 5\%$, while for ϵ and s_{eff} is $\sim 10\%$. Error on ξ has been quantified as 15%.

Temperature (K)	$T_{1,n}$ (s)	$T_{\text{Build-up}}$ (s)	$T_{1,\text{n}}^{\text{dia}}$ (s)[a]	f	s_{eff}	ϵ	ξ
230[b]	1.1	1.15	29.3	0.96	0.63	-24	0.063
230[b]	1.1	1.15	29.3	0.97	0.61	-43	0.11
240[b]	1.55	1.4	32.8	0.96	0.39	-36	0.15
240[b]	1.55	1.4	32.8	0.96	0.55	-44	0.13
250[b]	1.69	1.8	38.1	0.96	0.46	-55	0.19
250[b]	1.69	1.8	38.1	0.96	0.50	-58	0.18
250	1.69	1.8	44.9	0.96	0.48	-49	0.16
250	1.69	1.8	44.9	0.96	0.48	-55	0.18
260	2.1	2.1	52.7	0.96	0.45	-57	0.20
270	2.2	2.3	61.2	0.96	0.49	-60	0.19
270	2.2	2.3	61.2	0.96	0.45	-55	0.19
280[c]	2.7	2.4	69.9	0.96	0.44	-62	0.22
280[c]	–	–	69.9	≈ 0.96	0.45	-81	0.28
297	2.8	2.9	82.5	0.97	0.45	-85	0.30[d]

[a] $T_{1,\text{n}}$ of chloroform without radical. [b] Temperature calibrated with $T_{\text{Build-up}}$. [c] Due to temperature instabilities, error on this data point has been quantified as 20%. [d] Within the experimental error, the value agrees with the prediction from MD theory reported in ref. [160].

to observe the ^{13}C NMR signal and limit heating effects. Overhauser parameters obtained at 1.2 T are summarised in tab. 5.10.

^{13}C enhancements at 9.4 T and 14.1 T have been previously published in ref. [34]. The effective saturation s_{eff} at 14.1 T was previously estimated as $s_{\text{eff}} \sim 0.1$ and, being $f \sim 0.98$ for $c \sim 10\,\text{mM}$, the coupling factor results $\xi_{13\text{C}} = -0.01$. The effective saturation could not be experimentally measured at 9.4 T. We assumed a variability interval between $s_{\text{eff}} = 0.1$, considering that the mw is provided by a gyrotron source,[34] and $s_{\text{eff}} = 0.6$, which can be assumed as the maximum value in case the irradiated line is fully saturated.[88] Therefore, the coupling factor range is $\xi_{13\text{C}} = 0.0002 - 0.035$. Despite the error is quite large, the absolute values are small and do not compromise our analysis.

Table 5.8: Nuclear relaxation times and ^{1}H Overhauser parameters for chloroform doped with nitroxide derivatives ($c \sim 1-1.5$ mM) at room temperature at 0.34 T.

Solvent	Radical	$T_{1,n}$ (s)	$T_{\text{Build-up}}$ (s)	f	s_{eff}	ϵ	ξ
Chloroform	TP-CLST	2.2	2.2	0.97	0.60	-104	0.27
Chloroform	FN-1a	0.9	0.9	0.99	0.86	-104	0.21
Chloroform	FN-2a	0.7	0.7	0.99	0.87	-116	0.20

Table 5.9: Nuclear relaxation times and ^{1}H Overhauser parameters at 0.34 T for tempol and FN-2a in chloroform at room temperature. Radical concentration was $\sim$ 10 mM.

Solvent	Radical	$T_{1,n}$ (s)	$T_{\text{Build-up}}$ (s)	f	s_{eff}	ϵ	ξ
Chloroform	tempol	0.18	0.13	0.998	0.70	-170	0.37[a]
Chloroform	FN-2a	0.11	0.10	0.998	0.93	-121	0.20

[a] A severe temperature deviation has been observed for this sample, causing a shift of the coupling factor value with respect to the one measured with $c \sim 1$ mM (tab. 5.7).

Table 5.10: Nuclear relaxation times and ^{13}C Overhauser parameters for nitroxide derivatives at room temperature at 1.2 T. Radical concentration is $\sim$10 mM for all the samples. Relative error in coupling factors is 15%.

Solvent	Radical	$T_{1,n}$ (s)	$T_{\text{Build-up}}$ (s)	f	s_{eff}	ϵ	ξ
$^{13}CCl_4$	TN	18.5	16.6	0.925	0.25	252	-0.41[a]
$^{13}CCl_4$	TP-CLST	2.9	3.4	0.99	0.12	150	-0.48
$^{13}CCl_4$	FN-2a	19.6	18.4	0.90	0.28	425	-0.64
$^{13}CCl_4$	FN-2a	3.8	3.8	0.98	0.33	550	-0.65[a]
$^{13}CHCl_3$	TN	4.5	4.0	0.85	0.25	260	-0.46[a]
$^{13}CHCl_3$	TP-CLST	2.8	2.9	0.90	0.29	350	-0.51
$^{13}CHCl_3$	FN1a	2.6	2.8	0.92	0.22	355	-0.67[b]
$^{13}CHCl_3$	FN-2a	3.5	3.1	0.89	0.30	370	-0.53[a]

[a] ref. [34]. [b] Instability of the fullerene nitroxide FN-1a was observed in labelled compound ^{13}C labelled chloroform. Error for this data point has been estimated as 20%.

5.3.8 Simulation of the ^{1}H Coupling Factor

The fit of ξ_{1H} as a function of the temperature for TL either in chloroform or toluene was performed with eq. 5.4. The rotational contribution $R_{1,rot}$ and the scalar component $R_{1,con}$ are both negligible. Therefore, eq. 5.4 reduces to

$$\xi = \frac{5}{7}\left(1 - \frac{3J_D(\omega_n,\tau_D)}{7J_D(\omega_e,\tau_D) + 3J_D(\omega_n,\tau_D)}\right), \tag{5.6}$$

where $J_D(\omega_i,\tau_D)$ is defined by the ffhs model (eq. 2.33). The diffusion coefficients D_s and $D_{TL,s}$ have been obtained as described in section 5.3.3. Consequently, the fit required only r_D as fit parameter. The best fit is obtained for $r_D^{ring} = 3.5$ Å and $r_D^{methyl} = 3.9$ Å for toluene, and $r_D = 3.65$ Å for chloroform.

ξ_{1H} for nitroxide derivatives as polarizing agents was measured at room temperature and simulated with eq. 5.4 as a function of the rotational correlation time $\tau_C = \tau_C^{EPR}$. With the scalar contribution being $R_{1,con} = 0$, eq. 5.4 results

$$\xi = \frac{5}{7}\left(1 - \frac{3k_{rot}J_{rot}(\omega_n,\tau_C) + 3k_D J_D(\omega_n,\tau_D)}{R_{1,D} + R_{1,rot}}\right). \tag{5.7}$$

The translational diffusion contribution is completely defined (i.e. R_{1D} independent of τ_C^{EPR}) by the diffusion coefficient D_s (for either chloroform or toluene), the distance of minimum approach r_D as determined from the previous analysis, and the radical concentration c experimentally determined. The rotational contribution has $\tau_C = \tau_C^{EPR}$ as correlation time, where τ_C^{EPR} was measured by cw EPR (Section 5.3.2). The amplitude k_{rot} is the only fit parameter, and resulted $k_{rot} = 0.8 \times 10^8$ for toluene and $k_{rot} = 0.5 \cdot 10^8$ for chloroform. The summary of the parameters used in the fit procedure is reported in tab. 5.11.

Figure 5.14 is the same figure as fig. 5.2 with a larger τ_C^{EPR} range. It showcases that for very short and very long τ_C^{EPR} values (20×10^{-12} s$> \tau_C > 10^{-5}$ s), R_{1rot} becomes negligible and the coupling factor is dominated by translational diffusion.

Table 5.11: Fit parameters used in eq. 5.2 to fit ξ_{1H} as a function of the correlation time $\tau_C = \tau_C^{EPR}$. Error on k_{rot} is ~10%.

	Translational diffusion				Rotation
Solvent	D_s (m^2/s)[a]	r_D (Å)	τ_D (ps)[b]	c (mM)	k_{rot}
Toluene (ring)	2.14×10^{-9}	3.5	57	1.5	0.8×10^8
Toluene (methyl)	2.14×10^{-9}	3.9	73	1.5	0.8×10^8
Chloroform	2.16×10^{-9}	3.65	61	1	0.5×10^8

[a] Self-diffusion coefficient of the solvent at 297 K. [b] $\tau_D = r_D^2/D_s$.

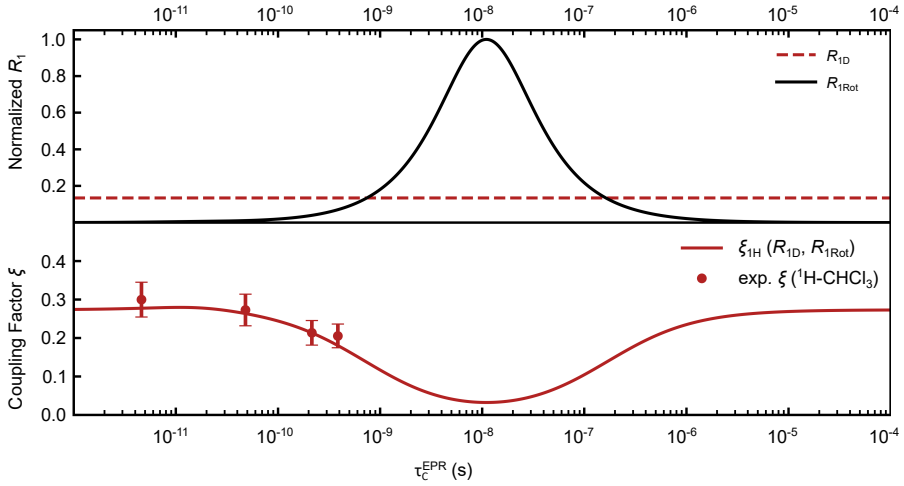

Figure 5.14: Experimental data (red dots) and simulation (red line) of ξ_{1H} as a function of τ_C of of the PA in $CHCl_3$. $R_{1,rot}$ (black line) and $R_{1,D}$ (dashed red) are displayed in the top panel. For clarity, values were normalized to unity as a maximum value.

5.3.9 Simulation of the ^{13}C Coupling Factor

Coupling factor ξ_{13C} was measured at room temperature in $^{13}CCl_4$ and $^{13}CHCl_3$ doped with nitroxide derivatives. Equation 5.4 can be used to predict ξ_{13C} as a function of τ_C. The translational diffusion contribution was computed with the ffhs model and the values r_D from ref. [34] and the diffusion coefficient rescaled for large polarizing agent. We note that r_D is larger for ^{13}C (3.85 Å) than for ^{1}H (3.65 Å), as expected. However, as previously noted by Sezer in ref. [153], r_D only partly correlate with a single structural property, while it reflects a more complex dynamic behaviour (and includes, for instance,

Table 5.12: Parameters used for simulating ξ_{13C} as a function of τ_C at 1.2 T for $^{13}CCl_4$ (eq. 5.8) and $^{13}CHCl_3$ (eq. 5.9) doped with nitroxide derivatives.

	Transl. diffusion[a]	Rotation		Contact 1[a]		Contact 1,H[a]	
	τ_D (ps)	k_{rot}	τ_C^{EPR} (ps)	$\sqrt{F_1}$ rad/s	$\tau_{con,1}$ (ps)	$\sqrt{F_{1,H}}$ rad/s	$\tau_{1,H}$ (ps)
CCl_4	115[b]	$5 \cdot 10^8$	637	$1.25 \cdot 10^{12}$	0.5	–	–
$CHCl_3$	76/55[c]	$5 \cdot 10^8$	385	$1.25 \cdot 10^{12}$	0.5	$0.5 \cdot 10^{12}$	12

[a] ref. [34]. [b] r_D^{Cl} = 4.0 Å; $D_{CCl_4} = 1.4 \cdot 10^{-9}$ m^2/s. [c] r_D^{Cl} = 4.0 Å; r_D^{H} = 3.4 Å; $D_{CHCl_3} = 2.1 \cdot 10^{-9}$ m^2/s.

the angle of approach). Therefore, the comparison of r_D extracted from the ffhs model should take into account such approximation.

The contact contribution was described with the pulse model (eq. 5.3) and consists of short timescale collisions with duration $\tau_{con,1}$ = 0.5 ps.[34,60] The rotational contribution was calculated with: (*i*) the amplitude k_{rot} obtained from the analysis performed at 0.34 T and rescaled linearly for a concentration of $c \sim 10$ mM; since a bound state due to secondary interactions is unlikely, we did not include other scaling factors (such as the distance). (*ii*) $\tau_C = \tau_C^{EPR}$, where τ_C^{EPR} was measured by cw EPR for FN-2a. For $^{13}CCl_4$ doped with nitroxide derivative, the coupling factor results

$$\xi = \frac{5}{7}\left(1 - \frac{3k_D^{Cl}J_D(\omega_n,\tau_D^{Cl}) + 3k_{rot}J_{rot}(\omega_n,\tau_C)}{R_{1,D}^{Cl} + R_{1,rot} + R_{1,con1}}\right) - \frac{12}{7}\left(\frac{R_{1,con}}{R_{1,D}^{Cl} + R_{1,rot} + R_{1,con1}}\right). \quad (5.8)$$

In the case of chloroform, the polarization transfer is mediated by either H or Cl. The coupling factor has been calculated considering 3/4 of the CCl_4 contribution, accounting for Cl mediated collisions and diffusion[34,60]

$$\xi = \frac{5}{7}\left(1 - \frac{0.75 \cdot 3k_D^{Cl}J_D^{Cl}(\omega_n,\tau_D^{Cl}) + 3k_D^{H}J_D^{H}(\omega_n,\tau_D^{H}) + 3k_{rot}J_{rot}(\omega_n,\tau_C)}{0.75 \cdot R_1^{Cl} + R_{1,rot} + R_{1,D}^{H} + R_{1,con1,H}}\right) \quad (5.9)$$

$$- \frac{12}{7}\left(\frac{0.75 \cdot R_{1,con1} + R_{1,con1,H}}{0.75 \cdot R_1^{Cl} + R_{1,rot} + R_{1,con1,H}}\right), \quad (5.10)$$

where $R_1^{Cl} = R_{1,D}^{Cl} + R_{1,con1}$. Table 5.12 shows a summary of the parameters used for simulating ξ_{13C} at 1.2 T as a function of τ_C for $^{13}CCl_4$ and $^{13}CHCl_3$.

The field dependence of ξ_{13C} was investigated for $^{13}CCl_4$ and $^{13}CHCl_3$ doped with FN-2a. The coupling factor was simulated with eq. 5.8 and eq. 5.9 plus an additional contact

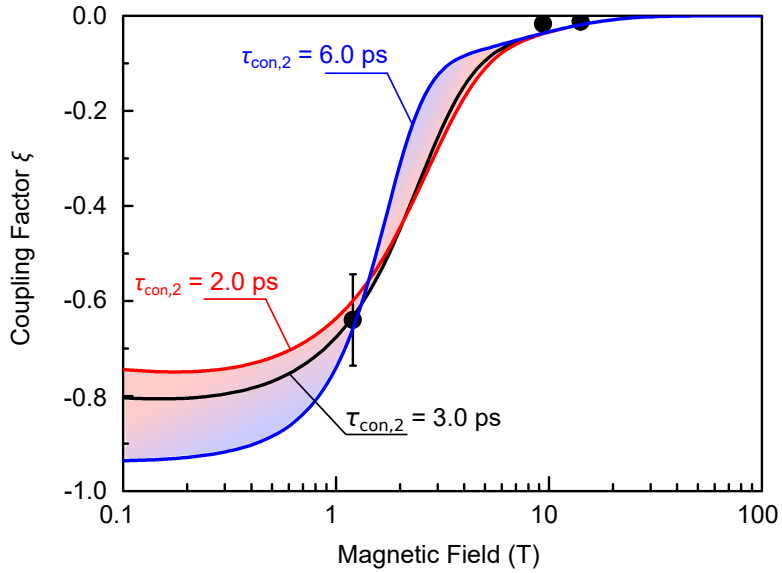

Figure 5.15: Coupling factor of FN-2a in CCl_4 as a function of the magnetic field. The simulations were performed with eq. 5.8 and a second contact contribution $R_{1,con2}$ with $\tau_{con,2}$ as collision time and $\sqrt{F_2} = 1.2 \cdot 10^{12}$ as amplitude.

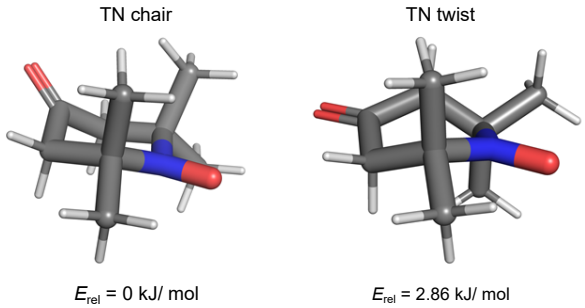

Figure 5.16: DFT-optimized conformations and relative energies (excluding dispersion correction) for TN.

component $R_{1,con2}$ described with the Pulse model and having $\sqrt{F_2} = 1.2 \cdot 10^{12}$ for CCl_4 ($\sqrt{F_2} = 0.8 \cdot 10^{12}$ for $CHCl_3$) and $\overline{\tau_{con,2}} = 3.0$ ps (see tab. 5.15). The latter has been chosen as the best fit parameter within the range $\tau_{con,2} = 2.0 - 6.0$ ps (fig. 5.15).

5.3.10 DFT and MD Simulations of TN and FN-2a

5.3.10.1 DFT Calculations

All calculations were performed with Orca 4.0.1.[120,121] For the investigation of the conformations of the TN and FN-2a polarizing agents, geometry optimizations were performed using the B3LYP functional in combination with the def2-TZVPP basis set.[170] Additionally, the resolution-of-the-identity and chains-of-spheres approximations (RIJCOSX with def2/J auxiliary basis set) as well as dispersion correction (D3BJ) were employed.[122,123,171,172] Tight convergence criteria for the SCF (TIGHTSCF) and the optimization procedure (TIGHTOPT) were chosen. For comparison of the relative energies of the various conformations, the calculated dispersion corrections were neglected. To reduce the computational demand, a small model system for FN-2a was used, wherein only two six-membered rings of the C_{60} moiety were retained. Graphical representations of the determined minima and corresponding relative energies are summarized in fig.5.16 and fig.5.18.

5.3.10.2 MD Parameters and Simulations

Partial charges Partial charges for chloroform and TN were obtained by the following approach: the structure of the respective system was geometry-optimized (Orca 4.0.1, HF/6-31g*). Based on this, charges were fitted using the RESP methodology as implemented in Multiwfn 3.6.[173,174] During the fitting procedure, identical charges were imposed for symmetry-related positions. Charges for chemically equivalent groups (e.g. nitroxide methyl groups) were subsequently averaged. The charges for chloroform are summarized in tab. 5.13. Notably, the values for Cl and H are close to previously reported data with some variation for the central carbon atom.[175]

Table 5.13: Partial charges for chloroform.

Atom	Partial charge (e)
C	−0.16354
Cl	−0.03217
H	0.26005

Table 5.14: Partial charges for TN, labeling of the atoms is displayed in fig.5.17.

Atom	Partial charge (e)	Atom	Partial charge (e)
O1	−0.29810	C3	0.87587
O2	−0.59783	C4	−0.44168
N	−0.15144	H1	0.16391
C1	0.59983	H2	0.11526
C2	−0.65010		

The large system size of FN-2a leads to uneconomical computational demand of the direct DFT investigation. In addition, the RESP methodology is known to give inaccurate results for buried atoms.[173] Thus, charges for this molecule were determined using several smaller models for parts of the system. The structures of all model systems were geometry-optimized (Orca 4.0.1, HF/6-31g*), prior to RESP fitting. First, the effect of the radical linker on the fullerene was investigated using a system containing a C_{60} core and an attached *N*-methyl pyrrolidine ring (see fig. 5.20, left). RESP fitting showed that all fullerene carbon atoms except those in the pyrrolidine ring (+0.40319 e) have charges very close to zero with a total charge of −0.34694 e (sum over 58 atoms).
Similarly, a model of a fullerene with an attached dimethyl malonate ester was used to study the effect of this type of substitution (fig. 5.20, right). For this second system, RESP fitting indicated that the fullerene carbons in the cyclopropane ring (+0.54709 e) and their nearest neighbors (−0.19764 e) have partial charges significantly different from zero, leaving a total of +0.20118 e on the remaining 52 fullerene carbon atoms. The charges for the malonate group were also derived with this model and are included

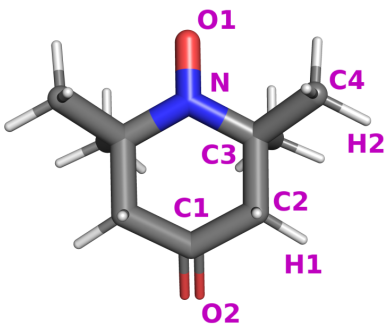

Figure 5.17: Atom numbering scheme for TN.

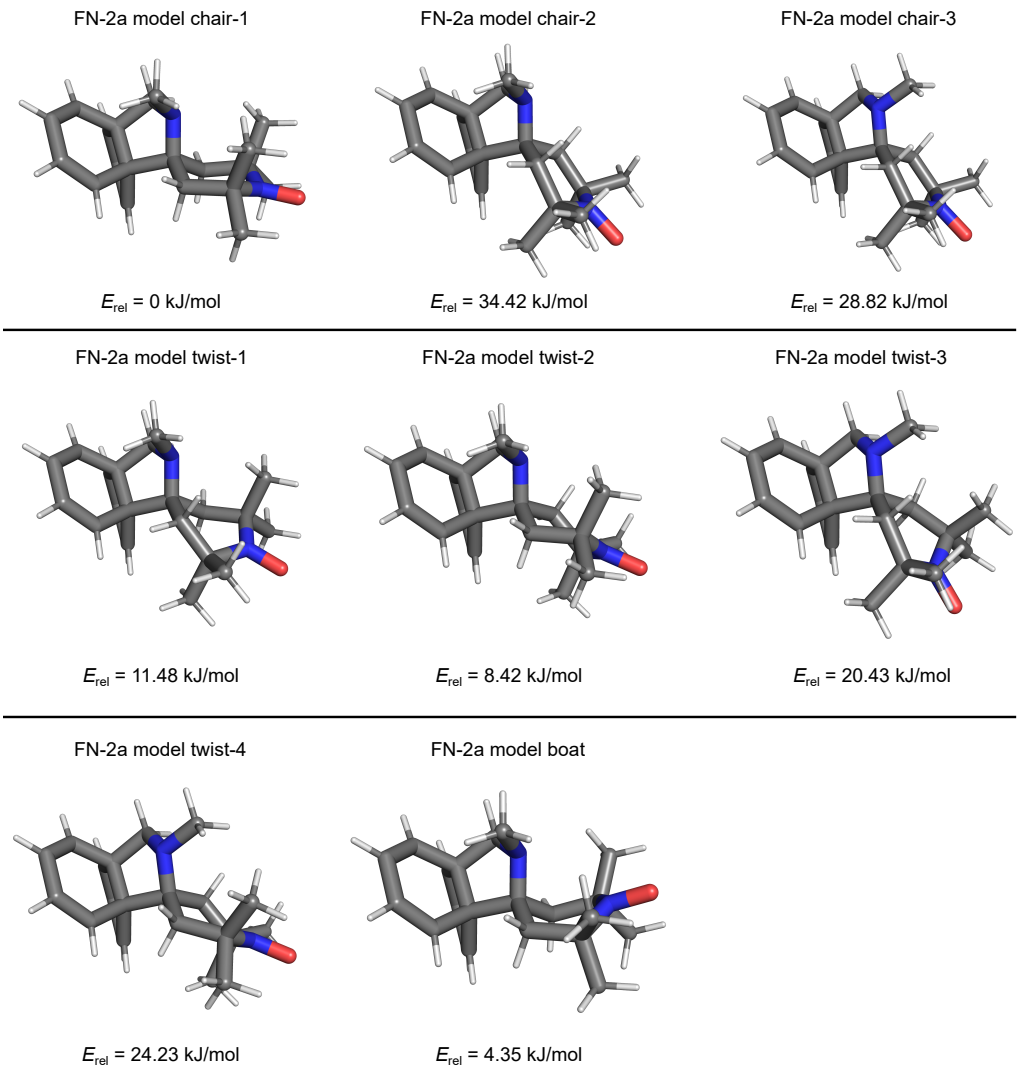

Figure 5.18: DFT-optimized conformations and relative energies (excluding dispersion correction) for the FN-2a model system.

in tab. 5.15. Finally, the sum charge of the methyl groups (0.50406 e) was used as a restraint for the charges of the various chain conformations (see below).

Next, the charges of the TEMPO radical and pyrrolidine linker were inferred from the model depicted in fig. 5.21, corresponding to the most favorable conformation as determined by DFT (chair-1, see above). For the RESP fitting procedure, the charges of the fullerene carbon atoms were fixed to +0.40319 e for those in the pyrrolidine ring and −0.00598 e for the remainder (−0.34694 e evenly distributed over 58 atoms). The charge values

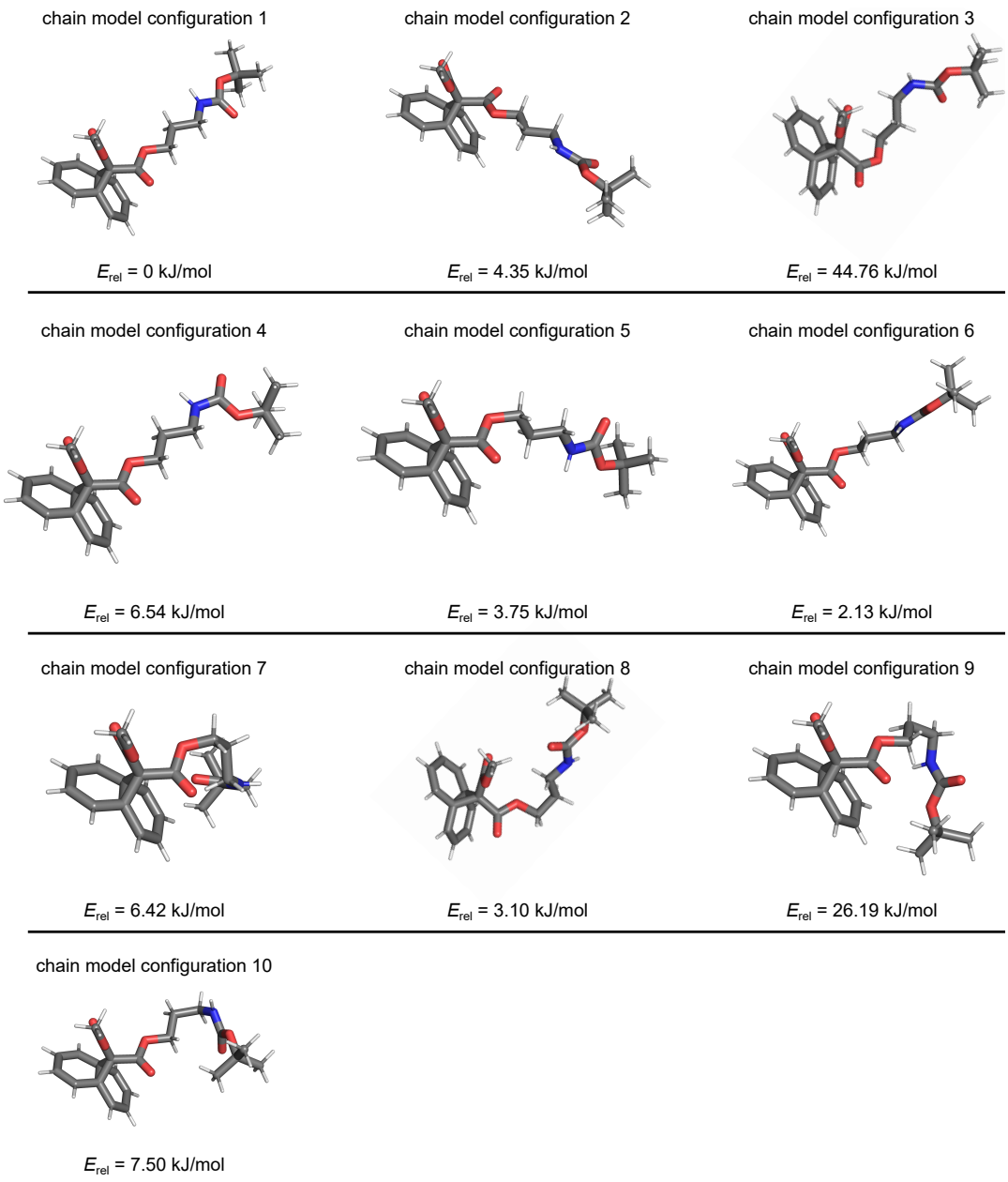

Figure 5.19: DFT-optimized conformations and relative energies (excluding dispersion corrections) for the chain model system.

obtained for this system (except those in the fullerene) were directly used for FN-2a (see tab. 5.15).

Finally, for the determination of the charges in the substituent chain, various conformations

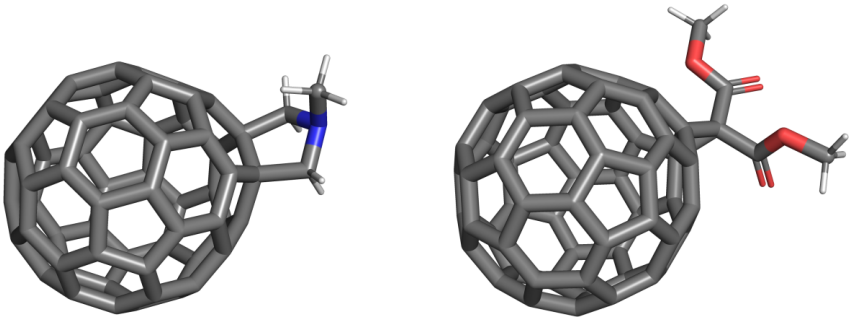

Figure 5.20: Model systems for investigations of fullerene charges.

of a suitable model system (see fig. 5.19) were DFT-optimized (Orca 4.0.1, HF/6-31g*). As previously, the fullerene was replaced by two six-membered rings to reduce the computational demand. As expected, the all-*trans* conformation 1 is the most favourable one. Gauche conformations involving the C_3 chain are associated with only slightly higher energies (conformations 5-8) unless they lead to significant steric interaction of the *tert*-butyloxycarbonyl protecting group (conformations 9 and 10). Additionally, the rotation of the entire chain (resulting in parallel orientation of both ester groups, conformation 2) and formation of a *cis*-peptide bond (conformation 4) appears to be possible at 300 K. For the ester group, the *Z*-isomer is clearly preferred (compare conformation 3).
Partial charges for the atoms in the chain substituent were obtained by RESP fitting of the conformations given in fig. 5.19, excluding the high-energy conformations 3 and 9. The total sum charge of the chain was constrained to 0.25203 e, the value for each of the methyl groups in the model system discussed above (fig. 5.20, right). The charges were subsequently averaged based on the Boltzmann populations of the remaining 9

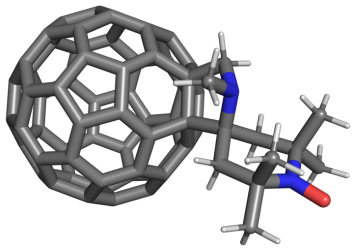

Figure 5.21: Model system for the determination of the partial charges of the nitroxide group and linker.

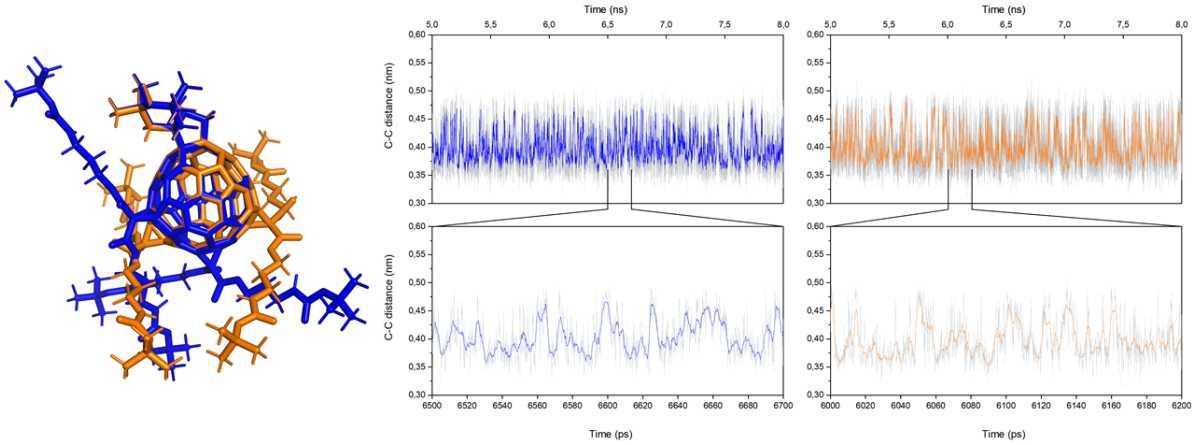

Figure 5.22: (Left) FN-2a molecules with different positions for the two cyclopropyl substitutions. (Right) Time traces of the C-C distance between the methyl groups on the nitroxide ring. Simulation details are described in the text.

conformations at 300 K, leading to the values given in tab. 5.15. For the fullerene carbon atoms in FN-2a an additive model was assumed, combining the weak electron-donating and electron-withdrawing effects of the pyrrolidine and cyclopropyl substituents, respectively (models in fig. 5.20). The resulting charge value was evenly distributed over all fullerene carbon atoms not directly influenced by the substitutions (46 atoms in FN-2a).
Since the precise position of the cyclopropyl substitutions on the FN-2a molecule is unknown (it is likely a mixture of different substitutions), two models with different substitution patterns were arbitrarily chosen for the MD simulations (fig. 5.22). The results indicate that the dynamic behavior of the nitroxide moiety - responsible for DNP - is independent on the substitution positions (fig. 5.22).

Bond, angle and non-bonding parameters For chloroform, the relevant bond and angle parameters were taken from the literature[175] and translated to the Gromacs format. Parameters for the TN and FN-2a systems were built using Acpype 0.1.[176] The parameters for the TEMPO moiety were then adjusted manually to match those specifically derived for nitroxide radicals.[165] The dummy atoms representing the nitroxide oxygen lone pairs in the original setup were omitted in our simulations.

Table 5.15: Partial charges for FN-2a. All fullerene carbon atoms except those indicated and their sysmmetry equivalent ones are assumed to have the same charge as C1. For atoms labels please refer to fig. 5.23.

Atom	Partial charge (e)	Atom	Partial charge (e)
O1	−0.27273	C11	−0.98987
O2	−0.62003	C12	1.08481
O3	−0.47427	C13	0.04027
O4	−0.61824	C14	0.06630
O5	−0.58987	C15	0.32713
N1	0.12799	C16	1.05500
N2	−0.32471	C17	0.74084
N3	−0.86661	C18	−0.45627
C1	0.00121	H1	0.28600
C2	0.40318	H2	0.18655
C3	−0.19764	H3	−0.22414
C4	0.54706	H4	0.14261
C5	−1.08335	H5	0.06602
C6	0.29144	H6	0.01557
C7	−0.71061	H7	−0.02143
C8	0.31753	H8	0.38150
C9	0.61905	H9	0.10713
C10	−0.57676		

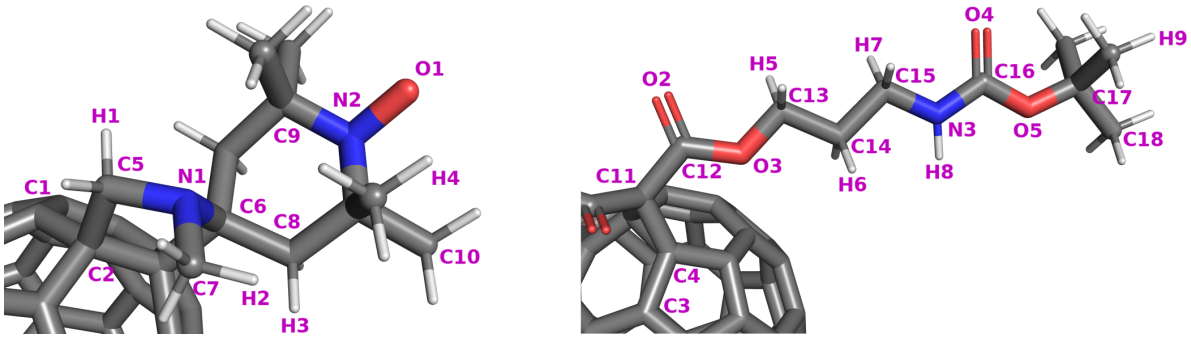

Figure 5.23: Atom numbering scheme for the side chain and the nitroxide group of the fullerene nitroxide.

System setup, equilibration and simulation details All MD simulations were carried out with Gromacs 2018.4.[125–128] The PA was placed in a pre-equilibrated box of chloroform molecules (1348 for TN, 2485 for FN-2a), energy minimized and equilibrated for 500 ps in

the nvt and 500 ps in the npt ensembles, giving final densities ($1.485\,g \cdot cm^{-3}$) very close to the experimental value for chloroform (1.49 g/cm^3 at 25°C from Sigma-Aldrich catalogue). The isothermal compressibility was matched to the literature value of $1.01 \cdot 10^{-4}\,bar^{-1}$.[177] Simulation runs of 10 ns duration were then conducted with a temporal resolution of 200 ps. For all procedures integration steps of 2 fs were used.

Electron Spin Relaxation Times at 9.4 Tesla

6

Electron spin relaxation properties are essential in liquid state DNP. Specifically, the electron spin transverse relaxation time (T_{2e}) and the electron spin longitudinal relaxation time (T_{1e}) contribute significantly to the saturation factor s of the Overhauser equation (see eq. 2.17 and eq. 2.56).[85] Knowledge of T_{1e} and T_{2e} enables the evaluation of the microwave efficiency from DNP experiments.[85] Additionally, optimization of T_{1e} and T_{2e} may significantly boost the saturation factor and therefore the NMR signal enhancement.[84]

While T_{2e} is obtained from the linewidth (LW) of a cw EPR measurement, T_{1e} is usually determined via pulsed EPR experiments.[96,178]

However, experimental data at magnetic fields larger than 3.4 T (93 GHz) are rare,[134] because only a few pulsed EPR spectrometers exist beyond this frequency ($\nu > 93$ GHz). Furthermore, due to strong mw absorption of the solvent, pulsed EPR experiments at $\sim$ 263 GHz are challenging. Therefore, the product $T_{1e}T_{2e} \approx 3.5 \cdot 10^{-16}\,s^2$ for tempol (TL) in water was estimated from a cw power saturation curve.[51] Together with $T_{2e} \approx 28$ ns,[179] determined from the cw EPR linewidth of 50 mM TL in H_2O, T_{1e} was estimated to be $\sim$ 120 ns for TL in water.[179]

Notably, these measurements were performed in the presence of dissolved oxygen, which should decrease the electron spin relaxation times.[95] This could be one explanation for the discrepancy of $T_{1e} \approx 120$ ns to a prediction from semi-classical relaxation theory of $T_{1e} \approx 850$ ns reported by the same group.[101] The latter value also agrees with T_{1e} reported at 3.4 T ($T_{1e} \approx 830$ ns)[100] and with a simulation of the T_{1e} frequency

dependence (see fig. 2.8).[96]
In order to critically evaluate the mw performance of the DNP instrument and optimize the sample preparation and the mw efficiency, T_{1e} and T_{2e} were measured with a 263 GHz (9.4 T) EPR spectrometer. To ensure comparability of the experimental results with DNP samples, the electron spin relaxation times were measured at room temperature and under exclusion of oxygen that would otherwise drastically reduce both T_{1e} and T_{2e}. Furthermore, the radical concentration and the solvent were also the same as for DNP experiments being $3 - 15$ mM of ^{15}N-TN-d_{16} (4-Oxo-2,2,6,6-tetramethylpiperidine-d_{16},1-^{15}N-1-oxyl) in CCl_4.

6.1 Electron Spin Transversal Relaxation Time

The electron spin transverse relaxation time was accessed by evaluation of the LW of cw EPR experiments. T_{2e} depends mostly on the radical concentration and the presence of other paramagnetic species such as oxygen.[178,180] Yet, the LW of a cw spectrum at high magnetic field may be broadened due to the residual (i.e. not averaged) g anisotropy at high magnetic fields and frequencies.[178,181] Therefore, the same sample was measured at low magnetic field (0.34 T, $\sim$ 9.5 GHz) as well as high field (9.4 T, and $\sim$ 263 GHz). Continuous wave experiments at 263 GHz were conducted on a Bruker 263 GHz spectrometer (see sec. 3.2.4) with a non-resonant probe that allowed for large sample volumes ($\sim 1 - 4\,\mu$L). The samples were prepared in commercial Q-band tubes (O.D. = 1.6 mm, I.D. = 1.1 mm, Wilmad Labglass), degassed by freeze-pump-thaw cycles and sealed with a torch. However, as the probehead limits the tube height to $\sim 4 - 5$ cm, sealing of the tube was performed close to the solution, thereby partially quenching the radical during the sealing process. Additionally, some solvent ($\sim 0 - 50$ %) evaporated during the freeze-pump-thaw cycles. Nevertheless, through careful monitoring by X-band cw measurements, the radical concentration was determined to be $c \approx 5 - 15$ mM during experiments at 9.5 GHz and 263 GHz.
Figure 6.1 shows the first derivative of cw spectra of three different samples at X-band as

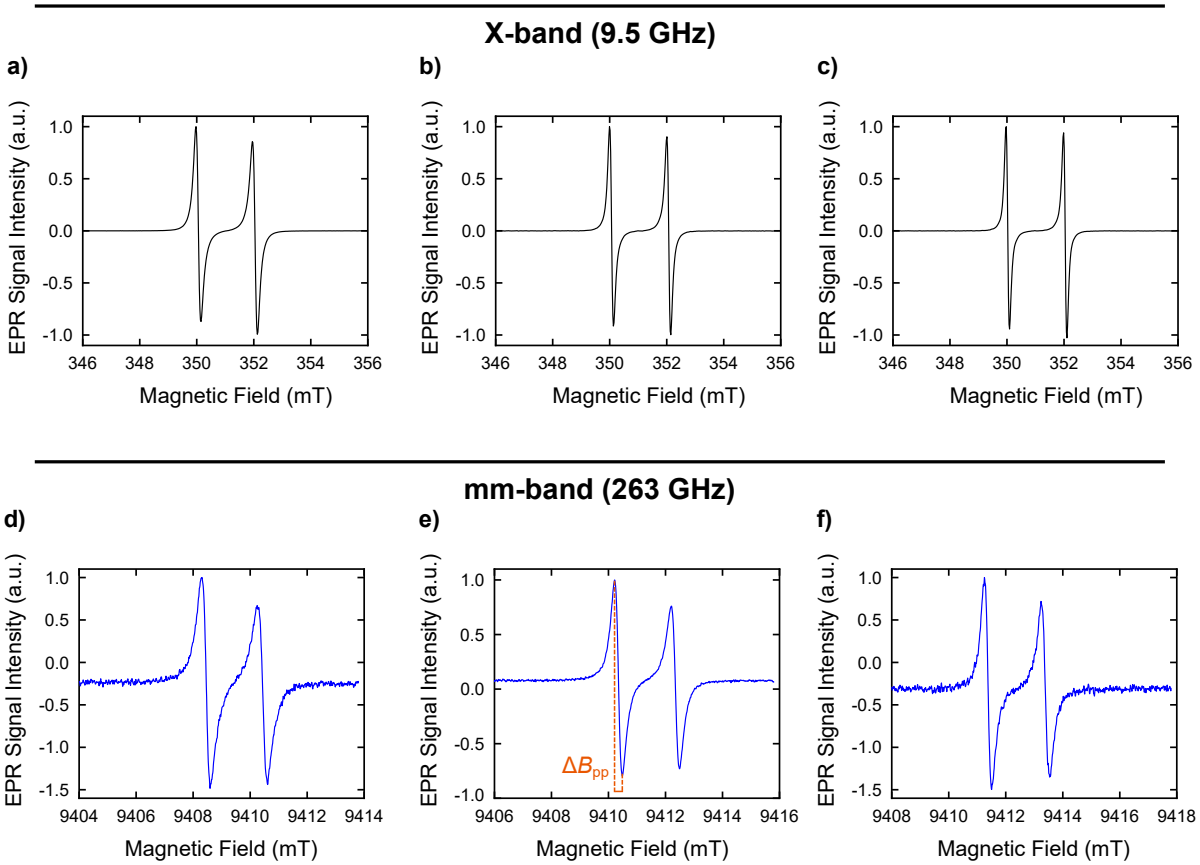

Figure 6.1: Continuous wave measurements at 9.5 GHz (a-c) and 263 GHz (d-f). Experimental parameters for a), b), and c): modulation frequency (MF) = 100 kHz, modulation amplitude (MA) = 0.2 G, RG = 60 dB, power P = 20 dB, (≈ 2.0 mW), number of scans (NS) = 3, 1024 points, sweep width (SW) = 100 G. Experimental parameters for d), e), and f): MF = 100 kHz, MA = 1.5 G, RG = 39 dB, $P = 10-20$ dB ($\approx 0.5-5$ mW), NS = 1, 1024 points, SW = 100 G. Measurements were performed on $5-15$ mM ^{15}N-TN-d$_{16}$ in CCl_4.

well as at mm-band. In order to determine T_{2e} from such a spectrum, first the general form of a complex signal $h(t)$ in the time domain is considered,[74,182]

$$h(t) = \exp(^{-t}/_{T_{2e}}) \exp(i\omega_0 t). \tag{6.1}$$

Here, ω_0 is the resonance offset and t the time. Fourier transformation of such a signal leads to[10,74]

$$F\{h(t)\} = \int_0^{+\infty} h(t)\exp(-\mathrm{i}\omega t)\mathrm{d}t = H(\omega) = A(\omega) + \mathrm{i}D(\omega), \tag{6.2}$$

with ω being the angular frequency, $A(\omega)$ the real and $D(\omega)$ the complex (absorption) and imaginary (dispersion) part of the EPR signal, respectively. In cw EPR, the first derivative of the absorption spectrum is detected (fig. 6.1). The absorption part of the signal is expressed as[74,182]

$$A(\omega) = \frac{T_{2e}}{1 + (\omega - \omega_0)^2 T_{2e}^2}. \tag{6.3}$$

Calculation of the full width at half maximum (FWHM, Γ) leads to[74,182]

$$\Gamma = \frac{2}{T_{2e}}. \tag{6.4}$$

Finally, the FWHM in the absorption spectrum is converted to the peak-to-peak distance of the first derivative.[182,183]

$$T_{2e} = \frac{2}{\sqrt{3}\Delta B_{pp}\gamma_e}, \tag{6.5}$$

where ΔB_{pp} is the separation between the two maxima of the EPR derivative and the gyromagnetic ratio $\gamma_e \approx 1.760859 \cdot 10^{11}\,[\frac{\mathrm{Hz\cdot rad}}{\mathrm{T}}]$.[73] The factor $1/\sqrt{3}$ arises from the conversion from absorption signal to the first derivative and γ_e converts from an angular frequency to a magnetic field.[183]

The results for T_{2e} are listed in tab. 6.1 and show that the average T_{2e} at 0.34 T is a factor of two larger than at 9.4 T ($\overline{T_{2e}}(0.34\,\mathrm{T}) \approx 47\,\mathrm{ns}$ and $\overline{T_{2e}}(9.4\,\mathrm{T}) \approx 24\,\mathrm{ns}$). The experimental error is estimated to be $\sim 5 - 10\,\%$ and mainly depends on the uncertainty of c. This difference of T_{2e} between X-band and mm-band indicates a more significant contribution of the g anisotropy to T_{2e} at high magnetic field and highlights the importance of measuring relaxation properties at the field of interest instead of extrapolating from low field values. Notably, at W-band (3.4 T), $T_{2e} = 28\,\mathrm{ns}$[60] for 20 mM of ^{15}N-TN in

Table 6.1: Peak-to-peak distance ΔB_{pp} and T_{2e} obtained from fig. 6.1 from the low field resonance of the spectrum. The average T_{2e} at 0.34 T (X-band) ist $\overline{T_{2e}} \approx 47$ ns and at 9.4 T $\overline{T_{2e}} \approx 24$ ns. Uncertainties of these measurements are $\leq 5 - 10\,\%$ at both magnetic fields.

ΔB_{pp} at 0.34 T (G)	ΔB_{pp} at 9.4 T (G)	T_{2e} at 0.34 T (ns)	T_{2e} at 9.4 T (ns)
1.4	3.1	39	21
1.4	2.6	47	25
1.2	2.6	25	25

CCl_4 was reported, while at 9.4 T $T_{2e} = 28$ ns[179] was obtained for 50 mM TL in H_2O. Both reports are in agreement with the herein reported T_{2e} values.

6.2 Electron Spin Longitudinal Relaxation Time

6.2.1 Electron Spin Longitudinal Relaxation Time at 0.35 T, 1.2 T, and 3.4 T

Electron spin longitudinal relaxation times T_{1e} at high magnetic fields in the liquid state are rare and mostly do not extend beyond 3.4 T (93 GHz).[60,100,179] Furthermore, while up to magnetic fields of 3.4 T ($\sim$ 93 GHz) the frequency dependence for T_{1e} of TN-d_{16} in water was experimentally determined and theoretically reproduced,[96,100] no experimental data exists at higher magnetic fields to test the theoretical treatment. However, another study predicted $T_{1e} \approx 850$ ns[101] at 263 GHz, which agrees with the frequency dependence calculated by ref. [96] and suggests a frequency independent T_{1e} for magnetic fields larger than 1.2 T (34 GHz) (see fig. 2.8). Nevertheless, as already demonstrated for T_{2e}, experimental evidence is important to draw definitive conclusions for liquid state DNP. Moreover, these calculations exist only for water and absolute values of T_{1e} may vary significantly among different solvents.[60,96]

Thus, to experimentally demonstrate the frequency dependence of T_{1e}, measurements were performed at X-, Q-, W-, and mm-band covering a frequency range of 250 GHz. Following the theoretical framework established in sec. 2.7, experiments were compared to theoretical predictions. As the goal was to understand the saturation behaviour during

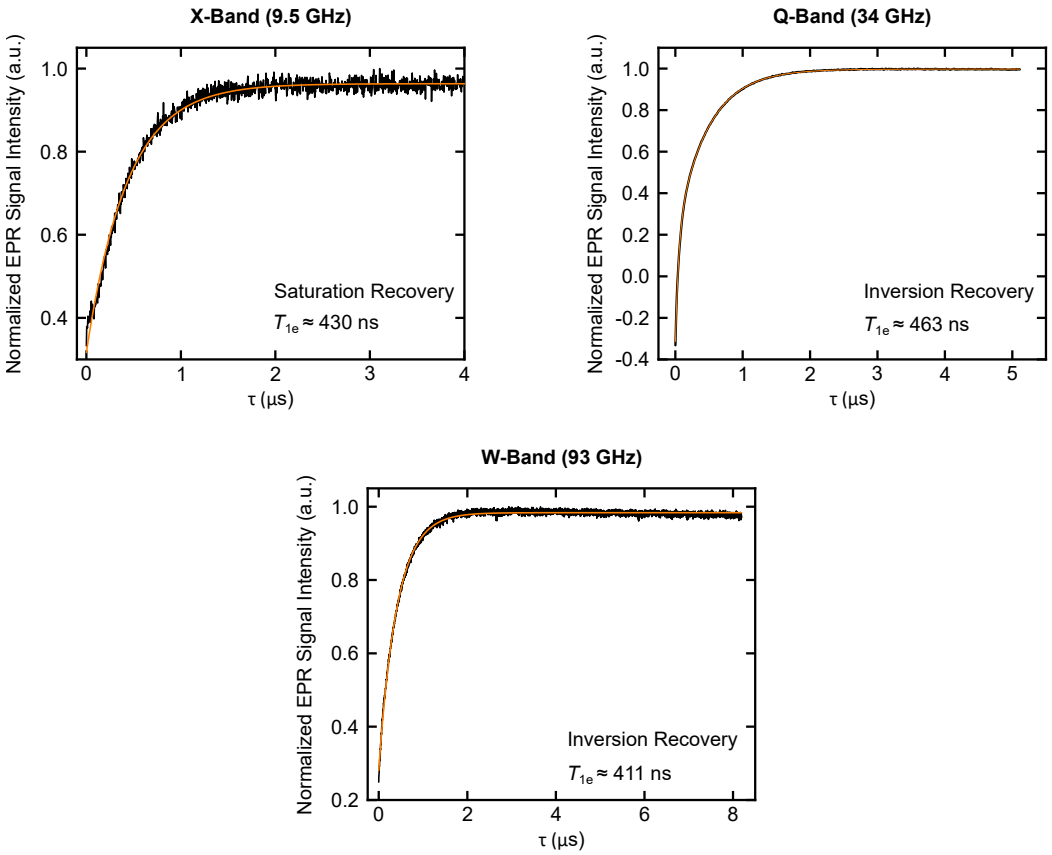

Figure 6.2: a) Saturation recovery experiment to obtain T_{1e} at X-band. Experimental parameters: $\nu = 9.692\,\text{GHz}$, $B_0 = 343.5\,\text{mT}$, $P = 10\,\text{dB}$, video gain (VG) = 33 dB, video bandwidth (VB) = 200 MHz, 1024 points, $t_p(\pi/2) = 36\,\text{ns}$, $t_p(\text{saturation}) = 5\,\mu\text{s}$, $\tau(\text{increment}) = 4\,\text{ns}$, shots per point (SPP) = 10, shot repetition time (SRT) = 10 ms, NS = 7, dead time after $\pi/2$ detection pulse 370 ns. Phase adjustment after the measurement was 25 °. b) Inversion recovery experiment to obtain T_{1e} at Q-band. Experimental parameters: $\nu = 34.909\,\text{GHz}$, $B_0 = 1241\,\text{mT}$, $P = 0\,\text{dB}$, VG = 0 dB, VB = 200 MHz, 512 points, $t_p(\pi/2) = 20\,\text{ns}$, $\tau(\text{increment}) = 10\,\text{ns}$, SPP = 20, SRT = 15 ms, NS = 1, dead time after $\pi/2$ detection pulse 296 ns, two step phase cycling (x and $-x$) of π-pulse. Phase adjustment after the measurement was 7 °. c) Inversion recovery experiment to obtain T_{1e} at W-band. Experimental parameters: $\nu = 94.114\,\text{GHz}$, $B_0 = 3343\,\text{mT}$, $P = 0\,\text{dB}$ ($\approx 0.6\,\text{W}$), VG = 0 dB, VB = 25 MHz, 4096 points, $t_p(\pi/2) = 20\,\text{ns}$, $\tau(\text{increment}) = 2\,\text{ns}$, SPP = 1, SRT = 3 μs, NS = 1, dead time after $\pi/2$ detection pulse 300 ns. Phase adjustment after the measurement was 0 °. Orange lines are mono-exponential fits ($y = A\exp(-\tau/T_{1e}) + y_0$) for a) and c) and a bi-exponential fit ($y = A\exp(-\tau/T_{1e}) + B\exp(-\tau/T_b) + y_0$) for b). Radical c was $\sim 10\,\text{mM}$ ^{15}N-TN-d$_{16}$ for X- and Q-band and $\sim 3\,\text{mM}$ at W-band in CCl_4.

DNP, the experiments were performed with $\sim 3-10\,\mathrm{mM}$ ^{15}N-TN-d$_{16}$ in CCl_4.
Access to the electron spin longitudinal relaxation time is usually gained by pulsed EPR with the inversion recovery or saturation recovery experiment (see sec. 3.3.1), where the magnetization is either inverted or depleted and its return to equilibrium is monitored via FID detection. Figure 6.2 shows an FID detected saturation recovery measurement at X-Band and inversion recovery experiments at Q- and W-band. Measurements at X- and W-band were performed without phase cycling, while at Q-band a two step phase cycle for the π pulse was applied. This removed undesirable signals during the FID detection. Fitting the Q-band data to a bi-exponential fit ($y = A\exp(^{-\tau}/_{T_{1e}}) + B\exp(^{-\tau}/_{T_b}) + y_0)$) produced $T_{1e} \approx 463\,\mathrm{ns}$ and $T_b \approx 49\,\mathrm{ns}$ for the second time constant. The error for T_{1e} is approximately $10-15\,\%$ and mainly depends on the signal-to-noise ratio and the phase stability of the spectrometer during the experiment. Bi-exponential fits for inversion recovery experiments were previously reported to analyze the Heisenberg exchange contribution.[84,87,88,103] In such cases, an inversion recovery curve is fitted together with an electron double resonance (ELDOR) recovery experiment to[84]

$$i_{1,2} = A_{1,2}\exp(-2w_e t) \pm B_{1,2}\exp(-2w_e + 2w_n + cK_X). \tag{6.6}$$

Here, $i_{1,2}$ is the signal intensity of the two experiments, w_e the electron transition rate ($(2w_e)^{-1} = T_{1e}$), w_n the nuclear transition rate of the nitrogen of the nitroxide, c the nitroxide concentration, and K_X the Heisenberg exchange factor. In the ELDOR recovery experiments, the inversion pulse is performed on the second hyperfine resonance of the spectrum, while detection is performed on the first resonance.[84]
Even though in this work no ELDOR recovery experiments were performed, T_b was still used to evaluate the Heisenberg exchange factor using $T_b = (2w_e + 2w_n + cK_X)^{-1}$. Neglecting w_n due to a negligible contribution at high radical concentration,[84] leads to $K_X \approx 2\,\mathrm{GHz\,M^{-1}}$. Both values ($T_{1e} \approx 463\,\mathrm{ns}$, $K_X \approx 2.0\,\mathrm{GHz\,M^{-1}}$) agree with previously reported values obtained on 4 mM ^{15}N-TN in CCl_4 ($T_{1e} \approx 520 \pm 50\,\mathrm{ns}$ and $K_X \approx 2.5 \pm 0.8\mathrm{GHz\,M^{-1}}$)[60] at the same frequency.
On the other hand, saturation and inversion recovery curves recorded at X- and W-band (fig. 6.2a and c) were fitted to a mono-exponential decay ($T_{1e}(0.34\,\mathrm{T}) \approx 463\,\mathrm{ns}$ and $T_{1e}(3.4\,\mathrm{T}) \approx 411\,\mathrm{ns}$), because a bi-exponential fit led to $T_{1e} \approx T_b$ and therefore did

not improve the fit quality. At W-band this may be reasonable, because the radical concentration was only $c \approx 3.5\,\mathrm{mM}$ and therefore Heisenberg exchange may be less significant for the relaxation.[103] A similar behaviour was reported earlier in toluene, albeit for a concentration below 1 mM.[103] As at X-band, measurements were performed on the same sample as at Q-band, this behaviour remains peculiar, however the obtained results at X-band ($T_{1e} \approx 463\,\mathrm{ns}$) as well as at W-band ($T_{1e} \approx 411\,\mathrm{ns}$) are in the same range as results reported in the literature ($T_{1e}(0.34\,\mathrm{T}) \approx 500\,\mathrm{ns}$[184] and $T_{1e}(3.4\,\mathrm{T}) \approx 280 - 380\,\mathrm{ns}$).[60]

6.2.2 Electron Spin Lattice Relaxation Time at 9.4 T

After the initial measurements at low to mid magnetic fields, EPR measurements were performed at 9.4 T. As the size of the sample tubes (O.D. = 0.33 mm, I.D. = 0.2 mm) reduces significantly at 263 GHz, a large amount of solution $\sim 100\,\mu\mathrm{L}$ was degassed by freeze-pump-thaw cycles and transferred to a glove box. The sample consisted of $\sim 10\,\mathrm{mM}$ ^{15}N-TN-d$_{16}$ in CCl_4. Sample capillaries were filled with the solution under N_2

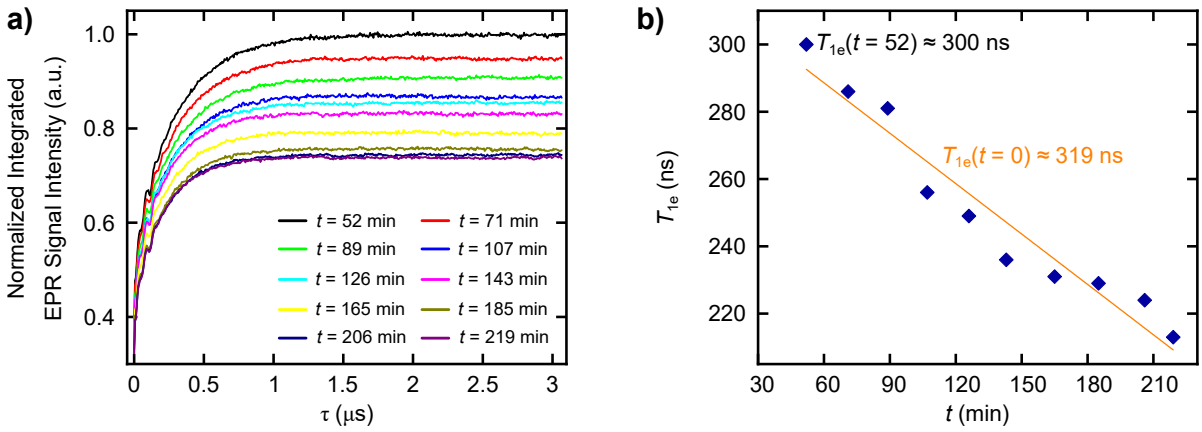

Figure 6.3: a) Inversion recovery experiments to obtain T_{1e} of 10 mM ^{15}N-TN-d$_{16}$ in CCl_4 at 263 GHz at different time points t after removing the sample from N_2 atmosphere. Experimental parameters: $\nu = 264.139\,\mathrm{GHz}$, $B_0 = 9417\,\mathrm{mT}$, $P = 0\,\mathrm{dB}$ ($\approx 50\,\mathrm{mW}$), VG = 21 dB, VB = 200 MHz, 512 points, $t_p(\pi/2) = 80\,\mathrm{ns}$, $\tau(\mathrm{increment}) = 6\,\mathrm{ns}$, SPP = 50, SRT = 8 ms, NS = 5, dead time after $\pi/2$ detection pulse = 130 ns, measurement time $\approx 20\,\mathrm{min}$. Phase adjustment was between 0 and $-16°$. b) Blue circles are the T_{1e} values as obtained from the experiments shown in a) as a function of the time the sample was exposed to atmospheric oxygen. The orange line is a linear fit of the T_{1e} data.

Table 6.2: T_{1e} at 263 GHz obtained from inversion recovery experiments on different samples. Measurements were performed on 10 mM ^{15}N-TN-d_{16} in CCl_4. (*) $c(^{15}\text{N-TN-d}_{16}) \approx 5$ mM. Inversion recovery measurements and the experimental parameters of the samples $3-6$ are shown in appendix A (fig. A.1 and tab. A.1), while sample 1 and sample 2 are described in fig. 6.3 and fig. 6.4, respectively.

Sample	1	2	3	4*	5	6	∅
T_{1e} (ns)	300	378	271	226	240	322	289
T_b (ns)	13	0	25	10	17	9	

atmosphere and both ends were closed with sealing rubber (Critoseal). Samples were transported to the spectrometer under N_2 atmosphere and only upon insertion into the resonator exposed to air.

Figure 6.3a shows inversion recovery experiments at 263 GHz at different times after the sample was exposed to air. The inversion recovery experiments were fitted to a bi-exponential decay ($y = A\exp(^{-\tau}/_{T_{1e}}) + B\exp(^{-\tau}/_{T_b}) + y_0$) that produced the electron spin relaxation time ($T_{1e} \approx 300$ ns) and a second time constant $T_b \approx 13$ ns (see tab. 6.2, T_b will be discussed later). Even though the resonator is constantly flushed with He gas, it is evident that with increasing time T_{1e} reduces. This is attributed to oxygen dissolving in the sample, thereby reducing the electron spin longitudinal relaxation time. Figure 6.3b shows a linear dependence of T_{1e} on the time between measurement and exposing the sample to air. Therefore, the time between the experiment and sample contact to air was minimized.

Due to the challenging experimental conditions reproduction of the experimental results was carefully monitored. Table 6.2 lists T_{1e} for six samples, measured under comparable experimental conditions. The results show that the T_{1e} values range from $T_{1e} \approx 226$ ns to $T_{1e} \approx 378$ ns, with reintroduced oxygen probably contributing significantly to the shorter T_{1e} values.

In contrast to the measurements at Q-band, T_b was too short ($T_b \approx 0 - 25$ ns) to correspond to the Heisenberg exchange rate (see $T_b \approx 49$ ns at Q-band).[84] The shorter time constant may therefore be explained by hardware limitations of the setup, because the short FID at 9.4 T ($\lesssim 300$ ns) required a small dead time (~ 135 ns) after the $\pi/2$ pulse. This led to significant background signal, due to residual signal produced by the

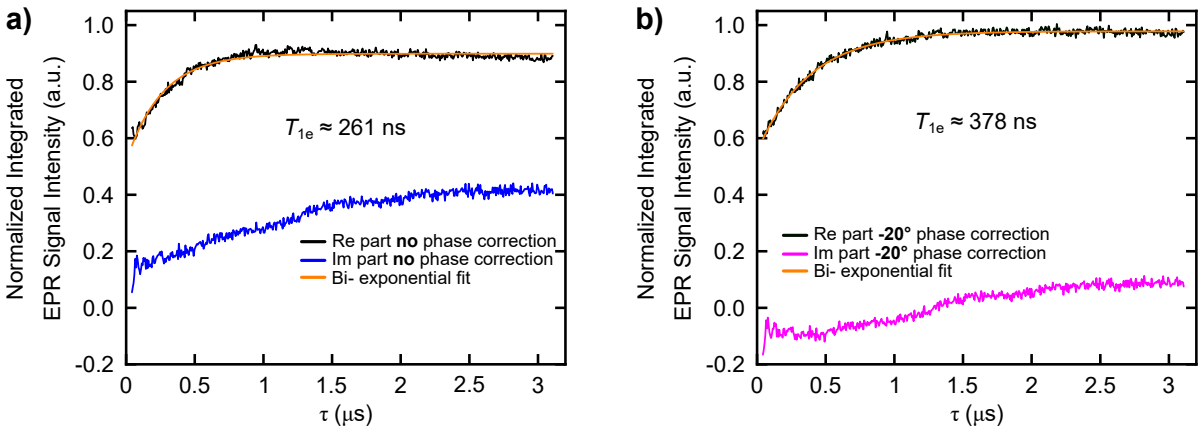

Figure 6.4: a) Real and imaginary part of the inversion recovery experiment to obtain T_{1e} of 10 mM ^{15}N-TN-d$_{16}$ in CCl_4 at 263 GHz without phase adjustment and b) after phase adjustment by 20 °. Experimental parameters: $\nu = 264.2417$ GHz, $B_0 = 9431.1$ mT, $P = 0$ dB (≈ 50 mW), VG = 27 dB, VB = 200 MHz, 512 points, $t_p(\pi/2) = 100$ ns, τ(increment) = 4 ns, SPP = 50, SRT = 15.3 ms, NS = 4, dead time after $\pi/2$ detection pulse = 146 ns, measurement time $\approx$ 20 min.

pulse, and may have produced the shorter time constant.

Additionally, the phase stability during the experiment was challenging. Figure 6.4 shows the real and imaginary part of an inversion recovery experiment without and with phase adjustment during post processing in a and b, respectively. Under optimized conditions, the signal intensity of the imaginary part would be zero, however even after phase adjustment real and imaginary part are not entirely separated.

Furthermore, to assess the quality of the experimental results, the frequency dependence of T_{1e} was calculated based on the framework established in sec. 2.7. For this eq. 2.75 was used and is recalled here for clarity,[95,96]

$$\frac{1}{T_{1e}} = \frac{1}{T_{1e}^{SR}} + \frac{1}{T_{1e}^{A}} + \frac{1}{T_{1e}^{g}} + \frac{1}{T_{1e}^{therm}} + \frac{1}{T_{1e}^{SD}} + \frac{1}{T_{1e}^{Ox}}. \tag{6.7}$$

The different contributions to $\frac{1}{T_{1e}}$ are spin rotation $\frac{1}{T_{1e}^{SR}}$, anisotropy of the hyperfine coupling $\frac{1}{T_{1e}^{A}}$, anisotropy of the g tensor $\frac{1}{T_{1e}^{g}}$, rotation of the methyl groups of the nitroxide,[98,99] $\frac{1}{T_{1e}^{therm}}$, spin diffusion $\frac{1}{T_{1e}^{SD}}$, and relaxation caused by dissolved oxygen $\frac{1}{T_{1e}^{Ox}}$. For the calculation $\frac{1}{T_{1e}^{SD}}$ and $\frac{1}{T_{1e}^{Ox}}$ were neglected, because oxygen was removed during the sample preparation (although insufficiently at 9.4 T). As input data for the other contributions were used:

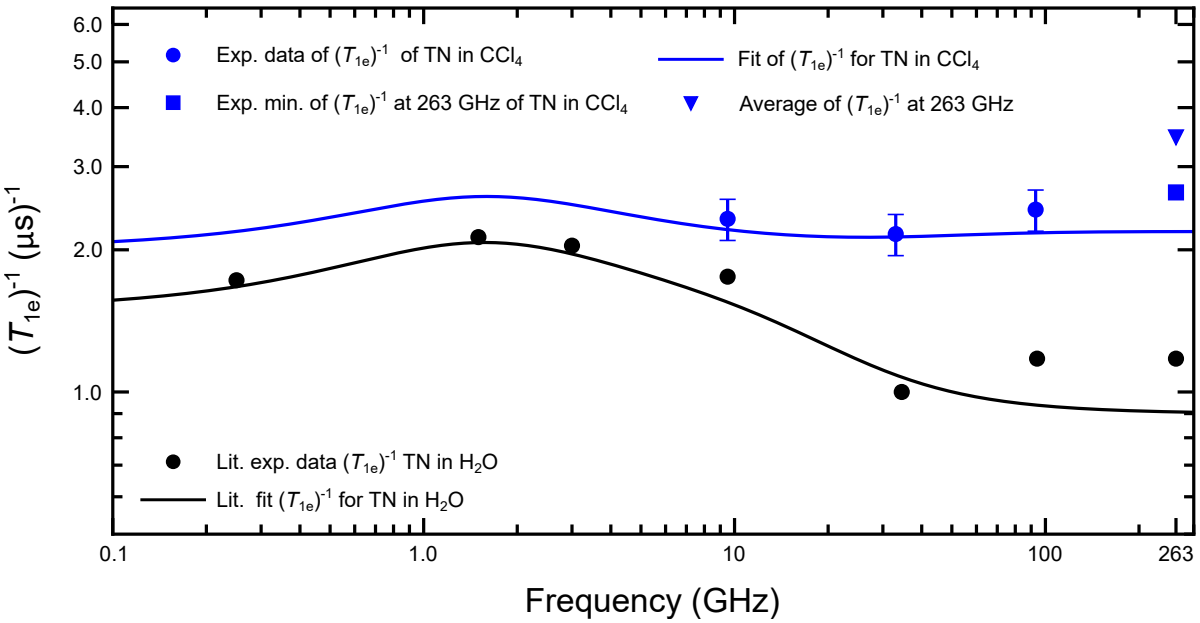

Figure 6.5: Experimental values of $(T_{1e})^{-1}$ of ^{15}N-TN-d$_{16}$ in CCl_4 as a function of the frequency (blue symbols). Circles indicate measurements at $\sim$ 9.5 GHz, $\sim$ 33 GHz, and $\sim$ 93 GHz, while the blue square is the smallest experimental $(T_{1e})^{-1}$ and the triangle the average $(T_{1e})^{-1}$ at 263 GHz. Equation 2.75 (blue line) produced the theoretical predication for the field dependence considering contributions from spin rotation, g anisotropy, A anisotropy, and methyl group rotation (spin diffusion). Error bars for measurements at 9.5 – 93 GHz represent an uncertainty of 10 %. Simulation parameter: $g = [2.0092, 2.0061, 2.0022]$,[96] $A = [29.0, 29.0, 127.0]$ MHz,[185] $I(^{15}\text{N}) = 0.5$, $\tau_C = 3.7$ ps (free parameter), $C_{\text{therm}} = 7.0 \cdot 10^{16}$, $\tau_{\text{therm}} = 100$ ps, and $\omega_{\text{ref}} = 9.5$ GHz.[96,98] Black circles and black line are the experimental and calculated $(T_{1e})^{-1}$ frequency dependence of TN in H_2O and are reproduced from fig. 2.8. Errors for the literature data were reported to be $\sim$ 3 %, which lie within the symbol.

$g = [2.0092, 2.0061, 2.0022]$,[96] $A = [29.0, 29.0, 127.0]$ MHz,[185] $I(^{15}\text{N}) = 0.5$, $\tau_C = 3.7$ ps (free parameter), $C_{\text{therm}} = 7.0 \cdot 10^{16}$, $\tau_{\text{therm}} = 100$ ps, and $\omega_{\text{ref}} = 9.5$ GHz.[96,98] Figure 6.5 shows the calculated frequency dependence of $(T_{1e})^{-1}$ for 10 mM ^{15}N-TN-d$_{16}$ in CCl_4 (blue line) together with the herein obtained experimental values at 9.5, 33, and 93 GHz (blue circles). At 263 GHz, the blue triangle represents the experimental average $(T_{1e})^{-1} = 1/\overline{T_{1e}} \approx 1/282\,\text{ns} \approx 3.5\,\mu\text{s}$ and the blue square indicates the experimental minimum $(T_{1e})^{-1} = 1/T_{1e} \approx 1/378\,\text{ns} \approx 2.6\,\mu\text{s}$. As a comparison, the frequency dependence of TN-d$_{16}$ in water is also reproduced from the literature (black, for details see fig. 2.8).[96] The experimental data at low to medium frequency agree well with the calculated behaviour,

while the mean T_{1e}^{-1} at 263 GHz deviates significantly from the predicted dependency. On the other hand, the discrepancy of the minimum T_{1e}^{-1} at 263 GHz and the simulation is comparable to the deviations between theory and experiment observed in the literature (see black data points).[96] This comparison indicates that T_{1e} at high magnetic field follows the predicted behaviour, if O_2 is excluded efficiently from the sample solution.
Notably, the only free parameter of the simulation was the rotational correlation time τ_C and the displayed simulation was obtained with $\tau_C = 3.7$ ps. A previous study obtained $\tau_C = 7.7$ ps from fitting cw EPR spectra at 3.4 T for ^{15}N-TN.[60] However, for the herein presented T_{1e} simulation, g values of TN-d_{16} in water were employed.[96] As the g values depend on the solvent,[181] measurement of the g tensor of ^{15}N-TN-d_{16} in CCl_4 will improve the quality of the simulation. Yet, as the main contribution to T_{1e} at high magnetic field is the radical (spin) rotation, the g anisotropy only partially accounts for the discrepancy of τ_C that should be further investigated.
In summary, the electron spin transverse relaxation time T_{2e} was successfully measured at 263 GHz. Furthermore, also the electron spin longitudinal relaxation time T_{1e} was measured at four different frequencies including 263 GHz. Despite hardware and sample preparation limitations, T_{1e} was obtained from inversion recovery experiments and the comparison to the theoretical prediction delivered evidence that the experimental results are indeed in the range expected by calculations. Further confirmation of the data could be achieved by improving the phase stability during acquisition as well as better exclusion of O_2 from the sample.
Nevertheless, these results are important for further optimization of DNP at 9.4 T, because they enabled the calculation of the saturation factor as well as an estimation of B_{1e}. The saturation was estimated to be $s \approx 0.3 - 0.4$ (see sec. 7.1.5) using the ^{13}C NMR signal enhancement in neat CCl_4 ($\epsilon \approx 135$, see fig. C.10), and data from the literature ($\xi \approx -0.17$, $f \approx 0.9 - 1$).[34] With this and the herein obtained relaxation data ($T_{1e} \approx 280 - 500$ ns, $T_{2e} \approx 13 - 25$ ns) the effective microwave field strength B_{1e} at the sample was estimated ($B_{1e} \approx 0.5 - 1.0$ G). A detailed discussion is given in sec. 7.1.5. As B_{1e} quantifies the efficiency of the mw irradiation, this enabled the evaluation of the mw components of the DNP setup and contributes to further improvements of the mw irradiation and sample preparation. Additionally, with the knowledge of T_{1e} and T_{2e} of

^{15}N-TN-d_{16}, other promising polarizing agents may be identified based on their electron spin relaxation behaviour.

Dynamic Nuclear Polarization at 9.4 Tesla

7

Dynamic Nuclear Polarization at 9.4 Tesla in liquids at room temperature is the core of this work. Until recently, DNP in liquids at high magnetic field was deemed mechanistically unfeasible, because the enhancement of ^{1}H decays rapidly with increasing magnetic field.[46] Yet, our recent studies reported very large ^{13}C signal enhancement on various compounds, i.e. $\epsilon(CCl_4) \approx 1000$ at 3.4 T and $\epsilon(CBr_4) \approx 600$ at 9.4 T.[34,60] This demonstrated the mechanistic viability of liquid state DNP at high magnetic field ($B_0 \geq 9.4\,T$).

Not only delivered these studies the proof of concept for DNP at high magnetic field, they also defined the necessary microwave capabilities for a DNP instrument operating at a frequency of $\sim 263\,GHz$ ($B_0 \sim 9.4\,T$). In order to reach a saturation factor of $s \approx 0.5$, an average microwave field of $B_{1e} \approx 0.5 - 1.0\,G$ is necessary for nitroxide radicals in CCl_4.[34,60]

Currently, only a few other DNP instruments that operate at high magnetic field have been reported.[33,68,69] Non-resonant (i.e. without microwave resonator) setups are built with unconventional geometries: the sample is distributed over a metal mirror, creating a thin layer of sample[68] or placed in a tube with mw irradiation applied along the axis of B_0.[69] These allow for sample volumes of up to 100 µL but, due to mw absorption of the solvent, cause severe sample heating. Microwave resonant setups either use a helical resonator or a Fabry-Pérot assembly, which, for the most part, solves the heating problem but limits the sample volume to $V \leq 100\,nL$ and the magnetic field homogeneity at the sample position.[33,51]

Building on these results and electron spin relaxation measurements (chapter 6), a new

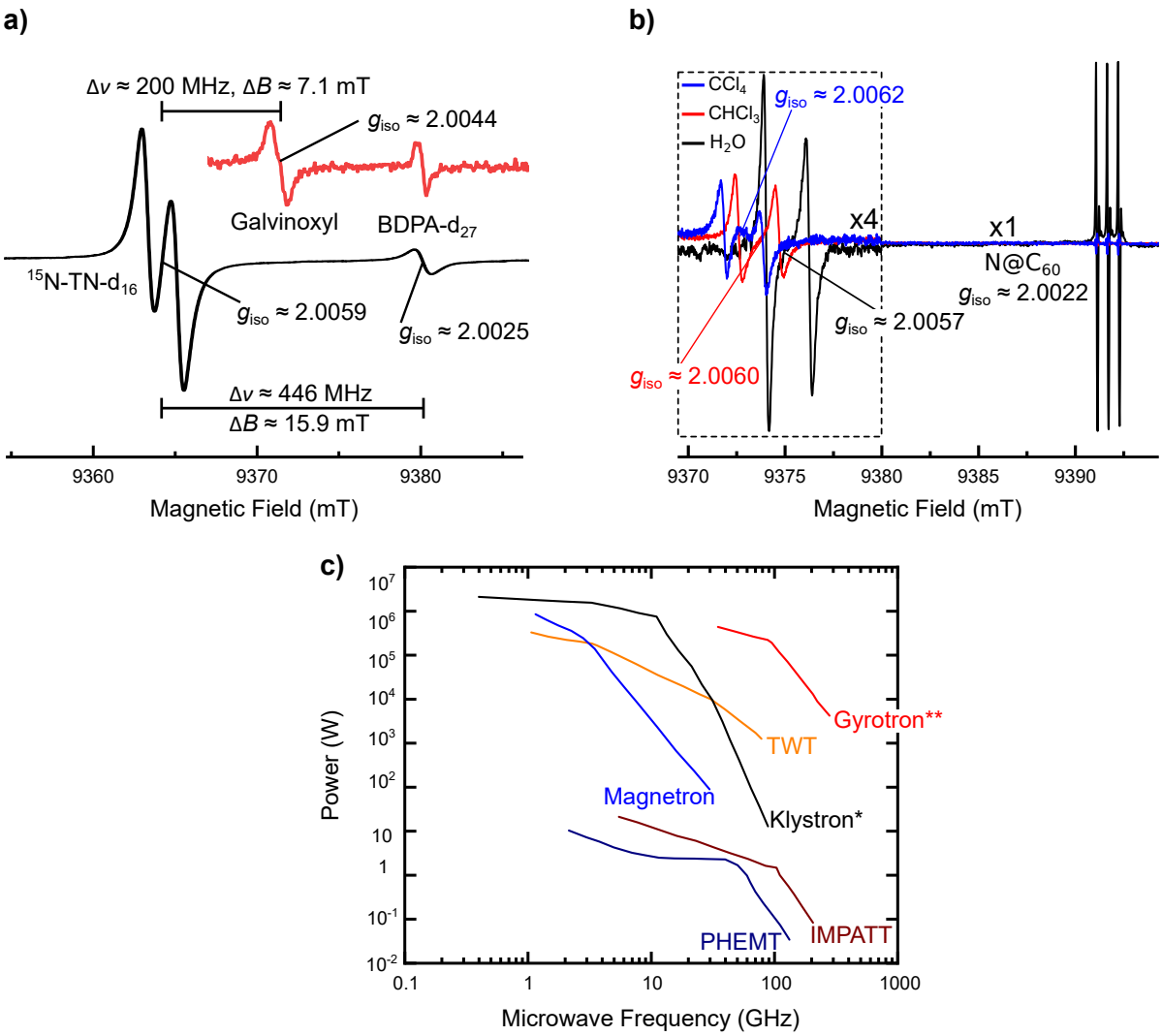

Figure 7.1: a) 263 GHz cw EPR wave measurement of $\sim 25-50$ mM ^{15}N-TN-d$_{16}$ and $\sim 5-10$ mM BDPA in toluene (black) and ~ 10 mM BDPA and ~ 10 mM galvinoxyl in toluene (red). The spectra were referenced to g_{iso} of BDPA.[186] b) 263 GHz cw EPR measurement of ~ 2 mM ^{15}N-TN-d$_{16}$ in CCl_4 (blue), $CHCl_3$ (red), and H_2O (black, $c(^{15}\text{N-TN-d}_{16}) \approx 10$ mM). N@C$_{60}$ was used as a reference and calibrated to a carbon fiber (see appendix B fig. B.1).[105] Experimental parameters are listed in appendix B tab. B.2 and tab. B.3. c) Microwave power of different sources at varying frequency. Here, PHEMT means pseudomorphic high electron mobility transistor and IMPATT impact ionization avalanche transit time diode. (*) Klystrons are available at 263 GHz with 5 W output power. (**) Gyrotrons for DNP reach $\nu = 593$ GHz with an output power of at least $P \approx 50$ W.[187,188] Figure adapted from [189, 190].

Table 7.1: A_{iso} and g_{iso} of different PAs in different solvents at 9.4 T obtained from the cw EPR spectra at 263 GHz displayed in fig. 7.1. (*) Referenced to g_{iso} of BDPA in toluene.[186] (**) referenced to N@C_{60}. The g_{iso} factor of N@C_{60} was calibrated to the literature using a carbon fiber (see appendix B fig. B.1).[105]

PA	solvent	A_{iso} (MHz)	g_{iso}
BDPA	toluene	–	2.0025[186]
Galvinoxyl	toluene	–	2.0044*
N@C_{60}	$CHCl_3$	–	2.0022
N@C_{60}	CCl_4	–	2.0022
^{15}N-TN-d_{16}	toluene	50	2.0059*
^{15}N-TN-d_{16}	CCl_4	53	2.0062**
^{15}N-TN-d_{16}	$CHCl_3$	56	2.0060**
^{15}N-TN-d_{16}	H_2O	62	2.0057**

liquid state ODNP setup at 9.4 T was developed as part of the herein presented work. Due to the advantage of large sample volumes and high magnetic field homogeneity, which enables narrow NMR linewidths at 50 % peak intensity (LW $\lesssim$ 30 Hz, under DNP conditions, see sec. 7.2.2), a non-resonant mw irradiation approach was chosen. Furthermore, our laboratory houses a 263 GHz EPR spectrometer that enables the measurement of parameters that are important for DNP, such as electron spin relaxation times and EPR linewidths of different polarizing agents in a variety of solvents at 9.4 T (chapter 6). Therefore, a mw frequency of 263 GHz was selected for the new DNP setup. The EPR spectrometer was used to characterize the properties of radicals commonly used as PAs in liquid state DNP.[58,60,191] Figure. 7.1a shows the cw EPR spectra of $\sim 25 - 50$ mM ^{15}N-TN-d_{16} (4-Oxo-2,2,6,6-tetramethylpiperidine-d_{16},1-^{15}N-1-oxyl) and $\sim 5 - 10$ mM BDPA-d_{27} (α,γ-Bisdiphenylene-β-phenylallyl-d_{27}) in toluene (black) and of ~ 10 mM BDPA and ~ 10 mM galvinoxyl in toluene (red) that were referenced to g_{iso} of BDPA.[186] At $B_0 \approx 9.4$ T, the resonance frequencies of ^{15}N-TN-d_{16} and galvinoxyl differ by ~ 200 MHz and the separation between ^{15}N-TN-d_{16} and BDPA is $\Delta\nu \approx 446$ MHz (see tab. 7.1 for g_{iso} values).

Moreover, fig. 7.1b shows the cw EPR spectra of ~ 2 mM ^{15}N-TN-d_{16} in CCl_4, $CHCl_3$, and H_2O referenced to an N@C_{60} standard, a fullerene with a nitrogen placed in the center ($g_{iso} \approx 2.022$, see appendix B fig. B.1 for g value calibration according to ref. [105]).

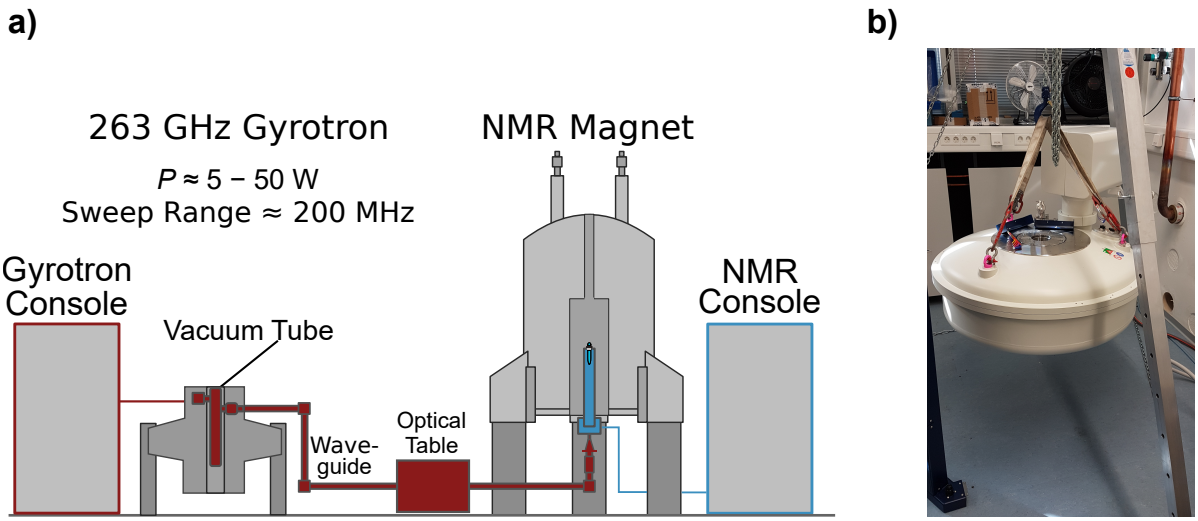

Figure 7.2: a) Sketch of the 9.4 T DNP setup that includes all relevant components and connections. b) Picture of the installation of the gyrotron in 2020.

Table 7.1 reports the A_{iso} and g_{iso} values, determined from the spectra shown in fig. 7.1. The comparison reveals that both A_{iso} and g_{iso} are affected by the choice of the solvent. Along with the observed EPR linewidth of ^{15}N-TN-d_{16} in CCl_4 at $\sim$ 9.4 T (2 – 3 G, 5.5 – 8.5 MHz for a degassed sample, see fig. 6.1), the in fig. 7.1 reported variations of g_{iso} indicated that a frequency agile mw source would be necessary to perform DNP with different PAs and in different solvents.

Aside from the mw frequency, also the mw power is important for ODNP and one goal of the new setup was to avoid any power limitations due to the choice of the mw source. Figure 7.1c shows the mw output power of different mw sources: Although the plot is from 1999,[189,190] it is still valid for the frequencies that concern DNP NMR and demonstrates that the gyrotron enables the largest flexibility in terms of mw power at a frequency of 263 GHz.

These two requirements (high power and frequency flexibility) led to the decision to equip the liquid state DNP setup with a frequency agile gyrotron, which is shown in fig. 7.2 together with a picture of the installation. The tunability of the gyrotron was specifically developed for our setup and covers a range of $\sim$ 200 MHz at high mw output power ($P \approx 10 - 50$ W) and by changing the magnetic field of the gyrotron a range of $\sim$ 500 MHz at low power ($P \leq 10$ W). To further improve the control over the mw,

a quasi-optical table equipped with a mechanical shutter, a power attenuator, and a polarization transforming reflector (PTR) enable mw gating, mw power adjustments, and control over the polarization of the mw beam.
To ensure NMR linewidths compatible with routine NMR experiments, the DNP probehead was based on a commercial NMR probehead, in which the mw components were implemented. Microwave irradiation of the sample from the side was preferred over irradiation along the B_0 axis, because it allows for maximization of the irradiation window on the sample, which is further increased by sample tube rotation (along the B_0 axis).
In order to maximize the penetration of the sample by the mw, the liquid sample was confined to a layer that is thinner than the penetration depth of the mw (see sec. 7.1.4.3 and sec. 7.1.6 for details). This guaranteed efficient mw penetration of the sample and reduced sample heating induced by mw absorption of the solvent. The latter was further controlled by active cooling with a cold N_2 gas flow.
A combination of these considerations led to the current design of the DNP setup that is depicted in fig. 7.2a with a picture of the installation of the gyrotron shown in fig. 7.2b. In the following section (sec. 7.1) each component of the new setup is characterized and explained. Furthermore, the microwave field strength at the sample position is evaluated and compared with the literature. Section 7.2 compares the DNP signal enhancement of model systems with the literature and reports the DNP enhancements of a variety of target molecules. This is complemented by mechanistic considerations of possible new spin polarization transfer pathways. Section 7.3 demonstrates the capability to perform DNP in polar solvents such as water. Finally, sec. 7.4 shows 2D NMR experiments under DNP conditions.

7.1 Development of a 9.4 Tesla Liquid State DNP Setup

7.1.1 The Gyrotron as a Microwave Source

Figure 7.2a shows a sketch of the DNP setup, which comprises a gyrotron (Communications & Power Industries, CPI) and an accompanying console, an NMR magnet (400 MHz Bruker wide-bore Ultrashield), an NMR console (Bruker Avance NEO), and a quasi-optical table (Bridge12 Technologies Inc.).

The gyrotron produces mw on a second harmonic, meaning that the generated frequency ($\sim 263\,\mathrm{GHz}$) is twice the frequency of the fundamental frequency required by the magnetic field (4.8 T) of the gyrotron. This design choice is optimized for NMR DNP, where power requirements usually do not exceed $\sim 100\,\mathrm{W}$.[192] The gyrotron consists of a cryogen free magnet that hosts a vacuum tube ($p \leq 10^{-10}\,\mathrm{Torr}$), where mw irradiation is produced by acceleration of electrons. Figure 7.3b shows a sketch of the vacuum tube and indicates the different gyrotron parameters. Electrons are generated by a heated filament and accelerated by the cathode voltage V_0 to the collector.[192,193] The collector current I_0 regulates the amount of accelerated electrons. The gun coil produces a small additional magnetic field that focuses the electron beam[21] and can have the same or the opposite sign of the main gyrotron magnetic field.

The cavity is placed in the vacuum tube of the gyrotron. On their way from the heated filament to the collector, electrons perform a circular movement that, inside the cavity, leads to emission of mw irradiation.[21,192] The electromagnetic radiation is guided by a so-called launcher (not shown) and transferred through a set of mirrors to the corrugated waveguide (19.3 mm inner diameter (I.D.)) that ends at a taper at the beginning of the probehead.[21,192] Corrugated waveguides have a grooved surface that significantly reduces the losses if compared to flat waveguides.[194] The losses are minimized if the grooves have a depth of $\sim \lambda/4$, a period of $\sim \lambda/3$, and a width of $< \lambda/3$.[194] Commercially available gyrotrons (as the one discussed) produce a linearly polarized mw beam in the transverse electromagnetic mode (TEM_{00}, indices indicate the half-cycle variations of the oscillating electromagnetic wave in different dimensions),[183] which turns inside the corrugated waveguide into the hybrid electric mode (HE_{11}).[192]

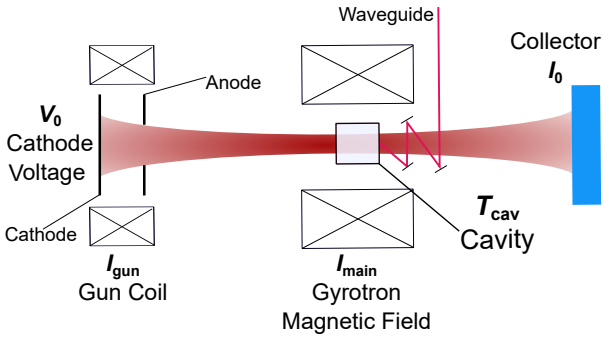

Figure 7.3: Sketch of the vacuum tube of the gyrotron. It shows the generation of the mw radiation inside the gyrotron and highlights all different gyrotron parameters.

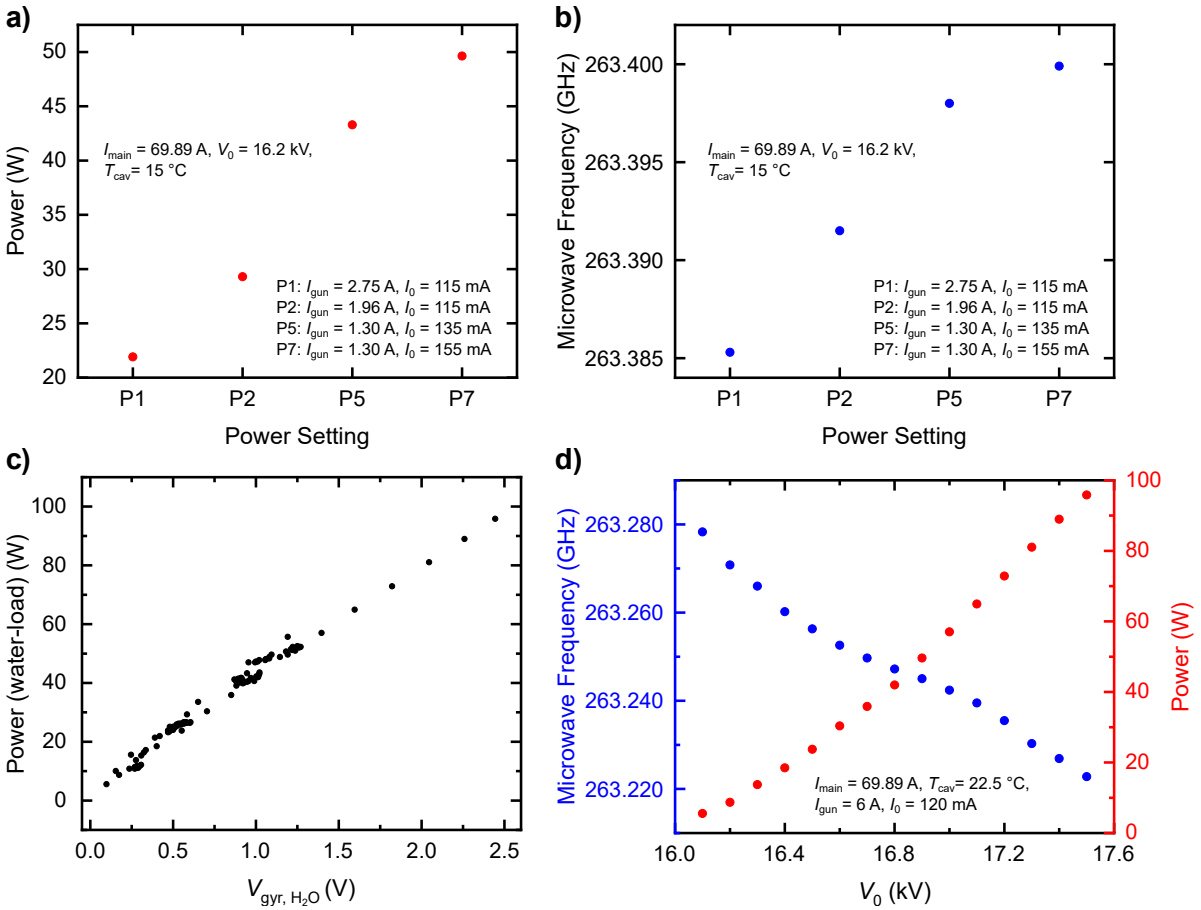

Figure 7.4: a) Power dependence for defined gyrotron power settings (tab. 7.2) and b) their microwave frequency. c) Correlation between the mw power observed with the water-load and the corresponding voltage detected by the calorimeter. d) Microwave output power and frequency of the gyrotron as a function of the cathode voltage V_0.

7.1.2 Gyrotron Output Power and Frequency Characterization

Microwave power monitoring during DNP experiments is important for the optimization of the signal enhancement. For the characterization of the mw output power, a water-load was therefore connected to the end of the wave guide, right before the probehead. A frequency meter (Virginia Diode), which was connected via directional coupler to the waveguide, was used to determine the microwave frequency. Experiments were carried out together with Nicolas Mathieu (Bruker service engineer), who also provided the frequency meter and the water-load.

Table 7.2: Power measurements performed for the most commonly used gyrotron power settings within this work. P9 was estimated with fig. 7.4c and the ratio $V_{\mathrm{Gyr,H_2O}}/V_{\mathrm{Gyr,DNP}}$.

Pn	$V_{\mathrm{Gyr,H_2O}}$ (V, H_2O load)	$V_{\mathrm{Gyr,DNP}}$ (V, DNP exp.)	$V_{\mathrm{Gyr,H_2O}}/V_{\mathrm{Gyr,DNP}}$	P (W)
P1	0.42	0.5	0.84	22
P2	0.58	0.85	0.68	29
P5	0.95	1.25	0.76	43
P7	1.05	1.5	0.7	50
P9	–	1.7	–	51 – 53

Additionally, a calorimeter that is mounted on the transmission line and allows for power monitoring during DNP measurements was calibrated. Figure 7.4c shows the mw power (P was changed by variation of the gyrotron parameters I_{gun}, I_0, V_0, and T_{cav}) measured with the water-load as a function of the corresponding voltage measured with the calorimeter $V_{\mathrm{Gyr,H_2O}}$. Unfortunately, the calorimeter showed different values for the same measurement with attached water-load ($V_{\mathrm{Gyr,H_2O}}$) and without water-load (V_{Gyr}). In order to accurately determine the power of a DNP measurement with the calibration curve shown in fig. 7.4c, V_{Gyr} must be converted into $V_{\mathrm{Gyr,H_2O}}$. Table. 7.2 displays the ratio $V_{\mathrm{Gyr,H_2O}}/V_{\mathrm{Gyr,DNP}}$ of selected gyrotron settings that are used to convert from V_{Gyr} to $V_{\mathrm{Gyr,H_2O}}$. The reason for the differences may be reflections of the mw irradiation that are absent, if the water-load is connected to the waveguide.

To ensure that all DNP measurements were performed under comparable conditions, several sets of gyrotron parameters with a different output power were employed for most of the measurements presented in this thesis. Their power and frequency dependence is depicted in fig. 7.4a and b and the output power is listed in tab. 7.2. Reported mw power levels in this thesis always refer to the mw power at the end of the waveguide (entrance of the probehead).

Access to different electron spin resonance conditions during DNP experiments was previously realized by sweeping of the main magnetic field B_0 with an additional sweep-coil,[131] however in our setup the frequency agile gyrotron facilitates this task. Figure 7.5 shows the frequency ranges at different power levels at a main current of $I_{\mathrm{main}} = 69.89\,\mathrm{A}$. The sweep range is approximately 200 MHz at each power level. This is mainly achieved by varying the temperature of the cavity T_{cav}. However, all gyrotron parameters ($I_{\mathrm{main}}, V_0, I_{\mathrm{gun}}, I_0$,

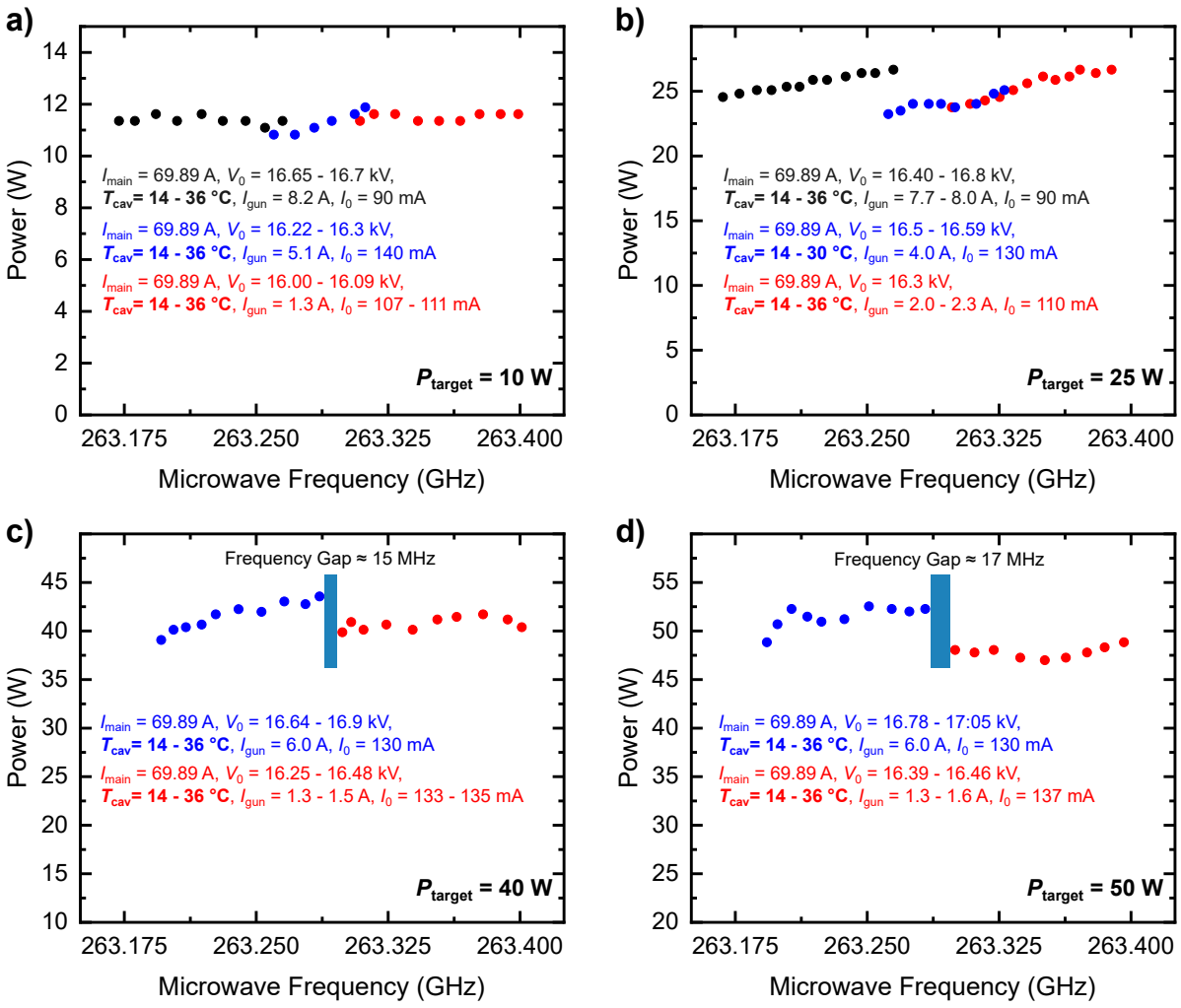

Figure 7.5: Frequency sweep by changing the cavity temperature T_{cav} at a target output power of P_{target} of a) $\sim$ 10 W, b) $\sim$ 25 W, c) $\sim$ 40 W, and d) $\sim$ 50 W. Minor variation of the collector current I_0 and the gun current I_{gun} were used to compensate for output power changes upon variation of T_{cav}. Gyrotron parameters are listed in the insets.

and T_{cav}) affect the frequency as well as the output power of the gyrotron. Unfortunately, the dependence is mostly nonlinear. For example, the gyrotron frequency may be further decreased than displayed in fig, 7.5d through changing V_0, however this comes with a significant increase in output power. The frequency and power dependency on V_0 is shown in fig. 7.4d. The maximum frequency sweep range of 500 MHz is available at a power of 10 W through variation of the main magnetic field (I_{main}).

Table 7.3: Frequency stability of the microwave at different power levels. Stability of the frequency is approximately ± 0.5 MHz during long term measurements ($t \geq 12$ h). (*) Measurement performed by the supplier CPI.

power (W)	mw frequency (t_0, GHz)	mw frequency (t_1, GHz)	$\Delta\nu$ (MHz)	Δt (h)
41	263.4014	263.4019	0.5	12.5
12	263.2946	263.2952	0.6	16.0
62	263.232	263.232*	–	336

Finally, the stability of the microwave frequency was characterized using the frequency meter. The frequency was measured at different power levels at two time points (t_0 and t_1) and the results are shown in tab. 7.3. During the course of $12 - 16$ h, the frequency varied by ± 0.5 MHz. However, during this time, the frequency was not monitored, therefore larger fluctuations cannot be excluded but appear rather unlikely. The frequency stability is thus assumed to be $\Delta\nu \approx \pm 0.5$ MHz over 12 h. Comparing this to the linewidth of the EPR line at 263 GHz ($5.5 - 8$ MHz) demonstrates that the mw frequency stability allows for long DNP measurements under microwave irradiation (measurement time ≥ 12 h).

7.1.3 The Quasi-Optical Table

As published recently,[69] a quasi optical table significantly improves the control over the microwave irradiation in liquid state DNP. The quasi-optical table (Bridge12 Technologies Inc.) is sketched in fig. 7.6.

The alignment of the components was tested with thermo-electric paper (Edmund Optics LtD.), which changes colour upon elevated temperatures (sensitivity range $T = 35 - 40\,^{\circ}$C), thanks to a liquid crystal medium that is coated on the surface of the paper. The beam shape was tested with a very low output power of the gyrotron ($I_{\text{main}} = 69.89$ A, $V_0 = 16.1$ kV, $T_{\text{cav}} = 15\,^{\circ}$C, $I_{\text{gun}} = 6.45$ A, $I_0 = 60$ mA, $P \ll 10$ W) and the alignment of the second absorber is shown in the top right inset of fig. 7.6.

The mw beam enters on the left side and proceeds through a variable grid. If the wires of a grid are aligned with the E - field of the electromagnetic wave, it will fully reflect the wave.[195] On the other hand, the beam will go through, if the grid wires are orthogonal to the E - field component (full transmission).[195] An angle in the range of $0 - 90\,^{\circ}$ will

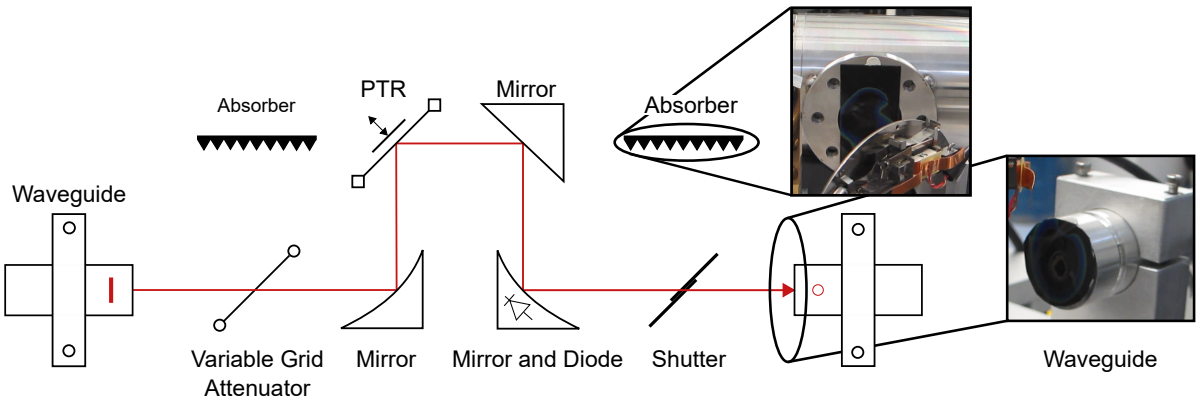

Figure 7.6: Sketch of the optical table with all components (wire grid, mirrors, polarization transforming reflector (PTR), and a shutter) and pictures of the alignment measurements at the absorber and at the end of the optical table.

partially reflect the mw beam, thereby, depending on the angle of the grid, attenuating the power of the mw beam.[195] The reflected microwave is directed into a water-cooled absorber.

After reflection from a mirror, the mw beam reaches the PTR that consists of a grid in front of a flat mirror. The distance between the grid and the mirror is variable as well as the orientation of the wire grid. Through that, this device enables the conversion from linearly to circularly polarized microwave irradiation. Moreover, it also allows for the adjustment of the polarization angle of a linearly polarized beam.[195]

A small outlet on the third mirror directs a small part ($\leq 1\,\%$) of the mw beam to a diode that monitors the power. Finally, a mechanical shutter with blades made of $AlMgF_2$ coated with a BeCu alloy (Uniblitz CS35, 35 mm aperture) was installed to gate the microwave beam. The opening time of the shutter is 3 ms and it can be triggered by a 5 V transistor-transistor logic (TTL) signal that enables implementation in routine NMR experiments. At the end of the optical table, the microwave beam re-enters the waveguide. The inset of fig. 7.6 shows that the microwave beam is still aligned with the entrance of the waveguide thereby minimizing losses.

So far, the wire grid attenuator and the PTR were not tested, because the remote control of the two components is still missing. The wire grids of the two components were therefore set to full transmission to not disturb the mw beam. The mw polarization inside the NMR magnet was therefore optimized by monitoring the ^{13}C NMR signal enhancement

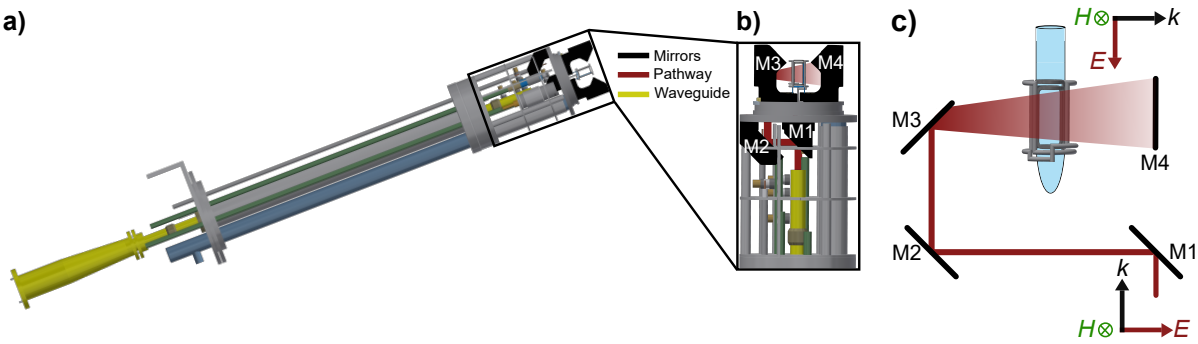

Figure 7.7: a) Drawing of the liquid state DNP probehead. At the bottom of the probehead the taper reduces the corrugated waveguide diameter from 19.3 to 7.6 mm. b) Enlarged picture of the quasi-optical mirror system of the probehead. The microwave is delivered from the side onto the sample. c) Schematic sketch of the mirror system. Mirror 3 expands the waist of the microwave beam to maximize the irradiated window on the sample. Here, k is the propagation vector of the electromagnetic wave, H indicates the magnetic field and E the electric field component, respectively.

while rotating the DNP probehead inside the NMR magnet (along the B_0 axis) until a maximum of the NMR signal was reached. The power diode is working, however power is usually monitored with the calibrated calorimeter (see fig. 7.4). Finally, the mechanical shutter is fully operational and was employed for DNP measurements in polar solvents (see sec. 7.3).

7.1.4 The Probehead

The probehead is a commercially available wide-bore liquid state Bruker NMR probehead (Z3829_0033), which was initially dedicated to an optimized NMR performance. There are two radiofrequency saddle coils, the larger one ($h = 17.2\,\text{mm}$, $d = 16.6\,\text{mm}$, $\nu \approx 380 - 400\,\text{MHz}$) is tuned to the resonance frequencies of ^{1}H or ^{19}F and the smaller one ($h = 16.3\,\text{mm}$, $d = 6.1\,\text{mm}$, $\nu \approx 100\,\text{MHz}$) to ^{13}C. The latter is also used for frequency locking and can therefore be tuned to ^{2}H.

In order to transmit the mw to the sample, the central support pillar of the probe was hollowed and a corrugated waveguide (I.D.= 7.6 mm) placed inside. At the end of the support pillar, the microwave beam propagates through open air, is guided by a three mirror system, and irradiates the sample from the side. A fourth mirror behind the sample reflects residual mw irradiation. Figure 7.7a and b show the DNP probehead including

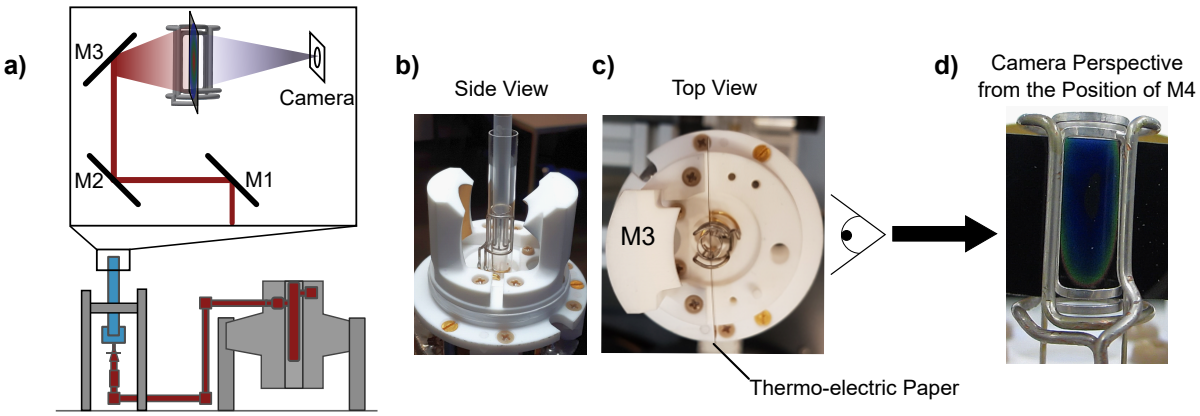

Figure 7.8: a) Sketch of the setup for the mw beam alignment tests. The probehead is mounted on an external support to enable the observation of the beam via digital camera. Side (b) and top (c) view of the mirror arrangement with the NMR coils. Quartz tubes that support the NMR coils are included in b). M4 was removed in c) and thermo-electric paper placed in the center of the NMR coils. d) Observation of the mw beam spot in the center of the NMR coils. The spot extends over the whole available irradiation window.

the taper, the waveguide, the mirror arrangement, and the NMR coils. The development of an efficient mw pathway to the sample was a collaboration with Bruker BioSpin and Thomas Keating LtD.

One key feature of the probehead is that the shape of the third mirror expands the mw beam over the whole irradiation window of the sample. Preliminary calculations, performed by Bruker, showed that the mw beam only propagates through the space between the NMR coils and is scattered by the NMR coils. Therefore, the mw beam was directed through the window of the NMR coils, to maximize the irradiation window of the sample. A sketch of the microwave propagation through the mirrors and its expansion at the third mirror is shown in fig. 7.7c.

As the microwave components were newly integrated into the probe, the shape, power and polarization of the mw beam inside the probehead were evaluated. The correct polarization of the mw beam at the sample is crucial, because only if the H-field component (with $\mu_0\mu_r H = B$, μ_0 and μ_r being the vacuum permeability and the relative permeability of the medium, respectively)[196] of the mw beam is orthogonal to the main magnetic field, it can induce electron spin transitions.[10,183]

7.1.4.1 Microwave Beam Shape

The mw beam shape at the center of the NMR coil was characterized, because the quasi-optical components were newly implemented in the probehead. For this, the probe was mounted on an external support outside the NMR magnet and a digital camera (Canon Ixus) was placed at the position of the fourth mirror (see fig 7.8). The gyrotron was connected to the probehead and operated at minimal power level ($I_{\text{main}} = 69.89\,\text{A}$, $V_0 = 16.1\,\text{kV}$, $T_{\text{cav}} = 15\,^{\circ}\text{C}$, $I_{\text{gun}} = 6.45\,\text{A}$, $I_0 = 60\,\text{mA}$, $P \ll 10\,\text{W}$). Figure 7.8d shows a picture of the thermo-electric paper (see sec. 7.1.3) in the center of the NMR coil. As expected from the design, the microwave beam is distributed over the whole available NMR coil window. Microwave beam alignment and mw polarization tests were performed in conjunction with Dr. Igor Tkach.

7.1.4.2 Microwave Beam Polarization and Power Losses

The polarization of the microwave beam at the sample position and the power losses in the probe were characterized. In order to ensure comparability to DNP measurements in the NMR magnet, it was important to verify that the mw beam polarization before M1 was comparable between the test setup (fig. 7.9a) and DNP measurements inside the NMR magnet. However, similar to the alignment test, the characterization of the mw polarization was not feasible inside the NMR magnet. Additionally, because the output power of the gyrotron was too high, a different microwave source was necessary.
The arrangement, used for the polarization tests, is displayed in fig. 7.9a. Because the microwave bridge of the 263 GHz EPR spectrometer feeds linearly polarized microwave radiation (with the same polarization as the gyrotron, stated by the manufacturer Bruker BioSpin) from the top, the probehead was mounted upside down on an external support. The probehead was then carefully aligned to guarantee the same polarization of the incident beam as in the DNP instrument.
A vectorial network analyzer (VNA, Keysight E5063A) served as a low microwave frequency source and detector of the scattering parameter S_{11} and fed mw with $\nu \approx 9.5\,\text{GHz}$ to the quasi-optical front-end of the 263 GHz spectrometer. There, mw irradiation was upconverted to 263 GHz and sent to the DNP probehead. Similarly, the reflected microwave is converted down to 9.5 GHz by the front-end of the 263 GHz EPR spectrometer

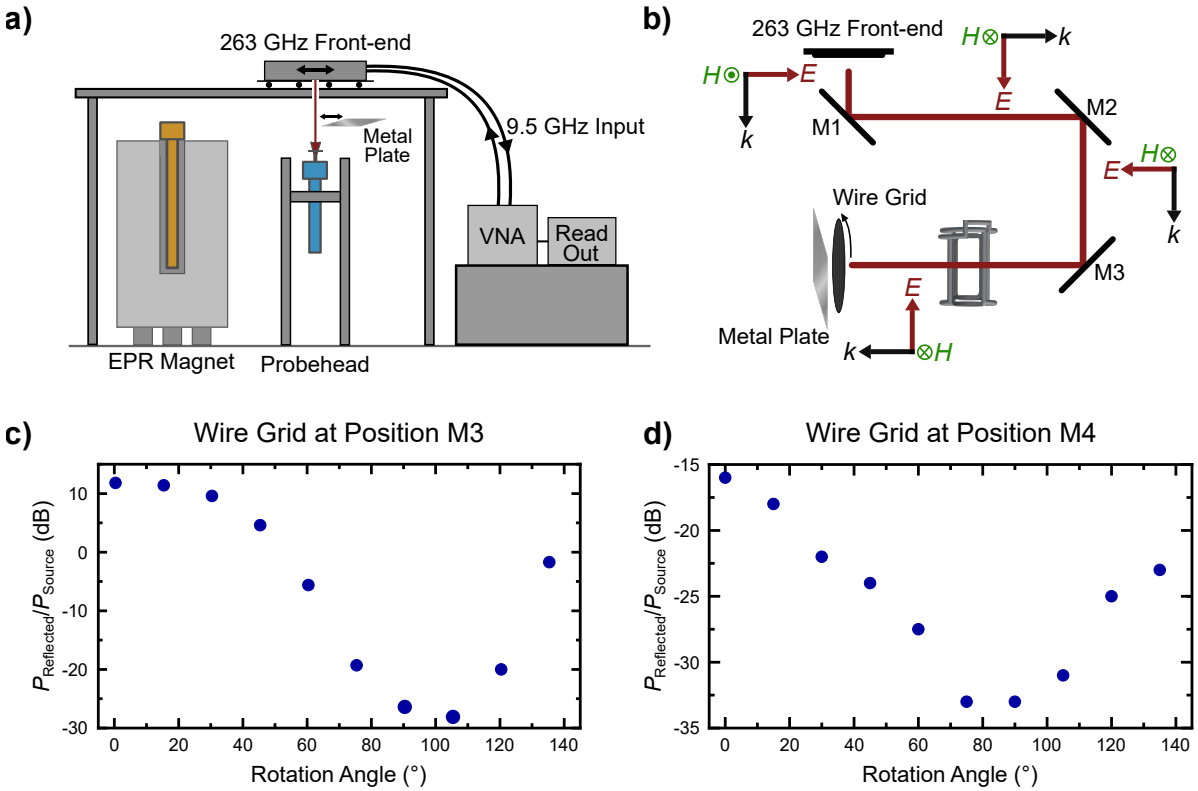

Figure 7.9: a) Sketch of the setup for the test of the polarization and power losses of the microwave in the probehead. b) Schematic representation of the microwave pathway including the mirrors. M4 is replaced by a wire grid (polarization measurement) or by a metal plate (power measurement). The same measurements were performed at position M3. Here, k is the propagation vector of the electromagnetic wave, H indicates the magnetic field and E the electric field component, respectively. c) Reflected mw power in dB as a function of the rotation angle of the wire grid at M3. d) Reflected mw power in dB as a function of the rotation angle of the wire grid at M4. 0 ° indicates that the wire grid is parallel to the E - field component of the mw beam. The difference between the measurement at M3 and M4 in reflected power arises from increased losses at M4 due to the NMR coils and the coil support quartz tubes and a possible worse alignment of the mw bridge and the probehead during the measurement at M4. This would reduce the reflected mw power but leave the mw polarization unaffected.

and detected by the VNA. The mw power was referenced to the source. Importantly, these measurements would have been impossible without the mm-band spectrometer. This highlights the benefits that the DNP setup and the EPR spectrometer operate at the same mw frequency.

Finally, either M3 or M4 were replaced by a wire grid with variable rotation angle (fig. 7.9b).

Table 7.4: Experimental one way power losses inside the probehead as measured in the setup described in fig. 7.9.

position	included components	power loss (dB)
M3	–	0.8
M4	NMR coil	2.0
M4	NMR coil and coil support quartz tubes	6.5

For the polarization test, the wire grid was rotated between 0 and 140 ° and the change in power was monitored with the VNA, with 0 ° corresponding to the grid being parallel to the E - field component of the mw beam. The measurements were performed with the NMR coil support tubes in place (see fig. 7.8b) and without sample tubes. Figure 7.9 shows the results for M3 in panel c and for M4 in d. Both measurements reveal the expected maximum at $\sim 0\,^\circ$ (full reflection) and minimum at $\sim 90\,^\circ$ (full transmission). The difference in reflected power at M3 and M4 arises from increased losses at M4 due to the NMR coils and the coil support quartz tubes (~ 13 dB two way power losses, see tab. 7.4) and a possible worse alignment of the mw bridge and the probehead during the measurement at M4. The latter would reduce the reflected mw power but leave the mw polarization unaffected. These measurements indicated that the polarization is preserved throughout the probehead and that the magnetic component is orthogonal to the axis of the sample tube.

Importantly, the orientation of the probehead, with respect to the polarization of the incoming microwave beam, was similar to DNP measurements in the NMR magnet. Therefore, the polarization of the mw beam at the sample during DNP experiments should be comparable between the polarization test arrangement (fig. 7.9a) and the DNP setup (fig. 7.2a).

Aside from the polarization, this setup also enabled the quantification of power losses in the probehead. For these measurements, the wire grid was replaced with a metal plate (full reflection) and results were compared with a reference (metal plate at the top of the waveguide entrance). The results are shown in tab. 7.4. Measurements were again performed without sample tubes. Overall, the power losses along the path from the input of the probehead to M4 are about 6.5 dB. This is reasonable, considering that the mw

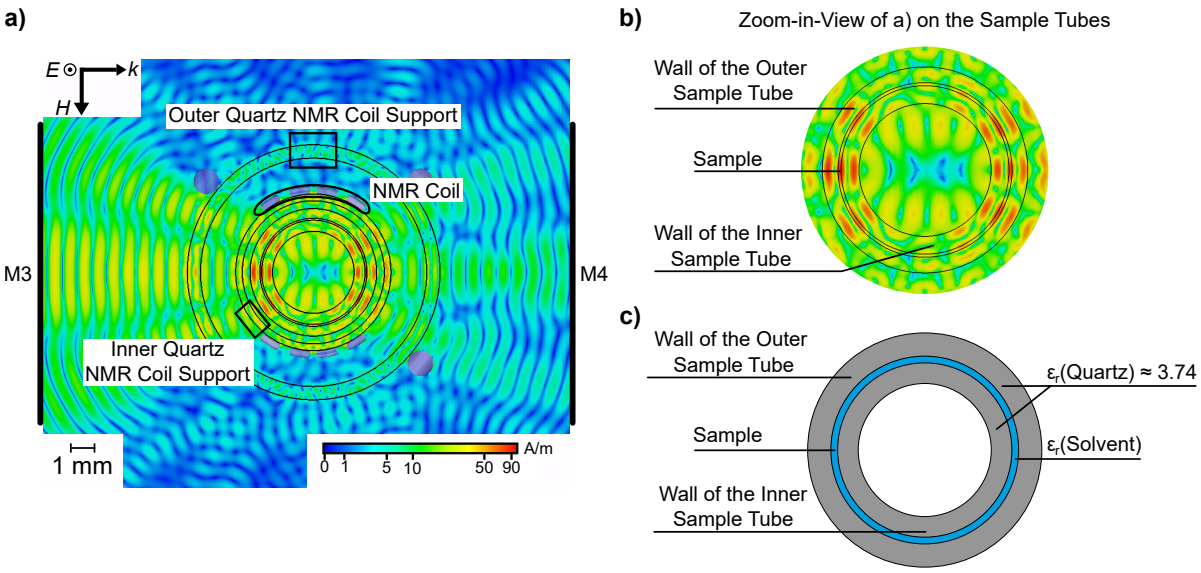

Figure 7.10: a) CST calculation of the absolute H-field distribution at the sample inside the probehead. Horizontal cross-section as sketched in fig. 7.11b. b) Zoom-in-view of a) on the sample tubes. c) Sketch of the sample tubes and the sample. For quartz a dielectric constant of $\epsilon_r(\text{quartz}) \approx 3.74$, while for CCl_4 $\epsilon_r(CCl_4) \approx 2.17$ was used (from the simulation software). A comparison of ϵ_r to the literature is drawn in the text below.

beam propagates through a four mirror system, two cylindrical quartz tubes and is partially scattered by a metal NMR coil.

7.1.4.3 Simulations of the Microwave Beam Propagation

To support the experimental results on the characterization of the probehead, the propagation of the beam along the probehad and through the sample was simulated. For this, numerical finite element simulations of the Maxwell equations were performed with CST Microwave Studio (Dassault Systemes / CST Studio Suite 2019). Simulations were executed and analyzed by Dr. Igor Tkach. Interpretation and evaluation was performed by Dr. Igor Tkach and the author. Simulation details are described in chapter 3.3.6.1. The simulations were conducted with a linearly polarized Gaussian beam (TEM_{00}-mode) at the entrance of a short waveguide, a power of 20 W and a frequency of $263.1 - 263.6$ GHz. The model included the corrugated waveguide, the four mirror system, NMR coils, support NMR coil quartz tubes, sample tubes and the solvents. The dielectric constants ϵ_r for the different materials were extracted at ~ 263 GHz with the Debye model[197]

implemented in the simulation software, being $\epsilon_r(\text{quartz}) \approx 3.74$, $\epsilon_r(CCl_4) \approx 2.17$, and $\epsilon_r(H_2O) \approx 5.37$. The dielectric constant of water at $\sim 263\,\text{GHz}$ agrees well with the literature ($\epsilon_r(H_2O) \approx 5.36$).[198,199] For quartz and CCl_4, the experimental values are reported only at 3.0 GHz ($\epsilon_r(\text{quartz}) \approx 3.82$ and $\epsilon_r(CCl_4) \approx 2$)[200,201] and agree with the estimated ones at $\sim 263\,\text{GHz}$ assuming a small frequency dependence.

Figure 7.10a shows a cross-section of the simulated H - field distribution on the sample. The two NMR coil support quartz tubes, the NMR coils, the sample tubes, and the sample are included in the calculation. A zoom-in-view on the on the sample tubes and the sample is shown together with a sketch for visual aid in fig. 7.10b and fig. 7.10c, respectively. Sample tube sizes and layer thicknesses of the sample are listed in tab. 7.5.

Several distinct maxima are obtained for the H - field component on the sample. Specifically, maxima of the H - field component of the mw beam are observed at areas close to a transition between components with different dielectric constant (ϵ_r).

One reason for the observed maxima of the H - field component may be that, due to a larger ϵ_r, the wavelength λ in quartz is decreased in comparison to air (or a solvent with smaller ϵ_r).[183,202] This increases the energy density of the mw, and thus the field strength of the H - component.[183] However, because the walls of the sample quartz tubes are smaller than λ ($\lambda \approx 1.1\,\text{mm}$ at 263 GHz), being $\sim 0.38\,\text{mm}$ and $0.5 \pm 0.2\,\text{mm}$ for the outer and inner sample tube, respectively (Wilmad Labglass and Hilgenberg GmbH), and the sample layer ($d \approx 25 - 75\,\mu\text{m}$) is smaller than $\lambda/4$, the energy density is also increased in areas close to the quartz tubes.[183,202] Furthermore, the reflectivity $R_0 = \left|\frac{n_1 - n_2}{n_1 + n_2}\right|^2$ (Fresnel law for the case of normal incidence with the refraction index $n = \sqrt{\mu_r \epsilon_r}$)[202] at the interface between materials of different ϵ_r depends on the difference of the two dielectric constants $\Delta\epsilon_r$ with a larger $\Delta\epsilon_r$ leading to a larger R_0. This causes a standing-wave-ratio ≥ 1 that leads to an enhancement of the microwave field strength.[202] A similar effect was observed upon addition of dielectric particles into a solid-state DNP sample, where the electromagnetic field confinement happened at the interface of the particles.[203]

In this work, the sample is restricted to a thin layer between two quartz tubes, therefore it is inherently confined to an area, where the microwave field is enhanced possibly by a combination of the aforementioned reasons.

The calculations also revealed that the microwave field is not homogeneous over the whole sample. Figure 7.11d showcases the B_{1e} distribution along the z axis for CCl_4 with

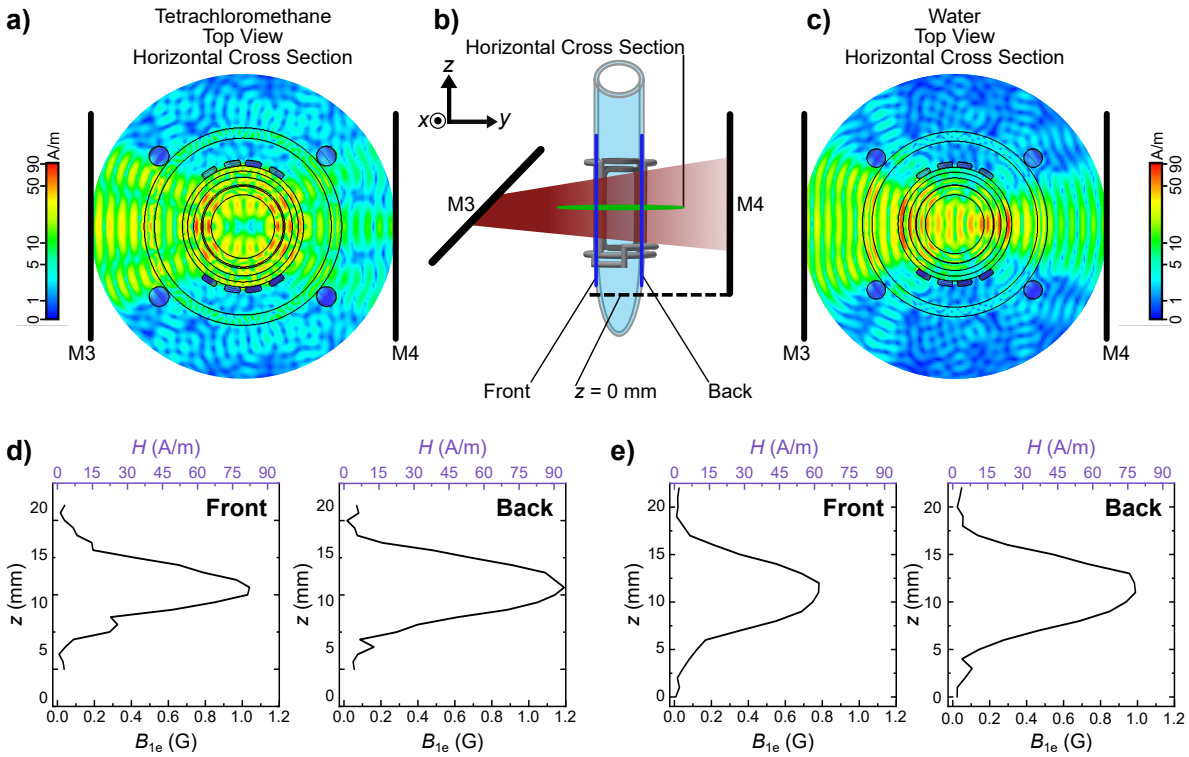

Figure 7.11: Horizontal cross-section of the calculated H-field distribution in the sample using (a) CCl_4 and (c) H_2O as a solvent, respectively. Sample layer thickness was $\sim 75\,\mu m$ and $\sim 25\,\mu m$ for CCl_4 and H_2O, respectively. b) Sketch of the mw pathway. H-field cross-section for the field pattern in a) and c) are indicated in green, while axes for the B_{1e} evaluation are indicated in dark blue. d) and e) display the B_{1e} distribution along the z axis at the position of the sample for CCl_4 and H_2O, respectively. For a better comparison with the experimental data, H and B can be interconverted using $\mu_0\mu_r H = B$,[196] because in MR the microwave field strength is usually expressed in units of Tesla (or Gauß). The y axis in d) and e) is referenced to the bottom of the fourth mirror as indicated in b).

B_{1e} roughly showing a Gaussian distribution along the z axis and a clear maximum of $B_{1e} \approx 1.2\,G$ at the center of the NMR coil around 11 mm (referenced to the bottom of fourth mirror, see fig. 7.11). Interestingly, the maximum at the front (see fig. 7.11d) is smaller than at the back, which might be counter-intuitive, because at the front the mw beam did not yet pass through the sample. However, even though no standing wave is observed, reflected mw irradiation from M4 might create interferences that seem to add up to an overall increased effective microwave field.

Figure 7.11 also shows the microwave propagation simulated for CCl_4 and H_2O. The

sample layers were chosen to stay significantly below the penetration depth of the solvents to enable optimized mw penetration of the sample and to reduce sample heating induced by mw absorption of the solvent. The penetration depth of the mw irradiation is $\sim 100\,\mu m$ and $\sim 500 - 700\,\mu m$ for H_2O and $CHCl_3$ at $\sim 263\,GHz$, respectively.[196,204] Due to its non-polar nature, the penetration depth of CCl_4 should be even larger than for $CHCl_3$. The comparison reveals a different microwave field distribution within the xy plane. Additionally, as shown in fig. 7.11d and fig. 7.11e, the difference in B_{1e} between CCl_4 and water is less pronounced as expected, with the maximum B_{1e} being $\sim 1.2\,G$ and $\sim 1.0\,G$ for CCl_4 and H_2O, respectively. Reasons for this might be the different sample layer thickness ($d \approx 75\,\mu m$ for CCl_4 and $\sim 25\,\mu m$ for H_2O) and the different dielectric constants ($\epsilon_r(CCl_4) \approx 2$ and $\epsilon_r(H_2O) \approx 80.4$ at 3.0 GHz) of the two solvents.[201]

7.1.5 Evaluation and Comparison of B_{1e} with the Literature

As in the herein presented setup no standing wave is created and B_{1e} is inhomogeneously distributed over the whole sample, an effective microwave field B_{1e} cannot be uniquely defined. Still, from DNP measurements, an "average" B_{1e} field may be estimated with the saturation factor and compared with CST calculations and the literature.
From the measured NMR signal enhancement in neat CCl_4 ($\epsilon \approx 135$, see fig. C.10) and data from the literature ($\xi \approx -0.17$, $f \approx 0.9 - 1$),[34] the saturation factor was calculated with the Overhauser equation (eq. 2.17) resulting in $s \approx 0.3 - 0.4$. Through combination of s with electron spin relaxation data ($T_{1e} \approx 280 - 500\,ns$, $T_{2e} \approx 13 - 25\,ns$, see chapter 6, $K_X \approx 2.5\,GHz\,mol^{-1}$[60]) and utilizing eq. 2.56, a microwave field strength of $B_{1e} \approx 0.5 - 1.0\,G$ was obtained. This value agrees well with the calculations in sec. 7.1.4.3, which predict a maximum $B_{1e} \approx 1.2\,G$ with a broad distribution over the whole sample. However, as already pointed out, a quantitative comparison of the two remains difficult, because the experimental B_{1e} originates from an NMR measurement that detects more nuclear spins compared to the nuclear spins which are exposed to the mw irradiation.
Other non-resonant setups report B_{1e} values on the order of $1.3 - 2.8\,G$.[61,68] Yet, their reported enhancement is smaller, which may be attributed to a limited irradiation time with a sample volume (100 µL) that could lead to a sample layer that significantly exceeds the penetration depth of the solvent.[61] As expected from DNP instruments with a mw

cavity, large B_{1e} values were reported for a Fabry-Pérot and a helical resonator with $B_{1e} \approx 4.5\,\mathrm{G}$ and $B_{1e} \approx 3.5\,\mathrm{G}$, respectively.[55,112] Interestingly, the helical mw resonator reaches a saturation factor of $s \approx 0.9$ with $B_{1e} \approx 1.4\,\mathrm{G}$ (100 mW with $0.45\,\frac{\mathrm{mT}}{\sqrt{\mathrm{W}}}$ as a conversion factor).[55] A comparison of this with the $B_{1e} \approx 0.5 - 1.0\,\mathrm{G}$ of the herein presented DNP instrument indicates that even small improvements on the mw irradiation efficiency can significantly boost the signal enhancement. This is also consistent with the theory, which predicts a steep increase of s upon small changes in B_{1e} in the range of $s \approx 0.2 - 0.8$ (see fig. 2.6).

7.1.6 Sample Volume and Geometrical Arrangement

The DNP probehead accommodates sample tubes with an outer diameter (O.D) of up to 5 mm. Due to sample heating caused by mw absorption of the solvent (see sec. 7.3), the solution is confined to a thin layer created by the insertion of a smaller tube (Hilgenberg GmbH, see tab. 7.5) into a larger 5 mm outer tube (O.D.= 4.936 ± 0.0065 mm and I.D.= 4.2065 ± 0.065 mm, Wilmad Labglass). To account for different penetration depths of the solvents, the layer thickness of the sample was adjusted by selecting tubes with different O.D. as inner tubes. A list of the layer thicknesses and sample volumes is given in tab. 7.5 and the sample arrangement is sketched in fig. 7.12a.

To reach the best magnetic field homogeneity and maximum saturation of the EPR resonance during DNP, the sample volume was optimized. To this end, DNP measurements of the same sample composition but with different sample heights (h) were performed. Figure 7.12b shows the DNP spectra collected with a mw power of $P \approx 43\,\mathrm{W}$ (P5) for different h of ~ 500 mM $^{13}CHCl_3$ in CCl_4 doped with ~ 25 mM ^{15}N-TN-d_{16} using a sample layer thickness of $d \approx 75\,\mu\mathrm{m}$. Comparing the sample height with the NMR coil (17.2 mm) reveals that the best linewidth and maximum signal enhancement is obtained with a sample height that exceeds the size of the NMR coil by almost a factor of two. Measurements with a sample height lower than the NMR coil show significant line distortions, while a larger sample height appears to have no influence on the signal. The lineshape distortions observed under DNP are invisible in the Boltzmann spectra (see appendix C fig. C.1) and likely a result of an increased temperature gradient in the sample caused by low sample volume or worse heat dissipation.

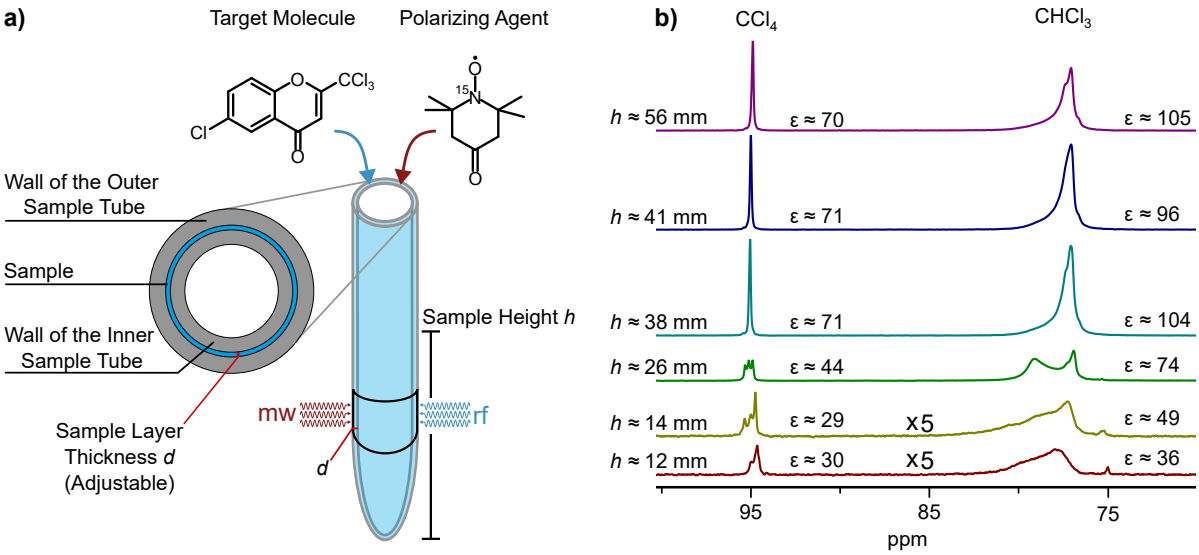

Figure 7.12: a) Sketch of a typical DNP sample. The sample is restricted to a thin layer between two concentric quartz tubes. b) DNP spectra of $\sim 500\,\text{mM}$ $^{13}CHCl_3$ in CCl_4 doped with $\sim 25\,\text{mM}$ ^{15}N-TN-d_{16} with different sample heights h using a layer thickness of $d \approx 75\,\mu\text{m}$. Microwave power (cw irradiation): $P = 43\,\text{W}$ (P5). NMR parameters (pulse sequence: zgig see fig. 3.4c): pulse length $t_p\,(\pi/2) = 10\,\mu\text{s}$, $P\,(\pi/2) = 43\,\text{W}$, NS = 8, Dummy Scans (DS) = 2, relaxation delay (RD) = 30 s, line broadening (LB) = 2 Hz (refers to exponential line broadening applied during processing of the spectrum), ^{1}H decoupling: waltz64, 0.58 W. Notably, the reported ϵ are smaller than in fig. 7.13, because experiments were performed at lower mw power ($P = 43\,\text{W}$) than in fig. 7.13 ($P = 51 - 53\,\text{W}$). Furthermore, here $c(^{13}CHCl_3) \approx 500\,\text{mM}$ and $c(^{15}\text{N-TN-d}_{16}) \approx 25\,\text{mM}$ was used, while in fig. 7.13 experiments were performed with $c(^{13}CHCl_3) \approx 200\,\text{mM}$ and $c(^{15}\text{N-TN-d}_{16}) \approx 10\,\text{mM}$.

The best signal enhancement and linewidth is obtained with a sample height of $\sim 40 - 45\,\text{mm}$ and a sample volume of $V_{\text{sample}} \approx 15 - 40\,\mu\text{L}$ depending on the thickness of the sample layer (see tab. 7.5). Notably, the sample volume that is directly irradiated by the mw beam is less ($V_{\text{irradiated}} \lesssim 15\,\mu\text{L}$), because the coil height is limited to $h \approx 17\,\text{mm}$. The sample preparation, in practice, requires $V \approx 60\,\mu\text{L}$ to account for the space on the bottom of the tube and losses on the walls.

Furthermore, tab. 7.5 reports the sample volume of a full tube calculated with the same filling height ($h \approx 40 - 45\,\text{mm}$). As the volume of a full tube is ~ 15 times larger than for a DNP sample, the NMR sensitivity under DNP exceeds the one of a full tube with similar sample composition and with the same pulse sequence as soon as an NMR signal

Table 7.5: Calculated sample volume and layer thickness for samples prepared with inner tubes of different O.D. as well as the corresponding suitable solvents for DNP measurements. Calculated sample volumes V_{sample} with $h \approx 40 - 45$ mm. Measurements conducted in this thesis were performed with outer tubes with O.D.$= 4.936 \pm 0.0065$ mm and I.D.$= 4.2065 \pm 0.065$ mm (Wilmad Labglass 528(535)-PP-7QTZ). Inner tubes were specifically manufactured for this project by Hilgenberg GmbH.

O.D (mm)	V_{sample} (µL)	layer thickness d (µm)	solvents
4.059	~ 40	~ 75	CCl_4, C_6H_6, C_6H_{12}
4.066	~ 40	~ 75	CCl_4, C_6H_6, C_6H_{12}
4.127	~ 20	~ 40	$CHCl_3$
4.158	~ 15	~ 25	CH_2Cl_2, CH_3CN, H_2O
full tube	~ 590	–	–

enhancement of $\epsilon \approx 15 - 20$ is reached. However, in cases where the amount of sample is limited,[205,206] small sample volumes are required and therefore DNP becomes useful even if the signal enhancements are smaller.

To reduce the influence of inhomogeneous mw irradiation of the sample, the tube spins with a frequency of 20 Hz around the B_0 axis. Rotation of the sample has previously been employed to improve the magnetic field homogeneity in commercial NMR and is therefore a very common feature of liquid state probeheads. Additionally, the sample is actively cooled with cold nitrogen gas that is directed through a liquid nitrogen bath (dewar from Cryogen Diffusion L2025, 25 L capacity). The sample temperature was carefully calibrated before performing DNP experiments (see sec. 7.3).

All DNP samples were prepared in a glove box (N_2 atmosphere, $O_2 \leq 0.1$ ppm, $H_2O \leq$ 0.1 ppm, MBraun). Usually, a solution of the PA and the target molecule was degassed together in the large outer tube by freeze pump thaw cycles (5 times at $p \approx 5 \times 10^{-5}$ mbar) and then transferred into a glove box. The inner tube was inserted and closed with a home-built gas-tight cap (see. sec. 3.1.1).

7.2 DNP in Non-Polar Solvents

In this section, first the signal enhancements of CCl_4 and $CHCl_3$ are presented and compared with the literature. The more exhaustive comparison with the literature also

includes diethylmalonate, ethylacetoacetate, and indole. Subsequently, the linewidth at 50 % peak intensity (LW) of the NMR signals under DNP is compared to Bruker test samples and to the literature.
Furthermore, to gain an understanding of the DNP efficiency at high magnetic field of different substrates and functional groups, the scope of target molecules is extended to halogenated compounds, a variety of functionalized aromatics, cyclic aliphatics, and esters. Examples with large signal enhancements and narrow linewidth are presented.
Several structural motifs that display large enhancements were identified and their possible DNP mechanisms are subsequently discussed. Based on these new insights, promising biologically active target molecules (drugs, pesticides and a protein inhibitor) were selected and DNP results of these compounds are presented in the last part of this section.
The report of ^{1}H signal enhancement is omitted, because this setup is dedicated to ^{13}C and initial tests produced insignificant ^{1}H signal enhancements ($\epsilon \approx -5 - 1$). Dr. Luming Yang is acknowledged for significant contributions to the measurements presented in sec 7.2.1-7.4.3. If not noted otherwise, spectra were referenced to the respective solvent peak.[207,208] Pulse acquire experiments are abbreviated by zg, pulse acquire power gating experiments by zgpg, pulse acquire inverse gating experiments by zgig, and pulse acquire gated decoupling by zggd. In pulse sequences, black bars in the pulse sequences indicate a $\pi/2$ pulse and empty bars resemble π pulses. Signal assignment is performed in the figures. Red letters indicate enhanced signals and black letters refer to signals that do not benefit from mw irradiation. The recycle delay (RD) during NMR experiments was $\sim 5 \cdot T_{1n}$. If not noted otherwise DNP and Boltzmann spectra were acquired with the same pulse sequence. All measurements used ^{15}N-TN-d_{16} as a PA.

7.2.1 Evaluation of the Signal Enhancement of Model Systems

Initial DNP experiments were performed on model systems that were previously investigated by our group. The model sample consisted of chloroform ($\sim$ 200 mM ^{13}C enriched) in tetrachloromethane (solvent, natural abundance) with $\sim$ 10 mM ^{15}N-TN-d_{16} as a PA. CCl_4 and $CHCl_3$ have been previously studied at high magnetic field.[34] Measurements were performed on a sample volume of $V_{sample} \approx 40\,\mu L$ with a layer thickness of $d \approx 75\,\mu m$. Figure 7.13e shows a ^{13}C NMR signal enhancement of $\epsilon \approx 120$ and $\epsilon \approx 200$ for $^{13}CCl_4$

and $^{13}CHCl_3$, respectively. Experimental details are given in the caption of the figure. During DNP experiments, cw mw irradiation caused sample heating and was compensated by active cooling with cold N_2 gas. The maximum of the EPR resonance was reached by

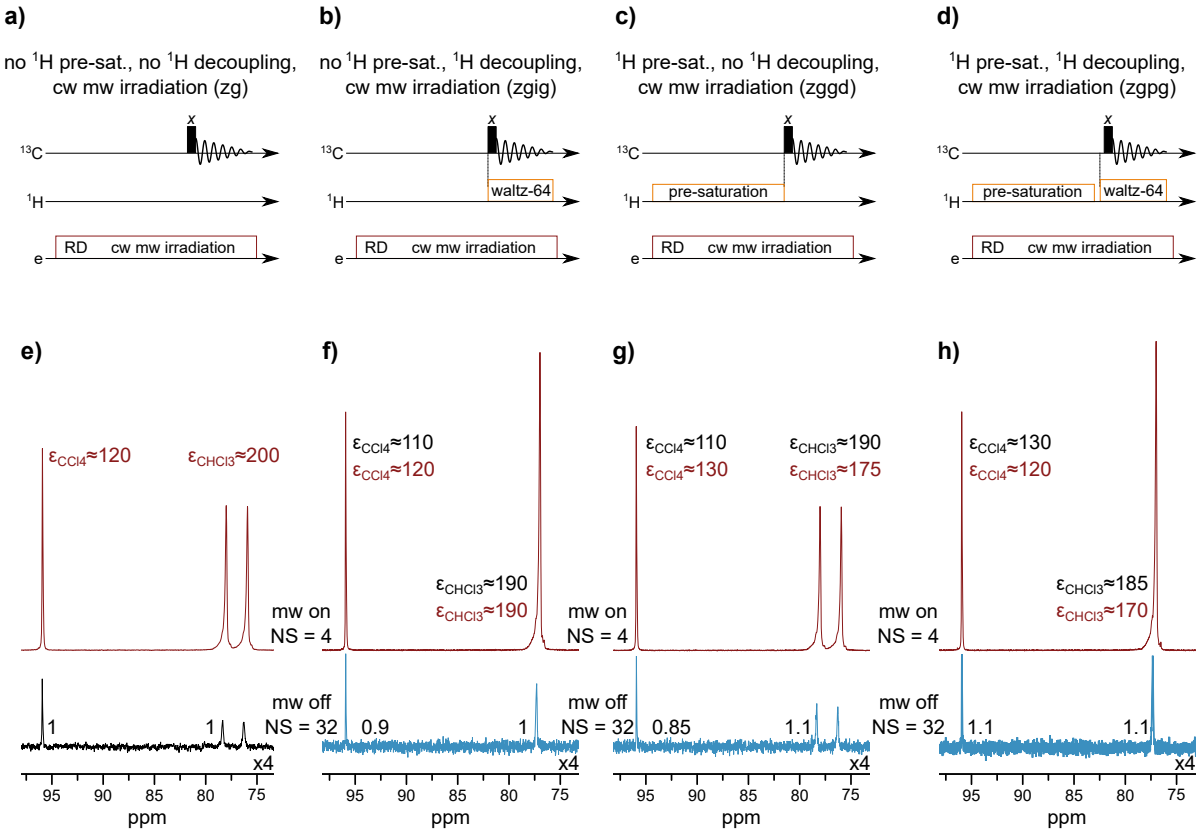

Figure 7.13: Pulse sequence of a) a pulse acquire (zg), b) a pulse acquire inverse gated (zgig), c) a pulse acquire gated decoupling (zggd), and d) a pulse acquire power gating experiment (zgpg). ^{1}H pre-saturation was applied in zggd and zgpg. The small delays in between pre-saturation and waltz-64 decoupling in the zgpg experiment are due to power switching. Enhanced and Boltzmann spectrum of $\sim 200\,\text{mM}$ $^{13}CHCl_3$ in CCl_4 doped with 10 mM ^{15}N-TN-d_{16} collected with the pulse sequences shown in the same column, i.e. e) with zg, f) with zgig, g) with zggd, and g) with zgpg. Note, black enhancements were obtained by comparing the enhanced spectrum to the Boltzmann spectrum of the zg experiment, while red enhancements were obtained by comparing to the Boltzmann spectrum acquired with the same pulse sequence. Boltzmann spectra were normalized to the zg spectrum shown in black. Experimental error for ϵ is estimated to be $10-20\,\%$. Microwave power (cw irradiation): $P = 51\,\text{W}$ (P9). NMR parameters: $t_p\,(\pi/2) = 10\,\mu\text{s}$, $P\,(\pi/2) = 41\,\text{W}$, DS = 2, RD = 30 s, LB = 2 Hz, ^{1}H decoupling: waltz64, 0.58 W, and ^{1}H pre-saturation (zggd and zgpg) with 0.29 W.

Table 7.6: Comparison of the ^{13}C NMR signal enhancement of $^{13}C_6$-BrC_6H_5, $^{13}C_6$-C_6H_5I, and diethylmalonate doped with ^{15}N-TN-d_{16} obtained with and without ^1H pre-saturation during mw irradiation. Importantly, reported signal enhancement were obtained from DNP and Boltzmann spectra collected with the same pulse sequence. Here, [^1H] indicates the apparent signal enhancements obtained with ^1H pre-saturation during DNP and Boltzmann measurement. The term apparent highlights to the fact that signal enhancements were obtained from Boltzmann spectra with ^1H pre-saturation. Experimental parameters are listed in the appendix C (tab. C.5 and tab. C.4). Spectra are shown in fig. C.3, fig. C.4, fig. 7.14b, and fig. C.9b. Experimental error for ϵ is estimated to be $10-20\,\%$.

target	$\epsilon(C_{ipso})$ [^1H]	$\epsilon(C_{ipso})$	$\epsilon(C_{o,m})$ [^1H]	$\epsilon(C_{o,m})$	$\epsilon(C_p)$ [^1H]	$\epsilon(C_p)$
$^{13}C_6$-BrC_6H_5Br	4	3	6	10	6	9
$^{13}C_6$-C_6H_5I	21	25	5	9	5	9
target	$\epsilon(C_A)$ [^1H]	$\epsilon(C_A)$	$\epsilon(C_B)$ [^1H]	$\epsilon(C_B)$	$\epsilon(C_D)$ [^1H]	$\epsilon(C_D)$
diethylmalonate	2	5	4	9	5	10

sweeping the NMR magnetic field, which is possible in a range of $\sim 2.2\,mT$ (see sec. 7.3.2). In order to reach the best signal enhancement, the mw power was gradually raised until no further increase in NMR signal intensity was observed. Notably, as $s \approx 0.3-0.4$ (see sec. 7.1.5), no saturation of the EPR resonance was reached. The observed plateau in NMR signal intensity was attributed to an increased temperature gradient of the sample. The uncertainty of the signal enhancement for all 1D measurements is estimated to be $10-20\,\%$ and this is indicated by the notation $\epsilon \approx n$ in this thesis. The uncertainty mainly arises from the sample temperature and the signal to noise ratio of the Boltzmann spectrum.

In routine NMR experiments, ^1H pre-saturation and decoupling are applied to increase the signal intensity of ^{13}C signals. In particular, ^{13}C signals benefit from ^1H-^{13}C NOE through ^1H pre-saturation by up to a theoretical maximum of $\eta = 3$ in the fast motion regime.[10] Furthermore, at low magnetic field a study reported the suppression of a three-spin effect by ^1H decoupling.[89]

In order to test the influence of ^1H pre-saturation and decoupling on the signal, DNP experiments were performed on the same sample with four different pulse sequences. Figures 7.13a-d show the zg, zgig, zggd, and the zgpg pulse sequence, while figs. 7.13e-h report the DNP and Boltzmann spectra obtained using these pulse sequences. Importantly,

the enhancements reported in black were obtained by comparing the enhanced spectrum (red) to the Boltzmann spectrum acquired with the zg pulse sequence (black, no ^{1}H pre-saturation). Enhancements listed in red were obtained by comparison of the enhanced spectrum with the Boltzmann spectrum of the same sequence (blue). Through comparison of the enhanced spectra to the Boltzmann spectrum obtained with the zg sequence, it is evident that the overall signal intensity of the DNP spectra is independent on the pulse sequence, because similar ^{13}C NMR signal enhancements for all sequences ($\epsilon_{CCl4} \approx 110 - 130$ and $\epsilon_{CHCl3} \approx 200 - 185$, see fig. 7.13e-f) were obtained.
The situation changes slightly if the DNP spectra are compared to Boltzmann spectra of the same pulse. Indeed, pulse sequences that utilize ^{1}H pre-saturation (zggd fig. 7.13g and zgpg fig. 7.13h) show a by $\sim 10\,\%$ reduced signal enhancement of $CHCl_3$ ($\epsilon_{CHCl3} \approx 170$) if the Boltzmann spectrum of the same sequence is considered. The reason for this is the different signal intensity of the Boltzmann signals obtained with different pulse sequences. The Boltzmann signals of $CHCl_3$ in fig. 7.13g (zggd) and fig. 7.13f (zgpg) are $\sim 10\,\%$ larger than in fig. 7.13e (zg), which is attributed to a ^{1}H-^{13}C NOE induced by ^{1}H pre-saturation. This is consistent with a recent report at 14 T, where a difference of $\sim 20\,\%$ of the Boltzmann spectra obtained with and without ^{1}H pre-saturation was observed.[41]
Even though the experimental error of the NMR signal enhancement is $10 - 20\,\%$, the difference of $\sim 10\,\%$ is important to demonstrate that the overall signal intensity of the DNP spectra is independent on ^{1}H pre-saturation. This also rules out a possible three-spin effect (see sec. 2.6), which is consistent with results at low field at high PA concentration ($c(\mathrm{PA}) \gtrsim 10\,\mathrm{mM}$)[89]
Additionally, the influence of ^{1}H pre-saturation on the Boltzmann spectra becomes more evident if other representative target molecules such as $^{13}C_6$-BrC_6H_5, $^{13}C_6$-C_6H_5I, and diethylmalonate are considered (spectra are shown in fig. C.3, fig. C.4, fig. 7.14b, and fig. C.9b). The ^{13}C signal enhancements of these compounds are listed in tab. 7.6. Notably, the reported apparent enhancements were obtained from DNP and Boltzmann spectra of the same pulse sequence. The terms apparent and formal are used to clarify that here the signal enhancement was obtained from a comparison of a DNP spectrum to a Boltzmann spectra acquired with ^{1}H pre-saturation (see tab. 7.6). The apparent ^{13}C NMR signal enhancements are $\sim 10 - 60\,\%$ smaller than ϵ obtained without ^{1}H pre-saturation. This

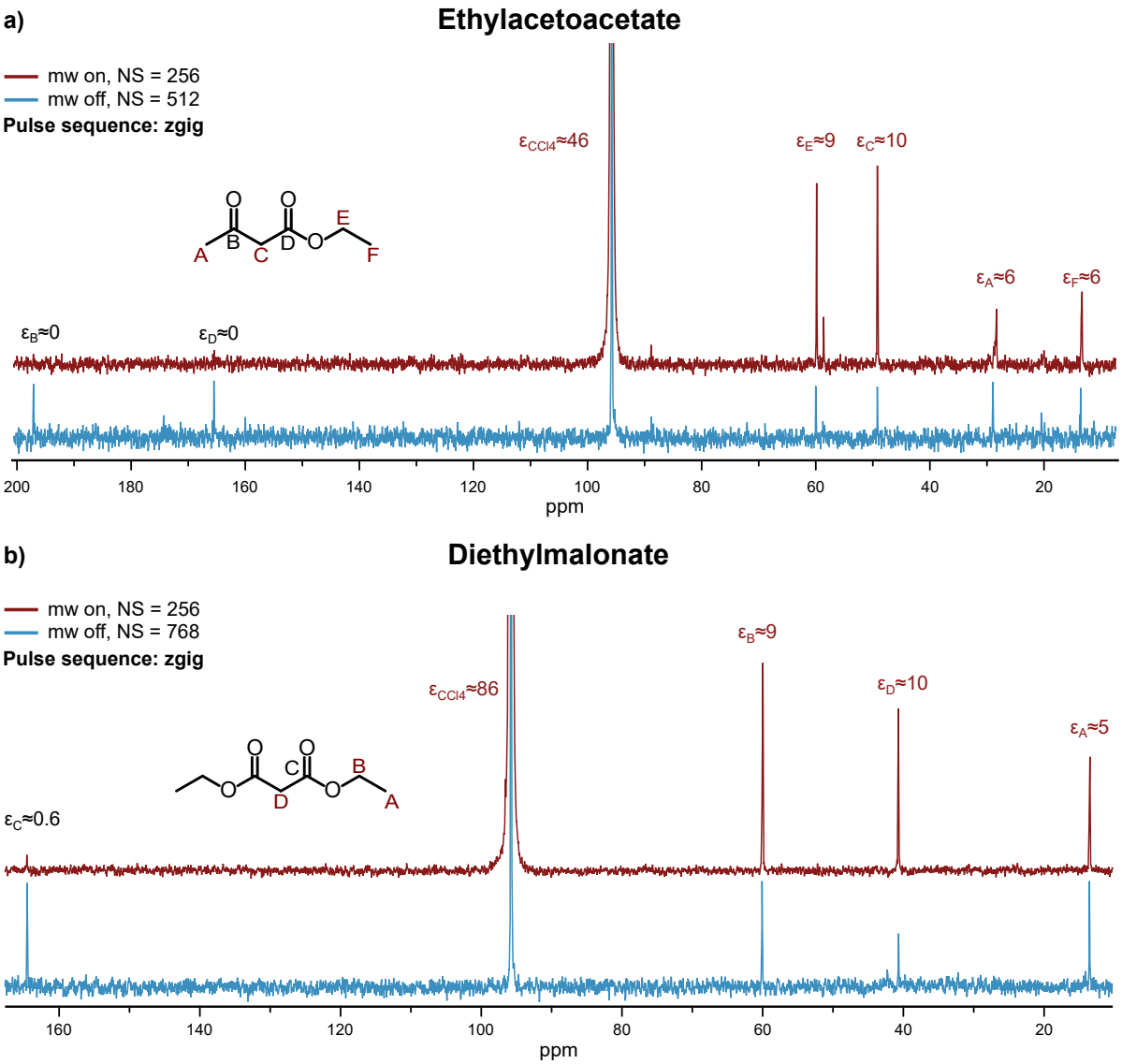

Figure 7.14: ^{13}C NMR spectra of $\sim$ 500 mM a) ethylacetoacetate and b) diethylmalonate with (red) and without (blue) mw irradiation. Concentration of ^{15}N-TN-d$_{16}$ was $\sim$ 25 mM. Experimental error for ϵ is estimated to be 10 – 20 %. Microwave power (cw irradiation): P = 43 W (P5). NMR parameters (pulse sequence: zgig): t_p ($\pi/2$) = 10 µs, P ($\pi/2$) = 41 W, DS = 2, RD = 30 s, LB = 4 Hz, ^{1}H decoupling: waltz64, 0.58 W. Boltzmann and DNP spectra were acquired with the same pulse sequence.

is caused by a stronger ^{1}H-^{13}C NOE of $^{13}C_6$-BrC_6H_5, $^{13}C_6$-C_6H_5I, and diethylmalonate compared to $CHCl_3$.

A molecule dependent efficiency of ^{1}H-^{13}C NOE can be rationalized considering the different relaxation pathways of the ^{13}C nuclei. In presence of a paramagnetic substance (here the PA), the nuclear relaxation time is reduced, because the electron spin acts as an additional relaxation pathway for the nuclear spin.[10,41] This reduces the contribution of other relaxation pathways such as ^{1}H-^{13}C NOE.[10,41] However, the interaction between the electron spin and the nuclear spin is molecule dependent, which explains the observed differences of the formal signal enhancements in tab. 7.6.

To properly relate the signal enhancement to the signal intensity of the DNP spectrum and to ensure comparability with the literature (ref. [41] is the first study to apply ^{1}H pre-saturation on more than one target molecule), unless noted otherwise DNP and Boltzmann experiments in this work are always performed without ^{1}H pre-saturation.

To date, only our previous study reported ^{13}C signal enhancements at 9.4 T on the model systems CCl_4 and $CHCl_3$.[34] In a cylindrical cavity with a sample volume of 35 nL and $c(\mathrm{PA}) \approx 100\,\mathrm{mM}$, we observed an enhancement of $\epsilon \approx 430$ and $\epsilon \approx 320$ for CCl_4 and $CHCl_3$, respectively.[34] The cavity arrangement enabled $s \approx 1$ with $c(\mathrm{PA}) \approx 100\,\mathrm{mM}$ and therefore large ϵ. The same study also reported NMR signal enhancements for diethylmalonate ($\epsilon \approx 30$) and ethylacetoacetate ($\epsilon \approx 13 - 18$). In these measurements, the target molecule served as the solvent with a PA concentration of $c(\mathrm{PA}) \approx 100\,\mathrm{mM}$.[34] A more recent study utilized the same cavity and reported $|\epsilon| \approx 2 - 25$ at 9.4 T for 2 M indole in CCl_4 with $c(\mathrm{PA}) \approx 100\,\mathrm{mM}$.[33]

Given the difference in saturation factor between this work ($s \approx 0.3 - 0.4$, see sec. 7.1.5) and our previous work ($s \approx 1$),[34] the observed ^{13}C signal enhancements for CCl_4 ($\epsilon \approx 120$) and $CHCl_3$ ($\epsilon \approx 200$) agree with the literature. Furthermore, fig. 7.14 reports the signal enhancement for $\sim 500\,\mathrm{mM}$ natural abundance ethylacetoacetate ($\epsilon(C_{2,4}) \approx 7 - 10$) and diethylmalonate ($\epsilon(C_2) \approx 10$) measured with $c(\mathrm{PA}) \approx 25\,\mathrm{mM}$ and fig. 7.15 the enhancement of 2 M indole with $c(\mathrm{PA}) \approx 100\,\mathrm{mM}$ in CCl_4 ($\epsilon \approx 0 - 7$). The sample composition of indole was chosen for comparison with the literature[33] and a second sample with 500 mM indole and 25 mM PA in CCl_4 displayed ^{13}C enhancements of $|\epsilon| \approx 0 - 5$ (see appendix C fig. C.18). Similar to the results obtained for CCl_4 and $CHCl_3$, the signal enhancements of diethylmalonate, ethylacetoacetate, and indole agree with the literature after rescaling with s.[16,33]

Notably, due to low sensitivity, all reports in the literature were obtained with ^{13}C

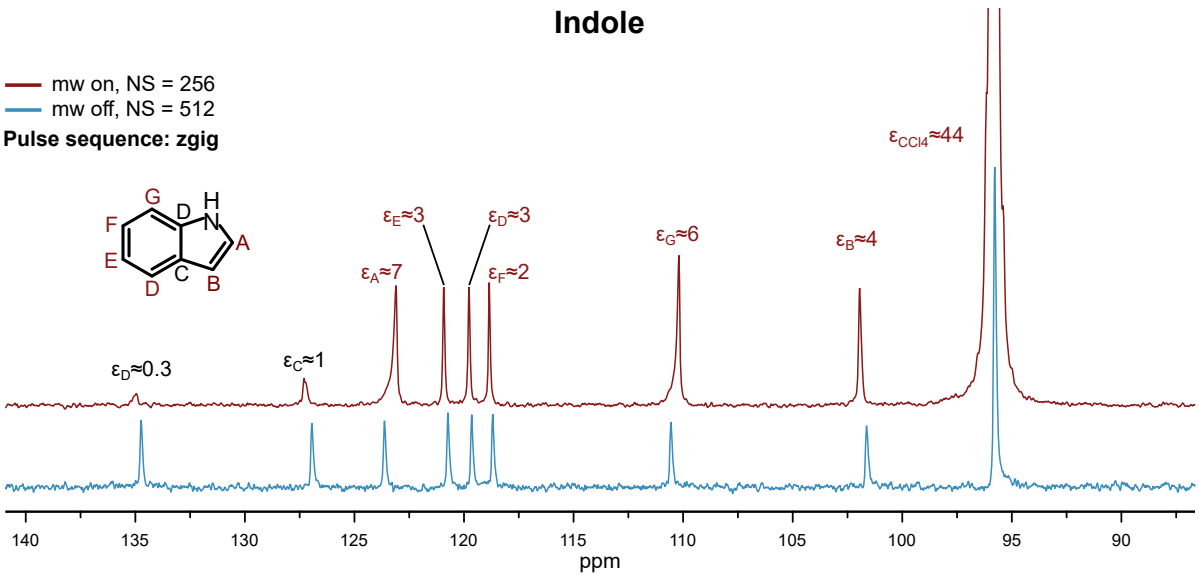

Figure 7.15: ^{13}C NMR spectra of 2 M with (red) and without (blue) mw irradiation. doped with $\sim$ 100 mM of ^{15}N-TN-d_{16}. The sample composition was chosen for a comparison with ref. [33]. Experimental error for ϵ is estimated to be $10-20\,\%$. Microwave power (cw irradiation): $P = 43$ W (P5). NMR parameters (pulse sequence: zgig): $t_p\,(\pi/2) = 10\,\mu$s, $P\,(\pi/2) = 41$ W, DS = 2, RD = 30 s, LB = 6 Hz, ^{1}H decoupling: waltz64, 0.58 W. Boltzmann and DNP spectra were acquired with the same pulse sequence.

enriched (labelled) compounds.[33,34] With the new instrument described here, measurement of natural abundance samples is performed routinely (e.g. fig. 7.14), as reasonable signal-to-noise ratios ($\geq 2-5$) are accessible with $\sim 1-2$ h measurement time (c(target molecule) ≈ 500 mM) under DNP conditions. Boltzmann spectra were usually recorded overnight ($\sim 12-16$ h). Measurement of natural abundant samples is enabled by a $500-1000$ fold larger sample volume ($V_{\text{sample}} \approx 40\,\mu$L).

A second study at 14 T, reported $|\epsilon| \approx 1-3$ for 440 mM $^{13}C_8$-indole in a mixture of heptane-d_{18} and *p*-xylene-d_{10} (4:1, v/v).[41] Considering a limited mw irradiation time (2 s) and power ($\sim$ 13 W), a comparison of the ^{13}C signal enhancement between this publication and the herein presented work is challenging but the results seem to agree with the observations in this work.

Furthermore, another study conducted with the same instrument at 14 T reported $\epsilon \approx 21$ and $\epsilon \approx 71$ for $^{13}CCl_4$ and $^{13}CHCl_3$, respectively in 100 µL *n*-pentane and with

Table 7.7: Pulse length t_p, power P, and NMR linewidth measurements performed with the DNP probehead and comparison to a commercial probehead. Pulse measurements were performed on 100 mM urea (^{15}N), 100 mM methanol (^{13}C) in DMSO (d_6) (Bruker sample Z10263). ^1H linewidth was measured at peak heights of 50 %, 0.55 % and 0.11 % with spinning 3 % $CHCl_3$, 0.2 % tetramethylsilane (TMS) in acetone (d_6) (Bruker sample Z10230) and for ^{13}C on 40 % dioxane in benzene (d_6, ASTM) (Bruker Sample Z10163). Measurements on both probeheads were performed with the same samples.

DNP Probehead					
nucleus	t_p ($\pi/2$) (µs)	P ($\pi/2$) (W)	50 % (Hz)	0.55 % (Hz)	0.11 % (Hz)
^1H	14.7	23.3	0.42	29.6	73.7
^{13}C	9.8	48.2	0.54	21.3	36.3
Commercial 400 MHz Standard Bore Probehead (Bruker Z116098)					
nucleus	t_p ($\pi/2$) (µs)	P ($\pi/2$) (W)	50 % (Hz)	0.55 % (Hz)	0.11 % (Hz)
^1H	≤ 10	–	≤ 0.5	≤ 6	≤ 12
^{13}C	≤ 10	–	≤ 0.2	≤ 2	≤ 4

c(PA) $\approx$ 10 mM.[61] Due to sample heating of this non-resonant setup, mw irradiation was limited to 3 s and caused NMR linewidth distortions. This will be discussed in the following section.

7.2.2 Evaluation of the NMR Linewidth During DNP of Model Compounds and Comparison with the Literature

As this work also aims at developing a liquid state DNP setup that retains an NMR LW that is comparable to commercial NMR spectrometers, the NMR linewidth was carefully evaluated.

The achievable LW without mw irradiation with our probehead was determined with standardized test samples provided by Bruker (see tab. 7.7 for sample details) and the results were compared with a commercial 400 MHz standard bore NMR probehead. The results are listed in tab. 7.7 and particularly the LW at full-width at half-maximum (FWHM, 50 % of the signal maximum intensity) is only $\sim$ 0.1 Hz (^1H) and $\sim$ 0.3 Hz (^{13}C) larger than for a standard liquid state NMR probehead at 400 MHz (see tab. 7.7). However, at 0.55 % and 0.11 % of the signal intensity the LW for ^1H and ^{13}C is increased by a factor of $\sim$ 5 and $\sim$ 10, respectively for the DNP probehead. This is probably caused

Table 7.8: Comparison of two sample under DNP conditions using a layer thickness of $\sim$ 75 µm. Sample A consists of $\sim$ 200 mM $^{13}CHCl_3$ in CCl_4 with $\sim$ 10 mM ^{15}N-TN-d_{16} (see fig. 7.13) and sample B of 90/10 of CCl_4 and $CHCl_3$ (v/v) (no PA, see fig. 7.22a). NMR parameters (pulse sequence: zg): $t_p\,(\pi/2) = 10.0\,\mu s$ and $P\,(\pi/2) = 41\,W$. Microwave power (cw irradiation): 51 W (P9)

sample A	FWHM (Hz)	mw	sample B	FWHM (Hz)	mw
$^{13}CCl_4$	$\sim$ 3.8	off	$^{13}CCl_4$	$\sim$ 5.5	off
$^{13}CHCl_3$	$\sim$ 15.5	off	$^{13}CHCl_3$	$\sim$ 5.2	off
$^{13}CCl_4$	$\sim$ 6.9	on	$^{13}CCl_4$	$\sim$ 18	on
$^{13}CHCl_3$	$\sim$ 16.6	on	$^{13}CHCl_3$	$\sim$ 5	on

by the introduction of two mirrors in close proximity of the NMR coils (see fig. 7.8), which increases the inhomogeneity of the external magnetic field and therefore affects the linewidth.

Secondly, the influence of mw irradiation on the LW was compared for two samples. Sample A was composed of $\sim$ 200 mM $^{13}CHCl_3$ in CCl_4 with $\sim$ 10 mM ^{15}N-TN-d_{16} (see fig. 7.13) and sample B of 90/10 of CCl_4 and $CHCl_3$ (v/v) (no PA, see fig. 7.22a). The Boltzmann signals of the two samples display differences in their LWs with $\sim$ 3.8 Hz (CCl_4) and 15.5 Hz ($CHCl_3$) for sample A and $\sim$ 5.5 Hz (CCl_4) and $\sim$ 5.2 Hz ($CHCl_3$) sample B (see tab. 7.8). This demonstrates that the influences of the PA on the LW varies significantly among different molecules. Furthermore, the LW obtained without PA is $\sim$ 5 Hz, significantly larger than LW $<$ 1 Hz obtained with Bruker standards, (see tab. 7.7). This indicates that the sample geometry also affects the LW.

Upon mw irradiation, the LWs of the signals of sample A and sample B are affected in a similar way. While for sample A the linewidth of $^{13}CCl_4$ increases to LW $\approx$ 6.9 Hz the one of $^{13}CHCl_3$ (LW $\approx$ 16.6 Hz) remains almost unchanged (see fig. 7.13e), for sample B the LW of CCl_4 increases from $\sim$ 5.5 Hz to $\sim$ 18 Hz and the LW of $CHCl_3$ also remains constant ($\sim$ 5 Hz, see fig. 7.22 for the spectra).

The increase in linewidth is mostly due to a temperature gradient over the sample, caused by inhomogeneous microwave irradiation across the sample tube. The chemical shift of an NMR signal is temperature dependent and therefore a temperature gradient of the sample is reflected in an increased LW.[61] Even though, these chemical shift variations are highly sample dependent, most signals measured under DNP conditions display a LW

in the range of $10 - 30$ Hz. For example ethylacetoacetate and diethylmalonate show LWs of $\sim 8 - 20$ Hz during cw mw irradiation (fig. 7.14) and for favorable cases such as C_6H_5F LWs as narrow as 2.3 Hz were measured (see fig. 7.18).
A comparison of the linewidth between different DNP setups is difficult, because many important parameters, such as PA concentration, sample arrangement, sample composition, mw irradiation scheme, and mw irradiation time are different. Yet, the crude numbers may give an idea on the current state of the research area. To recall the numbers of this setup: The LWs of CCl_4 and $CHCl_3$ under mw irradiation are ~ 6.9 Hz and ~ 16.6 Hz ($c(^{15}\text{N-TN-d}_{16}) \approx 10$ mM), respectively. A non-resonant setup at 14 T in Tallahassee (National High Magnetic Field Laboratory) was capable of a similar LW for CCl_4, while the two lines of the ^{13}C doublet of $CHCl_3$ were almost merged corresponding to LW ≥ 150 Hz,[61] probably due to a large temperature gradient inside the sample tube. A mw resonant setup using a helical resonator obtained LW ≈ 50 Hz for CCl_4 as well as for $CHCl_3$, while a Fabry-Pérot setup produced very sample dependent linewidths in a range of $\sim 20 - 100$ Hz in H_2O.[33,34]
In conclusion, the linewidths presented in this work are by a factor of $2 - 3$ narrower compared to other liquid state DNP instruments. This allows for the investigation of complex and crowded spectra of larger molecules.

7.2.3 DNP Efficiency of Various Substrates and Functional Groups

After a comparison with the literature, the scope of DNP was expanded by measuring different substrates and functional groups at 9.4 T. Specifically, the DNP efficiency of molecules such as halogenated aromatics and -aliphatics, functionalized aromatics, ester, and cyclic aliphatic compounds were investigated. Measurements were mostly performed in non-polar solvents such as CCl_4, C_6H_6 and C_6H_{12}, because they allowed for the largest sample volume. Selected molecules were also measured in chloroform to investigate the influence of the polarity of the solvent and to increase the solubility of the substrate.
The investigated target molecules along with the solvent are displayed in fig. 7.16. The signal enhancement differs considerably between carbon atoms. Interestingly, particularly large signal enhancements were obtained for iodinated compounds ($\epsilon \approx 10 - 33$ on the ipso position). Additionally, also -CCl_3 groups delivered significant signal enhancements

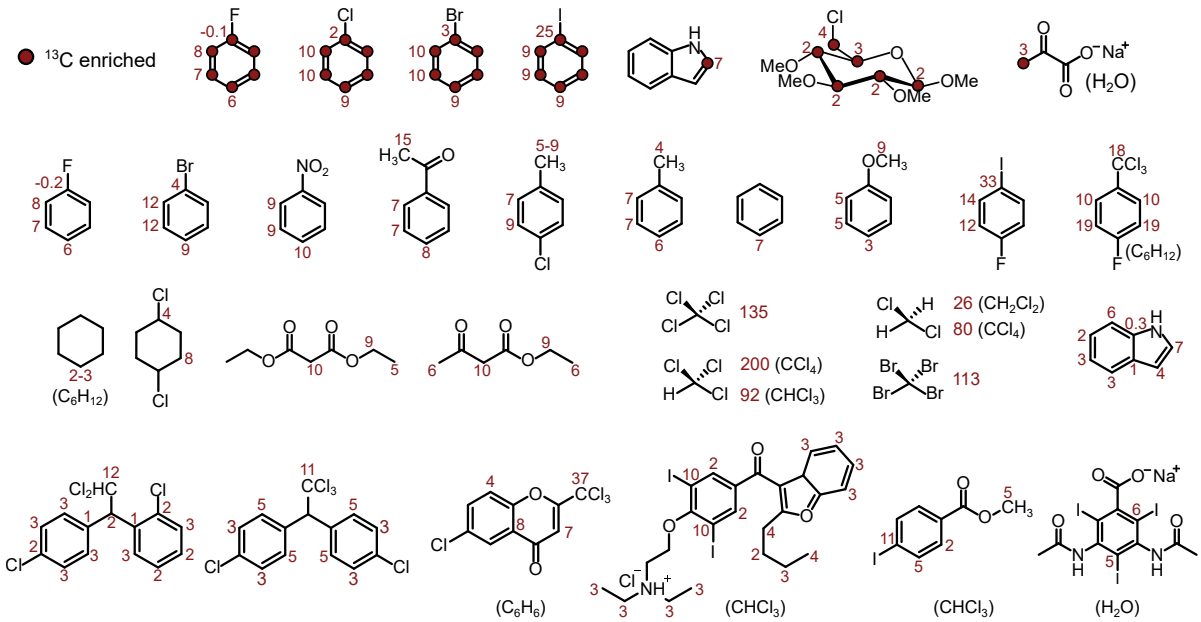

Figure 7.16: 1D signal enhancement of the investigated molecules (red). If not indicated differently, measurements were executed in CCl_4 (solvent shown in brackets). Experimental error of ϵ is $10-20\,\%$. V_{sample} for CCl_4, C_6H_6, and C_6H_{12} was $\sim 40\,\mu L$, for $CHCl_3$ $\sim 20\,\mu L$, and for CH_2Cl_2 and H_2O $\sim 15\,\mu L$. Microwave power (cw irradiation) in non-polar solvents was $P = 43\,W$ (P5) or $P = 50\,W$ (P7), (for $CHCl_3$ in CCl_4 $P = 51-53\,W$ was used). Measurements in $CHCl_3$ were performed with a mw power $P = 29\,W$ (P2, cw irradiation) and in other polar solvents (CH_2Cl_2, CH_3CN, and H_2O) with $P = 22-29\,W$ (P1, P2, $2-7\,s$ gated). NMR parameters (pulse sequences: zg and zgig): $t_p\,(\pi/2) = 10\,\mu s$, $P\,(\pi/2) = 41\,W$, DS = 2, RD = $30-40\,s$, LB = $0-4\,Hz$ (depending on the natural LW of the spectrum). Boltzmann and DNP spectra were acquired with the same pulse sequence. Sample temperatures were adjusted with calibration curves and were in the range of $T_{\text{sample}} \approx 290-310\,K$. All measurements were performed with ^{15}N-TN-d_{16} and a concentration of $c(PA) \approx 10-25\,mM$. Spectra and experimental details are shown in appendix C.

($\epsilon \approx 10-37$), which was expected, due to their similarity to $CHCl_3$. Furthermore, substitution of electron-withdrawing-groups (EWG) slightly increased the signal enhancement (ϵ (nitrobenzene) ≈ 10) on the aromatic ring, while electron-donating-groups (EDGs) decreased the enhancement (ϵ (anisol) ≈ 5) in comparison to unsubstituted benzene with $\epsilon \approx 7$. As expected, due to the previously observed dipolar dominated polarization transfer ($\epsilon \leq 0$), no significant enhancement is observed for carbonyl groups.[34,60] Additionally, also the loss of NMR signal of the C_{ipso} position of different aromatics and functional groups

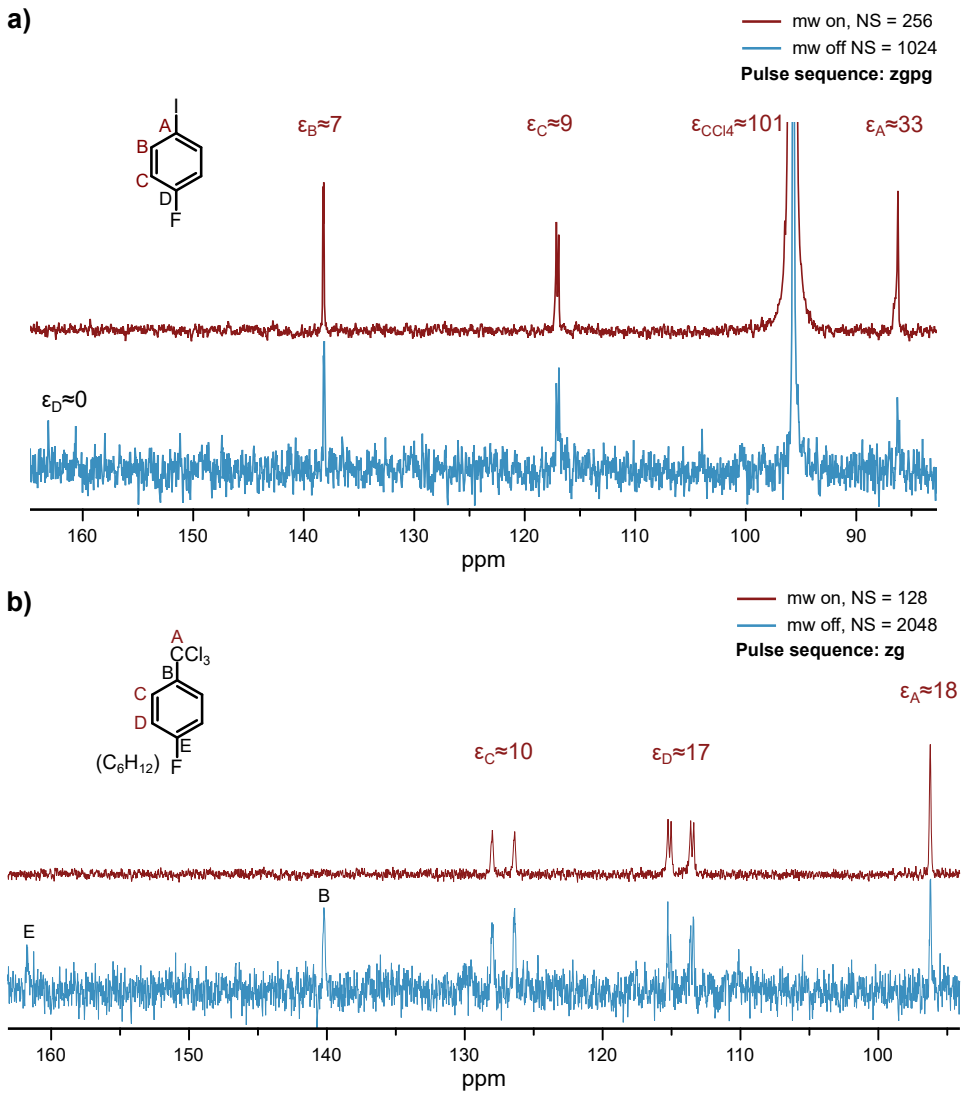

Figure 7.17: Enhanced (red) and Boltzmann spectra (blue) of a) 500 mM *p*-IC_6H_4F in CCl_4 and b) 500 mM 1-fluoro-4-(trichloromethyl)benzene in C_6H_{12}. Both measurements were performed with $c(^{15}\text{N-TN-d-}_{16}) \approx 25$ mM. The solvent peak in b) was omitted for clarity. Microwave power (cw irradiation): $P = 43$ W (P5). NMR parameters (pulse sequences: zg and zgpg): $t_p\,(\pi/2) = 10\,\mu s$, $P\,(\pi/2) = 41$ W, DS = 2, RD = 30 s, LB = 4 Hz (a), LB = 2 Hz (b). Sample temperatures were adjusted with calibration curves and were in the range of $T_{sample} \approx 290 - 310$ K. Experimental error for ϵ is estimated to be $10 - 20$ %. Boltzmann and DNP spectra were acquired with the same pulse sequence.

during DNP measurements may be ascribed to a dipolar dominated DNP mechanism. The exception to this are the C_{ipso} position of chlorinated, brominated, and iodinated

compounds.

The observed trends for halogenated and otherwise functionalized aromatics are discussed in sec. 7.2.4, however first, as examples for large ϵ, the DNP spectra *p*-IC_6H_4F and 1-fluoro-4-(trichloromethyl)benzene measured with $\sim 500\,\text{mM}$ natural abundance target molecule and $\sim 25\,\text{mM}$ PA are presented in fig. 7.17. For *p*-IC_6H_4F, the enhancement varies from $\epsilon \approx 33$ on the iodinated position to $\epsilon \approx 7$ on the respective ortho position, while no enhancement was observed for the fluorinated carbon signals in both compounds. The signal vanished during the DNP experiment, which is most likely a result of a dipolar dominated polarization transfer (see fig. 7.18 and sec. 2.2).

In order to further demonstrate the high resolution of DNP experiments, the spectra of ^{13}C enriched and natural abundant fluorobenzene are showcased in fig. 7.18. Both experiments were conducted with ^{1}H decoupling. Figure 7.18c shows in addition to the Boltzmann and DNP spectrum a simulation (performed with MestReNova Vers. 11.4.4-18998) of the ortho position of $^{13}C_6$-C_6H_5F. Notably, a coupling as small as 2.9 Hz arising from a C_{ortho}-C_{meta} coupling is resolved.[209]

Furthermore, 7.18d and 7.18f show zoom-in-views of the meta and ortho position of natural abundance C_6H_5F. While they display a well resolved J-coupling to ^{19}F ($^{3}J_{CF} \approx 7.9\,\text{Hz}$ and $^{2}J_{CF} \approx 21\,\text{Hz}$), the linewidth of both signals is $LW \approx 2.3\,\text{Hz}$ and remains almost unchanged upon mw irradiation.

7.2.4 New Mechanistic Insights in the DNP Enhancement of Small Molecules

A thorough understanding of the DNP mechanism is essential for the selection of favorable target molecules and polarizing agents. Because the dipolar contribution to the spin polarization transfer is almost negligible at 9.4 T, the transfer for carbon mainly proceeds via molecular collisions. Recalling the spectral density (eq. 2.37) of this process,

$$J_{con}(\omega_e, \tau_{con,i}) = \sum_{i=1}^{n} \frac{\langle A_{iso,i} \rangle^2}{\hbar^2 \tau_{p,i}} \left[\tau_{con,i} \cdot \exp(-\tau_{con,i}\omega_e)\right]^2 \tag{7.1}$$

shows the dependence of J_{con} on the isotropic hyperfine (hf) coupling A_{iso}, the collision frequency τ_p^{-1}, and the duration of such collisions $2\tau_{con}$. Experimental conditions such as

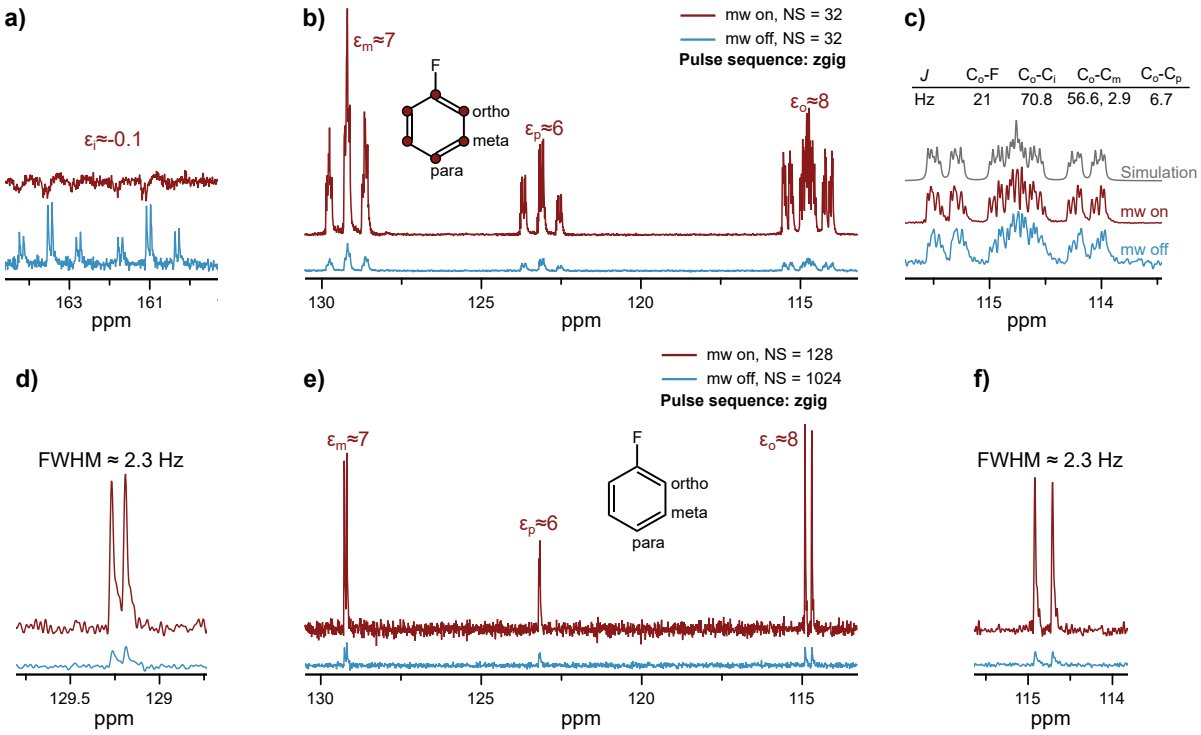

Figure 7.18: Enhanced (red) and Boltzmann spectrum (blue) of ^{13}C enriched ∼ 500 mM fluorobenzene in CCl_4 with zoom-in views on the a) C_{ipso} and b) $C_{o,m,p}$ positions. c) Excerpt of the ortho position including a spectral simulation with a table of the literature parameters.[209] The spectra are scaled to similar intensity. Enhanced (red) and Boltzmann spectrum (blue) of ∼ 500 mM natural abundance fluorobenzene doped with 25 mM ^{15}N-TN-d_{16} in CCl_4 with zoom-in views on the d) C_o, e) $C_{o,m,p}$ and f) C_m position (spectra were scaled according to their number of scans). d) and f) display a LW of LW ≈ 2.3 Hz and a J-coupling of $^2J_{CF} \approx 21$ Hz and $^3J_{CF} \approx 7.9$ Hz, respectively. For clarity, the CCl_4 signal is omitted. Microwave power (cw irradiation): $P = 43$ W (P5). NMR parameters (pulse sequence: zgig): $t_p\,(\pi/2) = 10\,\mu$s, $P\,(\pi/2) = 41$ W, DS = 2, RD = 30 s, LB = 0 Hz. Sample temperatures were adjusted with the calibration curves and were in the range of $T_{sample} \approx 290 - 310$ K. Experimental error for ϵ is estimated to be 10 – 20 %. Boltzmann and DNP spectra were acquired with the same pulse sequence.

^{13}C enrichment and the choice of the solvent might influence τ_p^{-1} or A_{iso}, respectively. Additionally, different functional groups may differ significantly in their collisions with ^{15}N-TN-d_{16}. In this context, the different collisions of C-Hal (Hal = F, Cl, Br, and I) and C-H σ-bonds with the PA are particularly important. However, also electronic changes in the π-system of a target molecule may alter the preferred molecular collision with nitroxides.[59]

Table 7.9: ^{13}C NMR signal enhancement of $^{13}C_6$-BrC_6H_5 and $^{13}C_6$-C_6H_5I doped with ^{15}N-TN-d16 in different solvents. Experimental parameters are listed in the appendix C (tab. C.5 and tab. C.4). Spectra are shown in the appendix C (fig. C.3a, fig. C.14a, fig. C.14b, fig. C.15, fig. C.4a, fig. C.16a, and fig. C.16b). Experimental error for ϵ is estimated to be $10-20\,\%$.

target	solvent	$\epsilon(C_{ipso})$	$\epsilon(C_{o,m})$	$\epsilon(C_p)$
$^{13}C_6$-BrC_6H_5	$^{13}CCl_4$	4	12	10
$^{13}C_6$-BrC_6H_5	CCl_4	3	10	9
$^{13}C_6$-BrC_6H_5	C_6H_6	3	10	7
$^{13}C_6$-BrC_6H_5	C_6H_{12}	4	11	9
$^{13}C_6$-C_6H_5I	CCl_4	25	9	9
$^{13}C_6$-C_6H_5I	C_6H_{12}	26	12	11
$^{13}C_6$-C_6H_5I	$CHCl_3$	14	6	5

First, the influence of the ^{13}C enrichment on ϵ was tested by comparing $^{13}C_6$-C_6H_5F with its natural abundance version (fig. 7.18). As ^{13}C enrichment may change the collision frequency, this could lead to an increased signal enhancement for ^{13}C enriched samples. However, no difference in ϵ was observed for C_6H_5F and BrC_6H_5 (appendix fig. C.3a and fig. C.5b). This is in agreement with a very recent study, where the influence of ^{13}C label content on the enhancement of $CHCl_3$ was investigated and also excludes a possible ^{13}C-^{13}C NOE effect.[40]

Next, the influence of the solvent on the DNP efficiency was quantified. From EPR, it is known that the solvent affects the *g*- and the intramolecular *A* tensor of nitroxides.[181] A similar behaviour might exist for the transient intermolecular hf coupling between the PA and the target molecule during DNP. Furthermore, solvation of the substrate or the radical could block the approach to either of them, thus reducing the DNP effect.[86]

The investigation of the model compounds bromobenzene and iodobenzene in different non-polar solvents revealed no solvent dependence of ϵ for measurements in CCl_4, C_6H_6, and C_6H_{12} (see tab. 7.9). However, the signal enhancement for $^{13}C_6$-C_6H_5I decreased by $\sim 50\,\%$ when the experiments were carried out in chloroform. A similar behaviour was observed for acetonitrile (see fig. 7.25) and might be related to the higher polarity and therefore stronger mw absorption of $CHCl_3$. Nevertheless, as the selection of solvents as well as the substrates are here not exhaustive, an influence of the solvent on the spin

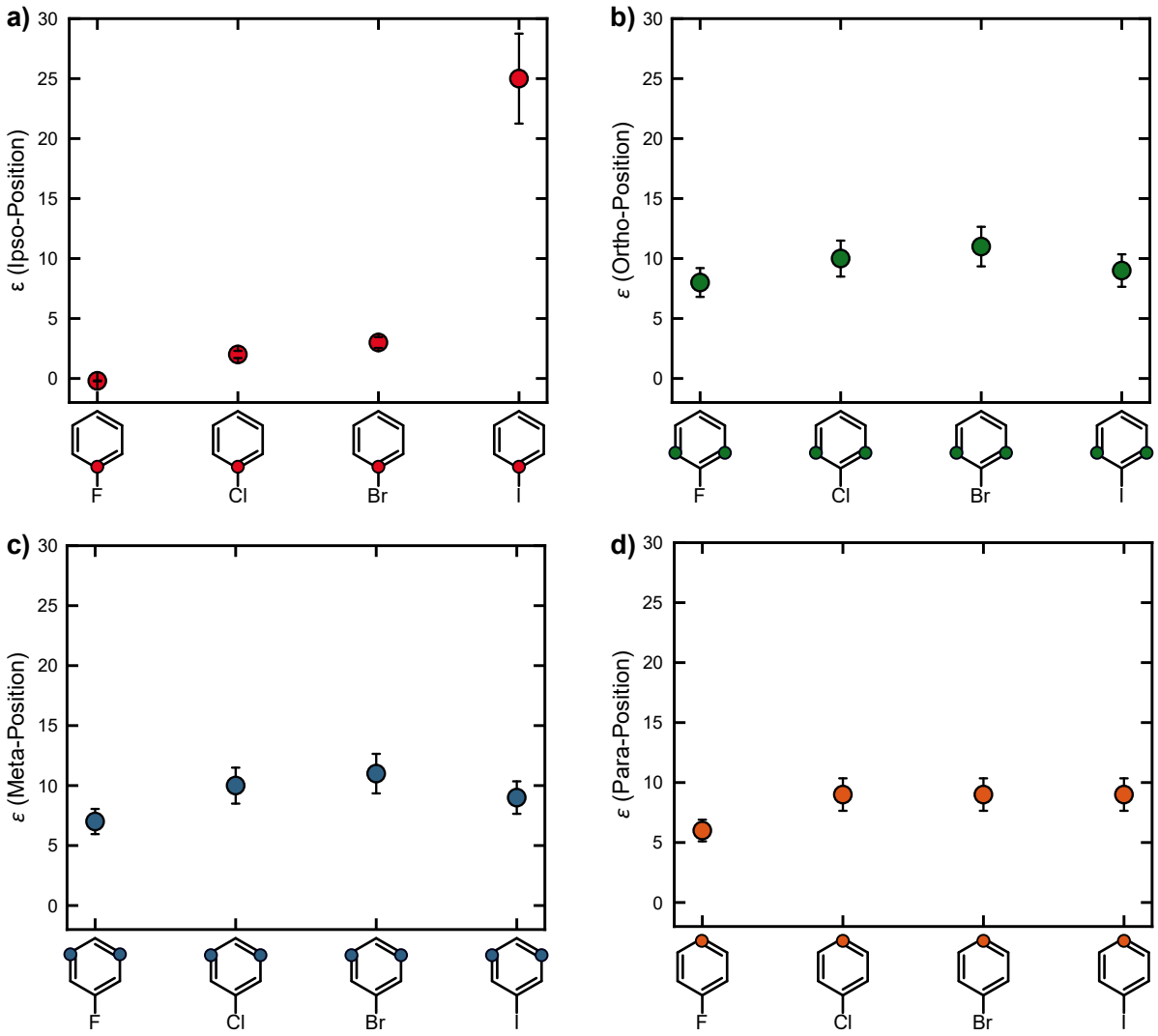

Figure 7.19: 1D signal enhancement of uniformly ^{13}C enriched halogenated benzenes in CCl_4 at the different ^{13}C positions. Experimental error for ϵ is estimated to be $10-20\,\%$. Experimental parameters are listed in the appendix C (tab. C.5 and tab. C.4). Spectra are shown in fig. 7.18 and in appendix C (fig. C.2a, fig. C.3a, and fig. C.4a).

polarization transfer cannot be excluded. Particularly, protic solvents could impact the DNP mechanism by solvating the NO moiety of the PA or the target molecule, thereby hampering the scalar hf interaction between the two molecules.[181] However, for these solvents (e.g. alcohols and H_2O) disentangling a mechanistic contribution of the solvent from mw absorption remains challenging.

After the verification of the sample conditions (choice of the solvent and ^{13}C content),

the spin polarization transfer mechnanism between PA and target molecule was analyzed. In principle, this can proceed on two pathways. First, the electron spin containing group interacts directly with the target nucleus and second the electron spin interacts with a substituent of the ^{13}C spin (e.g. H, F, Cl, Br, I, a π-system, and many others) and polarization reaches the spin for example via the σ-bond of the substituent. The latter appears to be the dominant pathway, because carbon nuclei that are in many cases inaccessible for a direct interaction, deliver very large signal enhancements ($\epsilon(CCl_4) \approx 430$, $\epsilon(CBr_4) \approx 600$ at 9.4 T).[34]

In this light, the comparison between C-H and C-Hal was investigated. Figure 7.19 shows the signal enhancement at the different carbon positions of different uniformly ^{13}C enriched mono halogenated benzenes (F, Cl, Br, and I). The enhancements on the ortho, meta, and para positions of all four investigated compounds are positive and comparable in magnitude. This suggests a similar scalar dominated spin polarization transfer mechanism. The nitroxide may interact with the carbon nuclei through the C-H bond or the π-system of the benzene ring. A direct interaction with the carbon atom is also possible, however, at low magnetic field, large signal enhancements were found preferably on carbons with acidic protons.[59] This would favor a polarization transfer via C-H bond.

The situation is different for the C_{ipso} position of the benzene rings (see fig. 7.19a). For $^{13}C_6$-C_6H_5F an enhancement of -0.1 is observed, which indicates a dipolar dominated polarization transfer ($\epsilon \leq 0$). The reason could be that F[210] as well as the NO moiety (see fig. 4.9) show a high and localized electron density, which could lead to a repulsive interaction between F and the NO group, thereby minimizing the hyperfine coupling. The other three compounds show positive signal enhancement on C_{ipso}, however, while the enhancement for $^{13}C_6$-C_6H_5Cl and $^{13}C_6$-C_6H_5Br are similar ($\epsilon \approx 2-3$), the signal enhancement for $^{13}C_6$-C_6H_5I is $\epsilon \approx 25$. This is a remarkable ten fold increase by replacing Cl/Br with I. Therefore, the spin polarization transfer mechanism not only differs between the ipso position and the other positions of the benzene ring (ortho, meta, and para) but also between the different substituents.

The large difference on C_{ipso} is surprising, because in previous experiments halogenation (Cl and Br) favored large signal enhancements on sp^3 hybridized carbon atoms.[34,59] On the other hand, fig. 7.16 shows that only minor/negligible signal enhancements are observed on C_{ipso} for all investigated aromatic systems independently on the substituent

(i.e. the functional group). The exception to this represent iodinated carbon atoms that show an increased signal enhancements with respect to other carbon atoms on the same molecule with an enhancement of up to $\epsilon \approx 33$ (see fig. 7.17a). Therefore, understanding the underlying spin polarization transfer mechanism of this particular moiety is of interest. A possible interaction favoring a strong hf interaction between iodine and the PA is halogen bonding. In a halogen bond, halogens act as an electron acceptor through an interaction of the so-called σ-hole of the halogen (a result of the antibonding orbital of the for example C-Hal σ-bond) with an electron donor (e.g. a nitroxide radical).[211–214] Halogen bond motifs between chlorinated,[215] brominated,[216] and iodinated,[211–214,217] compounds and nitroxides have been previously reported in the literature. EPR was used to observe the halogen bond complex between nitroxides and C_6F_5I, while NMR was, among many others, employed in the liquid- as well as in the solid-state to characterize halogen bonds.[218,219] Even ODNP in liquids was used to analyze the dynamics of a halogen bond between C_6F_5I and 1,4-diazabicyclo[2.2.2]octane (DABCO) at low magnetic field (0.35 T).[220]

Furthermore, halogen bonds are highly directional and contributions to the strength are of electrostatical, charge transfer, and also of dispersive nature. The strength increases with the introduction of functional groups that further reduce the electron density of the halogen atom. Generally, a higher polarizability of the halogen atom favors a strong halogen bond, meaning that the halogen bond strength increases from fluorine to iodine (F<Cl<Br<I).[211]

Indeed, the electrostatic potential at the same isosurface (0.001 au) of halogenated benzenes (C_6H_5Hal) calculated from DFT simulations reveals a larger positive potential for iodine than for chlorine (about a factor of ~ 3) and bromine (a factor of ~ 1.4)[221,222] This trend also holds, if the interaction between halogenated benzene and a halogen bond acceptor (e.g. acetone or trimethylamine) is investigated, and scales with the attractive interaction energy of the two molecules.[221,222] Furthermore, additional substitution of the aromatic ring with e.g. fluorine (i.e. EWGs) increases the halogen bond strength.[211,221,223] Interestingly, this correlates well with the observed enhancement for *p*-IC_6H_4F with $\epsilon(C_{ipso}) \approx 33$ (see fig. 7.17a), which is 25 % larger than for iodobenzene ($\epsilon(C_{ipso}) \approx 25$). Aside from theoretical calculations, also two experimental reports indicate a more significant role of the halogen bond for iodinated compounds than for chlorinated/brominated

molecules.[224,225] These studies compared the ^{1}H chemical shifts changes of $CHCl_3$, $CHBr_3$, and CHI_3 as well as of CH_2Cl_2, CH_2Br_2, and CH_2I_2 upon interaction with an electron donor (e.g. esters, ketones, ethers, and amines). While H-bonding causes a low field shift, halogen bonding increases the resonance frequency of the ^{1}H nucleus. Therefore, both interactions are counter-acting and can be distinguished from one another considering the chemical shift.[224,225] Both studies report almost negligible contributions of the halogen bond for the Cl and Br containing compounds, while for the two iodinated compounds halogen bonding plays a major role being the dominant interaction mechanism with amines.[224,225]

While a direct interaction between carbon and electron spin as well as a π-system interaction with the nitroxide cannot be excluded, the aforementioned reports suggest a significant involvement of the halogen bond in the spin polarization transfer mechanism. Experimental verification of this hypothesis could be achieved by DNP measurement of iodinated benzenes with substituents that increase the halogen bond strength (e.g. $C_6H_{5-n}F_{0+n}I$ with $n = 0 - 5$). Additionally, so far, only static contributions were considered, therefore the dynamics of the interaction (e.g. collision duration, collision frequency) could also influence the spin polarization transfer mechanism, but this is beyond the scope of this work.

Finally, the potential influence of an interaction of the π-system with the nitroxide radical on the DNP efficiency was tested. To this end, the electronic structure of the π-system was altered through introduction of different functional groups. Nitro (NO_2) and aceto ($COCH_3$) reduced (EWGs) while methoxy (OCH_3) and methyl (CH_3) increased (EDGs) the electron density of the π-system. Figure 7.20 shows the NMR signal enhancement at different carbon positions of substituted benzenes. None of the ipso positions show any significant signal enhancement. In contrast, benzene reveals $\epsilon \approx 7$. On the other hand, larger signal enhancements ($\epsilon(C_{o,m,p}) \approx 7 - 10$) than for benzene are observed for nitrobenzene and acetophenon, while anisole and toluene display smaller enhancements ($\epsilon(C_{o,m,p}) \approx 3 - 7$).

Even though a general trend is visible, certain features need further investigations. Indeed, as soon as benzene is functionalized, the electron density is inhomogeneously distributed among the ring. For example, EWGs reduce the electron density on the ortho position more than on the meta position, however this is not resembled by the obtained signal

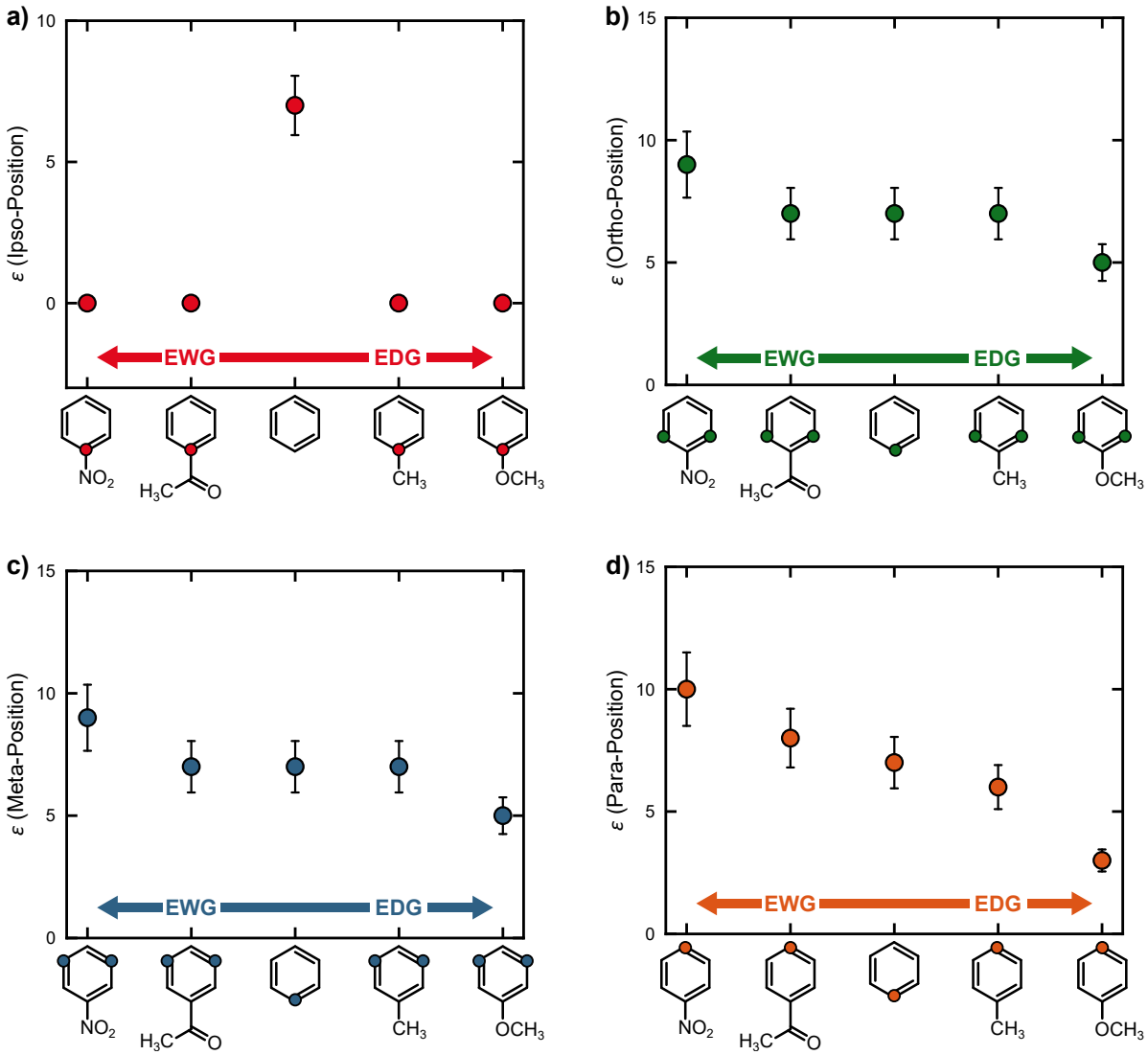

Figure 7.20: 1D signal enhancement of functionalized benzenes in CCl_4 at the different ^{13}C positions. Tendencies of the functional groups are indicated by the arrows. Experimental error for ϵ is estimated to be $10-20\,\%$. Experimental parameters are listed in the appendix C (tab. C.5 and tab. C.4). Spectra are shown in in appendix C (fig. C.6a, fig. C.6b, fig. C.8a, fig. C.8b, and fig. C.7b.).

enhancement with $\epsilon(C_o) \approx \epsilon(C_m)$ for nitrobenzene and acetophenone. In order to draw mechanistic conclusions on the influence of the electronic structure of the π-system, the data set needs to be expanded with additional functionalized aromatics.

In conclusion, the two discussed observations (iodination and EWG vs. EDG) affect ^{13}C

NMR the signal enhancement. In the case of iodo compounds, the halogen bond may play an important role in the spin polarization transfer. Additionally, according to the obtained results, ^{13}C enrichment and the choice of solvent (within the selection of investigated solvents) have little influence on the DNP enhancement. Notably, these observations were drawn from an unprecedented large data set that was enabled by the new liquid DNP instrument.

7.2.5 DNP Results on Biologically Active Compounds

DNP of small biological molecules is a promising application for ODNP in liquids but such experiments demand high resolution NMR spectra, because otherwise signal overlap may prevent an unambiguous assignment of the resonances. Section 7.2.2 and sec. 7.2.3 demonstrated that the newly developed setup is able to provide large signal enhancement combined with good resolution enabling the measurement of such biological active molecules.

Based on the observations reported in the previous sections, promising biologically active target molecules were investigated. Figure 7.21 shows the DNP enhanced spectra of an inhibitor of the adenylyl cyclase 1 (ST034307),[226] the drug mitotane, which is used to treat certain forms of cancer,[227] and amiodarone, an antiarrhythmic drug.[227]

All of these compounds display sizable signal enhancements ($\epsilon \geq 10$) with a signal enhancement of up to $\epsilon \approx 37$ for the CCl_3 group of ST034307. Indeed, the previously identified chemical environments (iodinated carbons and CCl_3 groups) show large enhancements ($\epsilon \approx 10-37$). Other positions produce $\epsilon \approx 2-7$, while some carbon signals are suppressed during DNP ($\epsilon \leq 1$). The large variations in the DNP enhancements may be due to the different accessibility the carbon sites, influences of the carbon chemical environment, and dynamic processes.[33,83,86] These preliminary observations suggest that large signal enhancements could be obtained with site-specific labelling (e.g. with iodine).[229]

Not only did the experiments depicted in fig. 7.21 reveal large signal enhancement, they also showed that the linewidth of the different NMR signals remained within a reasonable range (LW $\approx 5 - 30$ Hz of the largest NMR signals). Moreover, the change of the linewidth upon microwave irradiation was almost negligible for ST034307 with $\frac{LW_{Boltz}}{LW_{DNP}} \approx \frac{5.5\,Hz}{5.7\,Hz} \approx 1$ for the CCl_3 group of ST034307, while for mitotane and amiodarone

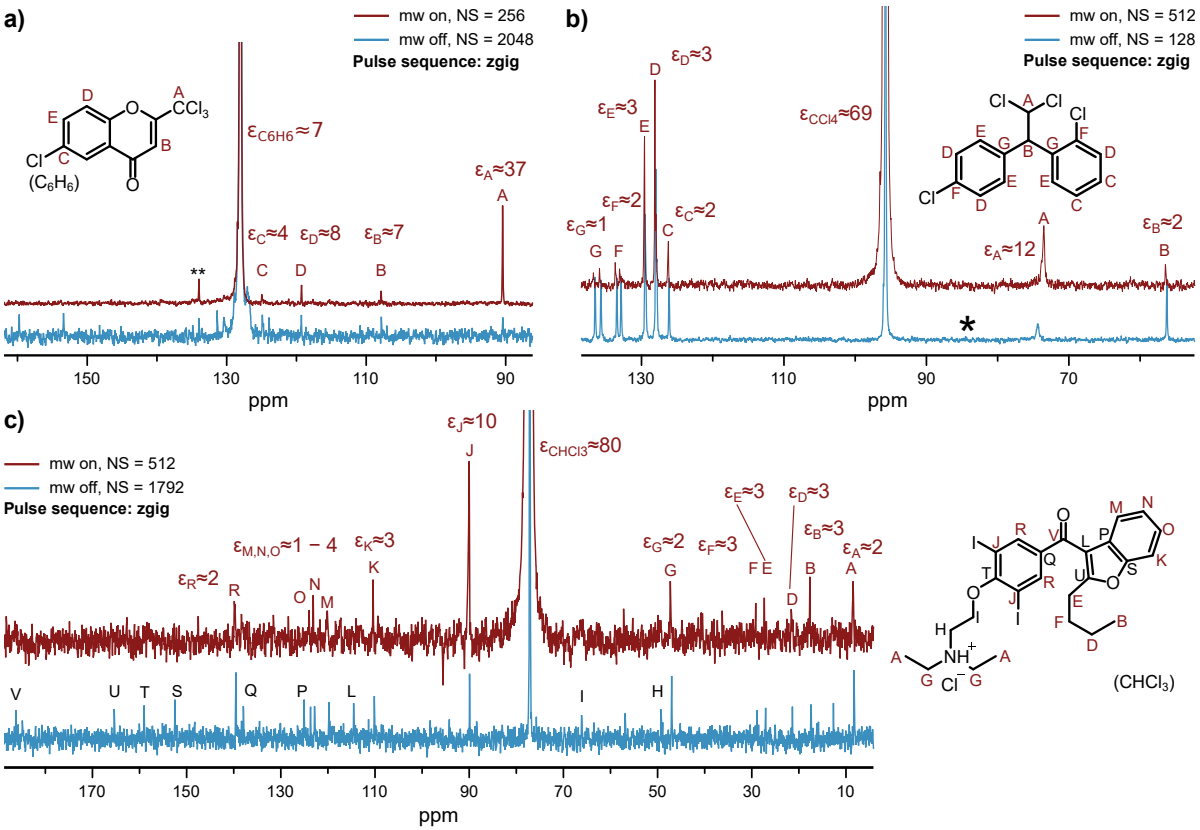

Figure 7.21: Enhanced (red) and Boltzmann spectrum (blue) of a) 100 mM ST034307[226] in benzene, b) of 500 mM mitotane in CCl_4, and c) 500 mM amiodarone in $CHCl_3$. The spectra in c) were scaled according to their number of scans. The three measurements were performed with $c(^{15}\text{N-TN-d-}_{16}) \approx 25$ mM. (*) The Boltzmann spectrum of b) was recorded with a full tube ($V_{\text{sample}} \approx 550 - 630\,\mu\text{L}$) and scaled based on the volumetric ratio. (**) Poor signal to noise of the Boltzmann signal. Assignment of a) is based on AIST database (SDBS 22206CDS-09-294) while b) is based on chemical shift increment calculation performed with ChemDraw Vers. 16.0.1.4(77), and c) was assigned according to the literature.[228] Enhanced signals are marked with red letters, while signals with $\epsilon \leq 1$ are marked in black or assignment is omitted. Microwave power (cw irradiation): $P = 43$ W (P5) (a,b), $P = 29$ W (P2) (c); NMR parameters for a), b), and c) (pulse sequence: zgig): $t_p\,(\pi/2) = 10\,\mu$s, $P\,(\pi/2) = 41$ W, DS = 2, RD = 30 s, LB = 4 Hz. Sample temperatures were adjusted with calibration curves and were in the range of $T_{\text{sample}} \approx 290 - 310$ K. Experimental error for ϵ is estimated to be $10 - 20$ %. Boltzmann and DNP spectra were acquired with the same pulse sequence.

linebroadening is observed with $\frac{\text{LW}_{\text{Boltz}}}{\text{LW}_{\text{DNP}}} \approx \frac{8.4\,\text{Hz}}{27.7\,\text{Hz}} \approx 0.3$ for the $CHCl_2$ group of mitotane and $\frac{\text{LW}_{\text{Boltz}}}{\text{LW}_{\text{DNP}}} \approx \frac{4.4\,\text{Hz}}{20\,\text{Hz}} \approx 0.2$ for the iodinated carbon positions of amiodarone (fig. 7.21). Notably,

amiodarone was measured in $CHCl_3$, where generally a larger temperature gradient during DNP measurements is observed (see sec. 7.3.1).
These experiments demonstrate the possibility of liquid state DNP of complex molecules with reasonable resolution, including biologically active drugs and other related compounds.

7.3 DNP in Polar Solvents

Because of extensive sample heating induced by mw absorption of the solvent, only two DNP instruments reported liquid state DNP measurements in water at high magnetic field (9.4 T). The Prisner group used a helical resonator as well as a Fabry Pérot resonator for DNP in water.[33,112,135] Particularly, the latter alleviates sample heating but limits the sample volume to $V_{\text{sample}} \leq 100\,\text{nL}$. Nevertheless, they reported a ^{13}C signal enhancement of up to $\epsilon \approx 50$ for imidazole and signal enhancements of $\epsilon \approx 2 - 11$ on different amino acids (glycine, alanine, serine, and proline) and glucose.[33] In a follow up study, they observed an enhancement of $\epsilon \approx 16$ for Na $^{13}C_1$-C_3-pyruvate.[112] Furthermore, the Ansermet group in Lausanne reported a ^1H enhancement of $\epsilon \approx -10$ on water with a volume of $V \approx 10\,\mu\text{L}$.[68] They built a probehead that confines the sample to a thin layer on a planar surface and mw irradiation is applied from the top, i.e. orthogonal to the sample plane.[68] However, the setup suffers from an inhomogeneous magnetic field and thus a large NMR linewidth (LW(^1H) $\approx 4000\,\text{Hz}$).[68]
As already mentioned, sample heating is also observed in the herein presented DNP instrument and is counteracted by sample rotation, thin sample layers, and active cooling with cold N_2 gas. Since the Boltzmann polarization depends on the temperature, similar sample temperatures during Boltzmann and DNP measurement are crucial to obtain reliable signal enhancements.[83]
Due to the fact that sample heating is caused by mw absorption of the solvent, it is mostly independent on the target molecule and the PA.[201] Therefore, the sample temperature for each solvent was carefully calibrated to reach $T_{\text{sample}} \approx 290 - 310\,\text{K}$ during DNP and Boltzmann measurements. As previously demonstrated (see fig. 7.1b) the g_{iso} of the organic radical depends on the solvent, therefore resonant mw irradiation was ensured by magnetic field and gyrotron frequency optimization. After this, the influence of microwave absorption on ϵ is described by the measurement of the ^{13}C NMR signal enhancement of

acetonitrile in different solvents and finally signal enhancements in H_2O of compounds such as Na pyruvate and Na diatrizoate are shown.

7.3.1 Temperature Calibration for DNP Experiments

The temperature of NMR samples is monitored by measuring the chemical shift difference Δ (in ppm) of two signals as a function of the temperature.[61] Figure 7.22 shows the temperature calibration for sample solutions of tetrachloromethane and chloroform. T_{set} was calibrated with a Bruker standard method using methanol and it was found that $T_{set} \approx T_{sample}$ in the range of $T_{set} \approx 270-300\,K$ (see appendix E fig. E.3) The chemical shift difference between the solvent and the reference compound (10 % $CHCl_3$ (v/v) in CCl_4) was measured without mw irradiation. The sample was then cooled to $T_{set} = 210 - 250\,K$ and mw irradiation at different power was applied. The NMR spectra are displayed in fig. 7.22a and Δ is plotted as a function of T_{set} in fig. 7.22b. The latter plot reveals that a sample temperature of $T_{sample} \approx 300\,K$ for CCl_4 is achieved even under high power cw mw irradiation. However, even for non-polar solvents, line broadening is observed during mw irradiation (see fig. 7.22a) that stems from a temperature gradient of the sample. Similar measurements were performed for other non-polar solvents (cyclohexane) and led to comparable results, which was expected due to their similar dielectric constants. Thus, the calibration curve of CCl_4 was also employed for solvents such as cyclohexane and benzene.

Temperature induced line broadening invigorates with increasing polarity of the solvent. By using CCl_4 as a solvent, a LW of LW($CHCl_3$)$\approx$ 16.6 Hz with a mw power of $P = 51 - 53\,W$ (P9) is obtained for $CHCl_3$ ($c \approx 200\,mM$, see fig. 7.13). Using $CHCl_3$ as a solvent (fig. 7.22c and d), allows for a mw power of $P = 43\,W$ for obtaining a sample temperature of $T \approx 300\,K$ under cw mw irradiation. However, largest ^{13}C NMR signal enhancements with $CHCl_3$ as a solvent are usually observed at P2 (29 W), possibly because of temperature induced line broadening. Nevertheless, for chloroform cw mw irradiation is possible, however, due to the increased dielectric heating in chloroform, the layer thickness of the sample is limited to 40 μm, whereas for CCl_4, C_6H_6, and C_6H_{12} a layer thickness of $d \approx 75\,\mu m$ is viable without compromises on the NMR LW (see tab. 7.5). Larger sample layers lead to significantly higher sample heating, lower enhancement, and NMR lineshape

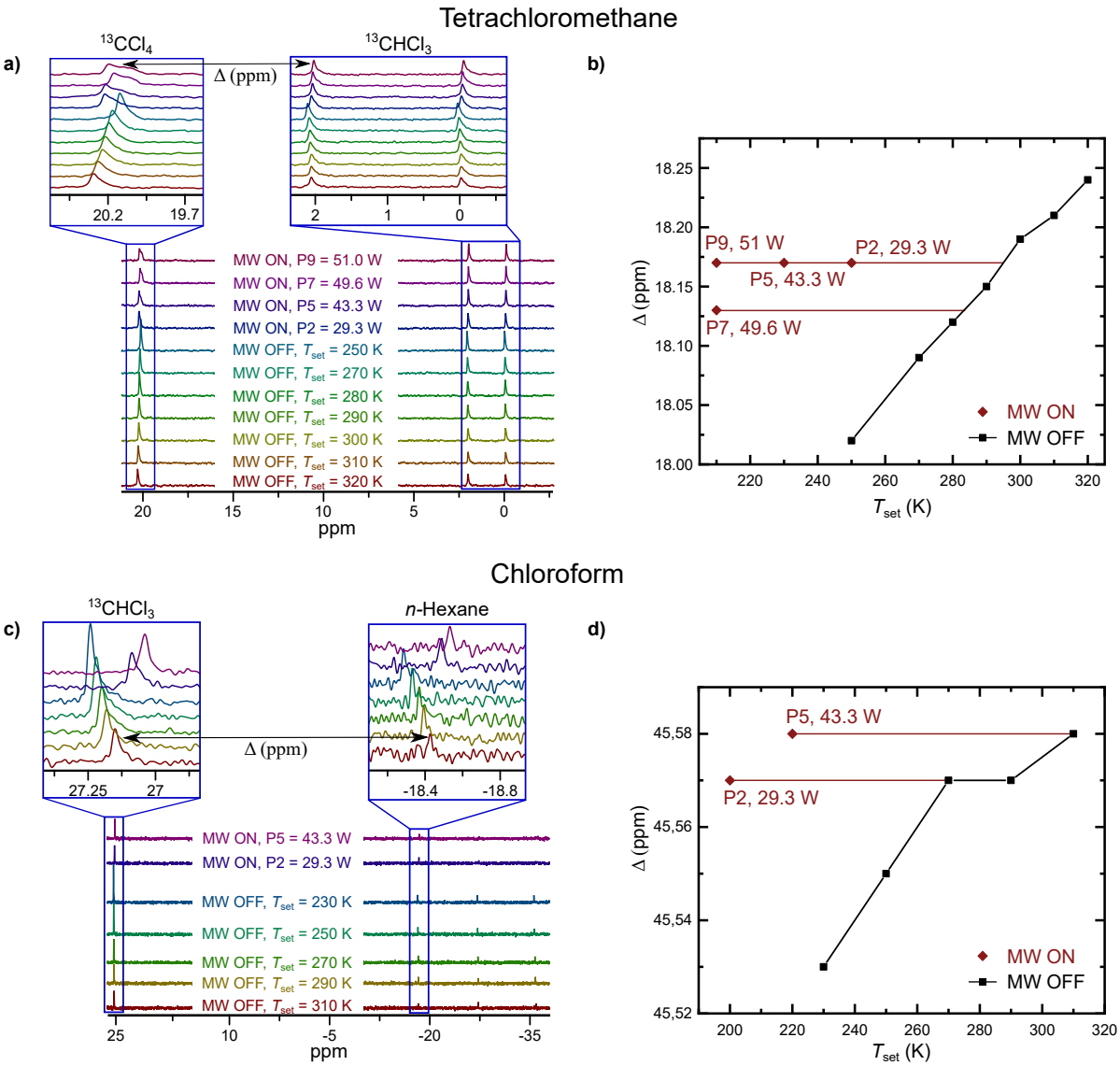

Figure 7.22: Temperature calibration of the solvents CCl_4 and $CHCl_3$. a) ^{13}C NMR spectra of 1 M $^{13}CHCl_3$ (10 % of the volume) in CCl_4 (10 % ^{13}C labelled) as a function of the temperature without microwave (mw off) and for different power levels under microwave irradiation (mw on). Microwave power settings are listed in fig 7.4. NMR parameters (pulse sequence: zg): NS = 4, DS = 2, LB = 2 Hz, D1 = 30 s, $P(\pi/2)$ = 41 W, $t_p\,(\pi/2)$ = 10 µs. b) Plot of the chemical shift difference of the reference compounds against the set sample temperature under Boltzmann conditions (black) and their chemical shift difference during cw mw irradiation (red). Lines are a guide for the eye. c) and d) The same temperature measurements but with chloroform as the solvent doped with ∼ 760 mM *n*-hexane (10 % of the volume). Microwave power settings are listed in tab. 7.2. NMR parameters (pulse sequence: zgpg): NS = 8, DS = 0, LB = 0.3 Hz, RD = 30 s, $P(\pi/2)$ = 41 W, $t_p\,(\pi/2)$ = 10 µs, waltz64, 0.58 W.

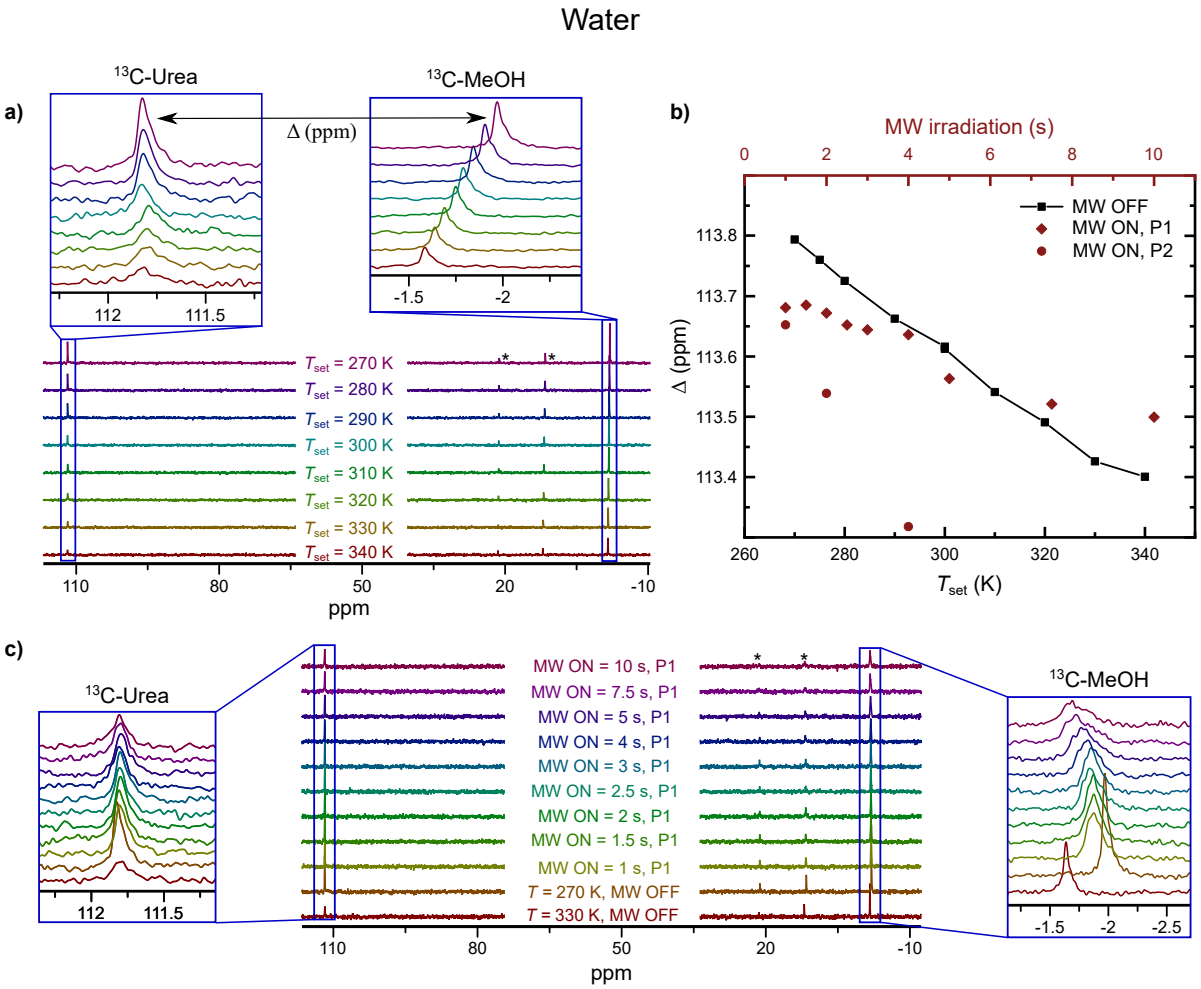

Figure 7.23: Temperature calibration of water with 10 % glycerol (w/w). a) ^{13}C NMR spectra of ∼ 250 mM ^{13}C-urea and ^{13}C-methanol in H_2O as a function of the temperature. b) Plot of the chemical shift difference of the reference compounds against the set sample temperature under Boltzmann conditions (black) and the duration of mw irradiation (red). c) The same spectra as in a) but for different mw irradiation times (T_{set} = 275 K). The asterisks mark glycerol. Microwave power settings are listed in fig 7.4. NMR parameters (pulse sequence: zgpg, see fig. 3.4b): NS = 8, DS = 2, LB = 2 Hz, RD = 30 s, $P(\pi/2)$ = 48 W, t_p $(\pi/2)$ = 10 µs, waltz64, 0.58 W.

distortion.

Accordingly, even smaller sample layers ($d \approx 25$ µm) were utilized for polar solvents such as dichloromethane, acetonitrile, and water. In order to exclude sample tube breaking inside the probehead caused by freezing water, DNP measurements were performed in a

mixture of 90 % water and 10 % glycerol (w/w), the latter serving as a glassing agent and therefore preventing volume expansion upon freezing.
Continuous wave mw irradiation in these solvents was impossible, because the NMR signal was broadened below the detection limit or bubbles formed in the solution that compromised the NMR spectrum. Instead, the microwave was gated at low power (P1 and P2) with the shutter introduced in sec. 7.1.3. Figure 7.23 shows the temperature calibration for H_2O that was performed with the same method as the one in CCl_4 and $CHCl_3$ but with ^{13}C-methanol and ^{13}C-urea as the chemical shift probes. It is evident that line broadening due to inhomogenous sample heating is the limiting factor for DNP in polar solvents. However, short microwave irradiation at low mw power (P1 and P2) of up to $4-7$ s is possible without compromising the NMR signal (see fig. 7.23c). Temperature calibration for CH_2Cl_2 and CH_3CN are shown in the appendix (fig. E.1 and fig. E.2).
In summary, temperature calibration of non-polar solvents demonstrated the possibility of DNP with high power mw irradiation. While cw mw irradiation is still possible for $CHCl_3$, more polar solvents such as CH_2Cl_2, CH_3CN, and H_2O were accessed via reduction of the mw power as well as the irradiation time. Nevertheless, the calibration data established mw irradiation schemes in all investigated solvents while retaining a sample temperature of $T_{\text{sample}} \approx 290-310$ K.

7.3.2 Magnetic Field Calibration

In order to maximize the signal enhancement, mw irradiation was applied precisely on resonance with the electron spins, however g_{iso} of the PA is solvent dependent (see fig. 7.1).[181] Therefore, the gyrotron frequency was matched with the resonance frequency of the electron spin for each sample. While for non-polar and most polar solvents, the sweep capabilities of the main magnetic field (~ 22 G) were sufficient to account for minor changes in the resonance frequency of the PA, measurements in water required changing of the gyrotron frequency (see fig. 7.1b).
This is illustrated in fig. 7.24. Here, the NMR signal intensity of acetonitrile is plotted as a function of the main magnetic field. Three field sweeps were performed, each with a different temperature of the gyrotron cavity (T_{cav}). A larger T_{cav} leads to a lower mw frequency ($\sim 4.3\frac{\text{MHz}}{\text{K}}$). At $T_{\text{cav}} = 22\,^{\circ}$C no increase in the NMR signal was observed

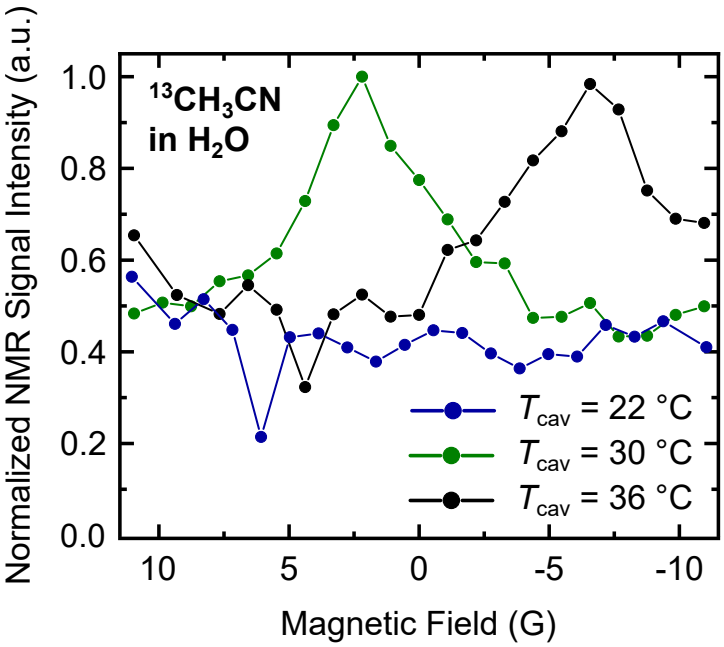

Figure 7.24: Magnetic field dependence of $^{13}C_2$-CH_3CN doped with $\sim 25\,mM$ ^{15}N-TN-d_{16} in H_2O obtained at different cavity temperatures of the gyrotron (T_{cav}). Microwave parameters: $I_{main} = 69.89\,A$, $V_0 = 16.27\,kV$, $I_{gun} = 2.75\,A$, $I_0 = 115\,mA$, $P \approx 22\,W$ (P1), mw gating = 2 s. NMR parameters (pulse sequence: zg with mw gating, see fig. 3.4d): $t_p\,(\pi/2) = 10\,\mu s$, $P\,(\pi/2) = 48\,W$, DS = 0, RD = 40 s, LB = 2 Hz, NS = 2.

(blue symbols and line). However, at $T_{cav} = 30\,°C$ a clear maximum was observed (green). With a cavity temperature of $T_{cav} = 36\,°C$, the maximum moved accordingly (black). As a result, water DNP experiments are performed on the high field resonance of the EPR spectrum, while irradiation in all other solvents is applied on the low field line. For a two line radical, irradiation of the first resonance is beneficial and boosts the saturation factor by $5 - 20\,\%$[34,83]

7.3.3 Analysis of DNP Experiments in Polar Solvents

Because of its high solubility in various solvents, acetonitrile (2-^{13}C $c(^{13}CH_3CN) \approx 500\,mM$ and $c(PA) \approx 25\,mM$) was used as a test molecule to compare the DNP performance of the same system in non-polar and polar solvents. Figure 7.25 shows the DNP experiments of acetonitrile in CCl_4, $CHCl_3$, CH_3CN, and H_2O. Measurements were performed with maximum available power (light red fig. 7.25a and b) and with an irradiation time of

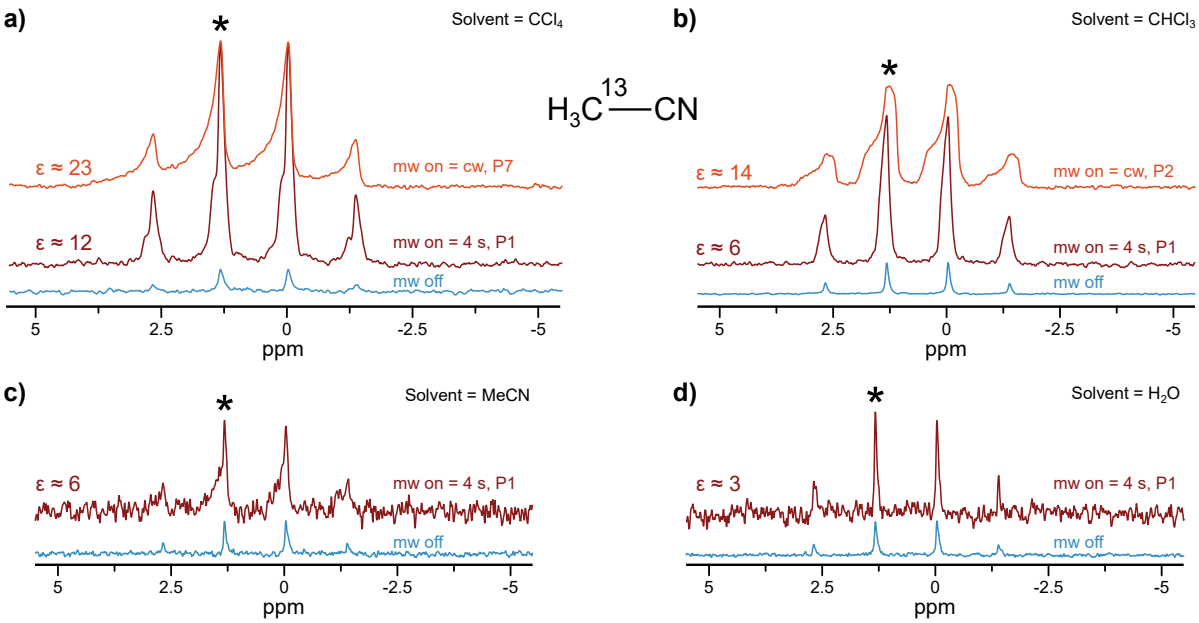

Figure 7.25: Comparison of the signal enhancement of the methyl group ($^{13}C_2$) of acetonitrile in different solvents. Spectra are scaled according to their number of scans. Spectra in light red were obtained under cw mw irradiation (P7 and P2 for measurements in CCl_4 and $CHCl_3$, respectively), while spectra displayed in dark red were measured with 4 s (2 s in H_2O) mw irradiation with $P = 22$ W (P1). Boltzmann spectra are shown in blue. NMR parameters for a), b), c), and d) (pulse sequence: zg): $t_p\,(\pi/2) = 10\,\mu s$, $P\,(\pi/2) = 41$ W, DS = 2, RD = 30 – 40 s, LB = 4 Hz (for a and b), LB = 2 Hz (for c and d). Sample temperatures were adjusted with the calibration curves and were in the range of $T_{sample} \approx 290 - 310$ K (mw off spectrum of CCl_4 was acquired at $T_{sample} \approx 275$ K). c(PA) ≈ 25 mM, $c(^{13}CH_3CN) \approx 500$ mM. (*) LW of these signals are listed in tab. 7.10. Experimental error for ϵ is estimated to be 10 – 20 %. Boltzmann and DNP spectra were acquired with the same pulse sequence.

4 s at P1 (red, 2 s mw irradiation in the case of water), the latter being the highest possible power setting in polar solvents. Sizable signal enhancement ranging from 23 to 3 were observed. The LW is highly solvent dependent, ranges from 6 Hz to 60 Hz, and is surprisingly the narrowest in H_2O. Enhancements and LWs are listed in tab. 7.10.

Under comparable power settings, the signal enhancement decreases from $\epsilon_{CCl4} \approx 12$ to $\epsilon_{H2O} \approx 3$. The smaller signal enhancement in H_2O compared to CCl_4 is most likely related to a reduced saturation factor that is caused by an increased mw absorption of the solvent. Assuming that the reduced ϵ results exclusively from a smaller s, the comparison of acetonitrile in different solvents leads to $s \approx 0.05$ in H_2O as opposed to $s \approx 0.3 - 0.4$

Table 7.10: Signal enhancements and linewidths of the marked signal (*) of acetonitrile in different solvents displayed in fig. 7.25. (†) The enhancement in dichloromethane was obtained with 6.0 s irradiation at P1. (‡) In water, mw irradiation was applied for 2 s. Experimental error for ϵ is estimated to be $10-20\,\%$.

parameter	CCl_4	$CHCl_3$	CH_2Cl_2	CH_3CN	H_2O
ϵ (mw on = cw)	22	14	$10^{\dagger}$	–	–
ϵ (mw on = 4 s)	12	6	7	6	$3^{\ddagger}$
LW (mw on = cw) (Hz)	23	40	–	–	–
LW (mw on = 4.0 s) (Hz)	11	17	~ 55	7.7	4.2
LW (Boltzmann) (Hz)	8.2	4.0	6.2	4.2	4.9

in CCl_4 (with $\epsilon(^{13}CH_3CN) \approx 21$ in CCl_4). Nevertheless, it is important to point out that these results demonstrate the feasibility of DNP with µL sample volume at high magnetic field in polar solvents including water.

To further investigate DNP in water, different target molecules such as Na pyruvate were tested. Na pyruvate is a biologically highly relevant compound and target of other hyperpolarization techniques such as dissolution DNP.[6,31,230] Figure 7.26a shows the DNP spectrum of the methyl group of Na pyruvate with an enhancement of (ϵ(3-^{13}C ≈ 3) with c (^{15}N-TN-d_{16}) ≈ 25 mM and a LW that is unaffected by mw irradiation (LW $\approx 6-7$ Hz). In comparison, a recent study reported ϵ(3-^{13}C) ≈ 16 (with $s \approx 1$) for 1 M Na pyruvate in water in a Fabry-Pérot cavity with ~ 100 mM TEMPOL as a PA and $V_{\text{sample}} \leq 100$ nL.[112] While the herein presented ϵ is a factor of five smaller than previously reported by another group,[112] the sample volume is a factor of ~ 100 larger than in the literature resulting in an overall increase in NMR signal sensitivity.

Furthermore, from the measurement of the nuclear relaxation time of the methyl group of pyruvate (see fig. D.1) with and without PA, a leakage factor of $f \approx 0.75$ was calculated. Considering f and scaling the obtained signal enhancement ($\epsilon \approx 3$) to the literature,[112] the saturation factor is estimated to be $s \approx 0.14$. However, the earlier reported comparison of acetonitrile in different solvents (see fig. 7.25) resulted in $s \approx 0.05$ in H_2O. As both calculations of s contain many uncertainties (comparison of different setups, possible solvent effects), a more precise estimation than $s \sim 0.05-0.14$ remains challenging. However, the results show that even though the mw efficiency is reduced due to mw absorption of the solvent, lower mw power, and shorter mw irradiation time, sizable signal

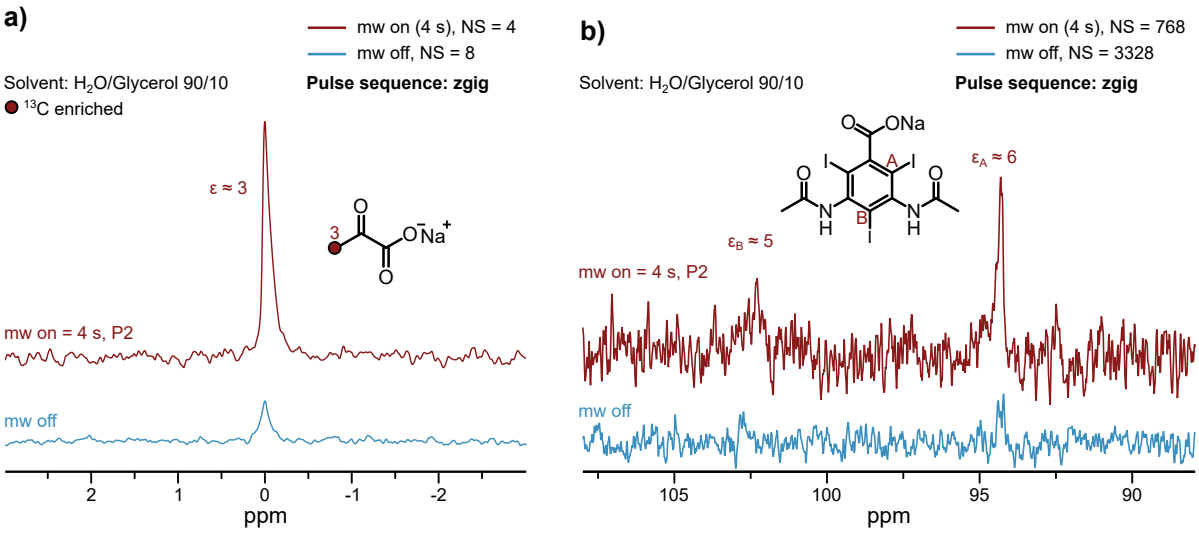

Figure 7.26: DNP enhanced spectra (red) and Boltzmann spectra (blue) of $^{13}C_3$ Na pyruvate ($\sim 500\,\text{mM}$, with $\sim 25\,\text{mM}$ ^{15}N-TN-d$_{16}$) and Na diatrizoate ($\sim 500\,\text{mM}$ with $\sim 25\,\text{mM}$ ^{15}N-TN-d$_{16}$ and $\sim 500\,\text{mM}$ $^{13}C_2$ acetonitrile) in H_2O. b) shows a zoom-in-view on the iodinated positions. The full spectrum is shown in appendix. C fig. C.13a. Microwave parameters: $P = 29\,\text{W}$ (P2) and 4 s mw irradiation for Na pyruvate and Na diatrizoate, respectively. $T_{\text{sample}} \approx 290 - 310\,\text{K}$. NMR parameters (pulse sequence: zgig, see fig. 3.4d): $t_p\,(\pi/2) = 10\,\mu\text{s}$, $P\,(\pi/2) = 41\,\text{W}$, DS = 2, RD= $26 - 40\,\text{s}$, LB = 4 Hz. b) shows a zoom-in-view on iodinated carbon positions. Experimental error for ϵ is estimated to be $10 - 20\,\%$. Spectrum a) was referenced to 0 ppm, while the ppm scale in b) is arbitrarily chosen, due to the lack of a reference. Boltzmann and DNP spectra were acquired with the same pulse sequence.

enhancements of $\epsilon \approx 3$ are accessible with Na pyruvate in H_2O, while retaining an NMR linewidth of $\sim 6\,\text{Hz}$. Optimization of the sample cooling setup could enable stronger and longer mw irradiation and therefore further boost DNP in water.

As large enhancements for iodinated compounds were observed in non-polar solvents (see sec7.2.3), this motif was also investigated in H_2O. Indeed, DNP measurements of Na diatrizoate, an X-ray contrast agent, showed $\epsilon \approx 6$ on the iodinated positions in H_2O (fig. 7.26), which is a factor of two larger than ϵ obtained for acetonitrile and pyruvate ($\epsilon \approx 3 - 4$). This demonstrates that also in water the spin polarization transfer to iodinated carbon positions is highly favored over, for example, methyl groups (e.g. Na pyruvate and acetonitrile). Consequently, site-specific iodination[229] might be a viable strategy to obtain large ^{13}C NMR signal enhancements also in water.

An analysis of the LW of Na diatrizoate revealed that the signal at 94 ppm is mostly unaffected by mw irradiation with LW $\approx$ 21 Hz for the Boltzmann and for the DNP spectrum. On the other hand, the signal at $\sim$ 102 ppm is significantly broadened (LW $\approx$ 100 Hz) but direct comparison with the Boltzmann signal remains difficult (see fig. 7.26b) due to a poor signal-to-noise-ratio.
These first results on polar solvents including water are a proof-of-principle for DNP in polar liquids with µL sample volume. It demonstrated the viability of DNP on different target molecules as well as in a variety of polar solvents. Sizable signal enhancements of up to $\epsilon \approx 6$ are accessible in DNP experiments in H_2O. It can be anticipated that further optimization of the cooling setup and irradiation scheme should enable stronger mw irradiation and boost the enhancements in water. More sophisticated tube arrangements, for example with many sample layers being exposed to the sample, enable mw irradiation at elevated mw power and allow for significant larger sample volumes.

7.4 2D Dynamic Nuclear Polarization in Liquids at 9.4 T

One strength of NMR is the ability to obtain structural resolution on the atomistic scale by identifying through bond but also through space correlations between different nuclei.[10,15] This allows not only for the determination of the structure[231] of large systems such as proteins but also enables the analysis of dynamical processes[4,232,233] and interactions between pharmaceutical drugs and biological macromolecules.[13,232,234]
Many experiments require chemical shift encoding during two or more delays (t_i) in the pulse sequence, thus resulting in a multidimensional spectrum. Throughout the past decades, hundreds of different iterations of multidimensional pulse sequences emerged[235] and are nowadays applied in routine NMR experiments.[10] Among these powerful tools, direct ^{13}C-^{13}C correlation experiments provide valuable information on large systems. For example ^{13}C detection may simplify NMR spectra in comparison to ^{1}H, due to a larger frequency range, and help with unambiguous signal assignment for the characterization of large proteins.[57] Moreover, large chemical shift dispersion as well as longer relaxation times for ^{13}C compared to ^{1}H in flexible and disordered proteins may promote the application of ^{13}C-^{13}C correlation experiments to detect intermolecular interactions.[57] Finally, paramagnetic samples may also benefit from direct ^{13}C measurements, due to a reduced

(in comparison to ^{1}H) paramagnetic relaxation.[236] However, these measurements are hampered by the low sensitivity of the ^{13}C nucleus stemming from its low gyromagnetic ratio ($\gamma_{1H}/\gamma_{13C} \approx 4$) and natural abundance (1.1 %). Therefore, hyperpolarization techniques can boost the sensitivity of these pulse sequences.

Hyperpolarized 2D experiments in liquids were demonstrated with dDNP, where the exchange of water protons with labile protons of proteins was used with ex situ hyperpolarized water.[32] Upon insertion of an unsaturated carbon-carbon bond, also PHIP was used for hyperpolarized 2D experiments, however similarly to dDNP, para-hydrogen based experiments exclude extensive signal averaging.[237] 2D experiments were also coupled with rapid-melt and temperature-jump DNP experiments,[63,236] where hyperpolarization is performed at $\sim$ 100 K and the signal is detected in the liquid state after rapid melting of the sample.

For Overhauser DNP, ^{1}H and ^{19}F 2D experiments were performed at low to medium magnetic fields ranging from 0.34 T over 1.2 T to 3.4 T, because at these magnetic fields, the polarization transfer mechanism of ^{1}H is still favorable, thus allowing for large signal enhancements.[191,238,239] However, at magnetic fields as high as 9.4 T, the NMR signal enhancement on proton has mostly decayed due to dipolar dominated cross-relaxation.[46] At such high magnetic fields ($B_0 \geq 9.4$ T), two recent studies demonstrated the spin polarization transfer from ^{13}C to ^{1}H on model systems via the insensitive nuclei enhancement by polarization transfer (INEPT) sequence and subsequent detection of ^{1}H under DNP conditions.[40,41] Furthermore, a triple resonant probehead (S, ^{1}H and ^{13}C) was reported and showed the possibility of proton decoupling upon ^{13}C detection.[41,112]

To demonstrate 2D liquid state DNP at 9.4 T, $^{13}C_6$-C_6H_5I as well as natural abundant p-IC_6H_4F were selected as model systems and investigated with representative 2D pulse sequences. Particularly, double quantum filtered correlation spectroscopy (DQF COSY), total correlation spectroscopy (TOCSY), and the incredible natural abundance double quantum transfer experiments (INADEQUATE) are pulse sequences that are routinely applied on a variety of systems including small molecules and therefore represent a good starting point for 2D DNP in the liquid state at 9.4 T. Enhancements were obtained from integration of the 2D signals.

7.4.1 Dynamic Nuclear Polarization Double Quantum Filtered Correlation Spectroscopy (DNP DQF COSY)

Because of its widespread application as a routine tool to characterize small molecules, correlation spectroscopy (COSY)[241,242] was the first 2D pulse sequence that was tested under DNP conditions. The experiment correlates J-coupled nuclei, thus giving rise to a cross peak in the 2D spectrum. Figure 7.27c shows a schematic spectrum of the target molecule $^{13}C_6$-C_6H_5I displayed in fig. 7.27a. In DQF COSY experiments, the intensity of cross peaks is governed by the size of the scalar coupling for any pair of spins.[10,92] As typically the coupling between direct neighboring ^{13}C nuclei is much larger than between ^{13}C atoms separated by two or more bonds ($^1J_{CC} \gg {}^nJ_{CC}$), in a routine ^{13}C DQF COSY spectra, cross peaks were only observed for neighboring ^{13}C-^{13}C pairs.[10,92]
In a traditional COSY, the antiphase doublet cross peaks are shifted by 90 ° (inset of fig. 7.27c) with respect to the diagonal peaks.[92] This leads to a dispersive lineshape of either the diagonal or the cross peak. A dispersive lineshape is undesirable, because peaks are significantly broadened and may cover important cross peaks. Furthermore, the antiphase structure of the cross peaks might lead to signal cancellation if LW $\approx J$.[92] Therefore, a double quantum filter (DQF) is applied to overcome this limitation by introducing an additional 90 ° pulse that selects double quantum coherences. This results in an antiphase absorptive signal for diagonal- as well as for cross peaks. However, the price to pay is that only half of the signal proceeds through the filter, thus reducing the sensitivity of the experiment.[92] The product operator evolution is presented in sec. 3.3.4.2 and coherence selection is achieved via phase cycling. DNP can effectively improve DQF COSY, because the obtained signal enhancement compensates for the reduced signal intensity caused by the DQF.
Figure 7.27b and d show the DQF COSY spectra of $\sim$ 500 mM $^{13}C_6$-C_6H_5I in CCl_4 doped with $\sim$ 25 mM ^{15}N-TN-d_{16} under DNP and Boltzmann conditions, respectively, with the experimental parameters listed in the caption. As indicated in the pulse sequence in fig. 7.27a, mw irradiation is applied continuously throughout the whole measurement. Sizable ^{13}C signal enhancements are observed for all cross- and diagonal-peaks and the observed ϵ is comparable to the values obtained in 1D DNP experiments of the same compound. As the DNP DQF COSY experiment was compared to a Boltzmann spectrum

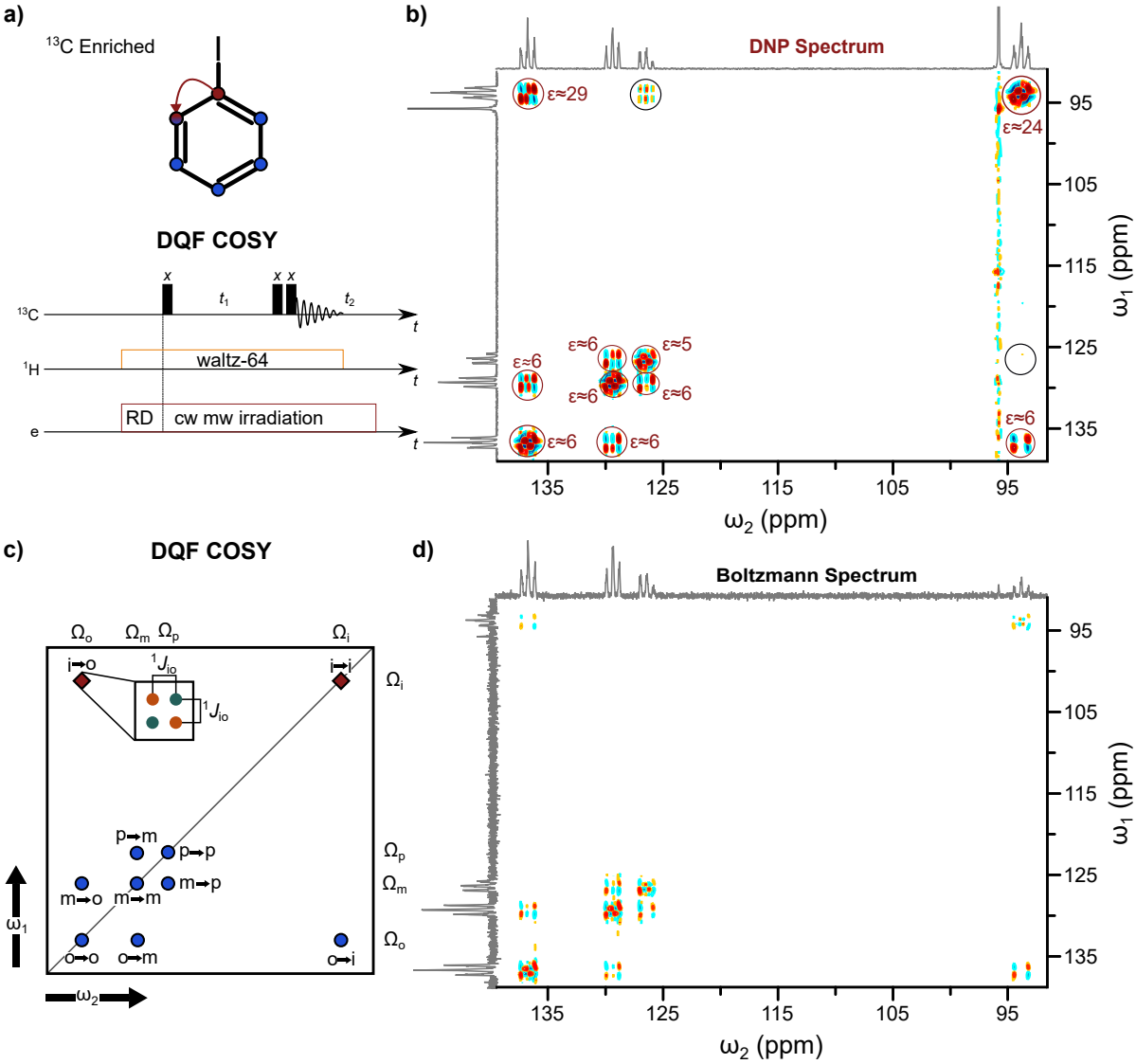

Figure 7.27: a) Structure of $^{13}C_6$-C_6H_5I indicating the magnetization transfer for the C_{ipso} position and the DQF COSY pulse sequence. b) DNP DQF COSY spectrum with an independently measured 1D DNP spectrum of the same sample as a guide on the ω_1 and ω_2 dimension. c) Sketch of the DQF COSY spectrum of C_6H_5I, representatively highlighting the magnetization transfer of C_{ipso}. d) Boltzmann DQF COSY spectrum with an independently measured 1D Boltzmann spectrum of the same sample as a guide on the ω_1 and ω_2 dimension. Sample composition: $\sim 500\,\text{mM}$ $^{13}C_6$-C_6H_5I and $\sim 25\,\text{mM}$ ^{15}N-TN-d_{16}. Microwave power (cw irradiation): $P = 43\,\text{W}$ (P5), $T_{\text{sample}} \approx 290 - 310\,\text{K}$. NMR parameters: NS = 8, DS = 16, RD = 6 s, $t_p\,(\pi/2) = 10\,\mu\text{s}$, $P\,(\pi/2) = 48\,\text{W}$, ^{1}H decoupling: waltz64, 0.58 W, number of points (TD)(ω_1,ω_2) = 128,2048, LB = 2 Hz, phase cycle:[240]. Experimental error for ϵ is estimated to be $10 - 20\,\%$.

of the same sequence, i.e. with ^{1}H pre-saturation, the obtained 2D enhancements are compared to the apparent 1D enhancements for $^{13}C_6$-C_6H_5I (see tab. C.3 and appendix C fig. C.4b). Notably, even though 2D measurements were acquired with a much shorter recycle delay (RD = 6 s) than in the 1D experiments (RD = 30 s), similar enhancement factors were obtained in 1D and 2D measurements (see tab. 7.6 and fig. C.4b).
A comparison of the two cross peaks arising from the coupling of C_{ipso} to C_{ortho} on the two sides of the spectrum shows a large difference in the observed enhancement being $\epsilon \approx 29$ and $\epsilon \approx 6$. This is rationalized by comparing of the evolution of the magnetization during the pulse sequence. For the cross peak with $\epsilon \approx 29$ (93.9 , 136.8) ppm, (ω_1, ω_2) initial excitation is performed on the C_{ipso} position ($\epsilon(1D) \approx 25$), which leads to transverse magnetization of C_{ipso} during t_1. Subsequent transfer of the magnetization via J-coupling to C_{ortho} and detection during t_2 results in the cross peak. On the other hand, magnetization of the cross peak with $\epsilon \approx 6$ (136.8 , 93.9) ppm, (ω_1, ω_2) stems from initial excitation of C_{ortho} with $\epsilon(1D) \approx 6$ (see tab. 7.6 ϵ with ^{1}H pres-saturation) and is transferred to C_{ipso} via J-coupling. Evidently, the ^{13}C NMR signal enhancement of the initially excited spin is decisive for the signal enhancement of the cross peak. Therefore, the initial spin polarization is efficiently transferred during the evolution of the magnetization within the COSY sequence.
Finally, even though in ^{13}C COSY experiments mostly ^{1}J-couplings deliver cross peaks, a cross peak is also observed for C_{ipso} coupled to the C_{para} position (black circled fig. 7.27b), while it is invisible in the Boltzmann (at the same noise level) as well as in the DNP spectrum in quadrant four (bottom right, black circle).

7.4.2 Dynamic Nuclear Polarization Total Correlation Spectroscopy (DNP TOCSY)

While COSY reveals correlations between adjacent nuclei, total correlation spectroscopy (TOCSY) extends this to the whole coupled spin system. In order to observe a cross peak between spin A and spin B, no J-coupling between these spins is necessary as long as they are connected by a third (or fourth) spin that is coupled to both spins.[92]
As observed in the COSY experiment, the large spin polarization is conserved throughout the pulse sequence and delivers large signal enhancements on the cross peaks. Therefore,

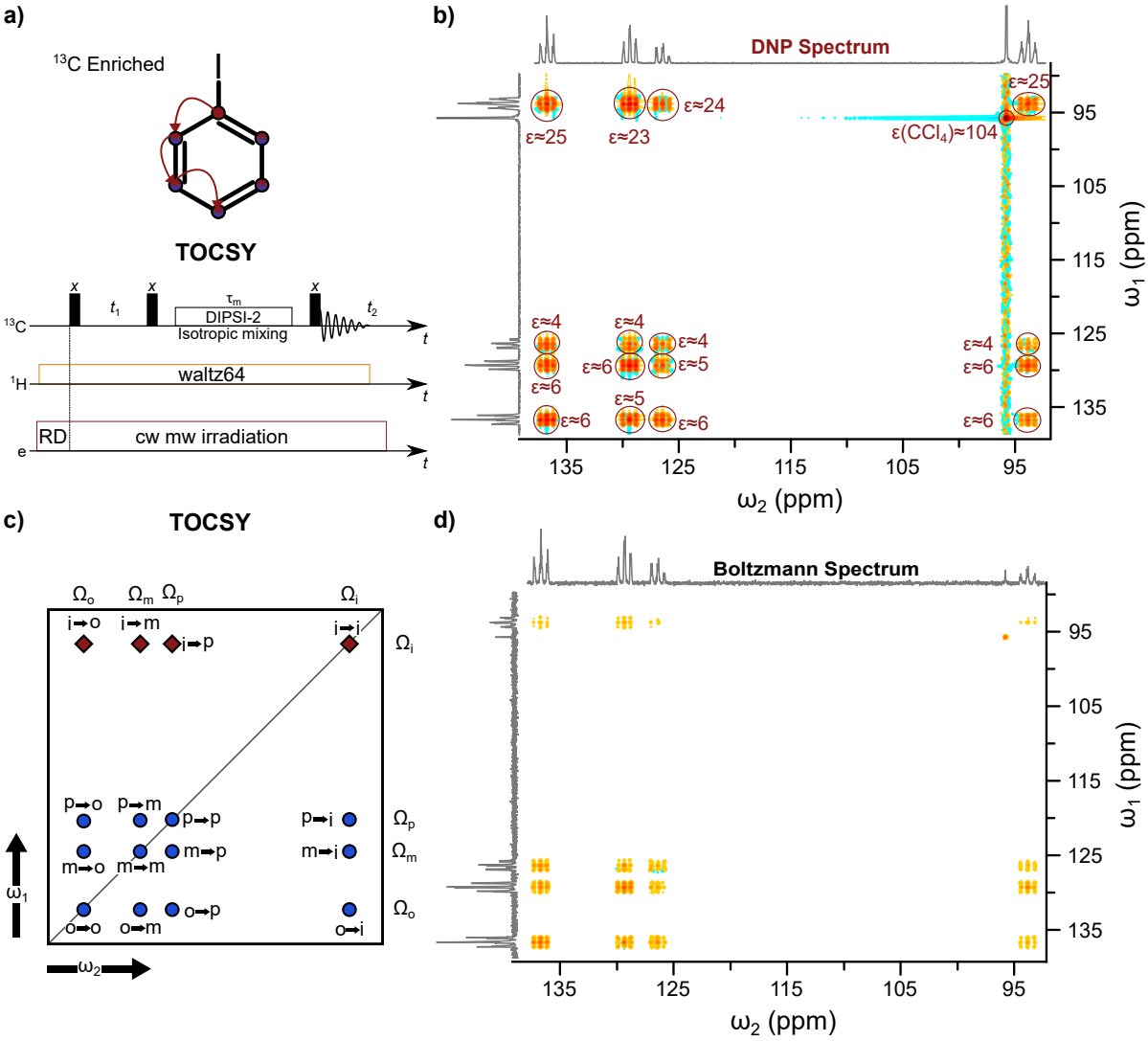

Figure 7.28: a) Structure of $^{13}C_6$-C_6H_5I indicating the magnetization transfer for the C_{ipso} position and the TOCSY pulse sequence. b) 2D DNP TOCSY spectrum with an independently measured 1D DNP spectrum of the same sample as a guide on the ω_1 and ω_2 dimension. c) Sketch of the TOCSY spectrum of C_6H_5I, representatively highlighting the magnetization transfer of C_{ipso}. d) Boltzmann TOCSY spectrum with an independently measured 1D Boltzmann spectrum of the same sample as a guide on the ω_1 and ω_2 dimension. Sample composition: $\sim 500\,\text{mM}$ $^{13}C_6$-C_6H_5I and $\sim 25\,\text{mM}$ ^{15}N-TN-d_{16}. Microwave power (cw irradiation): $P = 43\,\text{W}$ (P5), $T_{\text{sample}} \approx 290 - 310\,\text{K}$. NMR parameters: NS = 8, DS = 16, RD = 6 s, $t_p\,(\pi/2) = 10\,\mu\text{s}$, $P\,(\pi/2) = 48\,\text{W}$, ^{1}H decoupling: waltz64, 0.58 W, number of points TD(ω_1,ω_2 = 256,2048, τ_m=20 ms, LB = 2 Hz, phase cycle: 8 steps following the Topspin sequence dipsi2phdc. Experimental error for ϵ is estimated to be $10 - 20\,\%$.

it is expected that DNP TOCSY sequence can distribute the large spin polarization over the whole spin system.

Figure 7.28a sketches the pulse sequence with cw mw irradiation. In contrast to the COSY experiment, in TOCSY magnetization is transferred during a period of isotropic mixing, where a spin lock pulse train consisting of multiple π pulses is applied. There are multiple isotropic mixing schemes and therefore different iterations of TOCSY.[113–116] Here, the DIPSI-2 mixing scheme is employed.[116] During the isotropic mixing period, the spin system is in the strong coupling regime and magnetization is exchanged among the different spins.[10] The efficiency of this process is different for each cross peak and depends on the mixing time τ_m.[10] After initial tests, a mixing time of $\tau_m = 20\,\text{ms}$ was chosen for the herein presented experiments. Figure 7.28c sketches the schematic TOCSY spectrum of C_6H_5I that consists of a single spin system and cross peaks, that arise from the excitation of the C_{ipso} position, are highlighted.

Figure 7.28b and d show the DNP and Boltzmann spectrum of $^{13}C_6$-C_6H_5I in CCl_4 doped with $\sim 25\,\text{mM}$ ^{15}N-TN-d_{16}, respectively. As in DNP DQF COSY, ^{13}C signal enhancements are observed for all diagonal- and cross peaks being comparable in magnitude to ϵ obtained in the 1D experiments. Similarly to the DQF COSY experiment, the TOCSY was also performed with ^{1}H pre-saturation during DNP and Boltzmann measurement. Consequently, the obtained enhancements were compared to 1D apparent signal enhancements (tab. C.3 and appendix C fig. C.4b). As expected from the COSY, large signal enhancements ($\epsilon \approx 23 - 25$) are observed for the cross peaks centered at $\omega_1 \approx 93.8\,\text{ppm}$ originating from initial excitation of the C_{ipso} position. This demonstrates that the polarization transfer from highly polarized nuclei to nuclei with smaller signal enhancement is viable with the TOCSY sequence. A comparison of the signal enhancement between COSY and TOCSY also reveals that the spin polarization transfer efficiency is comparable between the two sequences, thereby establishing the possibility to transfer nuclear spin polarization of hyperpolarized nuclei with both pulse sequences to other nuclei on the same molecule.

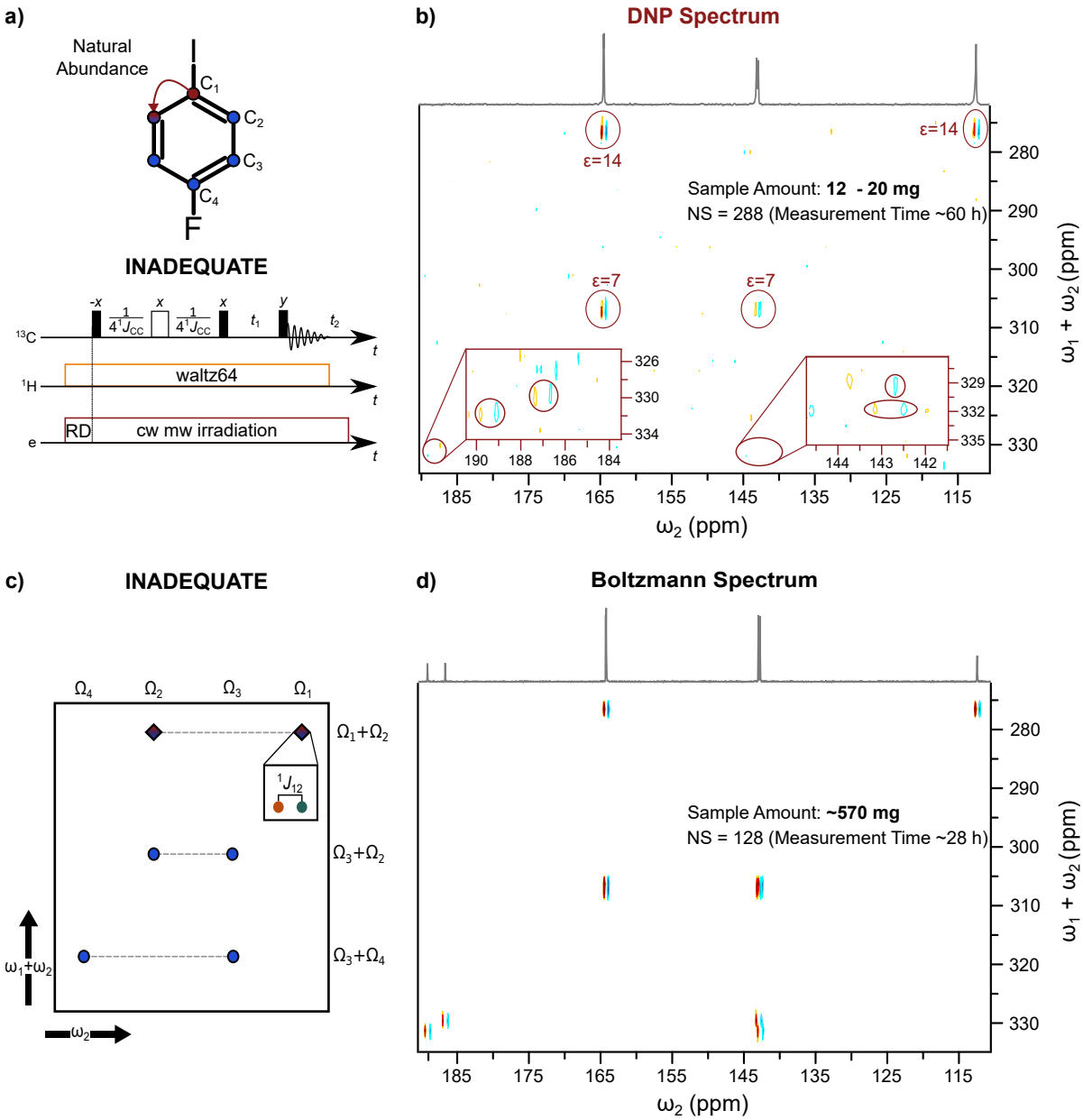

Figure 7.29: a) Structure of *p*-IC_6H_4F indicating the magnetization transfer for the C_{ipso} position and the INADEQUATE pulse sequence. b) 2D DNP INADEQUATE spectrum of ∼1.5 M *p*-IC_6H_4F doped with ∼ 25 mM ^{15}N-TN-d_{16} with an independently measured 1D DNP spectrum of the same sample as a guide in the ω_2 dimension. Microwave power (cw irradiation): $P = 43$ W (P5), $T_{sample} \approx 290 - 310$ K. NMR parameters: NS = 288, DS = 16, RD = 6 s, $^1J_{CC} \approx 55$ ms, $t_p\,(\pi/2) = 10\,\mu$s, $P\,(\pi/2) = 48$ W, ^{1}H decoupling: waltz64, 0.58 W, TD(ω_1,ω_2) = 128,2048, LB = 2 Hz, phase cycle: ref. [118]. c) Sketch of the INADEQUATE spectrum of *p*-IC_6H_4F. d) Boltzmann INADEQUATE spectrum with an independently measured 1D Boltzmann spectrum of the same sample as a guide in the ω_2 dimension. Sample composition: 50/50 (v/v) of *p*-IC_6H_4F and C_6H_{12}. NMR parameters: as in b) except for NS = 128. Experimental error for ϵ is estimated to be $10 - 20$ %.

7.4.3 Dynamic Nuclear Polarization Incredible Natural Abundance Double Quantum Transfer Experiment (DNP INADEQUATE)

The two previously discussed pulse sequences were tested with ^{13}C enriched iodobenzene. However, for the detection of ^{13}C-^{13}C correlations at natural abundance, neither of these two sequences is better suited than the incredible natural abundance double quantum transfer experiment (INADEQUATE), which was specifically designed for this purpose.[10,117]

As discussed earlier, TOCSY requires a chain of coupled spins, however the natural abundance of ^{13}C is only 1.1 %, thus the likelihood to have two ^{13}C spins next to each other is $\sim 10^{-4}$, rendering the TOCSY sequence unpractical. In principle, COSY is a viable option for the measurement of ^{13}C-^{13}C correlations on natural abundance samples but the intensity of the diagonal-peaks is a factor of 100 stronger than for the cross peaks. Therefore, the diagonal-peaks may cover the more important cross peaks. On the other hand, the INADEQUATE sequence suppresses signals stemming from isolated ^{13}C spins, thereby leaving only contributions to the spectrum originating from two coupled ^{13}C spins. The product operator treatment of the pulse sequence is summarized in sec. 3.3.4.4.

Figure 7.29c displays a sketch of the INADEQUATE spectrum of the tested compound *p*-IC_6H_4F (fig. 7.29a). Notably, the signals are centered at $\Omega_1 + \Omega_2$ in the ω_1 dimension and at Ω_1 and Ω_2 in the ω_2 dimension. *p*-IC_6H_4F serves as model a system, because in 1D measurements it displayed large signal enhancements of up to $\epsilon(C_{ipso}) \approx 33$. Unfortunately, and most likely due to complications during the sample preparation, the 1D signal enhancement of this particular sample was reduced to $\epsilon \lesssim 23$ (see appendix C fig. C.16b). As in COSY and TOCSY, 2D signal enhancements were compared to apparent 1D enhancements, because the 2D DNP and Boltzmann were acquired with ^{1}H pre-saturation. Notably, for a better comparison, 2D experiments could be repeated without ^{1}H pre-saturation, however based on the reported observations, 2D signal enhancements should follow the expected behaviour and reproduce 1D enhancements.

Nevertheless, the DNP INADEQUATE as well as the Boltzmann spectrum are displayed in fig. 7.29b and d, respectively. The sample composition used for DNP measurements consisted of 1.5 M target molecule ($\sim 12 - 20$ mg) in cyclohexane doped with ~ 25 mM ^{15}N-TN-d_{16}, while the Boltzmann spectrum was acquired with a mixture of 50 % target

molecule ($\sim 570\,\mathrm{mg}$) and 50 % cyclohexane (v/v).
Volumetric scaling of the Boltzmann spectrum and subsequent comparison with the DNP spectrum produces a ^{13}C NMR signal enhancement of up to $\epsilon \approx 14$, which is approximately 25 % smaller than the 1D enhancement on the same sample. In contrast to COSY and TOCSY, the expected enhancement for DNP INADEQUATE is obtained as the mean value of the 1D enhancements of the two coupled spins that lead to the cross peaks,

$$\epsilon_{C_1-C_2} \approx \frac{\epsilon_{1D}(C_1) + \epsilon_{1D}(C_2)}{2}, \tag{7.2}$$

if the Boltzmann polarization of the two spins is comparable. This originates from the pulse sequence that selects double quantum coherences arising from a coupled spin pair and rejects single quantum magnetization.[10] These coherences are converted into observable magnetization contributing to the signal centered at Ω_1 as well as at Ω_2, independently on the initially excited spin.[10] Considering this, the obtained signal enhancements during the INADEQUATE measurement agree with the 1D signal enhancement with $\frac{\epsilon_{1D}(C_1)+\epsilon_{1D}(C_2)}{2} \approx 15$ (see appendix C fig. C.16b).
Finally, the C_4 signal (see fig. 7.29a for carbon numbering) is suppressed in the 1D DNP spectrum (see ω_2 trace in fig. 7.29b), most likely due to a dipolar dominated spin polarization transfer mechanism. However, the C_4 signal is recovered in the 2D spectrum (see zoom-in-view insets fig. 7.29b).
This further solidifies the conclusion that, as soon as significant signal enhancement is observed at one carbon nucleus, the spin polarization can be transferred to different carbon sites of the molecule. Indeed, also carbon positions that do not show any signal enhancement in a 1D spectrum, due to an unfavorable DNP mechanism, are visible as hyperpolarized cross peaks in a 2D DNP experiment.
In summary, the presented experiments establish the viability of 2D NMR under DNP conditions. Implementation of 2D sequences under cw mw irradiation is possible without modifications of the NMR pulse sequence. These measurements on model systems demonstrated that routine NMR pulse sequences are possible under DNP conditions and will open up new possibilities for applications of liquid state DNP on, for example, biologically active molecules. Particularly, site-specific labelling with, for example, iodine[229] may

introduce a source of large signal enhancement on a biological target that could be transferred to nearby nuclei.

8 Conclusion and Outlook

Mechanistic Insights from DNP at Low Magnetic Field

^{13}C DNP experiments were performed on $^{13}CCl_4$ and $^{13}CHCl_3$ with different polarizing agents (chapter 4). A variation of up to a factor of four in DNP efficiency, represented by the coupling factor ξ of the Overhauser equation, was observed. Particularly, BDPA ($\xi(CHCl_3) \approx -0.12$) performs worse than nitroxide derivatives ($\xi_{^{15}N\text{-}TN\text{-}d16}(CHCl_3) \approx -0.49$).[34] This discrepancy was attributed to the highly delocalized electron density for BDPA, while most of the spin density is localized on the NO group of nitroxides.
However, ξ varied also among different nitroxides. Indeed, a variation of almost a factor of two was observed between the worst (TN-py, $\xi(CHCl_3) \approx -0.23$) and the best (^{15}N-TN-d_{16}, $\xi(CHCl_3) \approx -0.49$)[34] nitroxide. This difference correlated well with the accessibility of the NO moiety, where most of the spin density resides.
While chapter 4 focused on the molecular structure, chapter 5 dealt with the influence of molecular dynamics on the DNP efficiency. To this end, the different contributions to dipolar cross-relaxation mechanisms were experimentally disentangled by the variation of the temperature and the molecular size of the PA during ^1H DNP experiments. A similar study was recently performed by the Prisner group at 9.4 T and reported that the role of rotational diffusion is also evident at high magnetic field.[56] Combining rotational and translational diffusion with ^{13}C DNP experiments at 1.2 T revealed an unexpected high DNP efficiency for a nitroxide based radical functionalized with a fullerene (FN-2a) in comparison to ^{15}N-TN-d_{16}.[34] Complementary MD simulations showed that molecular

reorientations of the methyl group distinctive for FN-2a might be effectively increasing the DNP performance.

In summary, these two studies delivered general structural motifs for the design of efficient ^{13}C DNP PAs. First, the electron spin density should be highly localized and accessible and second the molecular structure should ideally facilitate structural reorientations (e.g. ring inversion, conformational changes, and methyl rotations) that act on a ps to sub-ps timescale. In combination with the knowledge of the electron spin relaxation properties, these insights can enable the optimization of PAs for high field DNP.

Furthermore, understanding the role of solvents and particularly water coordinating to a radical center is an active field of research and is investigated in protein complexes as well as in the gas phase.[243,244] ODNP was used for the analysis of translational diffusion to obtain structural information on water hydration,[139,245,246] however also scalar cross-relaxation may deliver important dynamic information.[78] For instance, in order for a chemical reaction to occur, the two educts must meet with the correct orientation and energy to form a transition state, which eventually leads to the product.[247] In the future, rates and durations of such encounters might be analyzed with ODNP, because the collision model for scalar cross-relaxation delivers collision durations and frequencies.[78]

Finally, dynamic investigations via DNP could be extended to a variety of nuclei such as ^{31}P and ^{19}F that already showed scalar dominated enhancements at low and high magnetic field.[69,191]

Dynamic Nuclear Polarization at 9.4 Tesla

The second avenue that was followed in this PhD thesis was the development of a new liquid state DNP instrument operating at 9.4 T. After the initial installation, the mw power and frequency range of the frequency agile gyrotron were characterized. This was followed by tests of the mw beam alignment, the mw polarization, and power losses at the sample position inside the probehead.

Microwave irradiation is performed from the side of the tube, where the sample is confined to a thin layer. This arrangement limits mw absorption of the solvent and with the integration of active sample cooling, enables DNP experiments in polar solvents with a sample volume of $V_{sample} \approx 15\,\mu L$ for water and of up to $V_{sample} \approx 40\,\mu L$ in non-polar

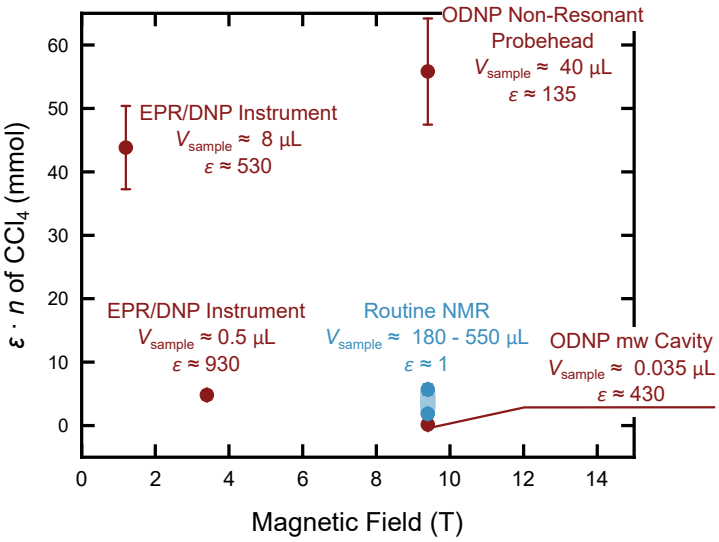

Figure 8.1: Experimental signal enhancement times amount of substance ($\epsilon \cdot n$ [mmol]) of neat CCl_4 doped with a nitroxide radical as a function of the magnetic field (red circle). Calculated $\epsilon \cdot n$ for a routine 3 mm and 5 mm NMR tube with $\epsilon = 1$ and $V_{sample} \approx 180\,\mu L$ and $V_{sample} \approx 550\,\mu L$ (blue circles) is shown for comparison. The following parameters were used to calculate $\epsilon \cdot n$: EPR/DNP instrument at 1.2 T: $\epsilon \approx 530$, $V_{sample} \approx 8\,\mu L$,[34] EPR/DNP instrument at 3.4 T: $\epsilon \approx 930$, $V_{sample} \approx 0.5\,\mu L$,[60] ODNP mw cavity at 9.4 T: $\epsilon \approx 430$, $V_{sample} \approx 0.035\,\mu L$,[34], and ODNP non-resonant probehead at 9.4 T: $\epsilon \approx 135$, $V_{sample} \approx 40\,\mu L$. $\rho(CCl_4) = 1.59\,g\,ml^{-1}$ (Sigma Aldrich data sheet).

solvents. As the sensitivity also depends on the homogeneity of the magnetic field, the probehead, and the spectrometer, a comparison of the signal enhancement multiplied with the amount of sample n [mmol] is a simple way to compare the absolute sensitivity of different DNP instruments. Figure 8.1 shows $\epsilon \cdot n$ of neat CCl_4 doped with nitroxide radicals for different DNP setups at different magnetic fields, which shows that the new DNP instrument outperforms the established DNP setups. A further comparison between standard NMR sample tubes (O.D = 3 mm and O.D = 5 mm, fig. 8.1) and the new DNP setup shows that as soon as a signal enhancement of $\epsilon \gtrsim 5 - 7$ and $\epsilon \gtrsim 15 - 20$ is reached, the sensitivity of the DNP instrument surpasses routine NMR experiments with $V_{sample} \approx 180\,\mu L$ (O.D = 3 mm) and $V_{sample} \approx 550\,\mu L$ (O.D = 5 mm), respectively.
Notably, this comparison holds true only if the same pulse sequences are used during DNP and routine NMR experiments. ^1H pre-saturation increases the signal of routine NMR experiments through ^1H-^{13}C NOE by up to a factor of $\eta = 3$ in the fast motion regime.[10]

This further boosts the sensitivity of routine NMR experiment, while the signal intensity in DNP experiments is unaffected by ^{1}H pre-saturation (see sec. 7.2.1). However, carbon atoms without attached protons do not gain sensitivity from ^{1}H-^{13}C NOE, but some of these nuclei (iodinated and CCl_3 groups) are among the moieties that show large signal enhancements ($\epsilon \approx 10 - 37$) in DNP experiments. Additionally, the presence of the PA reduces T_{1n} by a factor of $\sim 2 - 4$ (see appendix D fig. D.2 and fig. D.1), which allows for fast signal averaging during DNP experiments and mostly compensates the sensitivity gain of ^{1}H-^{13}C NOE.[1] Finally, as demonstrated by 2D DNP experiments, coherent transfer of the increased polarization under DNP allows for the distribution of significant signal enhancements to less enhanced carbon nuclei.

Furthermore, ^{13}C NMR signal enhancements ($\epsilon \geq 15$) were observed on a variety of different target molecules including biologically active compounds such as pharmaceutical drugs. Particularly, halogenated compounds displayed enhancements of up to $\epsilon \approx 37$. Among halogenated carbon nuclei, iodinated compounds are promising target molecules, because of their signal enhancements ($\epsilon \approx 10 - 33$) and the possibility to use site-specific iodine labelling on biological compounds.[229] Investigations on the spin polarization mechanism and comparison to the literature suggests an important role of the halogen bond between the nitroxide radical and the target molecule.

While mechanistic investigations and target screening was performed in non-polar solvents, also the capability to perform DNP in polar solvents was also explored. At low mw power ($P \approx 22 - 29\,\mathrm{W}$) and short irradiation time ($2 - 7\,\mathrm{s}$), DNP experiments are possible in polar solvents including water. Sizable enhancements of $\epsilon \approx 3 - 4$ were observed on Na pyruvate and acetonitrile in water. Additionally, an enhancement of $\epsilon \approx 6$ was obtained for the iodinated positions of the X-ray contrast agent Na diatrizoate. This is a factor of about two larger than for other compounds such as Na pyruvate and acetonitrile in water.

Another major goal of the new DNP instrument was to achieve a resolution comparable to routine NMR experiments. The LW during DNP experiments was sample and solvent dependent and in the range of $\sim 5 - 30\,\mathrm{Hz}$, while in favorable cases a LW of $\sim 2.3\,\mathrm{Hz}$ was observed. In comparison to other DNP instruments, this represents a $2 - 3$ fold improvement and enables DNP experiments on larger molecules with crowded spectra.[33,34,61]

[1] As the presence of the PA depletes the ^{1}H-^{13}C NOE (see sec. 7.2.1), Boltzmann experiments in the presence of a PA with ^{1}H pre-saturation are not beneficial for the NMR sensitivity.

Finally, the viability of 2D DNP NMR experiments was demonstrated on ^{13}C enriched and natural abundance samples. 2D DNP NMR measurements were performed with the pulse sequences DQFCOSY, TOCSY and INADEQUATE, with enhancements similar to 1D experiments were reported in 2D DNP NMR. This demonstrated the possibility to transfer polarization from hyperpolarized carbon nuclei to carbon atoms that are, due to poor DNP efficiency, less polarized.

Outlook

The new DNP instrument enables DNP experiments in non-polar and polar solvents with large signal enhancements ($\epsilon \approx 2 - 37$), increased sample volume of up to 40 µL, and high resolution (LW $\approx 2 - 35$ Hz) as well as 2D DNP NMR experiments with comparable enhancements as in 1D measurements. Each of the these four features represents an advancement for liquid state DNP. Together, they open up new perspectives for liquid state DNP.

Nevertheless, there are aspects of the current DNP instrument that need further optimization. Indeed, the active cooling arrangement employs the standard cooling path optimized for routine NMR experiments. Improvements on the cooling efficiency could reduce the temperature gradient of the sample and therefore decrease the LW during DNP experiments and would allow for stronger and longer mw irradiation. Along with this, the sample arrangement of two concentric tubes could be optimized by the addition of a second sample layer, thereby increasing V_{sample} by almost a factor of two.

The exploration of a large variety of target molecules may lead to new insights into the DNP mechanism and in turn to substantial improvements on the attainable signal enhancement. For example, the proposed dependency of the ^{13}C signal enhancement on the acidity of the attached proton[59] or on the paramagnetic shift of the ^{13}C moiety[33] may be probed on a broader set of molecules. This also includes the exploration of different target nuclei such as ^{31}P, ^{19}F, and ^{15}N that showed sizable signal enhancements at low to medium magnetic field (^{31}P also showed $\epsilon \geq 100$ at $B_0 \approx 9.4$ T and 14 T).[58,69,191] However, for these nuclei little is known on the spin polarization mechanism at high magnetic field and in different chemical environments. A clear picture on the expected enhancement of each nucleus and moiety would facilitate the application of liquid DNP as a tool in analytical chemistry.

In conjunction with this, a PA optimization similar to the one performed at low magnetic field and described in the chapters 4 and 5 should be carried out at high magnetic field. As reported in a recent study, the choice of the PA is dependent on the target nucleus and the chemical environment.[191] There, the comparison of nitroxide radicals with galvinoxyl, a carbon based radical, on ^{19}F at 3.4 T revealed a larger ^{19}F scalar dominated signal enhancement with galvinoxyl ($\epsilon(C_6F_6) \approx 21$) than with nitroxides ($\epsilon(C_6F_6) \approx 5$) as a PA.[191] Based on the experiments performed on ^{13}C within this work, this is counter-intuitive and deserves a more thorough investigation.

After the demonstration of 2D DNP NMR experiments, many different sequences may be developed to further disclose the full potential of the method for polarizing small and large target molecules. In this context several polarization transfer pathways should be evaluated. Particularly, homo- and heteronuclear nuclear Overhauser enhancement spectroscopy (NOESY) experiments could prove valuable, because they deliver not only through bond but also through space correlations.[92] Through this, polarization might be transferred from hyperpolarized small molecules (or solvents such as $CHCl_3$) to larger target molecule that might be difficult to hyperpolarize directly.

Liquid state DNP on biological systems was, so far, demonstrated only in lipid bilayers, where due to reduced PA mobility, a solid like DNP behaviour was observed.[248] These systems may serve as a good starting point for DNP measurements in water with the new DNP spectrometer and could be extended to, for example, proteins and other biological macromolecules. Particularly, site-specific labelling of iodine or of the PA at the protein may prove valuable. In this context, reverse micelles may be employed for caging biological macromolecules and dispersing them in organic solvents. As organic solvents are less influenced by mw induced sample heating, this could boost the amount of target molecules in liquid state DNP of such systems.[249]

Besides biological macromolecules, the characterization of solid-liquid interfaces is also a thriving research area, as these interactions are ubiquitous in catalysis.[250] Hyperpolarization experiments were recently performed on self-assembling thin aluminium oxide monolayers detected by nitrogen vacancies in diamonds.[251] In liquid state DNP, the PA could be attached to catalytic surfaces, thereby providing the necessary sensitivity and in parallel allow for the quantification of collision frequencies and collision duration of the target onto the surface.

Closing Remark

With the demonstration of sizable liquid state ^{13}C NMR signal enhancements at 9.4 T driven by a scalar dominated polarization transfer,[60] the perspective on ODNP changed and within the last years the number of studies on the DNP mechanism[33,34,56,70,83,86] and on hardware developments[40,41,61,68,69,112] substantially increased. The upgrade of the current generation of NMR spectrometers at 400 MHz to a full liquid state DNP NMR instrument (as presented in this work) requires a gyrotron and the integration of the quasi-optical components in the NMR probehead. This is possible without modifications to the current state-of-the-art design and could help to quickly increase the number of liquid state DNP instruments and allow other groups to contribute to the growing field of liquid state DNP. It is my sincere conviction that ODNP in liquids will continue to progress at a considerable pace.

Bibliography

[1] E. M. Purcell, H. C. Torey, R. V. Pound, "Resonance Absorption by Nuclear Magnetic Moments in a solid", *Phys. Rev.* **1946**, *69*, 37–38, DOI 10.1103/PhysRev.69.37.

[2] F. Bloch, "Nuclear Induction", *Phys. Rev.* **1946**, *70*, 460–474, DOI 10.1103/PhysRev.70.460.

[3] J. Cavanagh, W. J. Fairbrother, A. G. Palmer III, *Protein NMR Spectroscopy*, *Vol. 2*, Elsevier, **2007**, DOI https://doi.org/10.1016/B978-0-12-164491-8.X5000-3.

[4] O. F. Lange, N.-A. Lakomek, C. Fares, G. F. Schröder, K. F. A. Walter, S. Becker, J. Meiler, H. Grubmöller, C. Griesinger, B. L. de Groot, "Recognition Dynamics Up to Microseconds Revealed from an RDC-Derived Ubiquitin Ensemble in Solution", *Science* **2008**, *320*, 1471–1475, DOI 10.1126/science.1157092.

[5] F. A. Gallagher, M. I. Kettunen, S. E. Day, D.-E. Hu, J. H. Ardenkjaer-Larsen, R. Zandt, P. R. Jensen, M. Karlsson, K. Golman, M. H. Lerche, K. M. Brindle, "Magnetic resonance imaging of ph in vivo using hyperpolarized ^{13}C-labelled bicarbonate", *Nature* **2008**, *453*, 940–944, DOI 10.1038/nature07017.

[6] S. E. Day, M. I. Kettunen, F. A. Gallagher, D.-E. Hu, M. Lerche, J. Wolber, K. Golman, J. H. Ardenkjaer-Larsen, K. M. Brindle, "Detecting tumor response to treatment using hyperpolarized ^{13}C magnetic resonance imaging and spectroscopy", *Nat. Med.* **2007**, *13*, 1382–1387, DOI 10.1038/nm1650.

[7] A. J. Pell, G. Pintacuda, C. P. Grey, "Paramagnetic NMR in solution and the solid state", *Prog. Nucl. Magn. Reson. Spectrosc.* **2018**, DOI https://doi.org/10.1016/j.pnmrs.2018.05.001.

[8] E. W. Zhao, T. Liu, E. Jonsson, J. Lee, I. Temprano, R. B. Jethwa, A. Wang, H. Smith, J. Carretero-Gonzalez, Q. Song, C. P. Grey, "In situ NMR metrology reveals reaction mechanisms in redox flow batteries", *Nature* **2020**, *579*, 224–228.

[9] A. G. Rankin, J. Trébosc, F. Pourpoint, J.-P. Amoureux, O. Lafon, "Recent developments in MAS DNP-NMR of materials", *Solid State Nucl. Magn. Reson.* **2019**, *101*, 116–143, DOI https://doi.org/10.1016/j.ssnmr.2019.05.009.

[10] M. H. Levitt, *Spin dynamics: Basics of Nuclear Magnetic Resonance*, John Wiley and Sons, **2001**.

[11] P. C. Lauterbur, "Image Formation by Induced Local Interactions: Examples Employing Nuclear Magnetic Resonance", *Nature* **1973**, *242*, 190–191, DOI 10.1038/242190a0.

[12] T. K. Dayie, L. T. Olenginski, K. M. Taiwo, "Isotope Labels Combined with Solution NMR Spectroscopy Make Visible the Invisible Conformations of Small-to-Large RNAs", *Chem. Rev.* **2022**, *122*, 9357–9394, DOI https://doi.org/10.1021/acs.chemrev.1c00845.

[13] A. R. Camacho-Zarco, V. Schnapka, S. Guseva, A. Abyzov, W. Adamski, S. Milles, M. R. Jensen, L. Zidek, N. Salvi, M. Blackledge, "NMR Provides Unique Insight into the Functional Dynamics and Interactions of Intrisically Disordered Proteins", *Chem. Rev.* **2022**, *122*, 9331–9356, DOI https://doi.org/10.1021/acs.chemrev.1c010230.

[14] M. Bennati, I. Tkach, M. T. Türke, "Dynamic nuclear polarization in liquids", *Electron Paramag. Reson.* **2011**, *22*, 155–182, DOI 10.1039/9781849730877-00155.

[15] J. H. Ardenkjaer-Larsen, G. S. Boebinger, A. Comment, S. Duckett, A. S. Edison, F. Engelke, C. Griesinger, R. G. Griffin, C. Hilty, H. Maeda, G. Parigi, T. Prisner, E. Ravera, P. J. van Bentum, S. Vega, A. Webb, C. Luchinat, H. Schwalbe, L. Frydman, "Facing and Overcoming Sensitivity Challenges in Biomolecular NMR Spectroscopy", *Angew. Chem.* **2015**, *54*, 9162–9185, DOI 10.1002/anie.201410653.

[16] M. Bennati, T. Orlando, "Overhauser DNP in liquids on ^{13}C nuclei", *eMagRes* **2019**, *8*, 11–18, DOI 10.1002/9780470034590.emrstm1581.

[17] R. A. Green, R. W. Adams, S. B. Duckett, R. E. Mewis, D. C. Williamson, G. G. Green, "The theory and practice of hyperpolarization in magnetic resonance using parahydrogen", *Prog. Nucl. Magn. Reson. Spectrosc.* **2012**, *67*, 1–48, DOI http://dx.doi.org/10.1016/j.pnmrs.2012.03.001.

[18] J.-B. Hövener, A. N. Pravdivstev, B. Kidd, C. R. Bowers, S. Glöggler, K. V. Kovtunov, M. Plaumann, R. Katz-Brull, K. Buckenmaier, A. Jerschow, F. Reineri, T. Theis, R. V. Shchepin, S. Wagner, P. Bhattacharya, N. M. Zacharias, E. Y. Chekmenev, "Parahydrogen-Based Hyperpolarization for Biomedicine", *Angew. Chem. int. Ed.* **2018**, *57*, 11140–11162, DOI 10.1002/anie.201711842.

[19] G. Casano, H. Karoui, O. Ouari, "Polarizing Agents: Evolution and Outlook in Free Radical Development for DNP", *eMagRes* **2019**, *7*, 195–208, DOI 10.1002/9780470034590.emrstm1547.

[20] D. A. Hall, D. C. Maus, G. J. Gerfen, S. J. Inati, L. R. Becerra, F. W. Dahlquist, R. G. Griffin, "Polarization Enhanced NMR Spectroscopy of Biomolecules in Frozen Solution", *Science* **1997**, *276*, 930–932, DOI DOI:10.1126/science.276.5314.930.

[21] T. Maly, G. T. Debelouchina, V. S. Bajaj, K. Hu, C. Joo, M. L. Mak-Jurkauskas, J. R. Sirigiri, P. C. A. van der Wel, J. Herzfeld, R. J. Temkin, R. G. Griffin, "Dynamic nucelear polarization at high magnetic fields", *J. Chem. Phys.* **2008**, *128*, 052211, DOI https://doi.org/10.1063/1.28335820.

[22] B. Corzilius, "High-Field Dynamic Nuclear Polarization", *Annu. Rev. Phys. Chem.* **2020**, *71*, 143–170, DOI https://doi.org/10.1146/annurev-physchem-071119-040222.

[23] Ü. Akbey, H. Oschkinat, "Structural biology applications of solid-state MAS DNP NMR", *J. Magn. Reson.* **2016**, *269*, 213–224, DOI https://doi.org/10.1016/j.jmr.2016.04.003.

[24] S. Lange, W. T. Franks, N. Rajagogpalan, K. Döring, M. A. Geiger, A. Linden, B.-J. van Rossum, B. Kramer, B. Bukau, H. Oschkinat, "Structural analysis of a signal peptide inside the ribosome tunnel by DNP MAS NMR", *Sci. Adv.* **2016**, e1600379, DOI 10.1126/sciadv.1600379.

[25] W. Y. Chow, G. de Pape, S. Hediger, "Biomolecular and Biological Applications of Solid-State NMR with Dynamic Nuclear Polarization", *Chem. Rev.* **2022**, *122*, 9795–9847, DOI https://doi.org/10.1021/acs.chemrev.1c01043.

[26] C. Sauvee, M. Rosay, G. Casano, F. Aussenac, R. T. Weber, O. Ouari, P. Tordo, "Highly Efficient, Water-Soluble Polarizing Agents for Dynamic Nuclear Polarization at High Frequency", *Angew. Chem. Int. Ed.* **2013**, *52*, 10858–10861, DOI 10.1002/anie.201304657.

[27] C. Song, K.-N. hu, C.-G. Joo, T. M. Swager, R. G. Griffin, "TOTAPOL: A Biradical Polarizing Agent for Dynamic Nuclear Polarization Experiments in Aqueous Media", *J. Am. Chem. Soc.* **2006**, *128*, 11385–11390, DOI https://doi.org/10.1021/ja061284b.

[28] A. Lund, G. Casano, G. Menzildjian, M. Kaushik, G. Stevanato, M. Yulikov, R. Jabbour, D. Wisser, M. Renom-Carasco, C. Thieuleux, F. Bernada, H. Karoui, D. siri, M. Rosay, I. V. Sergeyev, D. Gajan, M. Lelli, L. Emsley, O. Ouari, A. Lesage, "TinyPols: a Family of Water-Soluble Binitroxides Tailored for Dynamic Nuclear Polarization Enhanced NMR Spectroscopy at 18.8 and 21.1 T", *Chem. Sci.* **2020**, 2810–2818, DOI 10.1039/C9SC05384K.

[29] G. Mathies, M. A. Caporini, V. K. Michaelis, Y. Liu, K.-N. Hu, D. Mance, J. L. . Zweier, M. Rosay, M. Baldus, R. G. Griffin, "Efficient Dynamic Nuclear Polarization at 800 MHz/527 GHz with Trityl-Nitroxide Biradicals", *Angew. Chem. Int. Ed.* **2015**, *54*, 11770–11774, DOI 10.1002/anie.201504292.

[30] D. Wisser, G. Karthikeyan, A. Lund, G. Casano, H. Karoui, M. Yulikov, G. Menzildjian, A. C. Pinon, A. Purea, F. Engelke, S. R. Chaudhari, D. Kubicki, A. J. Rossini, I. B. Moroz, D. Gajan, C. Coperet, G. Jeschke, M. Lelli, L. Emsley, A. Lesage, O. Ouari, "BDPA-Nitroxide Biradicals Tailored for Efficient Dynamic Nuclear Polarization Enhanced Solid-State NMR at Magnetic Fields up to 21.1 T", *J. Am. Chem. Soc.* **2018**, *140*, 13340–13349, DOI 10.1021/jacs.8b08081.

[31] J. H. Ardenkjaer-Larsen, B. Fridlund, A. Gram, G. Hansson, L. Hansson, M. H. Lerche, R. Servin, M. Thaning, K. Golman, "Increase in signal-to-noise ratio of >10.000 times in liquid-state NMR", *Proc. Natl. Acad. Sci.* **2003**, *100*, 10158–10163, DOI https://doi.org/10.1073/pnas.1733835100.

[32] C. Hilty, D. Kurzbach, L. Frydman, "Hyperpolarized water as universal sensitivity booster in biomolecular NMR", *Nat. Protoc.* **2022**, *17*, 1621–1657, DOI https://doi.org/10.1038/s41596-022-00693-8.

[33] D. Dai, X. Wang, Y. Liu, X.-L.Yang, C. Glaubitz, V. Denysenkov, X. He, T. Prisner, J. Mao, "Room-temperature dynamic nuclear polarization enhanced NMR spectroscopy of small biological molecules in water", *Nat. Commun.* **2021**, *12*, 6880, DOI https://doi.org/10.1038/s41467-021-27067-0.

[34] T. Orlando, R. Dervışoğlu, M. Levien, I. Tkach, T. F. Prisner, L. B. Andreas, V. P. Denysenkov, M. Bennati, "Dynamic nuclear polarization of ^{13}C nuclei in the liquid state over a 10 Tesla field range", *Angew. Chem.* **2019**, *58*, 1402–1406, DOI 10.1002/anie.201811892.

[35] K. Singh, C. Jacquemmoz, P. Giraudeau, L. Frydman, J.-N. Dumez, "Ultrafast 2D ^{1}H–^{1}H NMR spectroscopy of DNP-hyperpolarised substrates for the analysis of mixtures", *Chem. Commun.* **2021**, *57*, 8035–8038, DOI https://doi.org/10.1039/D1CC03079E.

[36] M. Novakovic, G. L. Olsen, G. Pinter, D. Hymon, B. Fürtig, H. Schwalbe, L. Frydman, "A 300-fold enhancement of imino nucleic acid resonances by hyperpolarized water provides a new window for probing RNA refolding by 1D and 2D NMR", *Proc. Natl. Acad. Sci.* **2020**, *117*, 2449–2455, DOI https://doi.org/10.1073/pnas.1916956117.

[37] Y. Wang, C. Hilty, "Determination of Ligand Binding Epitope Structures Using Polarization Transfer from Hyperpolarized Ligands", *J. Med. Chem.* **2019**, *62*, 2419–2427, DOI 10.1021/acs.jmedchem.8b01711.

[38] A. W. Overhauser, "Polarization of nuclei in metals", *Phys. Rev.* **1953**, *92*, 411–415, DOI 10.1103/PhysRev.92.411.

[39] T. R. Carver, C. P. Slichter, "Polarization of nuclear Spins in Metals", *Phys Rev.* **1953**, *92*, 212–213, DOI https://doi.org/10.1103/PhysRev.92.212.2.

[40] Y. Rao, A. Venkatesh, P. Moutzouri, L. Emsley, "^{1}H Hyperpolarization of Solutions by Overhauser Dynamic Nuclear Polarization with ^{13}C-^{1}H Polarization Transfer", *J. Phys. Chem. Let.* **2022**, *13*, 7749–7755, DOI https://doi.org/10.1021/acs.jpclett.2c01956.

[41] M. Soundararajan, T. Dubroca, J. van Tol, S. Hill, L. Frydman, S. Wi, "Proton-detected solution-state NMR at 14.1 T based on scalar-driven ^{13}C Overhauser dynamic nuclear polarization", *J. Magn. Reson.* **2022**, DOI https://doi.org/10.1016/j.jmr.2022.107304.

[42] K. H. Hausser, D. Stehlik, "Dynamic Nuclear Polarization in Liquids", *Adv. Magn. Reson.* **1968**, *3*, 79–139, DOI https://doi.org/10.1016/B978-1-4832-3116-7.50010-2.

[43] M. Bennati, C. Luchinat, G. Parigi, M. T. Türke, "Water ^{1}H relaxation dispersion analysis on a nitroxide radical provides information on the maximal signal enhancement in Overhauser dynamic nuclear polarization experiments", *Phys. Chem. Chem. Phys.* **2010**, *12*, 5902–5910, DOI 10.1039/c002146f.

[44] I. Solomon, "Relaxation Processes in a System of Two Spins", *Phys. Rev.* **1955**, *99*, 559–566, DOI 10.1103/PhysRev.99.559.

[45] A. Abragam, *Principles of Nucleear Magnetism*, Oxford University Press, **1961**.

[46] C. Griesinger, M. Bennati, H. M. Vieth, C. Luchinat, G. Parigi, P. Hoefer., F. Engelke, S. J. Glaser, V. Denysenkov, T. F. Prisner, "Dynamic nuclear Polarization at high magnetic fields in liquids", *Prog. Nucl. Mag. Res. Spectrosc.* **2012**, *64*, 4–28, DOI 10.1016/j.pnmrs.2011.10.002.

[47] D. Sezer, M. J. Prandolini, T. F. Prisner, "Dynamic nuclear polarization coupling factors calculated from molecular dynamics simulations of a nitroxide radical in water", *Phys. Chem. Chem. Phys.* **2009**, *11*, 6626–6637, DOI 10.1039/b905709a.

[48] P. J. M. van Bentum, G. H. A. van der Heijden, J. A. Villanueva-Garibay, A. P. M. Kentgens, "Quantitative analysis of high field liquid state dynamic nuclear polarization", *Phys. Chem. Chem. Phys.* **2011**, *13*, 17831, DOI 10.1039/c1cp22002k.

[49] G. H. A. van der Heijden, A. P. M. Kentgens, P. J. M. van Bentum, "Liquid state dynamic nuclear polarization of ethanol at 3.4 T (95 GHz)", *Phys. Chem. Chem. Phys.* **2014**, *16*, 8493–8502, DOI 10.1039/c3cp55254c.

[50] M.-T. Tuerke, I. Tkach, M. Reese, P. Hoefer, M. Bennati, "Optimization of dynamic nuclear polarization experiments in aqueous solution at 15 MHz/9.7 GHz: a comparative study with DNP at 140 MHz/94 GHz", *Phys Chem. Chem. Phys* **2010**, *12*, 5983–5901, DOI 10.1039/c002814m.

[51] V. P. Denysenkov, M. J. Prandolini, A. Krahn, M. Gafurov, B. Endeward, T. F. Prisner, "High-Field DNP Spectrometer for Liquids", *Appl. Magn. Reson.* **2008**, *34*, 289–299, DOI 10.1007//s00723-008-0127-3.

[52] M. J. Prandolini, V. P. Denysenkov, M. Gafurov, S. Lyubenova, B. Endeward, M. Bennati, T. F. Prisner, "First DNP Results from a Liquids Water-TEMPOL Sample at 400 MHz and 260 GHz", *Appl. Magn. Reson.* **2008**, *34*, 399–407, DOI 10.1007//s00723-008-0128-2.

[53] V. Denysenkov, M. J. Prandolini, M. Gafurov, D. Sezer, B. Endeward, T. F. Prisner, "Liquid state DNP using a 260 GHz high power gyrotron", *Phys. Chem. Chem. Phys.* **2010**, *12*, 5741–5751, DOI 10.1039/c002146f.

[54] V. Denysenkov, T. Prisner, "Liquid state Dynamic Nuclear Polarization probe with Fabry–Perot resonator at 9.2 T", *J. Magn. Reson.* **2012**, *217*, 1–5, DOI 10.1016/j.jmr.2012.01.014.

[55] P. Neugebauer, J. G. Krummenacker, V. P. Denysenkov, G. Parigi, C. Luchinat, T. F. Prisner, "Liquid state DNP of water at 9.2 T: an experimental access to saturation.", *Phys. Chem. Chem. Phys.* **2013**, *15*, 6049–6056, DOI 10.1039/c3cp44461a.

[56] A. A. Kuzhelev, D. Dai, V. Denysenkov, I. A. Kirilyuk, E. G. Bagryanskaya, T. F. Prisner, "Influence of Rotational Motion of Nitroxides on Overhauser Dynamic Nuclear Polarization: A Systematic Study at High Magnetic Fields", *J. Phys. Chem. C* **2021**, *125*, 25651–25659, DOI https://doi.org/10.1021/acs.jpcc.1c06979.

[57] I. C. Felli, R. Pierattelli, "^{13}C Direct Detected NMR for Challenging Systems", *Chem. Rev.* **2022**, *122*, 9468–9496, DOI https://doi.org/10.1021/acs.chemrev.1c00871.

[58] N. M. Loening, M. Rosay, V. Weis, R. G. Griffin, "Solution-state dynamic nuclear polarization at high magnetic field", *J. Am. Chem. Soc.* **2002**, *124*, 8808–8809, DOI 10.1021/ja026660g.

[59] X. Wang, W. C. Isley, S. Salido, Z. Sun, L. Song, C. J. Cramer, H. Dorn, "Optimization and Prediction of the Electron nuclear Diolar and Scalar interaction in ^{1}H and ^{13}C liquid state DNP", *Chem. Sci.* **2015**, *6*, 6482–6495, DOI 10.1039/c5sc02499d.

[60] G. Liu, M. Levien, N. Karschin, G. Parigi, C. Luchinat, M. Bennati, "One-thousand-fold enhancement of high field liquid nuclear magnetic resonance signals at room temperature", *Nat. Chem.* **2017**, *9*, 676–680, DOI 10.1038/nchem.2723.

[61] T. Dubroca, S. Wi, J. van Tol, L. Frydman, S. Hill, "Large Volume Liquid State Scalar Overhauser Dynamic Nuclear Polarization at High Magnetic Field", *Phys. Chem. Chem. Phys.* **2019**, 1–5, DOI 10.1039/c9cp02997d.

[62] M. Reese, M.-T. Tuerke, I. T. Parigi, C. Luchinat, T. Marquardsen, A. Tavernier, P. Hoefer, F. E. Griesinger, M. Bennati, "^{1}H and ^{13}C dynamic nuclear polarization in aqueous solution with a two field 0.35/14T shuttle DNP spectrometer", *J. Am. Chem. Soc.* **2009**, *131*, 15086–15087, DOI https://doi.org/10.1021/ja905959n.

[63] S. G. J. van Meerten, G. E. Janssen, A. P. M. Kentgens, "Rapid-melt DNP for multidimensional and heteronuclear high-field NMR experiments", *J. Magn. Reson.* **2020**, *310*, 106656, DOI https://doi.org/10.1016/j.jmr.2019.106656.

[64] M. D. Lingwood, T. A. Siaw, N. Sailasuta, B. D. Ross, P. Bhattacharya, S. Han, "Continuous flow Overhauser dynamic nuclear polarization of water in the fringe field of a clinical magnetic resonance imaging system for authentic image contrast", *J. Magn. Reson.* **2010**, *205*, 247–254, DOI 10.1016/j.jmr.2010.05.008.

[65] V. P. Denysenkov, M. Terekhov, R. Maeder, S. Fischer, S. Zangos, T. Vogl, T. F. Prisner, "Continuous-flow DNP polarizer for MRI applications at 1.5 T", *Sci. Rep.* **2017**, *7*, 44010, DOI 10.1038/srep44010.

[66] S. van Meerten, M. Tayler, A. Kentgens, P. van Bentum, "Towards Overhauser DNP in supercritical CO_2", *J. Magn. Reson* **2016**, *267*, 30–36, DOI http://dx.doi.org/10.1016/j.jmr.2016.04.002.

[67] R. Kircher, H. Hasse, K. Münnemann, "High Flow-Rate Benchtop NMR Spectroscopy Enabled by Continuous Overhauser DNP", *Anal. Chem.* **2021**, 8897–8905, DOI https://doi.org/10.1021/acs.analchem.1c01118.

[68] D. Yoon, A. I. Dimitriadis, M. Soundararajan, C. Caspers, J. Genoud, S. Alberti, E. de Rijk, J.-P. Ansermet, "High-Field Liquid-State Dynamic Nuclear Polarization in Microliter Samples", *Anal. Chem.* **2018**, *90*, 5620–5626, DOI 10.1021/acs.analchem.7b04700.

[69] T. Dubroca, A. N. Smith, K. J. Pike, S. Froud, R. Wylde, B. Trociewitz, J. McKay, F. Mentink-Vigier, J. van Tol, S. Wi, W. Brey, J. R. Long, L. Frydman, S. Hill, "quasi-optical and corrugated waveguide microwave transmission system for simultaneous dynamic nuclear polarization NMR on two separate 14.1 T spectrometers", *J. Magn. Reson.* **2018**, *289*, 35–44, DOI https://doi.org/10.1016/j.jmr.2018.01.015.

[70] T. Orlando, I. Kuprov, M. Hiller, "Theoretical analysis of scalar relaxation in ^{13}C-DNP in liquids", *J. Magn. Reson. Open* **2022**, *10-11*, 100040, DOI https://doi.org/10.1016/j.jmro.2022.100040.

[71] M. G. Concilio, M. Soundararajan, L. Frydman, I. Kuprov, "High-field solution state DNP using cross-correlations", *J. Magn. Reson.* **2021**, *326*, 106940, DOI https://doi.org/10.1016/j.jmr.2021.106940.

[72] M. G. Concilio, I. Kuprov, L. Frydman, "*J*-Driven dynamic nuclear polarization for sensitizing high field solution state NMR", *Phys. Chem. Chem. Phys.* **2022**, *24*, 2118–2125, DOI 10.1039/d1cp04186j.

[73] M. Brustolon, E. Giamello, *Electron Paramagnetic Resonance: A Practitioner's Toolkit*, John Wiley and Sons, **2009**, DOI 10.1002/9780470432235.

[74] A. Schweiger, G. Jeschke, *Principles of Pulsed Electron Paramagnetic Resonance*, Oxford University Press, **2001**.

[75] D. Goldfarb, S.Stoll, *EPR Spectroscopy: Fundamentals and Methods*, Wiley, **2018**.

[76] J. Potenza, "Measurement and Applications of Dynamic Nuclear Polarization", *Advan. Mol. Relaxation Process* **1972**, *4*, 229–354, DOI https://doi.org/10.1016/0001-8716(72)80016-6.

[77] M. Bennati, "EPR Spectroscopy: Fundamentals and Methods - EPR Interactions - Hyperfine Couplings", *eMagRes* **2017**, *6*, 271–282, DOI 10.1002/9780470034590.emrstm1503, DOI 10.1002/9780470034590.emrstm1503.

[78] W. Müller-Warmuth, R. van Steenwinkel, F. Noack, "Dynamic nuclear polarization experiments on ^{19}F in solutions and their interpretation by the "Pulse model" of molecular collisions", *Z. Naturforsch. A* **1968**, *23*, 506–513, DOI 10.1515/zna-1968-0408.

[79] W. Müller-Warmuth, R. Vilhjalmsson, P. Gerlof, J. Smidt, J. Trommel, "Intermolecular interactions of benzene and carbon tetrachloride with selected free radicals in solution as studied by ^{13}C and ^{1}H dynamic nuclear polarization", *Mol. Phys.* **1976**, *31*, 1055–1067, DOI 10.1080/00268977600100811.

[80] E. Ravera, C. Luchinat, G. Parigi, "Basic facts and perspectives of Overhauser DNP NMR", *J. Magn. Reson.* **2016**, *264*, 78–87, DOI 10.1016/j.jmr.2015.12.013.

[81] L.-P. Hwang, J. H. Freed, "Dynamic effect of pair correlation function on spin relaxation by translational diffusion in liquids", *J. Chem. Phys.* **1975**, *63*, 4017–4025, DOI https://doi.org/10.1063/1.431841.

[82] C. F. Polnaszek, R. G. Bryant, "Nitroxide radical induced solvent proton relaxation: Measurement of localized translational diffusion", *J. Chem. Phys.* **1984**, *81*, 4038–4045, DOI 10.1063/1.448147.

[83] M. Levien, M. Hiller, I. Tkach, M. Bennati, T. Orlando, "Nitroxide Derivatives for Dynamic Nuclear Polarization in Liquids:The Role of Rotational Diffusion", *J. Phys. Chem. Lett.* **2020**, *11*, 1629–1635, DOI https://dx.doi.org/10.1021/acs.jpclett.0c00270.

[84] M. T. Türke, M. Bennati, "Saturation factor of nitroxide radicals in liquid DNP by pulsed ELDOR experiments", *Phys. Chem. Chem. Phys.* **2011**, *13*, 3630, DOI 10.1039/c0cp02126a.

[85] M. T. Türke, G. Parigi, C. Luchinat, M. Bennati, "Overhauser DNP with ^{15}N labelled Frémy's salt at 0.35 Tesla", *Phys. Chem. Chem. Phys.* **2012**, *14*, 502–510, DOI 10.1039/C1CP22332A.

[86] M. Levien, M. Reinhard, M. Hiller, I. Tkach, M. Bennati, T. Orlando, "Spin density localization and accessibility of organic radicals affect liquid-state DNP efficiency", *Phys. Chem. Chem. Phys.* **2021**, *23*, 4480–4485, DOI 10.1039/d0cp05796g.

[87] N. Enkin, G. Liu, I. Tkach, M. Bennati, "High DNP efficiency of TEMPONE radicals in liquid toluene at low concentrations", *Phys. Chem. Chem. Phys.* **2014**, *16*, 8795–8800, DOI 10.1039/c4cp00854e.

[88] N. Enkin, G. Liu, M. del Carmen Gimenez-Lopez, K. Porfyrakis, I. Tkach, M. Bennati, "A high saturation factor in Overhauser DNP with nitroxide derivatives: the role of ^{14}N nuclear spin relaxation", *Phys. Chem. Chem. Phys.* **2015**, *17*, 11144–11149, DOI 10.1039/C5CP00935A.

[89] M. D. Lingwood, S. Han, "Dynamic Nuclear Polarization of ^{13}C in aq. solutions under ambient conditions", *J. Magn. Reson.* **2009**, *201*, 137–145, DOI 10.1016/j.jmr.2009.09.002.

[90] K. H. Hausser, F. Reinbold, "Dynamic Polarisation in a Three-Spin System", *Phys. Lett.* **1962**, *2*, 53–54, DOI https://doi.org/10.1016/0031-9163(62)90113-0.

[91] H. Brunner, K. H. Hausser, "Dynamic Nuclear Polarization of Protons, ^{19}F and ^{13}C Nuclei at 21 Kilogauss", *J. Magn. Reson.* **1972**, *6*, 605–611, DOI https://doi.org/10.1016/0022-2364(72)90171-0.

[92] J. Keeler, *Understanding NMR spectroscopy*, *Vol. 5*, John Wiley and Sons, **2010**.

[93] A. G. Redfield, "Nuclear Magnetic Resonance Saturation and Rotary Saturation in Solids", *Phys. Rev.* **1955**, *98*, 1787–1809, DOI 10.1103/PhysRev.98.1787.

[94] A. G. Redfield, "The Theory of Relaxation Processes", *Adv. Magn. Opt. Reson.* **1965**, *1*, 1–32, DOI https://doi.org/10.1016/B978-1-4832-3114-3.50007-6.

[95] B. H. Robinson, D. A. Haas, C. Mailer, "Molecular Dynamics in Liquids: Spin-Lattice Relaxation of Nitroxide Spin Labels", *Science* **1994**, *263*, 490–493, DOI 10.1126/science.8290958.

[96] J. R. Biller, V. M. Meyer, H. Elajaili, G. M. Rosen, S. S. Eaton, G. R. Eaton, "Frequency Dependence of Electron Spin Relaxation Times in Aqueous Solution for a Nitronyl Nitroxide Radical and Perdeuterated-Tempone between 250 MHz and 34 GHz", *J. Magn. Reson.* **2012**, *225*, 52–57, DOI http://dx.doi.org/10.1016/j.jmr.2012.10.002.

[97] C. Mailer, R. D. Nielsen, B. H. Robinson, "Explanation of Spin-Lattice Relaxation Rates of Spin Labels Obtained with Multifrequency Saturation Recovery EPR", *J. Phys. Chem. A* **2005**, *109*, 4049–4061, DOI https://doi.org/10.1021/jp0446711.

[98] S. S. Eaton, J. Harbridge, G. A. Rinard, G. R. Eaton, R. T. Weber, "Frequency Dependence of Electron Spin Relaxation for Three $S = 1/2$ Species Doped into Diamagnetic Solid Hosts", *Appl. Magn. Reson.* **2001**, *20*, 151–157, DOI https://doi.org/10.1007/BF03162316.

[99] R. Owenius, G. E. Terry, M. J. Williams, S. S. Eaton, G. R. Eaton, "Frequency Dependence of Electron Spin Relaxation of Nitroxyl Radicals in Fluid Solution", *J. Phys. Chem. B* **2004**, *108*, 9475–9481, DOI https://doi.org/10.1021/jp036020f.

[100] W. Froncisz, T. G. Camenisch, J. J. Ratke, J. R. Anderson, W. K. Subczynski, R. A. Strangeway, J. W. Sidabras, J. S. Hyde, "Saturation recovery EPR and ELDOR at W-band for spin labels", *J. Magn. Reson.* **2008**, *193*, 297–304, DOI 10.1016/j.jmr.2008.05.008.

[101] D. Sezer, M. Gafurov, M. J. Prandolini, V. P. Denysenkov, T. F. Prisner, "Dynamic nuclear polarization of water by a nitroxide radical: Rigorous treatment of the electron spin saturation and comparison with experiments at 9.2 Tesla", *Phys. Chem. Chem. Phys.* **2009**, *11*, 6638–66653, DOI https://doi.org/10.1039/B906719C.

[102] K. M. More, G. R. Eaton, S. S. Eaton, "Determination of T_1 and T_2 by Simulation of EPR Power Saturation Curves and Saturated Spectra. Application to Spin-Labeled Iron Porphyrins", *J. Magn. Reson.* **1984**, *60*, 54–65, DOI https://doi.org/10.1016/0022-2364(84)90025-8.

[103] J. R. Biller, J. E. McPeak, S. S. Eaton, G. R. Eaton, "Measurement of T_{1e}, T_{1N}, T_{1HE}, T_{2e}, and T_{2HE} by Pulse EPR at X-Band for Nitroxides at Concentrations Relevant to Solution DNP", *Appl. Magn. Reson.* **2018**, *49*, 1235–1251, DOI https://doi.org/10.1007/s00723-018-1049-3.

[104] D. A. Haas, C. Mailer, B. H. Robinson, "Using nitroxide spin labels", *Biophys. J.* **1993**, *64*, 594–604, DOI 10.1016/S0006-3495(93)81418-8.

[105] K. Herb, R. Tschaggelar, G. Denninger, G. Jescke, "Double resonance calibration of g factor standards: Carbon fibers as a high prescision standard", *J. Magn. Reson.* **2018**, *289*, 100–106, DOI https://doi.org/10.1016/j.jmr.2018.02.006.

[106] K. Sakai, K.-I. Yamada, T. Yamasaki, Y. Kinoshita, F. Mito, H. Utsumi, "Effective 2,6-substitution of piperidine nitroxyl radical by carbonyl compound", *Tetrahedron* **2010**, *66*, 2311–2315, DOI 10.1016/j.tet.2010.02.004.

[107] R. Kuhn, F. A. Neugebauer, "Über substituierte Bis-biphenylen-allyl-Radikale", *Monatsh. Chem.* **1964**, *95*, 3–23, DOI https://doi.org/10.1007/BF00909246.

[108] C. Do, J. Hatfield, S. Patel, D. Vasudevan, C. Tirla, N. S. Mills, "Dications of Benzylidenefluorene and Diphenylmethylidene Fluorene: The Relationship between Magnetic and Energetic Measures of Antiaromaticity", *J. Org. Chem.* **2011**, *76*, 181–187, DOI 10.1021/jo101871q.

[109] M. J. Moure, Y. Zhuo, G. J. Boons, J. H. Prestegard, "Perdeuterated and ^{13}C-enriched myo-inositol for DNP assisted monitoring of enzymatic phosphorylation by inositol-3-kinase", *Chem. Commun.* **2017**, *53*, 12398–12401, DOI 10.1039/c7cc07023c.

[110] G.-M. Lin, H. G. Sun, H.-W. Liu, "Study of Uridine 5'-Diphosphate (UDP)-Galactopyranose Mutase Using UDP-5-Fluorogalactopyranose as a Probe: Incubation Results and Mechanistic Implications", *Org. Lett.* **2016**, *18*, 3438–3441, DOI 10.1021/acs.orglett.6b01618.

[111] Z. Zhou, R. Kümmerle, X. Qiu, D. Redwine, R. Cong, A. Taha, D. Baugh, B. Winniford, "A new decoupling method for accurate quantification of polyethylene copolymer composition and triad sequence distribution with ^{13}C NMR", *J. Magn. Reson.* **2007**, 225–233, DOI 10.1016/j.jmr.2007.05.005.

[112] V. Denysenkov, D. Dai, T. F. Prisner, "A triple resonance (e, ^{1}H, ^{13}C) probehead for liquid−state DNP experiments at 9.4 Tesla", *J. Magn. Reson.* **2022**, *337*, 107185, DOI https://doi.org/10.1016/j.jmr.2022.107185.

[113] M. H. Levitt, R. Freeman, T. Frenkel, "Supercycles for Broadband Heteronuclear Decoupling", *J. Magn. Reson.* **1982**, *50*, 157–160, DOI https://doi.org/10.1016/0022-2364(82)90042-7.

[114] M. H. Levitt, R. Freeman, T. Frenkel, "Broadband Heteronuclear Decoupling", *J. Magn. Reson.* **1982**, DOI https://doi.org/10.1016/0022-2364(82)90124-X.

[115] C. Griesinger, G. Otting, K. Wüthrich, R. R. Ernst, "Clean TOCSY for ^{1}H Spin System Identification in Macromolecules", *J. Am. Chem. Soc.* **1988**, *110*, 7870–7872, DOI https://doi.org/10.1021/ja00231a044.

[116] S. P. Rucker, A. J. Shaka, "Broadband homonuclear cross polarization in 2D N.M.R. using DIPSI-2", *Mol. Phys.* **1989**, *68*, 509–517, DOI 10.1080/00268978900102331.

[117] A. Bax, R. Freeman, S. P. Kempsell, "Natural Abundance ^{13}C-^{13}C Coupling Observed via Double-Quantum Coherence", *J. Am. Chem. Soc.* **1980**, *102*, 4851–4852, DOI https://doi.org/10.1021/ja00534a056.

[118] M. Bourdonneau, B. Ancian, "Rapid-Pulsing Artifact-Free Double-Quantum-Filtered Homonuclear Spectroscopy", *J. Magn. Reson* **1998**, *132*, 316–327, DOI 10.1006/jmre.1998.1392.

[119] A. Jerschow, N. Müller, "Suppression of Convection Artifacts in Stimulated-Echo Diffusion Experiments. Double-Stimulated-Echo Experiments", *J. Magn. Reson.* **1997**, *125*, 372–375, DOI 10.1006/jmre.1997.1123.

[120] F. Neese, "The ORCA program system", *WIREs Comput. Mol. Sci.* **2012**, *2*, 73–78, DOI 10.1002/wcms.81.

[121] F. Neese, "Software update: the ORCA program system, version 4.0", *WIREs Comput. Mol. Sci.* **2018**, *8*, e1327, DOI https://doi.org/10.1002/wcms.1327.

[122] S. Grimme, J. Anthony, S. Ehrlich, H. Krieg, "A consistent and accurate ab initio parametrization of density functional dispersion correction (DFT-D) for the 94 elements H-Pu", *J. Chem. Phys.* **2010**, *132*, 154104, DOI https://doi.org/10.1063/1.3382344.

[123] S. Grimme, S. Ehrlich, L. Goerigk, "Effect of the damping function in dispersion corrected density functional theory", *J. Comput. Chem.* **2011**, *32*, 1456–1465, DOI https://doi.org/10.1002/jcc.21759.

[124] E. F. Pettersen, T. D. Goddard, C. C. Huang, G. S. Couch, D. M. Greenblatt, E. C. Meng, T. E. Ferrin, "UCSF Chimera — a visualization system for exploratory research and analysis", *J. Comput. Chem.* **2004**, *25*, 1605–1612, DOI 10.1002/jcc.20084.

[125] G. Bussi, D. Donadio, M. Parrinello, "Canonical sampling through velocity rescaling", *J. Chem. Phys.* **2007**, *126*, 014101, DOI 10.1063/1.2408420.

[126] U. Essmann, L. Perera, M. L. Berkowitz, T. Darden, H. Lee, L. G. Pedersen, "A smooth particle mesh Ewald method", *J. Chem. Phys.* **1995**, *103*, 8577–8593, DOI 10.1063/1.470117.

[127] B. Hess, H. Bekker, H. J. C. Berendsen, J. G. E. M. Fraaije, "LINCS: A linear constraint solver for molecular simulations", *J. Comput. Chem.* **1997**, *18*, 1463–1472, DOI 10.1002/(SICI)1096-987X(199709)18:12<1463::AID-JCC4>3.0.CO;2-H.

[128] S. Pronk, S. Páll, R. Schulz, P. Larsson, P. Bjelkmar, R. Apostolov, M. R. Shirts, J. C. Smith, P. M. Kasson, D. van der Spoel, B. Hess, E. Lindahl, "GROMACS 4.5: a high-throughput and highly parallel open source molecular simulation toolkit", *Bioinformatics* **2013**, *29*, 845–854, DOI 10.1093/bioinformatics/btt055.

[129] M. Reinhard, "Polarizer Comparison in Liquid State ^{1}H and ^{13}C Overhauser Dynamic Nuclear Polarization at 1.2 T and 0.34 T", *Master Thesis* **2020**.

[130] *Handbook of High Field Dynamic Nuclear Polarization*, (Eds.: V. K. Michaelis, R. G. Griffin, B. Corzilius, S. Vega), Wiley, **2019**.

[131] A. S. L. Thankamony, J. J. Wittmann, M. Kaushik, B. Corzilius, "Dynamic nuclear polarization for sensitivity enhancement in modern solid-state NMR", *Prog. Nucl. Mag. Res. Spectrosc* **2017**, *102-103*, 120–195, DOI http://dx.doi.org/10.1016/j.pnmrs.2017.06.002.

[132] T. Kobayashi, M. Pruski, "Spatial Distribution of Silica-Bound Catalytic Organic Functional Groups Can Now Be Revealed by Conventional and DNP-Enhanced Solid-State NMR Methods", *ACS Catalysis* **2019**, *9*, 7238–7249, DOI 10.1021/acscatal.9b02017.

[133] G. Casano, H. Karoui, O. Ouari, "Polarizing agents: evolution and outlook in free radical development for DNP", *eMagRes* **2018**, 195–208, DOI 10.1002/9780470034590.emrstm1547.

[134] V. P. Denysenkov, T. F. Prisner, "Liquid-state Overhauser DNP at high magnetic fields", *eMagRes* **2019**, *8*, 41–54, DOI 10.1002/9780470034590.emrstm1557.

[135] P. Neugebauer, J. G. Krummenacker, V. P. Denysenkov, C. Helmling, C. Luchinat, G. Parigi, T. F. Prisner, "High-field liquid state NMR hyperpolarization: a combined DNP/NMRD approach", *Phys. Chem. Chem. Phys.* **2014**, *16*, 18781–18787, DOI 10.1039/C4CP02451F.

[136] S. Stevenson, H. C. Dorn, "^{13}C Dynamic Nuclear Polarization: A Detector for Continuous-Flow, On-Line Chromatography", *Anal. Chem.* **1994**, *66*, 2993–2999, DOI 10.1021/ac00091a003.

[137] S. van Meerten, F. van Zelst, K. Tijssen, A. Kentgens, "An Optimized NMR Stripline for Sensitive Supercritical Fluid Chromatography-Nuclear Magnetic Resonance of Microliter Sample Volumes", *Anal. Chem.* **2020**, *92*, 13010–13016, DOI 10.1021/acs.analchem.0c01827.

[138] B. Gizatullin, C. Mattea, S. Stapf, "X-nuclei hyperpolarization for studying molecular dynamics by DNP-FFC", *J. Magn. Reson.* **2019**, *307*, 106583, DOI 10.1016/j.jmr.2019.106583.

[139] B. D. Armstrong, S. Han, "Overhauser Dynamic Nuclear Polarization to Study Local Water Dynamics", *J. Am. Chem. Soc.* **2009**, *131*, 4641–4647, DOI https://doi.org/10.1021/ja809259q.

[140] J. R. Biller, R. Barnes, S. Han, "Perspective of Overhauser dynamic nuclear polarization for the study of soft materials", *Curr. Opin. Colloid Interface Sci.* **2018**, *33*, 72–85, DOI 10.1016/j.cocis.2018.02.007.

[141] O. Jakdetchai, V. Denysenkov, J. Becker-Baldus, B. Dutagaci, T. F. Prisner, C. Glaubitz, "Dynamic nuclear polarization-enhanced NMR on aligned lipid bilayers at ambient temperature", *J. Am . Chem. Soc.* **2014**, *136*, 15533–15536, DOI 10.1021/ja509799s.

[142] T. J. Keller, A. J. Laut, J. Sirigiri, T. Maly, "High-resolution Overhauser dynamic nuclear polarization enhanced proton NMR spectroscopy at low magnetic fields", *J. Magn. Reson* **2020**, *313*, 106719, DOI https://doi.org/10.1016/j.jmr.2020.106719.

[143] M. Lingwood, S. Han, "Solution-State Dynamic Nuclear Polarization", *Annu. Rep. NMR Spectrosc.* **2011**, *73*, 83–126, DOI 10.1016/B978-0-08-097074-5.00003-7.

[144] R. A. Wind, J. H. Ardenkjær-Larsen, "^{1}H DNP at 1.4 T of water doped with a triarylmethyl-based radical", *J. Magn. Reson.* **1999**, *141*, 347–354, DOI https://doi.org/10.1006/jmre.1999.1910.

[145] P. Hoefer, G. Parigi, C. Luchinat, P. Carl, G. Guthausen, M. Reese, T. Carlomagno, C. Griesinger, M. Bennati, "Field Dependent Dynamic Nuclear Polarization with Radicals in Aqueous Solution", *J. Am. Chem. Soc.* **2008**, *130*, 3254–3255, DOI https://doi.org/10.1021/ja0783207.

[146] T. V. Can, M. A. Caporini, F. Mentink-Vigier, B. Corzilius, J. J. Walish, M. Rosay, W. E. Maas, M. Baldus, S. Vega, T. M. Swager, R. G. Griffin, "Overhauser effects in insulating solids", *J. Chem. Phys.* **2014**, *141*, 064202, DOI 10.1063/1.4891866.

[147] A. N. Tikhonov, L. N. Ikryannikova, L. Y. Ustynyuk, "DFT study of nitroxide radicals: Explicit modeling of solvent effects on the structural and electronic characteristics of 4-amino-2,2,6,6-tetramethyl- piperidine-N-oxyl", *Magn. Reson. Chem.* **2010**, *48*, 337–349, DOI 10.1002/mrc.2585.

[148] H. H. Haeri, P. Spindler, J. Plackmeyer, T. Prisner, "Double quantum coherence ESR spectroscopy and quantum chemical calculations on a BDPA biradical", *Phys. Chem. Chem. Phys.* **2016**, *18*, 29164–29169, DOI 10.1039/c6cp05847g.

[149] G. Stevanato, G. Casano, D. J. Kubicki, Y. Rao, L. Esteban Hofer, G. Menzildjian, H. Karoui, D. Siri, M. Cordova, M. Yulikov, G. Jeschke, M. Lelli, A. Lesage, O. Ouari, L. Emsley, "Open and Closed Radicals: Local Geometry around Unpaired Electrons Governs Magic-Angle Spinning Dynamic Nuclear Polarization Performance", *J. Am. Chem. Soc.* **2020**, *142*, 16587–16599, DOI 10.1021/jacs.0c04911.

[150] W. Kutzelnigg, U. Fleischer, C. van Wüllen, "Shielding Calculations: IGLO Method", *eMagRes* **2007**, DOI 10.1002/9780470034590.emrstm0495.

[151] J. M. Franck, A. Pavlova, J. A. Scott, S. Han, "Quantitative cw Overhauser effect dynamic nuclear polarization for the analysis of local water dynamics", *Prog. Nucl. Mag. Res. Sp.* **2013**, *74*, 33–56, DOI 10.1016/j.pnmrs.2013.06.001.

[152] J. Van Bentum, B. Van Meerten, M. Sharma, A. Kentgens, "Perspectives on DNP-enhanced NMR spectroscopy in solutions", *J. Magn. Reson.* **2016**, *264*, 59–67, DOI 10.1016/j.jmr.2016.01.010.

[153] D. Sezer, "Computation of DNP coupling factors of a nitroxide radical in toluene: seamless combination of MD simulations and analytical calculations", *Phys. Chem. Chem. Phys.* **2013**, *15*, 526–540, DOI 10.1039/c2cp42430d.

[154] T. Prisner, V. Denysenkov, D. Sezer, "Liquid state DNP at high magnetic fields: Instrumentation, experimental results and atomistic modelling by molecular dynamics simulations", *J. Magn. Reson.* **2016**, *264*, 68–77, DOI https://doi.org/10.1016/j.jmr.2015.11.004.

[155] G. Parigi, E. Ravera, M. Bennati, C. Luchinat, "Understanding Overhauser Dynamic Nuclear Polarisation through NMR relaxometry", *Mol. Phys.* **2018**, *117*, 888–897, DOI 10.1080/00268976.2018.1527409.

[156] P. Höfer, G. Parigi, C. Luchinat, P. Carl, G. Guthausen, M. Reese, T. Carlomagno, C. Griesinger, M. Bennati, "Field dependent dynamic nuclear polarization with radicals in aqueous solution", *J. Am. Chem. Soc.* **2008**, *130*, 3254–3255, DOI https://doi.org/10.1021/ja0783207.

[157] B. C. Dollmann, A. L. Kleschyov, V. Sen, V. Golubev, L. M. Schreiber, H. W. Spiess, K. Münnemann, D. Hinderberger, "Spin-labeled heparins as polarizing agents for dynamic nuclear polarization", *ChemPhysChem* **2010**, *11*, 3656–3663, DOI 10.1002/cphc.201000559.

[158] D. J. Kubicki, L. Emsley, "Improving sensitivity of solid-state NMR spectroscopy by rational design of polarizing agents for dynamic nuclear polarization", *Chimia* **2017**, *71*, 190–194, DOI 10.2533/chimia.2017.190.

[159] D. Kruk, A. Korpała, J. Kowalewski, E. A. Rössler, J. Moscicki, "^{1}H relaxation dispersion in solutions of nitroxide radicals: Effects of hyperfine interactions with ^{14}N and ^{15}N nuclei", *J. Chem. Phys.* **2012**, *137*, 044512, DOI 10.1063/1.4736854.

[160] S. E. Küçük, D. Sezer, "Multiscale computational modeling of ^{13}C DNP in liquids", *Phys. Chem. Chem. Phys.* **2016**, *18*, 9353–9357, DOI 10.1039/c6cp01028h.

[161] J. Winkelmann in *Diffusion in Gases, Liquids and Electrolytes*, *Vol. 15B1*, (Ed.: M. D. Lechner), Springer, Berlin, Heidelberg, **2017**, pp. 317–319, DOI 10.1007/978-3-540-73735-3_181.

[162] D. Kruk, A. Korpala, E. Rössler, K. A. Earle, W. Medycki, J. Moscicki, "^{1}H NMR relaxation in glycerol solutions of nitroxide radicals: Effects of translational and rotational dynamics", *J. Chem. Phys.* **2012**, *136*, 114504, DOI 10.1063/1.3692603.

[163] D. E. O'Reilly, E. M. Peterson, "Self-diffusion coefficients and rotational correlation times in polar liquids. III. Toluene", *J. Chem. Phys.* **1971**, *56*, 2262–2266, DOI 10.1063/1.1678335.

[164] I. G. Tironi, W. F. Van Gunsteren, "A molecular dynamics simulation study of chloroform", *Mol. Phys.* **1994**, *83*, 381–403, DOI https://doi.org/10.1080/00268979400101331.

[165] E. Stendardo, A. Pedone, P. Cimino, M. C. Menziani, O. Crescenzii, V. Barone, "Extension of the AMBER force-field for the study of large nitroxides in condensed phases: an ab initio parameterization", *Phys. Chem. Chem. Phys.* **2010**, *12*, 11697–11709, DOI https://doi.org/10.1039/C001481H.

[166] S. Stoll, A. Schweiger, "EasySpin, a comprehensive software package for spectral simulation and analysis in EPR", *J. Magn. Reson.* **2006**, *178*, 42–55, DOI 10.1016/j.jmr.2005.08.013.

[167] G. Zheng, T. Stait-Gardner, P. G. A. Kumar, A. M. Torres, W. S. Price, "PGSTE-WATERGATE: An STE-based PGSE NMR sequence with excellent solvent suppression", *J. Magn. Reson.* **2008**, *191*, 159–163, DOI 10.1016/j.jmr.2007.12.001.

[168] K.-C. Chung, H.-Y. Yu, S. Ahn, "Convection Effects on PGSE-NMR Self-Diffusion Measurements at Low Temperature: Investigation into Sources of Induced Convective Flows", *Bull. Korean Chem. Soc.* **2011**, *32*, 1970–1974, DOI 10.5012/bkcs.2011.32.6.1970.

[169] M. Holz, S. R. Heil, A. Sacco, "Temperature-dependent self-diffusion coefficients of water and six selected molecular liquids for calibration in accurate ^{1}H NMR PFG measurements", *Phys. Chem. Chem. Phys.* **2000**, *2*, 4740–4742, DOI 10.1039/b005319h.

[170] F. Weigend, R. Ahlrichs, "Balanced basis sets of split valence, triple zeta valence and quadruple zeta valence quality for H to Rn: Design and assessment of accuracy", *Phys. Chem. Chem. Phys.* **2005**, *7*, 3297–3305, DOI https://doi.org/10.1039/B508541A.

[171] F. Weigend, "Accurate Coulomb-fitting basis sets for H to Rn", *Phys. Chem. Chem. Phys.* **2006**, *8*, 1057–1065, DOI https://doi.org/10.1039/B515623H.

[172] F. Neese, F. Wennmohs, A. Hansen, U. Becker, "Efficient, approximate and parallel Hartree-Fock and hybrid DFT calculations. A 'chain-of-spheres' algorithm for the Hartree-Fock exchange", *Chem. Phys.* **2009**, *356*, 98–109, DOI https://doi.org/10.1016/j.chemphys.2008.10.036.

[173] C. I. Bayly, P. Cieplak, W. D. Cornell, P. A. Kollman, "A well-behaved electrostatic potential based method using charge restraints for deriving atomic charges: the RESP model", *J. Phys. Chem.* **1993**, *97*, 10269–10280, DOI https://doi.org/10.1021/j100142a004.

[174] T. Lu, F. Chen, "Multiwfn: A multifunctional wavefunction analyzer", *J. Comput. Chem.* **2012**, *33*, 580–592, DOI https://doi.org/10.1002/jcc.22885.

[175] T. Fox, P. A. Kollman, "Application of the RESP Methodology in the Parametrization of Organic Solvents", *J. Phys. Chem. B* **1998**, *102*, 8070–8079, DOI https://doi.org/10.1021/jp9717655.

[176] A. W. S. da Silva, W. F. Vfranken, "ACPYPE - AnteChamber PYthon Parser interfacE", *BMC Research Notes* **2012**, *5*, 367, DOI https://doi.org/10.1186/1756-0500-5-367.

[177] A. J. Richards, K. S. Rogers, "The Isothermal Compressibility of Organic Liquids by Ultracentrifugation. Correlation with Surface Tension", *Can. J. Chem.* **1971**, *49*, 3956–3959, DOI https://doi.org/10.1139/v71-662.

[178] S. S. Eaton, G. R. Eaton, "EPR Spectroscopy: Fundamentals and Methods - Relaxation Mechanisms", *eMagRes* **2017**, *6*, 175–192.

[179] M. J. Prandolini, V. P. Denysenkov, M. Gafurov, B. Endeward, T. F. Prisner, "High-Field Dynamic Nuclear Polarization in Aqueous Solutions", *J. Am. Chem. Soc.* **2009**, *131*, 6090–6092, DOI https://doi.org/10.1021/ja901496g.

[180] J. R. Biller, V. Meyer, H. Elajaili, G. M. Rosen, J. P. Y. Kao, S. S. Eaton, G. R. Eaton, "Relaxation times and line widths of isotopically-substituted nitroxides in aqueous solution at X-band", *J. Magn. Reson.* **2013**, *212*, 370–377.

[181] E. Bordignon, "EPR Spectroscopy: Fundamentals and Methods - EPR Spectroscopy of Nitroxide Probes", *eMagRes* **2017**, *6*, 277–301.

[182] A. Carrington, A. D. McLachlan, *Introduction to Magnetic Resonance*, (Ed.: S. A. Rice), Harper and Row, **1967**.

[183] C. P. Poole, *Electron Spin Resonance: A Comprehensive Treatise on Experimental Techniques*, *Vol. 2*, Wiley, **1969**.

[184] M. Levien, "Saturation Experiments and DNP at 3.4 Tesla", *Bachelor Thesis* **2015**.

[185] J. J. Windle, "Hyperfine Coupling Constants for Nitroxide Spin Probesin Water and Carbon Tetrachloride", *J. Magn. Reson.* **1981**, *45*, 432–439, DOI https://doi.org/10.1016/0022-2364(81)90150-5.

[186] V. Weis, M. Bennati, M. Rosay, J. A. Bryant, R. G. Griffin, "High-field DNP and ENDOR with a novel Multiple Frequency Resonance Structure", *J. Magn. Reson.* **1999**, *140*, 293–299, DOI https://doi.org/10.1006/jmre.1999.1841.

[187] M. Blank, P. Borchard, S. Cauffman, K. Felch in 2018 43rd International Conference on Infrared, Millimeter, and Terahertz Waves (IRMMW-THz), IEEE, **2018**, pp. 1–2, DOI 10.1109/IRMMW-THz.2018.8510010.

[188] P. Berruyer, A. B. S. Björgvinsdottir, G. Stevanato, Y. Rao, G. Karthikeyan, G. Casano, O. Ouari, M. Lelli, C. Reiter, F. Engelke, L. Emsley, "Dynamic Nuclear Polarization Enhancement of 200 at 21.15 T Enabled by 65 kHz Magic Angle Spinning", *J. Phys. Chem. Lett.* **2020**, *11*, 8386–8391.

[189] V. L. Granatstein, R. K. Parker, C. M. Armstrong, "Scanning the Technology - Vacuum Elevtronics at the Dawn of the Twenty-First Century", *Proc. IEEE* **1999**, *84*, 702–716, DOI 10.1109/5.757251.

[190] M. Hruszowiec, K. Nowak, B. Szlachetko, M. Grzelczak, W. Czarczynski, E. F. Plinski, T. Wieckowski, "The Microwave Sources for EPR Spectroscopy", *J. Telecommun. Inf. Technol.* **2017**, 18–25, DOI 10.26636/jtit.2017.107616.

[191] C. George, N. Chandrakumar, "Chemical-shift resolved ^{19}F NMR spectroscopy between 13.5 and 135 MHz Overhauser enhanced Diagonal suppressed correlation spectroscopy", *Angew. Chem. Int. Ed.* **2014**, *126*, 8581–8584, DOI 10.1002/ange.201402320.

[192] M. Rosay, M. Blank, F. Engelke, "Instrumentation for solid-state dynamic nuclear polarization with magic angle spinning NMR", *J. Magn. Reson.* **2016**, *264*, 88–98, DOI http://dx.doi.org/10.1016/j.jmr.2015.12.026.

[193] P. Bharta, I. J. Bahl, *Millimeter Wave Engineering and Applications*, Wiley-Interscience, **1984**.

[194] E. A. Nanni, S. K. Jawla, M. A. Shapiro, P. P. Woskov, R. J. Temkin, "Low-Loss Transmission Lines for High-power Terahertz Radiation", *J. Infrared Milli Terahz Waves* **2012**, *33*, 695–714, DOI 10.1007/s10762-012-9870-5.

[195] J. Chen, T. Maly, "Compact, tunable polarization transforming reflector for quasi-optical devices used in terahertz science", *Rev. Sci. Instrum.* **2022**, *93*, 013102, DOI https://doi.org/10.1063/5.0036292.

[196] J. D. Jackson, *Classical Electrodynamics*, Wiley, **1999**.

[197] *Broadband Dielectric Spectroscopy*, *Vol. 1*, (Eds.: F. Kremer, A. Schönhals), Springer, **2003**, DOI 10.1007/978-3-642-56120-7.

[198] H. J. Liebe, G. A. Hufford, T. Manabe, "A MODEL FOR THE COMPLEX PERMITTIVITY OF WATER AT FREQUENCIES BELOW 1 THz", *Int. J. Infrared millim. waves* **1991**, *12*, 659–675, DOI https://doi.org/10.1007/BF01008897.

[199] C. Ronne, L. Thrane, P. Astrand, A. Wallqvist, K. V. Mikkelsen, S. R. Keiding, "Investigation of the temperature dependence of dielectric relaxation in liquid water by THz reflection spectroscopy and molecular dynamics simulation", *J. Chem. Phys.* **1997**, *107*, 5319–5331, DOI https://doi.org/10.1063/1.474242.

[200] Heraeus, accessed 04.10.2022, 19:24 h, DOI https://www.heraeus.com/en/hca/fused_silica_quartz_knowledge_base_1/properties_1/properties_hca.html\#tabs-608478-8.

[201] C. Gabriel, S. Gabriel, E. H. Grant, B. S. J. Halstead, D. M. P. Mingos, "Dielectric parameters relevant to microwave dielectric heating", *Chem. Soc. Rev.* **1998**, *27*, 213–223, DOI https://doi.org/10.1039/A827213Z.

[202] M. Young, *Optik, Laser, Wellenleiter*, *Vol. 4*, Springer, **1993**.

[203] D. J. Kubicki, A. J. Rossini, A. Purea, A. Zagdoun, O. Ouari, P. Tordo, F. Engelke, A. Lesage, L. Emsley, "Amplifying Dynamic Nuclear Polarization of Frozen Solutions by Incorporating Dielectric Particles", *J. Am. Chem. Soc.* **2014**, *136*, 15711–15718, DOI https://doi.org/10.1021/ja5088453.

[204] N. Y. Tan, R. Li, P. Bräuer, C. D'Agostino, L. F. Gladden, J. A. Zeitler, "Probing hydrogen-bonding in binary liquid mixtures with terahertz time-domain spectroscopy: a comparison of Debye and absorption analysis", *Phys. Chem. Chem. Phys.* **2015**, *17*, 5999–6008, DOI 10.1039/c4cp04477k.

[205] S. L. Robinette, R. Brüschweiler, F. C. Schroeder, A. S. Edison, "NMR in Metabolomics and Natrual Products Research: Two Sides of the Same Coin", *Acc. Chem. Resn.* **2012**, *45*, 288–297, DOI 10.1021/ar2001606.

[206] N. Karshin, K. Wolkenstein, C. Griesinger, "Magnetically Induced Alignment of Natural Products for Stereochemical Structure Determination via NMR", *Angew. Chem. Int. Ed.* **2020**, *59*, 1–6, DOI doi.org/10.1002/anie.202004881.

[207] T. Stadelmann, C. Balmer, S. Riniker, M.-O. Ebert, "Impact of solvent interactions on ^{1}H and ^{13}C chemical shifts investigated using DFT and a reference dataset recorded in $CDCl_3$ and CCl_4", *Phys. Chem. Chem. Phys.* **2022**, *24*, 23551–23560, DOI 10.1039/d2cp03205h.

[208] G. R. Fulmer, A. J. M. Miller, N. H. Sherden, H. E. Gottlieb, A. Nudelman, B. M. Stoltz, J. . Bercaw, K. I. Goldberg, "NMR Chemical Shifts of Trace Impurities: Common Laboratory Solvents, Organics, and Gases in Deuterated Solvents Relevant to the Organometallic Chemist", *Organometallics* **2010**, *29*, 2176–2179, DOI 10.1021/om100106e.

[209] V. Wray, L. Ernst, T. Lund, H. J. Jakobsen, "Carbon-Carbon Spin-Spin Coupling constants in Monosubstituted Benzenes", *J. Magn. Reson.* **1980**, *40*, DOI https://doi.org/10.1016/0022-2364(80)90229-2.

[210] P. Auffinger, F. A. Hays, E. Westhof, P. S. Ho, "Halogen Bonds in biological molecules", *Proc. Natl. Acad. Sci.* **2004**, *101*, 16789–16794, DOI https://doi.org/10.1073/pnas.0407607101.

[211] G. Cavallo, P. Metrangolo, R. Milani, T. Pilati, A. Priimagi, G. Resnati, G. Terraneo, "The Halogen Bond", *Chem. Rev.* **2016**, *116*, 2478–2601, DOI 10.1021/acs.chemrev.5b00484.

[212] G. M. Espallargas, A. Recuenco, F. M. Romero, L. Brammer, S. Libri, "One-dimensional organization of free radicals via halogen bonding", *CrystEngComm* **2012**, *14*, 6381–6383, DOI 10.1039/c2ce26131f.

[213] K. Boubekeur, J.-L. Syssa-Magale, P. Palvadeau, B. Schöllhorn, "Self-assembly of nitroxide radicals via halogen bonding - directional NO I interactions", *Tetrahedron Lett.* **2006**, *47*, 1249–1252, DOI 10.1016/j.tetlet.2005.12.088.

[214] X. Pang, X. R. Zhao, H. Wang, H.-L. Sun, W. J. Jin, "Modulating Crystal Packing and Magnetic Properties of Nitroxide Free Radicals by Halogen Bonding", *Cryst. Growth Des.* **2013**, *13*, 3439–3745, DOI dx.doi.org/10.1021/cg400776x.

[215] I. M. Ganiev, Q. K. Timerghazin, A. F. Khalizov, V. V. Shereshovets, A. I. Grigorev, G. A. Tolstikov, "Complex of chlorine dioxide with TEMPO and its conversion into oxoammonium salt", *J. Phys. Org. Chem.* **2001**, *14*, 38–42, DOI https://doi.org/10.1002/1099-1395(200101)14:1<38::AID-POC334>3.0.CO;2-Z.

[216] Y. Hosokashi, M. Tamura, K. Nozawa, S. Suzuki, M. Kinoshita, H. Sawa, R. Kato, "Magnetic properties and crystal structures of 2-hydro and 2-halo nitronyl nitroxidc radical crystals", *Synth Met.* **1995**, *71*, 1795–1796, DOI https://doi.org/10.1016/0379-6779(94)03054-A.

[217] T. Lohmüller, M. A. Vibhute, W. Lubitz, A. Savitsky, "Multifrequency Multiresonance EPR Investigation of Halogen-bonded Complexes Involving Neutral Nitroxide Radicals", *Z. Phys. Chem.* **2017**, *231*, 867–886, DOI 10.1515/zpch-2016-0870.

[218] X. Jiang., B. Rodrigues-Molina, N. Nazarian, M. A. Garcia-Garibay, "Rotation of a Bulky Triptycene in the Solid State: Toward Engineered Nanoscale Artificial Molecular Machines", *J. Am. Chem. Soc.* **2014**, *136*, 8871–8874, DOI dx.doi.org/10.1021/ja503467e.

[219] R. A. Thorson, G. R. Woller, Z. L. Driscoll, B. E. Geiger, C. A. Moss, A. L. Schlapper, E. D. Speetzen, E. Bosch, M. Erdelyi, N. P. Bowling, "Intramolecular Halogen Bonding in Solution: ^{15}N, ^{13}C, and ^{19}F NMR Studies of Temperature and Solvent Effect", *Eur. J. org. Chem.* **2015**, 1685–1695, DOI 10.1002/ejoc.201403671.

[220] A. Banerjee, A. Dey, N. Chandrakumar, "Motional Dynamics of Halogen bonded complexes probed by low field NMR relaxometry and Overhauser Dynamic Nuclear Polarization", *Chem. Asian J.* **2019**, *14*, 2785–2789, DOI 10.1002/asia.201900754.

[221] K. E. Riley, J. S. Murray, J. Fanfrlik, J. Rezac, R. J. Sola, M. C. Concha, F. M. Ramos, P. Politzer, "Halogen bond tunability I: the effects of aromatic fluorine substitution on the strengths of halogen-bonding interactions involving chlorine, bromine, and iodine", *J. Mol. Model* **2011**, *17*, 3309–3318, DOI 10.1007/s00894-011-1015-6.

[222] J. Rezac, K. E. Riley, P. Hobza, "Benchmark Calculations of Noncovalent Interactions of Halogenated Molecules", *J. Chem. Theory Comput.* **2012**, *8*, 4285–4292, DOI https://doi.org/10.1021/ct300647k.

[223] C. Präsang, A. C. Whitwood, D. W. Bruce, "Halogen-Bonded Cocrystals of 4-(N,N-Dimethylamino)pyridine with Fluorinated Iodobenzenes", *Cryst. Growth Des.* **2009**, *9*, 5319–5326, DOI 10.1021/cg900823d.

[224] J. F. Bertran, M. Rodriguez, "Detection of Halogen Bond Formation by Correlation of Proton Solvent Shifts; 1. Haloforms in *n*-Electron Donor Solvents", *Org. Magn. Reson.* **1979**, *12*, 92–94, DOI https://doi.org/10.1002/mrc.1270120210.

[225] J. F. Bertran, M. Rodriguez, "Detection of Halogen Bond Formation by Correlation of Proton Solvent Shifts; II – Methylene Halides in *n*-Electron Donor Solvents", *Org. Magn. Reson.* **1980**, *14*, 244–246, DOI https://doi.org/10.1002/mrc.1270140404.

[226] T. F. Brust, D. Alongkronrusmee, M. Soto-Velasquez, T. A. Baldwin, Z. Ye, M. D. C. W. Dessauer, R. M. van Rijn, V. J. Watts, "Identification of a selective small-molecule inhibitor of type 1 adenylyl cyclase activity with analgesic properties", *Sci. Signal* **2017**, *10*, eaah5381, DOI 10.1126/scisignal.aah5381.

[227] B. R. Smith, C. M. Eastman, J. T. Njardarson, "Beyond C, H, O, and N Analysis of the Elemental Composition of U.S. FDA Approved Drug Architectures", *J. Med. Chem.* **2014**, *57*, 9764–9773, DOI dx.doi.org/10.1021/jm501105n.

[228] A. A. Ribeiro, G. L. Jendrasiak, "^{1}H and ^{13}C NMR Analyses of Amiodarone, Desethylamiodaroneand Desoxoamiodarone", *Magn. Reson. Chem* **1991**, *29*, 482–493, DOI https://doi.org/10.1002/mrc.1260290513.

[229] L. Meng, J. Fang, L. Zhao, T. Wang, P. Yuan, Z. Zhao, R. Zhuang, Q. Lin, H. Chen, X. Chen, X. Zhang, Z. Guo, "Rational Design and Pharmacomodulation of Protein−Binding Theranostic Radioligands for Targeting the Fibroblast Activation Protein", *J. Med. Chem.* **2022**, *65*, 8245–8257, DOI https://doi.org/10.1021/acs.jmedchem.1c02162.

[230] S. J. Nelson, J. Kurhanewicz, D. B. Vigneron, P. E. Z. Larson, A. L. Harzstark, M. Ferrone, M. V. Criekinge, J. W. Chang, R. Bok, I. Park, G. Reed, L. Carcajal, E. J. Small, P. Munster, V. K. Weinberg, J. H. Ardenkjaer-Larsen, A. P. Chen, R. E. Hurd, L.-I. Odegardstuen, F. J. Robb, J. Tropp, J. A. Murray, "Metabolic Imaging of Patiens with Prostate Cancer using Hyperpolarized [1-^{13}C]Pyruvate", *Sci. Transl. Med.* **2013**, *5*, 198ra108, DOI 10.1126/scitranslmed.3006070.

[231] M. Sattler, J. Schleucher, C. Griesinger, "Heteronuclear multidimensional NMR experiments for the structure determination of proteins in solution employing pulsed field gradients", *Prog. Nucl. Mag. Res. Spectrosc.* **1999**, *34*, 93–158, DOI https://doi.org/10.1016/S0079-6565(98)00025-9.

[232] T. Carlomagno, "Ligand-Target Interactions: What Can We Learn from NMR?", *Annu. Rev. Biomol. Struct.* **2005**, *34*, 245–266, DOI 10.1146/annurev.biophys.34.040204.144419.

[233] D. M. Dias, A. Ciulli, "NMR approaches in structure-based lead discovery: Recent developments and new frontiers for targeting multi-protein complexes", *Prog. Biophys. Mol. Biol.* **2014**, *116*, 101–112, DOI http://dx.doi.org/10.1016/j.pbiomolbio.2014.08.012.

[234] L. Antonschmidt, D. Matthes, R. Dervisoglu, B. Frieg, C. Dienemann, A. Leonov, E. Nimerovski, V. Sant, S. Ryazanov, A. Giese, G. F. Schröder, S. Becker, B. L. de Groot, C. Griesinger, L. B. Andreas, "The clinical drug candidate anle138b binds in a cavity of lipidic α-synuclein fibrils", *Nat. Commun.* **2022**, *13*, 5385, DOI https://doi.org/10.1038/s41467-022-32797-w.

[235] H. Kessler, M. Gehrke, C. Griesinger, "Two-Dimensional NMR Spectroscopy: Background and Overview of the Experiments", *Angew. Chem. Int. Ed.* **1988**, *27*, 490–536, DOI https://doi.org/10.1002/anie.198804901.

[236] C.-G. Joo, A. Casey, C. J. Turner, R. G. Griffin, "In Situ Temperature-Jump Dynamic Nuclear Polarization: Enhanced Sensitivity in Two Dimensional ^{13}C-^{13}C Correlation Spectroscopy in Solution", *J. Am. Chem. Soc.* **2009**, *131*, 12–13, DOI https://doi.org/10.1021/ja805521y.

[237] A. S. Kiryutin, G. Sauer, D. Tietze, M. Brodrecht, S. Knecht, A. V. Yurkovskaya, K. L. Ivanov, O. Avrutina, H. Kolmar, G. Buntkowsky, "Ultrafast Single-Scan 2D NMR Spectroscopic Detection of a PHIP-Hyperpolarized Protease Inhibitor", *Chem. Eur. J.* **2019**, *25*, 4025–4030, DOI 10.1002/chem.201900079.

[238] T. J. Keller, T. Maly, "Overhauser dynamic nuclear polarization (ODNP)-enhanced two-dimensional proton NMR spectroscopy at low magnetic fields", *Magn. Reson.* **2021**, *2*, 117–128, DOI https://doi.org/10.5194/mr-2-117-2021.

[239] A. Dey, A. Banerjee, N. Chandrakumar, "Transferred Overhauser DNP: A Fast, Efficient Approach for Room Temperature ^{13}C ODNP at Moderately Low Fields and Natural Abundance", *J. Phys. Chem. B* **2017**, 7156–7162, DOI 10.1021/acs.jpcb.7b05081.

[240] A. E. Derome, M. P. Williamson, "Rapid-Pulsing Artifacts in Double-Quantum-Filtered COSY", *J. Magn. Reson.* **1990**, *88*, 177–185, DOI https://doi.org/10.1016/0022-2364(90)90123-Q.

[241] K. Nagayama, A. Kumar, K. Wüthrich, R. R. Ernst, "Experimental Techniques of Two-Dimensional Correlated Spectroscopy", *J. Magn. Reson.* **1980**, *40*, 321–334, DOI https://doi.org/10.1016/0022-2364(80)90255-3.

[242] C. Griesinger, O. W. Sorensen, R. R. Ernst, "Two-Dimensional Correlation of Connected NMR Transitions", *J. Am. Chem. Soc.* **1985**, *107*, 6394–6396, DOI https://doi.org/10.1021/ja00308a042.

[243] F. Hecker, J. Stubbe, M. Bennati, "Detection of Water Molecules on the Radical Transfer Pathway of Ribonucleotide Reductase by ^{17}O Electron-Nuclear Double Resonance Spectroscopy", *J. Am. Chem. Soc.* **2021**, *143*, 7237–7241, DOI https://doi.org/10.1021/jacs.1c01359.

[244] E. M. Bras, T. L. Fischer, M. A. Suhm, "The Hydrates of TEMPO: Water Vibrations Reveal Radical Microsolvation", *Angew. Chem. Int. Ed.* **2021**, *60*, 19013–19017, DOI doi.org/10.1002/anie.202104496.

[245] J. M. Franck, Y. Ding, K. Stone, P. Z. Qin, S. Han, "Anomalously Rapid Hydration Water Diffusion Dynamics Near DNA Surfaces", *J. Am. Chem. Soc.* **2015**, *137*, 12013–12023, DOI 10.1021/jacs.5b05813.

[246] J. M. Franck, S. Han, "Overhauser Dynamic Nuclear Polarization for the Study of Hydration Dynamics, Explained", *Methods in Enzymology* **2019**, *615*, 131–175, DOI https://doi.org/10.1016/bs.mie.2018.09.024.

[247] P. W. Atkins, J. de Paula, *Physikalische Chemie*, WILEY-VCH, **2013**.

[248] A. A. Kuzhelev, D. Dai, V. Denysenkov, T. F. Prisner, "Solid-like Dynamic Nuclear Polarization Observed in the Fluid Phase of Lipid Bilayers at 9.4 T", *J. Am. Chem. Soc.* **2022**, *144*, 1164–1168, DOI https://doi.org/10.1021/jacs.1c12837.

[249] K. G. Valentine, G. Mathies, S. Bedard, N. V. Nucci, I. Dodevski, M. A. Stetz, T. V. Can, R. G. Griffin, A. J. Wand, "Reverse Micelles As a Plattform for Dynamic Nuclear Polarization in Solution NMR or Proteins", *J. Am. Chem. Soc.* **2014**, *136*, 1800–2807, DOI dx.doi.org/10.1021/ja4107176.

[250] F. Zaera, "Probing Liquid/Solid Interfaces at the Molecular Level", *Chem. Rev.* **2012**, *112*, 2920–2986, DOI https://doi.org/10.1021/cr2002068.

[251] K. S. Liu, A. Henning, M. W. Heindl, R. D. Albert, J. H. Bartl, I. D. Sharp, R. Rizzato, D. B. Bucher, "Surface NMR using quantum sensors in diamond", *Proc. Natl. Acad. Sci.* **2022**, *119*, e2111607119, DOI https://doi.org/10.1073/pnas.2111607119.

Appendix

A Electron Spin Longitudinal Relaxation Time at 9.4 T

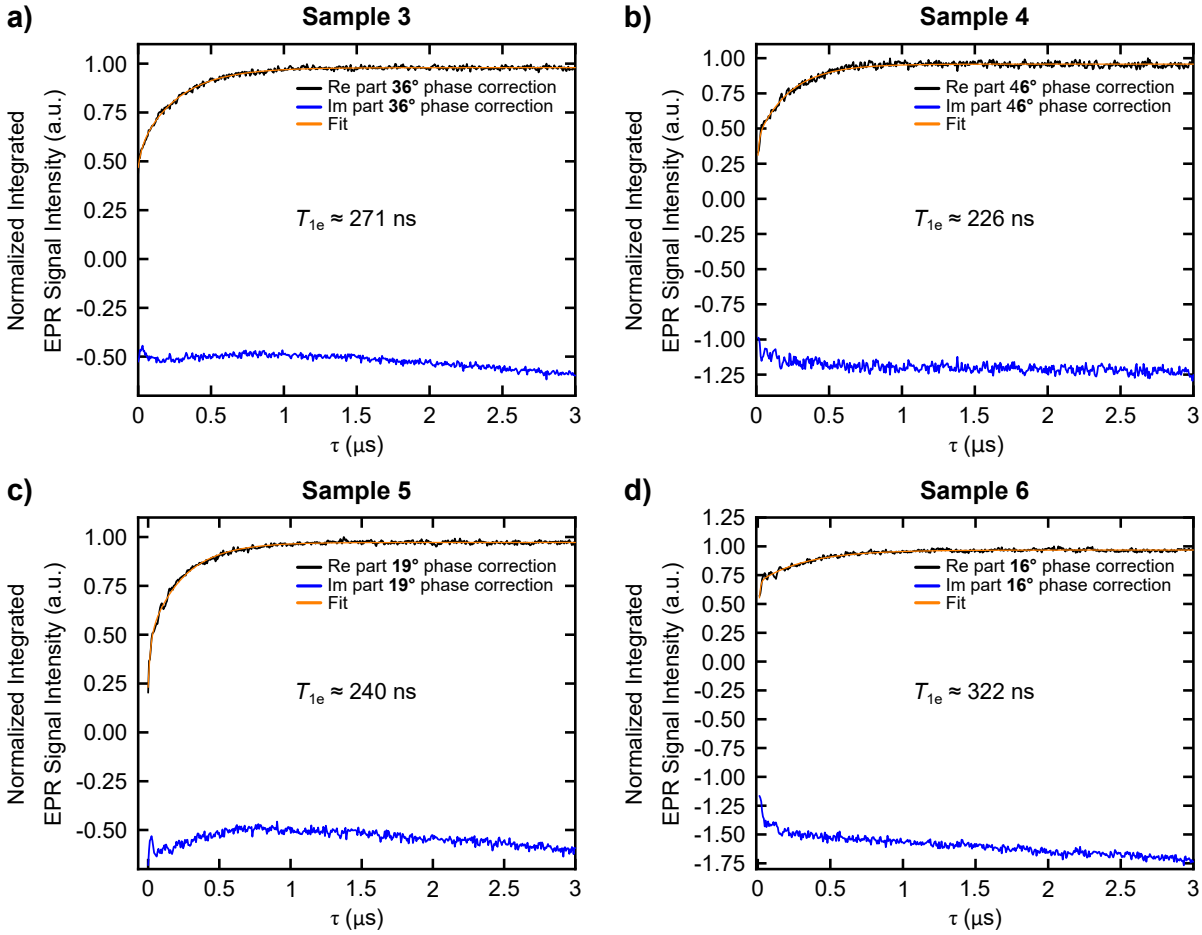

Figure A.1: Real and imaginary part of the inversion recovery experiments of the samples 3 – 6 of tab. 6.2. Table A.1 lists the experimental parameters used for data acquisition. Experimental data was fitted to $y = A \exp(-\tau/T_{1e}) + B \exp(-\tau/T_2) + y_0$.

Table A.1: Experimental parameters of inversion recovery experiments on different samples in CCl_4 (fig. 6.3, fig. 6.4, and fig. A.1). Radical concentration for sample 4 was 5 mM, while for the other samples 10 mM of ^{15}N-TN-d_{16} was used. Experimental data was fitted to $y = A\exp(-\tau/T_{1e}) + B\exp(-\tau/T_b) + y_0$. $P = 0$ dB refers to a power of $P \approx 50$ mW. Phase adjustment was applied during post processing of the experimental data. The dead time refers to the time between the detection pulse and start of the signal detection. N.a. means not available. Measurements were acquired with 512 points per scan.

sample	1	2	3	4	5	6
T_{1e} (ns)	300	378	271	226	240	321
T_b (ns)	13	0	25	10	17	9
t exposed to air (min)	52	75	25	27	30	16
ν (GHz)	264.139	264.242	263.468	263.702	263.766	263.713
B_0 (mT)	9417	9431	9394	9403	9406	9403
P (dB)	0	0	0	0	0	10
VG (dB)	21	27	21	21	21	21
VB (MHz)	200	200	200	200	200	200
t_p (ns)	80	100	80	60	80	80
τ increment (ns)	6	4	6	6	6	6
dead time (ns)	130	146	130	130	n.a.	130
NS	5	4	5	5	5	5
SPP	50	50	50	50	50	50
SRT (ms)	8	15.3	8	8	8	8
phase adjustment (°)	−16	20	37	46	19	16

B Continuous Wave EPR Measurements at 263 GHz of Different Radicals

Table B.2: Samples used for the determination of g_{iso} and A_{iso} of different PAs in different solvents (see fig. 7.1 and tab. 7.1). As N@C_{60} was insoluble in any of the solvents, spurious amounts were dispersed in the solvent directly inside the sample tube. BDPA-d_{27} was dispersed in a polystyrene matrix, which was dissolved together with the radical in toluene for the cw experiments.

sample	1	2	3	4	5
PA1	^{15}N-TN-d_{16}	galvinoxyl	^{15}N-TN-d_{16}	^{15}N-TN-d_{16}	^{15}N-TN-d_{16}
c(PA1) (mM)	$\sim 25-50$	~ 10	~ 2	~ 2	~ 10
PA2	BDPA-d_{27}	BDPA-d_{27}	N@C_{60}	N@C_{60}	N@C_{60}
c(PA2) (mM)	$\sim 5-10$	~ 10	–	–	–
solvent	toluene	toluene	CCl_4	$CHCl_3$	H_2O

Table B.3: Experimental parameters for cw EPR at 263 GHz of different PAs in different solvents (tab. B.3) to obtain g_{iso} and A_{iso} (see fig. 7.1 and tab. 7.1). Note, due to hardware problems, the absolute values of the magnetic field in fig. 7.1 were calculated with the g standards and the mw frequency.

sample	1	2	3	4	5
MF (kHz)	100	100	100	100	100
MA (mT)	0.05	0.05	0.01	0.01	0.02
RG (dB)	39	39	39	39	39
P (mW)	0.5	0.5	0.2	0.3	0.2
NS	1	10	1	1	5
points	3072	1250	3500	3500	2700
SW (mT)	45	25	35	35	27
ν (GHz)	262.901	263.185	263.185	263.185	263.185

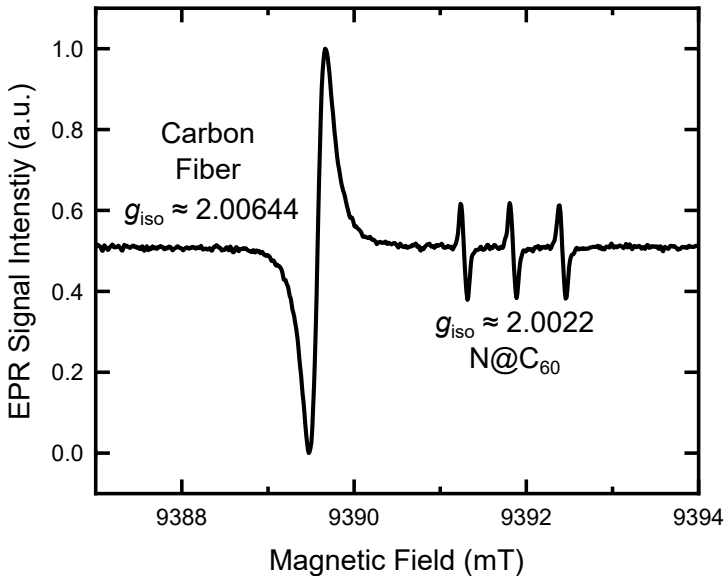

Figure B.1: Calibration of g_{iso} of $N@C_{60}$ at 263 GHz using a carbon fiber according to the protocol from ref. [105]. The g_{iso} value of the carbon fiber $g_{iso} \approx 2.0644$ was reported in the literature and $N@C_{60}$ was adjusted accordingly. Experimental parameters: MF = 100 kHz, MA = 0.1 G, RG = 39 dB, P = 20 dB ($\approx$ 0.5 mW), NS = 1, 1000 points, SW = 100 G, $\nu \approx 263.185$ GHz.

C ^{13}C NMR Signal Enhancements at 9.4 T

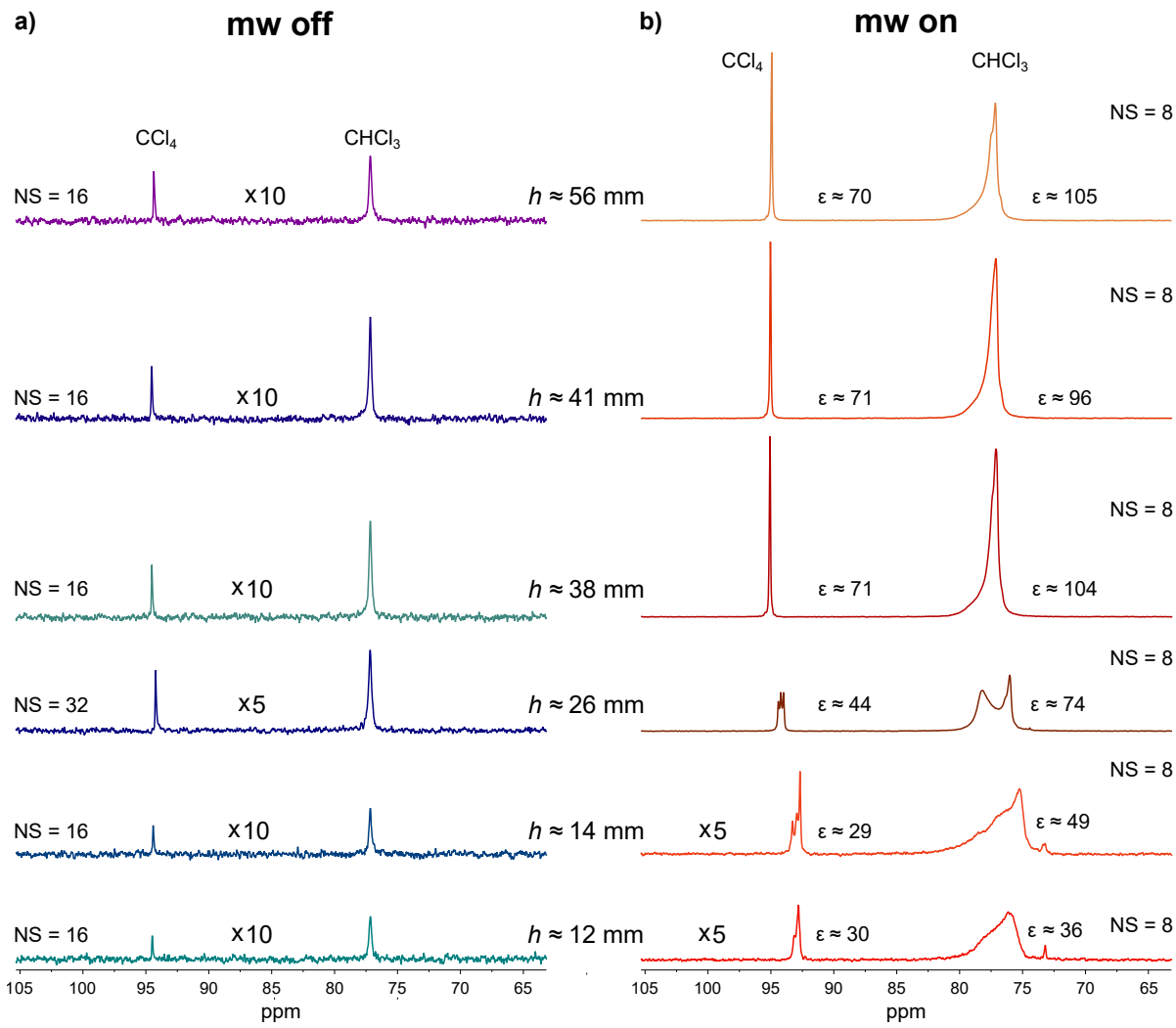

Figure C.1: a) Boltzmann spectra and b) DNP spectra of ∼ 500 mM $^{13}CHCl_3$ in CCl_4 doped with ∼ 25 mM ^{15}N-TN-d_{16} with different sample heights h using a layer thickness of $d \approx 75\,\mu m$. Microwave power (cw irradiation): $P = 43$ W (P5). NMR parameters (zgig): $t_p\,(\pi/2) = 10\,\mu s$, $P\,(\pi/2) = 41$ W, DS = 2, relaxation delay (RD) = 30 s, line broadening (LB) = 2 Hz, ^{1}H decoupling: waltz64, 0.58 W. Boltzmann and DNP spectra were acquired with the same pulse sequence.

Table C.4: NMR parameters for ^{13}C 1D DNP NMR measurements presented in chapter 7. $P(\mathrm{rf}_{13\mathrm{C}}) = 41\,\mathrm{W}$ and $t_\mathrm{p}(^{13}\mathrm{C}) = 10\,\mu\mathrm{s}$ was used in all experiments except for the Boltzmann spectra of fig. C.4b and fig. C.13a, which were measured with $P(\mathrm{rf}_{13\mathrm{C}}) = 48\,\mathrm{W}$. The sequences zgpg and zgig used ^{1}H decoupling (waltz) with a power of $P(\mathrm{rf}_{1\mathrm{H}}) = 0.58\,\mathrm{W}$ and $P(\mathrm{rf}_{1\mathrm{H}}) = 0.3\,\mathrm{W}$ for ^{1}H pre-saturation. All measurements were performed with DS = 2 except $^{13}C_1$-C_2-indole in CCl_4 (DS = 4, fig. C.2b) and neat CCl_4 (DS = 0, fig. C.10b). Boltzmann and DNP spectra were acquired with the same pulse sequence.

spectrum	target	c (mM)	pulse seq.	NS (DNP/Boltz.)	LB (Hz)
fig. C.2a	$^{13}C_6$-C_6H_5Cl	200	zg	4/64	2
fig. C.2b	$^{13}C_1$-C_2-indole	2000	zg	4/8	2
fig. C.3a	$^{13}C_6$-C_6H_5Br	200	zg	4/64	2
fig. C.3b	$^{13}C_6$-C_6H_5Br	200	zgpg	4/8	2
fig. C.4a	$^{13}C_6$-C_6H_5I	500	zg	8/32	0
fig. C.4b	$^{13}C_6$-C_6H_5I	500	zgpg	4/8	0.3
fig. C.5a	$^{13}C_6$-GlcOMe	200	zg	16/32	2
fig. C.5b	C_6H_5Br	500	zg	128/2048	2
fig. C.6a	$C_6H_5NO_2$	500	zgig	64/512	0.3
fig. C.6b	$C_6H_5COCH_3$	500	zg	128/1024	2
fig. C.7a	*p*-Cl-toluene	500	zg	128/1024	2
fig. C.7b	Toluene	500	zg	128/1024	2
fig. C.8a	Benzene	200	zg	16/128	2
fig. C.8b	Anisole	200	zg	128/1024	2
fig. C.9a	1,4-$Cl_2C_6H_{10}$	500	zg	256/1024	5
fig. C.9b	Diethylmalonate	500	zgpg	256/768	4
fig. C.10a	$^{13}CBr_4$	200	zg	1/16	2
fig. C.10b	CCl_4	neat	zg	1/8	2
fig. C.10c	$CHCl_3$	neat	zg	4/16	2
fig. C.11a	$^{13}CHCl_3$	200	zg	1/16	2
fig. C.11b	$^{13}CH_2Cl_2$	200	zgig	4/16	0.3
fig. C.12a	DDT	500	zg	128/1024	2
fig. C.12b	*p*-I-C_6H_4-$COOCH_3$	500	zg	256/1024	2
fig. C.13a	Na diatrizoate	≥ 500	zgig	768/3328	4
fig. C.13b	*p*-I-C_6H_4F	1500	zgpg	64/128	4
fig. C.14a	$^{13}C_6$-C_6H_5Br	200	zg	4/64	2
fig. C.14b	$^{13}C_6$-C_6H_5Br	200	zg	4/32	2
fig. C.15	$^{13}C_6$-C_6H_5Br	200	zg	4/32	2
fig. C.16a	$^{13}C_6$-C_6H_5I	500	zgig	4/64	12.67
fig. C.16b	$^{13}C_6$-C_6H_5I	500	zgig	8/32	0.3
fig. C.17	$^{13}CH_3CN$	400	zg	8/64	2
fig. C.18	Indole	500	zgig	256/1024	2

Table C.5: The DNP enhancement of Na diatrizoate (fig. C.13a), $^{13}CHCl_3$ (fig. C.11a), and $^{13}CH_3CN$ (fig. C.17) were obtained with a mw irradiation of 4 s, 6 s, and 4 s, respectively. Sample temperature was calibrated to be $T_{sample} \approx 290 - 310$ K. V_{sample} was $\sim 40\,\mu$L for measurements in CCl_4, C_6H_6, and C_6H_{12}, $\sim 20\,\mu$L for $CHCl_3$, and $\sim 15\,\mu$L for H_2O and CH_2Cl_2.

spectrum	target	c (mM)	solvent	c(PA) (mM)	P(mw) (W)	RD (s)
fig. C.2a	$^{13}C_6$-C_6H_5Cl	200	CCl_4	10	50 (P7)	40
fig. C.2b	$^{13}C_1$-C_2-indole	2000	CCl_4	100	50 (P7)	30
fig. C.3a	$^{13}C_6$-C_6H_5Br	200	CCl_4	25	50 (P7)	60
fig. C.3b	$^{13}C_6$-C_6H_5Br	200	CCl_4	25	50 (P7)	60
fig. C.4a	$^{13}C_6$-C_6H_5I	500	CCl_4	25	43 (P5)	30
fig. C.4b	$^{13}C_6$-C_6H_5I	500	CCl_4	25	43 (P5)	30
fig. C.5a	$^{13}C_6$-GlcOMe	200	CCl_4	10	50 (P7)	60
fig. C.5b	C_6H_5Br	500	CCl_4	25	50 (P7)	30
fig. C.6a	$C_6H_5NO_2$	500	CCl_4	25	43 (P5)	30
fig. C.6b	$C_6H_5COCH_3$	500	CCl_4	25	50 (P7)	30
fig. C.7a	*p*-Cl-toluene	500	CCl_4	25	50 (P7)	30
fig. C.7b	Toluene	500	CCl_4	25	50 (P7)	30
fig. C.8a	Benzene	200	CCl_4	10	43 (P5)	20
fig. C.8b	Anisole	500	CCl_4	25	50 (P7)	30
fig. C.9a	1,4-$Cl_2C_6H_{10}$	500	CCl_4	25	43 (P5)	30
fig. C.9b	Diethylmalonate	500	CCl_4	25	43 (P5)	30
fig. C.10a	$^{13}CBr_4$	200	CCl_4	10	50 (P7)	100
fig. C.10b	CCl_4	pure	CCl_4	10	43 (P5)	100
fig. C.10c	$CHCl_3$	pure	$CHCl_3$	25	29 (P2)	60
fig. C.11a	$^{13}CHCl_3$	200	CH_2Cl_2	10	22 (P1)	40
fig. C.11b	$^{13}CH_2Cl_2$	200	CCl_4	10	51 – 53 (P9)	30
fig. C.12a	DDT	500	CCl_4	25	50 (P7)	30
fig. C.12b	*p*-I-C_6H_4-$COOCH_3$	500	$CHCl_3$	25	29 (P2)	30
fig. C.13a	Na diatrizoate	≥ 500	H_2O	25	22 (P1)	30
fig. C.13b	*p*-I-C_6H_4F	1500	C_6H_{12}	25	43 (P5)	30
fig. C.14a	$^{13}C_6$-C_6H_5Br	200	$^{13}CCl_4$	10	50 (P7)	60
fig. C.14b	$^{13}C_6$-C_6H_5Br	200	C_6H_6	10	50 (P7)	60
fig. C.15	$^{13}C_6$-C_6H_5Br	200	C_6H_6	25	50 (P7)	60
fig. C.16a	$^{13}C_6$-C_6H_5I	500	C_6H_{12}	25	43 (P5)	30
fig. C.16b	$^{13}C_6$-C_6H_5I	500	$CHCl_3$	25	43 (P5)	30
fig. C.17	$^{13}CH_3CN$	400	CH_2Cl_2	25	22 (P1)	30
fig. C.18	Indole	500	CCl_4	25	43 (P5)	20

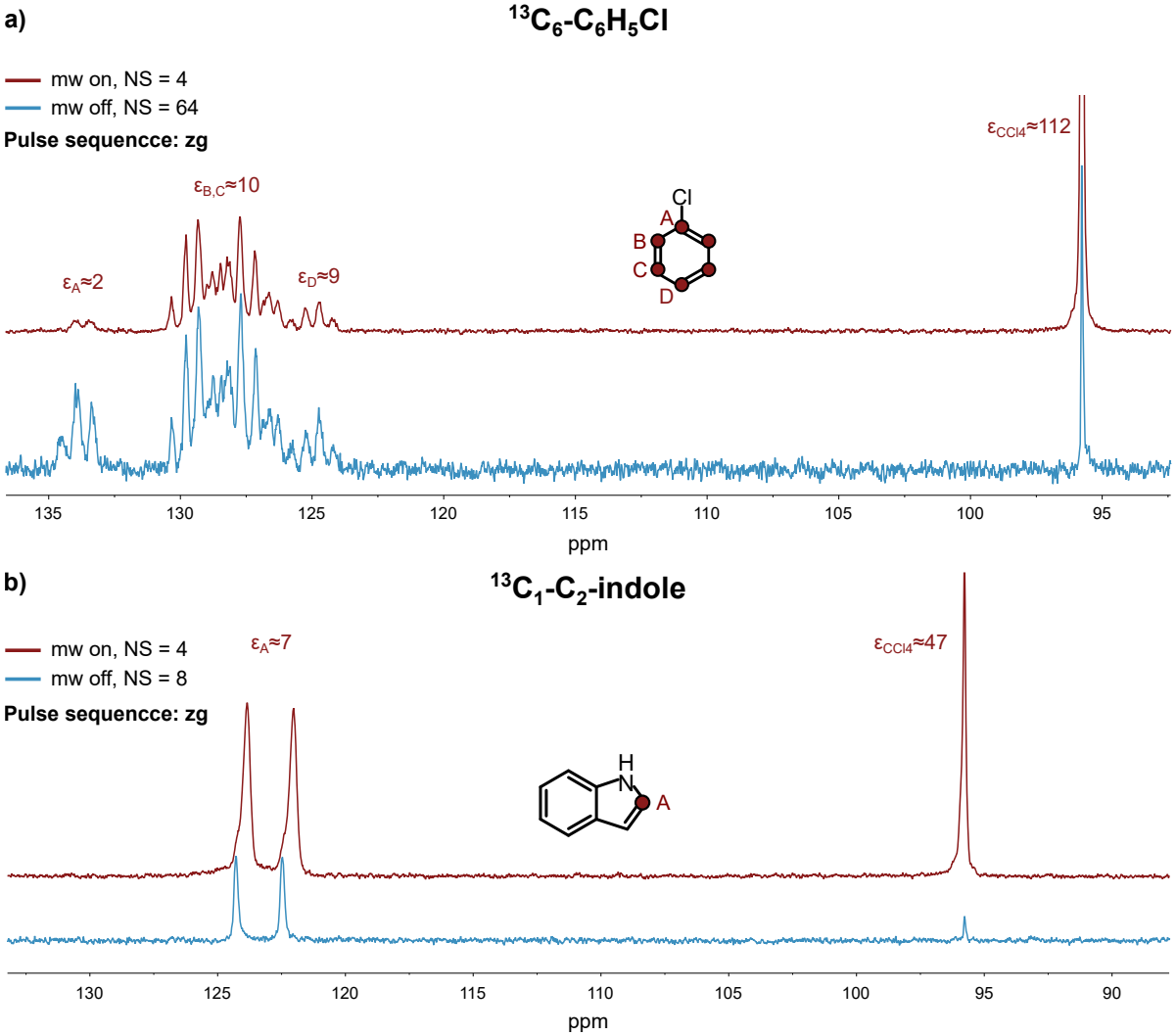

Figure C.2: ^{13}C NMR spectra of a) $^{13}C_6$-C_6H_5Cl and b) $^{13}C_1$-C_2-indole with (red) and without (blue) mw irradiation. Experimental parameters are listed in tab. C.5 and tab. C.4. The solvent signals in a) was cut for clarity. Boltzmann and DNP spectra were acquired with the same pulse sequence.

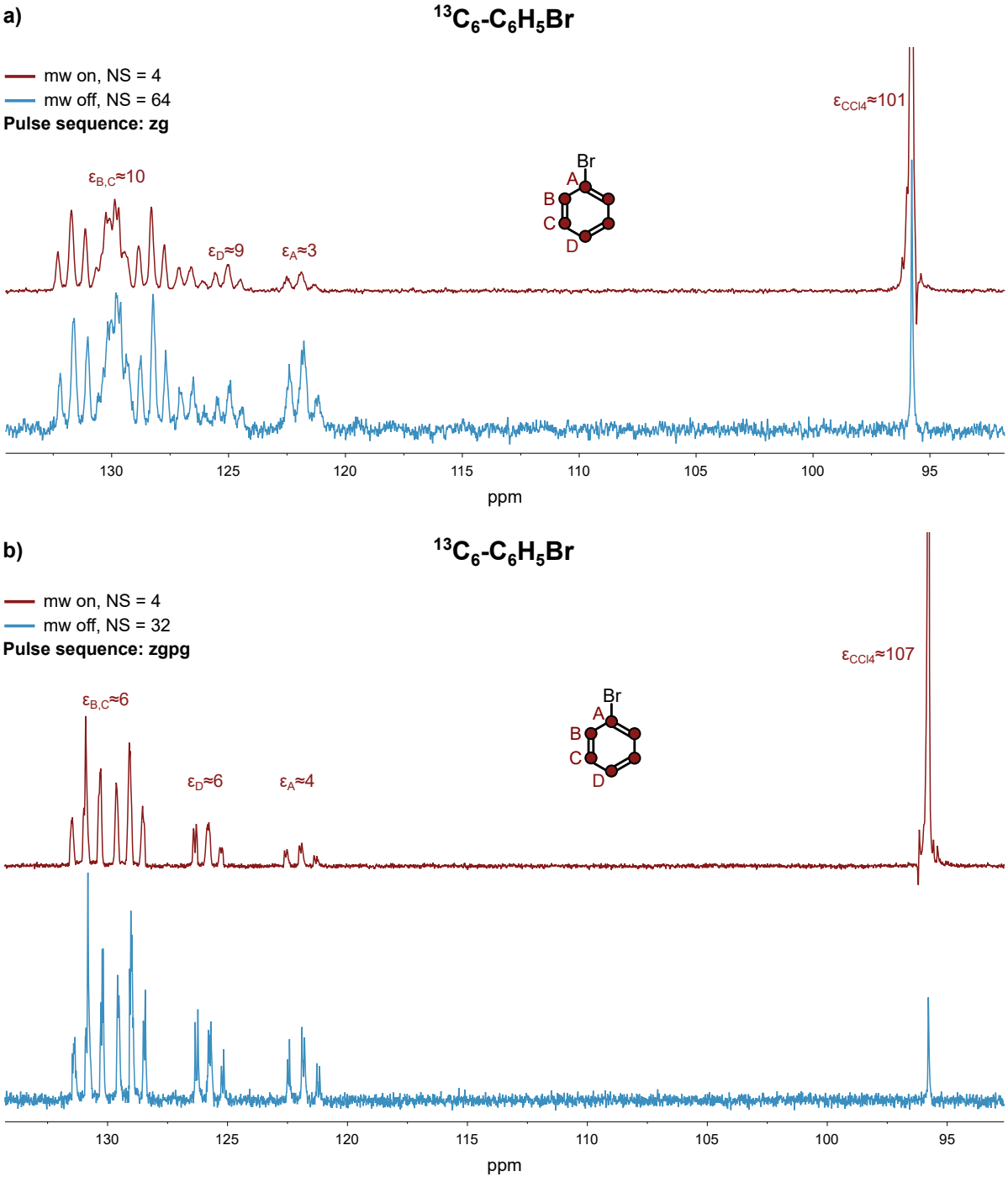

Figure C.3: ^{13}C NMR spectra of a) $^{13}C_6$-C_6H_5Br (no ^1H pre-saturation) and b) $^{13}C_6$-C_6H_5Br (^1H pre-saturation) with (red) and without (blue) mw irradiation. Experimental parameters are listed in tab. C.5 and tab. C.4. The solvent signals were cut for clarity. Boltzmann and DNP spectra were acquired with the same pulse sequence.

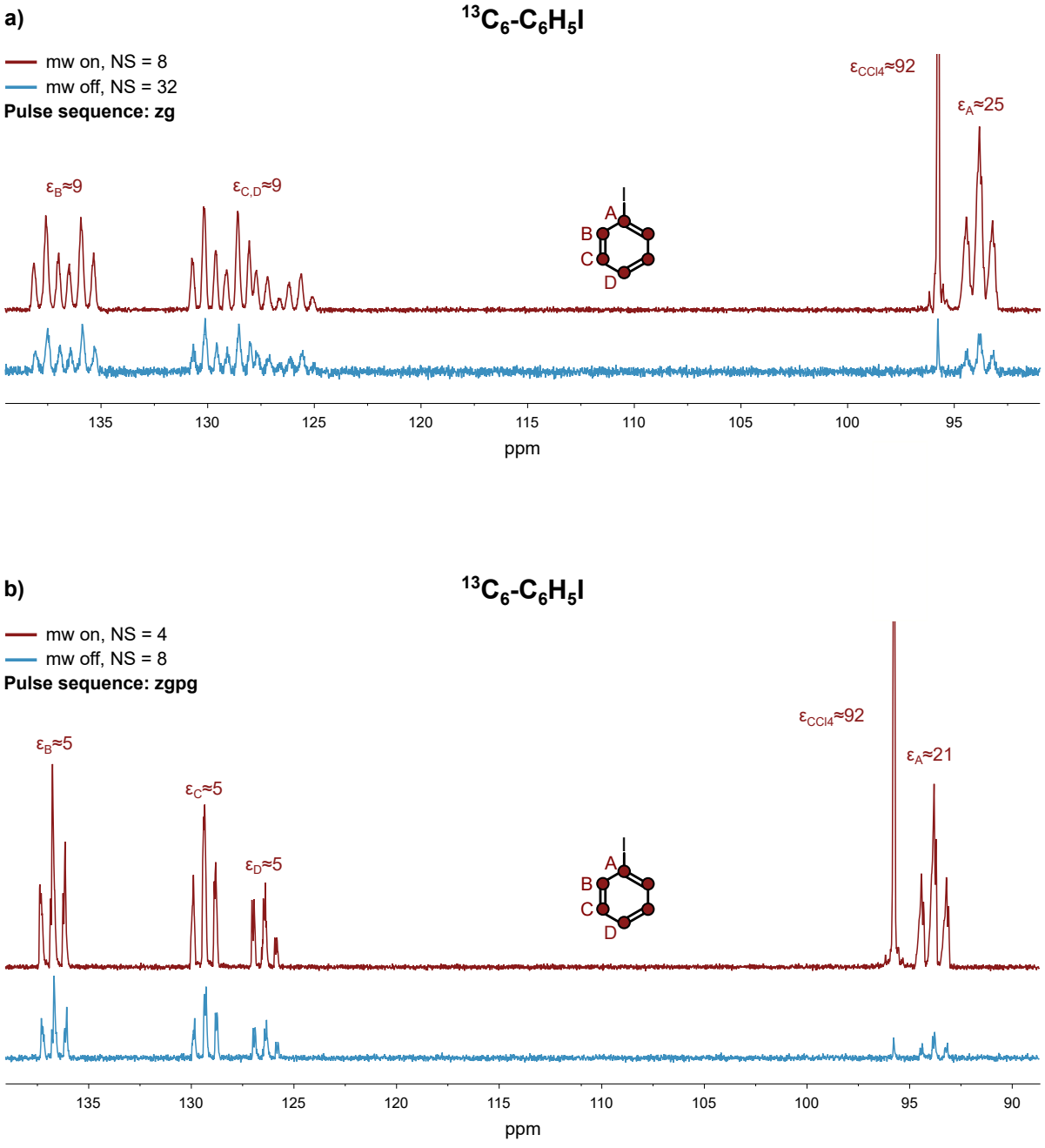

Figure C.4: ^{13}C NMR spectra of a) $^{13}C_6$-C_6H_5I (no ^{1}H pre-saturation) and b) $^{13}C_6$-C_6H_5I (^{1}H pre-saturation) with (red) and without (blue) mw irradiation. Experimental parameters are listed in tab. C.5 and tab. C.4.The solvent signals were cut for clarity. Boltzmann and DNP spectra were acquired with the same pulse sequence.

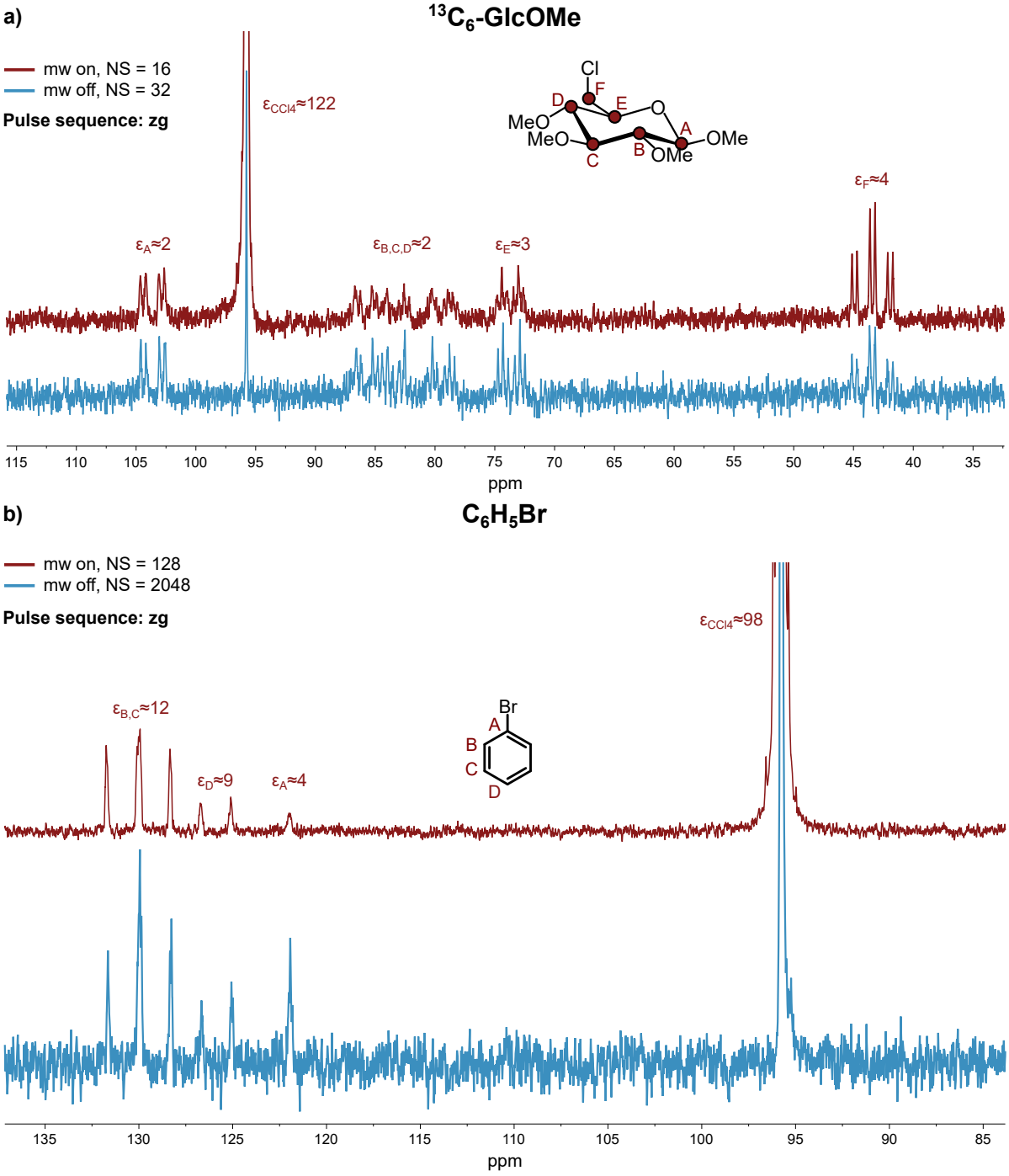

Figure C.5: ^{13}C NMR spectra of a) $^{13}C_6$-GlcOMe and b) C_6H_5Br with (red) and without (blue) mw irradiation. Experimental parameters are listed in tab. C.5 and tab. C.4. The solvent signals were cut for clarity. Boltzmann and DNP spectra were acquired with the same pulse sequence.

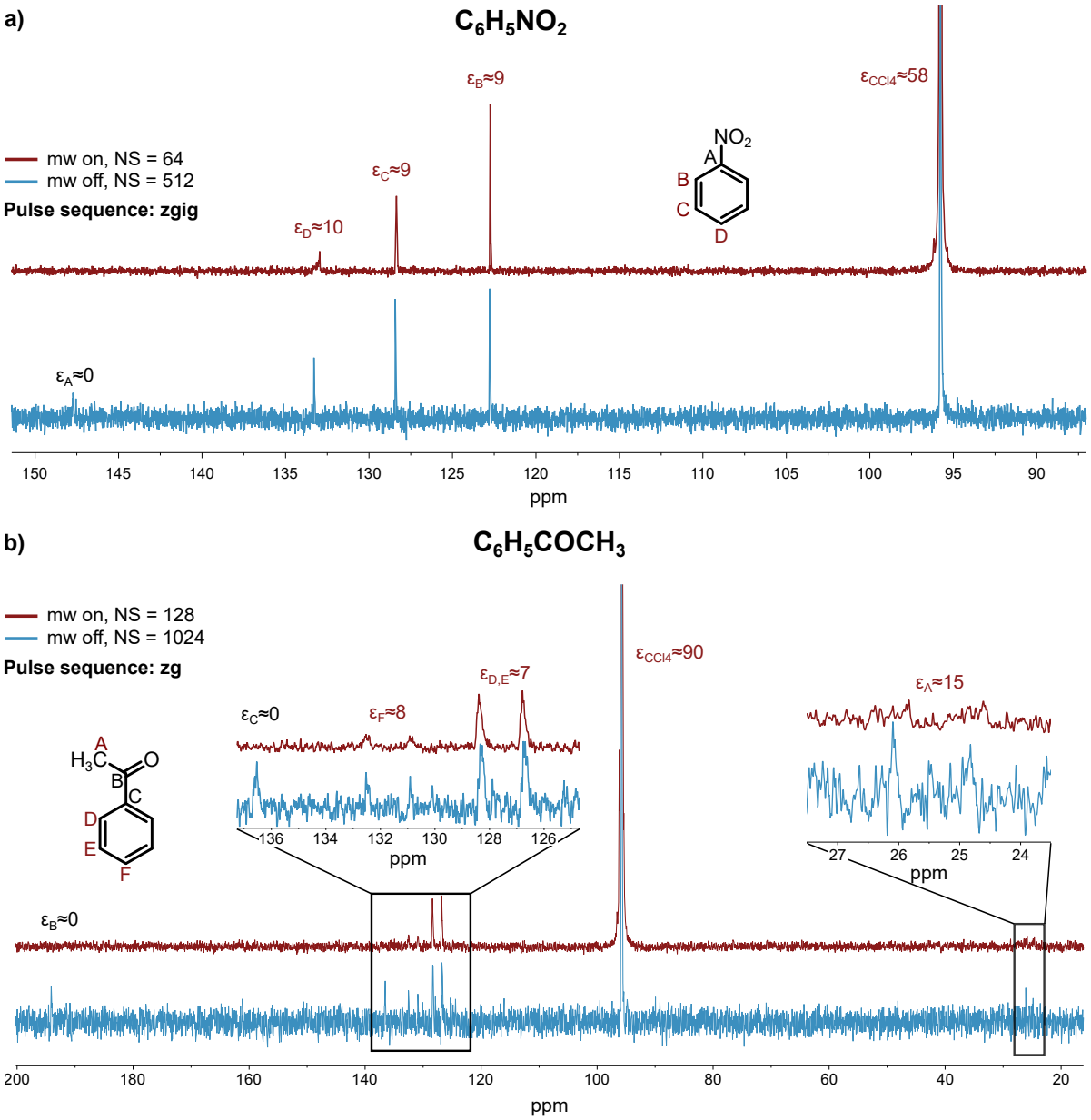

Figure C.6: ^{13}C NMR spectra of a) $C_6H_5NO_2$ and b) $C_6H_5COOCH_3$ with (red) and without (blue) mw irradiation. Experimental parameters are listed in tab. C.5 and tab. C.4. The solvent signals were cut for clarity. Boltzmann and DNP spectra were acquired with the same pulse sequence.

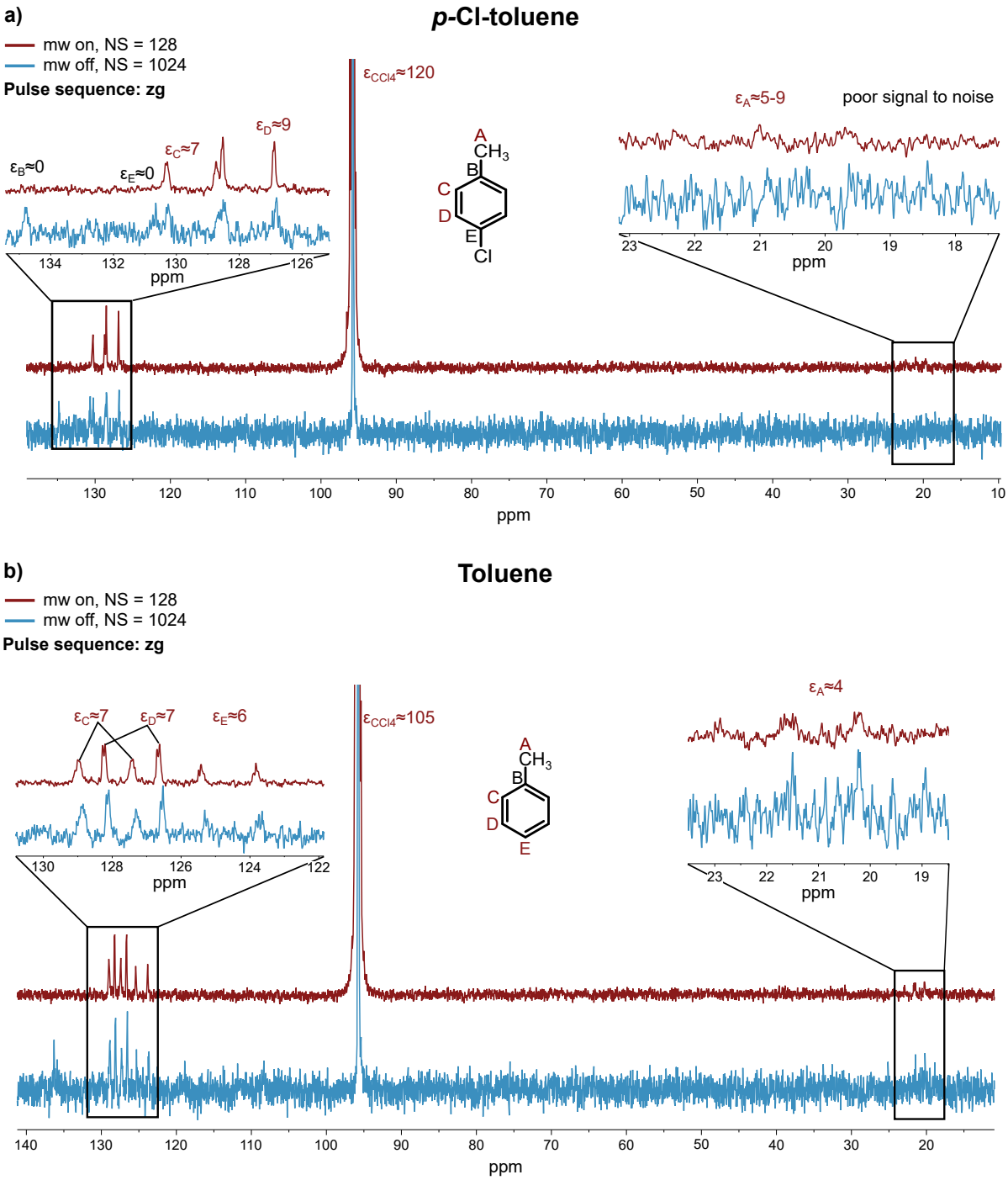

Figure C.7: ^{13}C NMR spectra of a) *p*-Cl-toluene and b) toluene with (red) and without (blue) mw irradiation. Experimental parameters are listed in tab. C.5 and tab. C.4. The solvent signals were cut for clarity. Boltzmann and DNP spectra were acquired with the same pulse sequence.

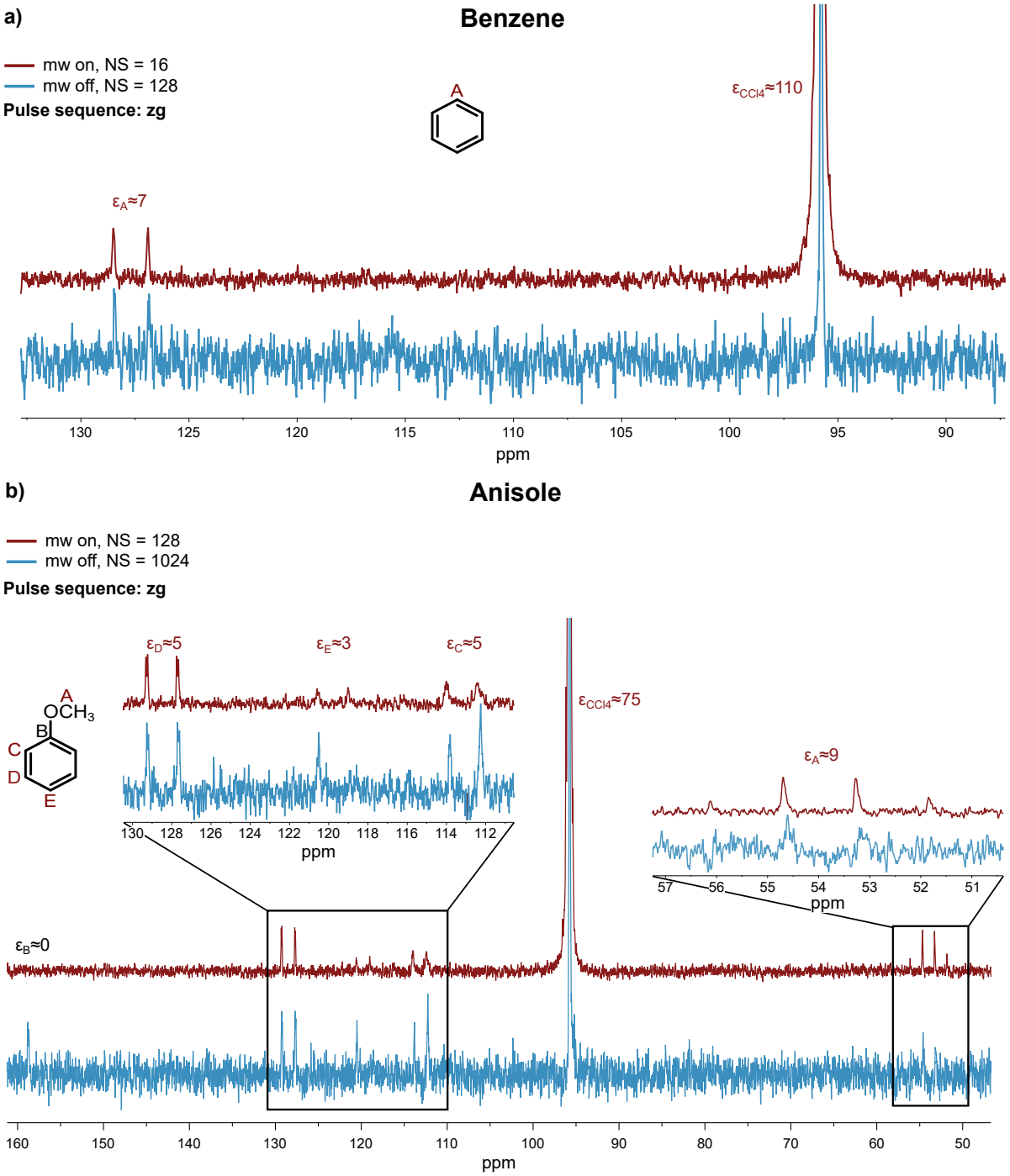

Figure C.8: ^{13}C NMR spectra of a) benzene and b) anisole with (red) and without (blue) mw irradiation. Experimental parameters are listed in tab. C.5 and tab. C.4. The solvent signals were cut for clarity. Boltzmann and DNP spectra were acquired with the same pulse sequence.

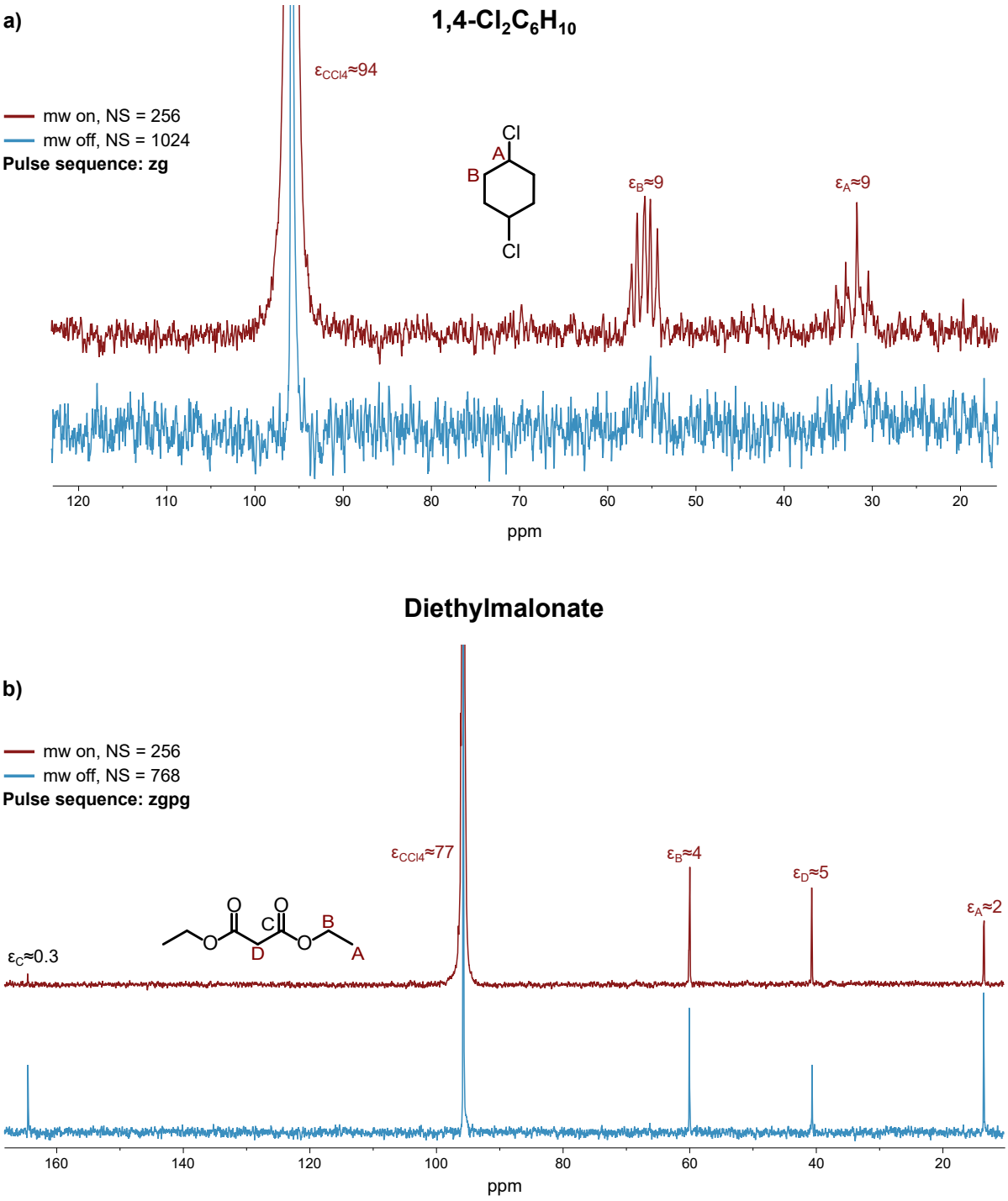

Figure C.9: ^{13}C NMR spectra of a) 1,4-$Cl_2C_6H_{10}$ and b) diethylmalonate with (red) and without (blue) mw irradiation. Experimental parameters are listed in tab. C.5 and tab. C.4. The solvent signals were cut for clarity. Boltzmann and DNP spectra were acquired with the same pulse sequence.

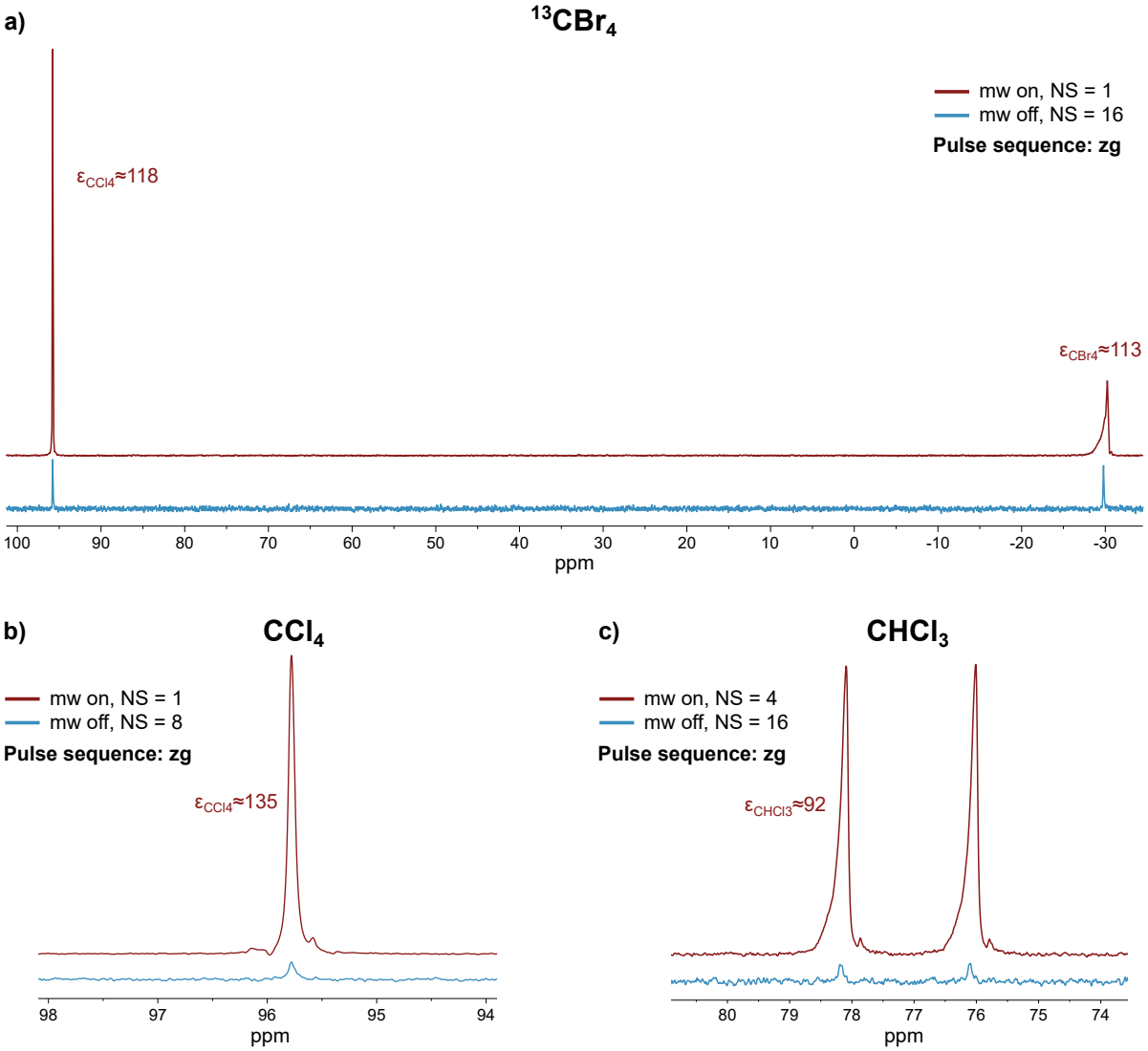

Figure C.10: ^{13}C NMR spectra of a) $^{13}CBr_4$, b) neat CCl_4, and c) neat $CHCl_3$ with (red) and without (blue) mw irradiation. Experimental parameters are listed in tab. C.5 and tab. C.4. Boltzmann and DNP spectra were acquired with the same pulse sequence.

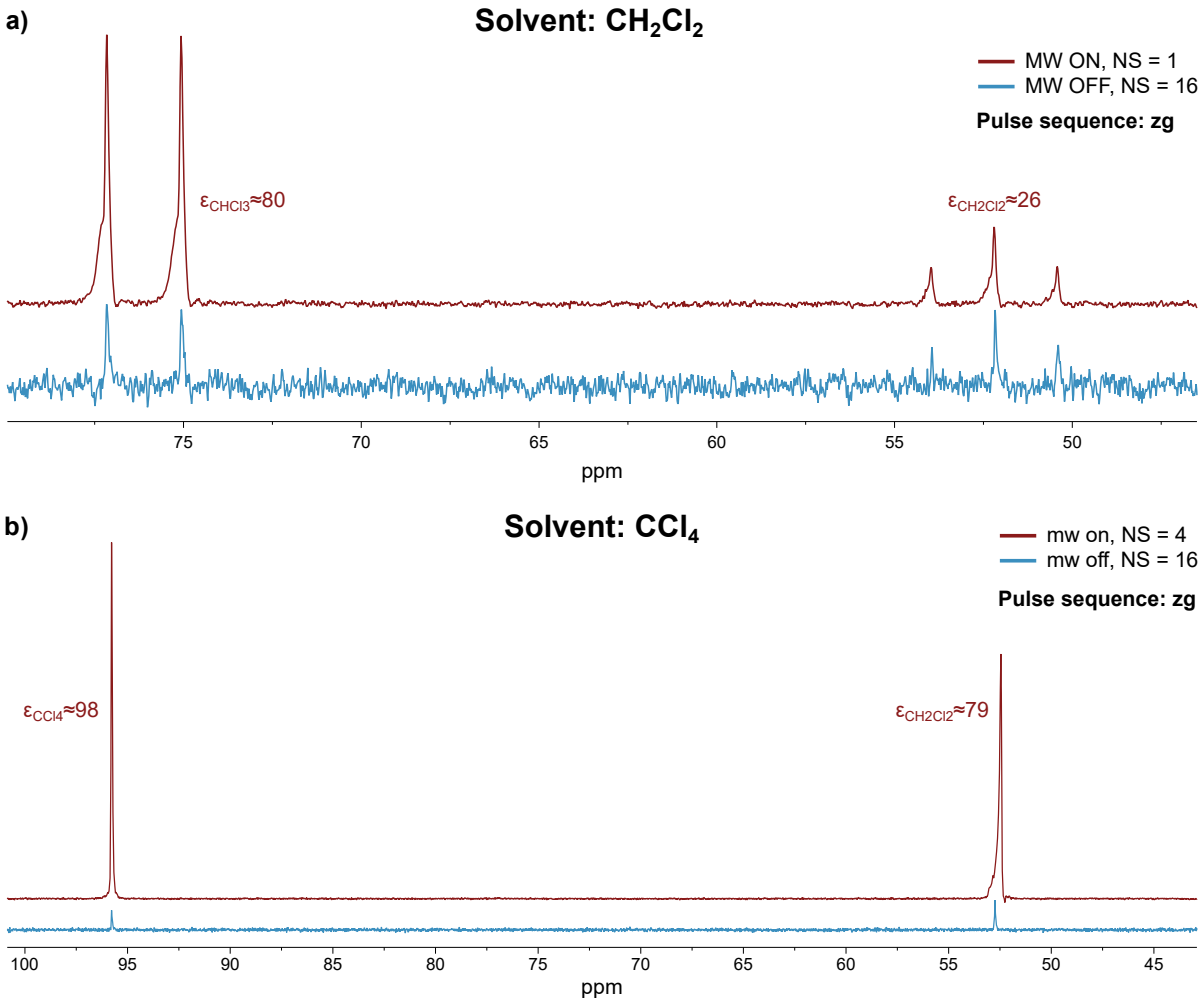

Figure C.11: ^{13}C NMR spectra of a) $CHCl_3$ (and CH_2Cl_2) in CH_2Cl_2 and b) CH_2Cl_2 in CCl_4 with (red) and without (blue) mw irradiation. Experimental parameters are listed in tab. C.5 and tab. C.4. Boltzmann and DNP spectra were acquired with the same pulse sequence.

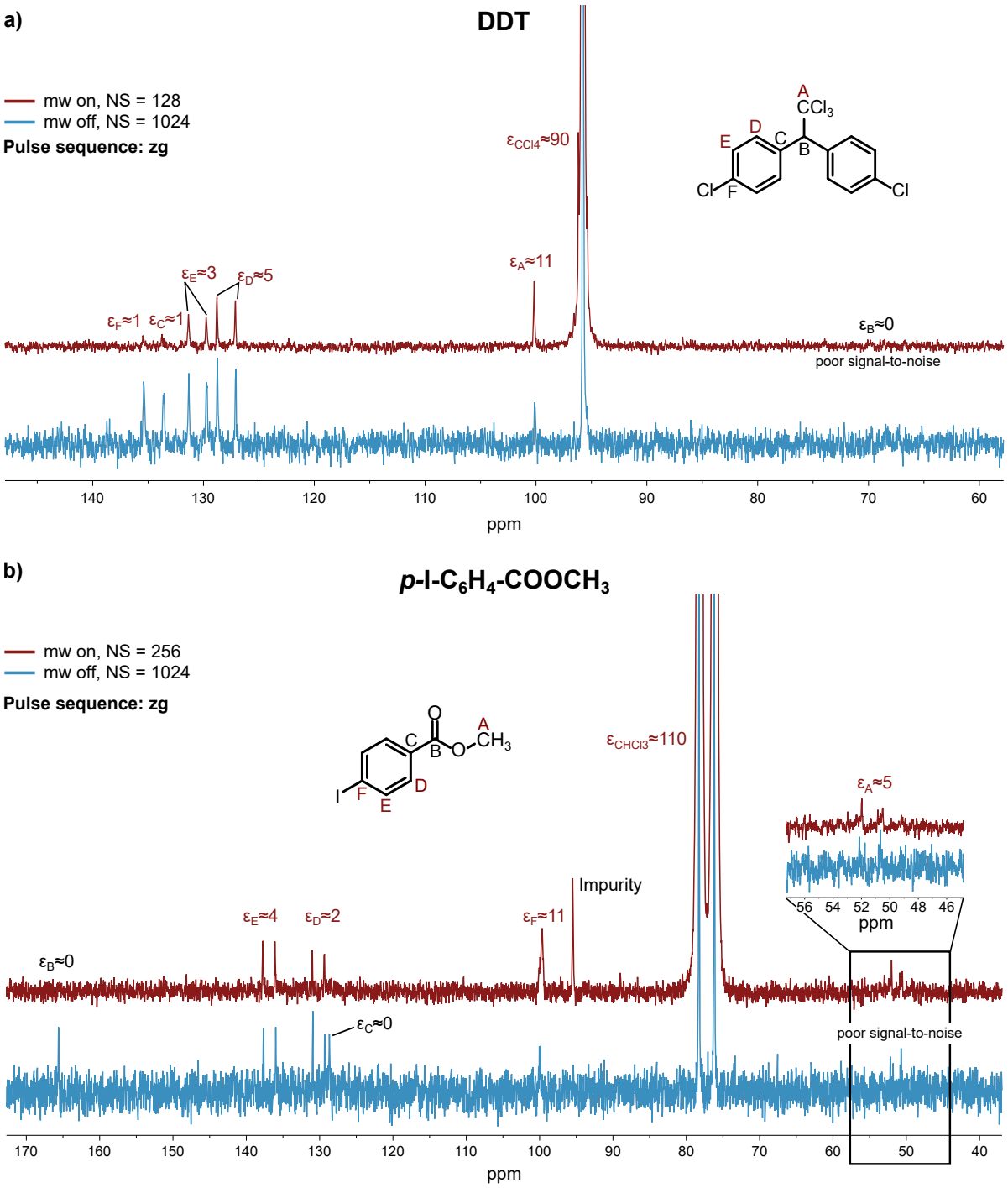

Figure C.12: ^{13}C NMR spectra of a) DDT and b) *P*-I-C_6H_4-$COOCH_3$ with (red) and without (blue) mw irradiation. Experimental parameters are listed in tab. C.5 and tab. C.4. The solvent signals were cut for clarity. Boltzmann and DNP spectra were acquired with the same pulse sequence.

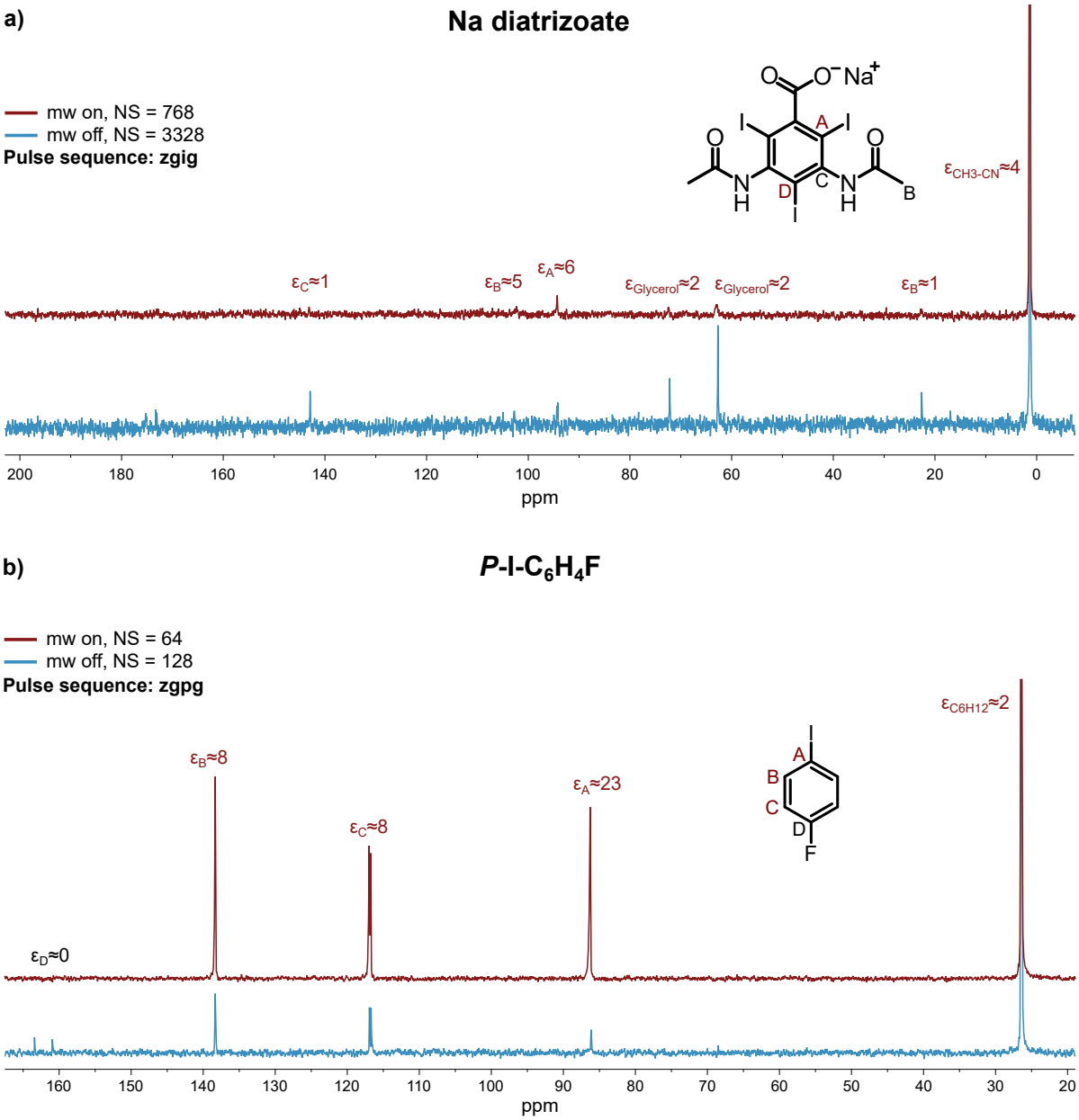

Figure C.13: ^{13}C NMR spectra of a) Na diatrizoate and b) *p*-I-C_6H_4F with (red) and without (blue) mw irradiation. Experimental parameters are listed in tab. C.5 and tab. C.4. Na diatrizoate was measured in a mixture of 9/1 water/glycerol (w/w) and 500 mM $^{13}CH_3CN$. The reported signal enhancement for *P*-I-C_6H_4F was measured on the same sample that was used for the 2D DNP INADEQUATE presented in sec. 7.4.3. 500 mM $^{13}CH_3CN$ were added to a) for signal referencing. The $^{13}CH_3CN$ in a) was cut for clarity as well as the solvent signal in b). Boltzmann and DNP spectra were acquired with the same pulse sequence.

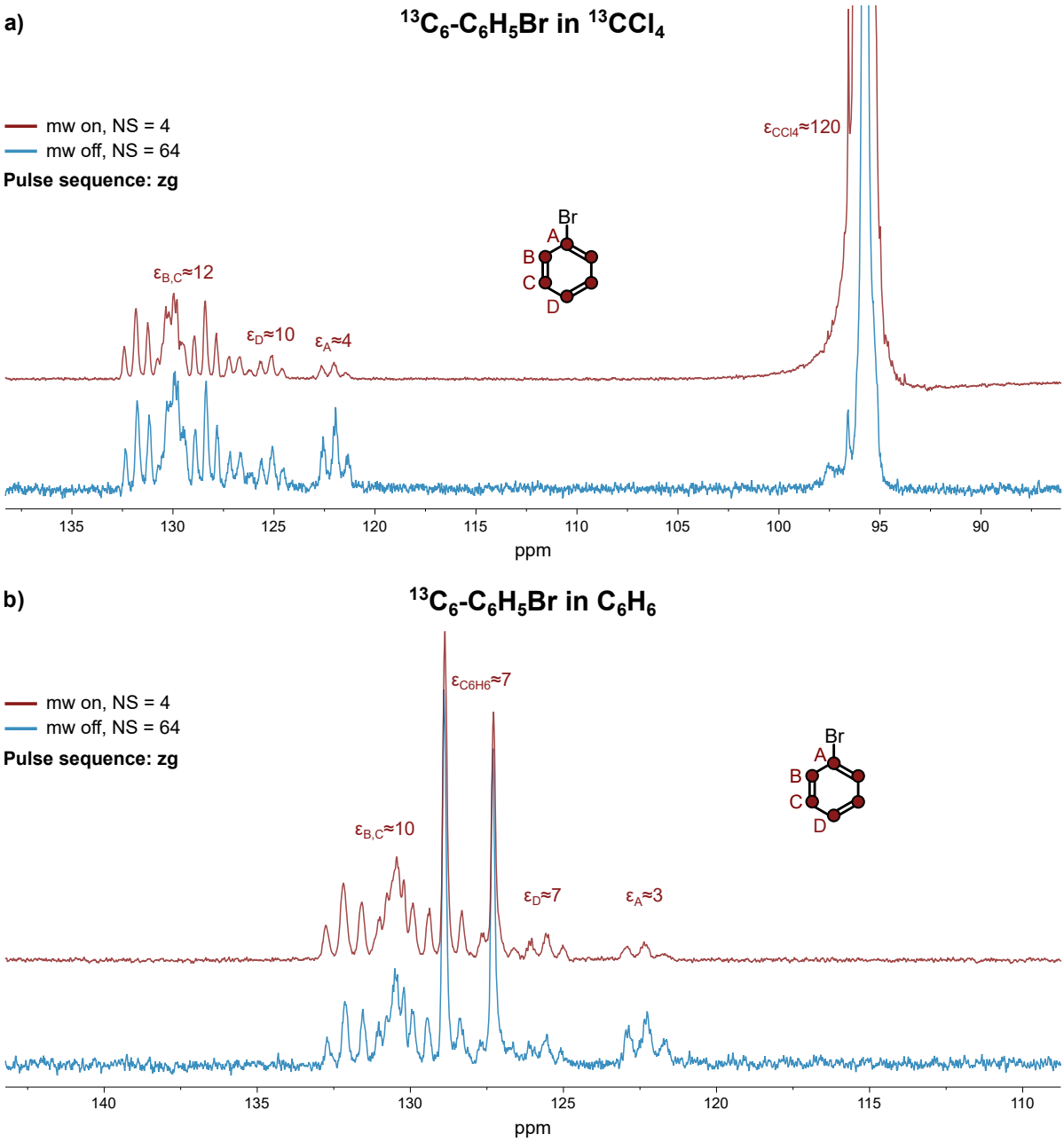

Figure C.14: ^{13}C NMR spectra of a) $^{13}C_6$-C_6H_5Br in $^{13}CCl_4$ and b) $^{13}C_6$-C_6H_5Br in C_6H_6 with (red) and without (blue) mw irradiation. Experimental parameters are listed in tab. C.5 and tab. C.4. The solvent signal in a) was cut for clarity. Boltzmann and DNP spectra were acquired with the same pulse sequence.

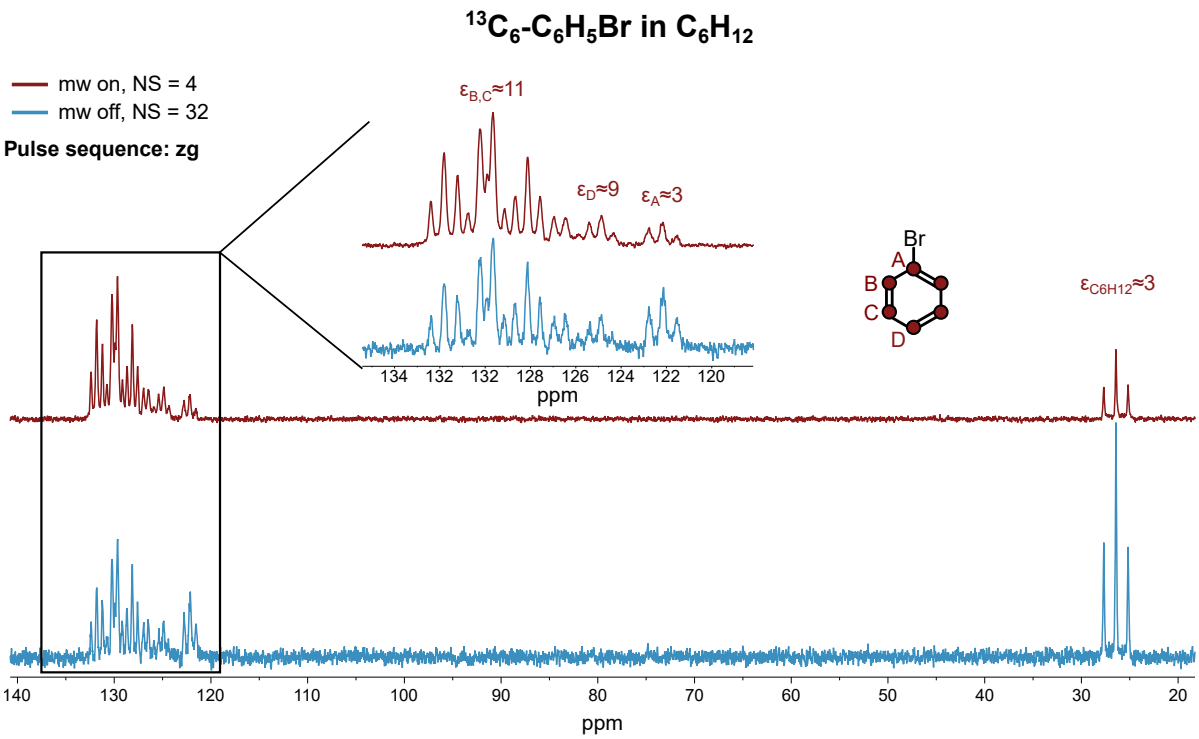

Figure C.15: ^{13}C NMR spectra of $^{13}C_6$-C_6H_5Br in C_6H_{12} with (red) and without (blue) mw irradiation. Experimental parameters are listed in tab. C.5 and tab. C.4. Boltzmann and DNP spectra were acquired with the same pulse sequence.

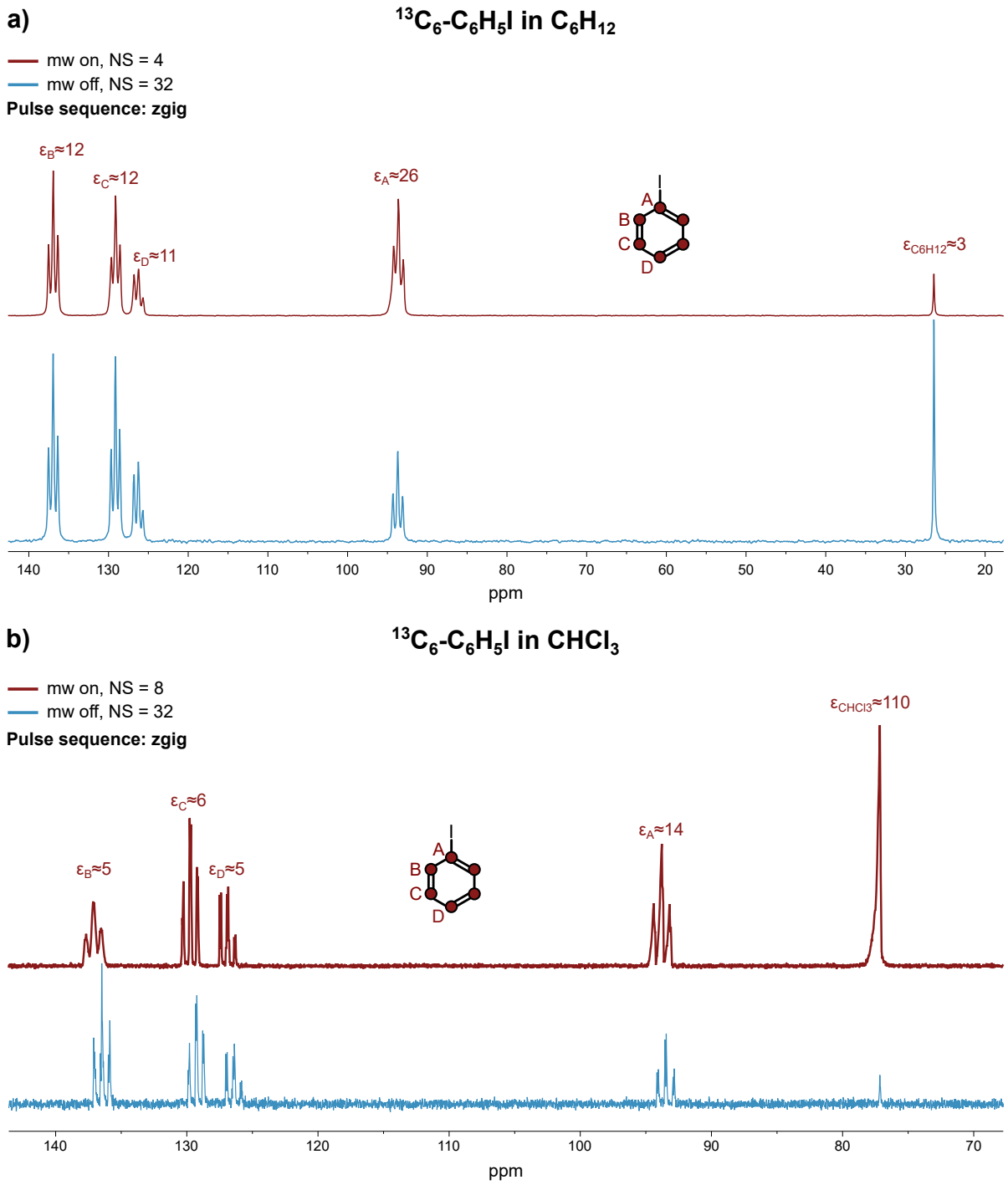

Figure C.16: ^{13}C NMR spectra of a) $^{13}C_6$-C_6H_5I in C_6H_{12} and b) $^{13}C_6$-C_6H_5I in $CHCl_3$ with (red) and without (blue) mw irradiation. Experimental parameters are listed in tab. C.5 and tab. C.4. Boltzmann and DNP spectra were acquired with the same pulse sequence.

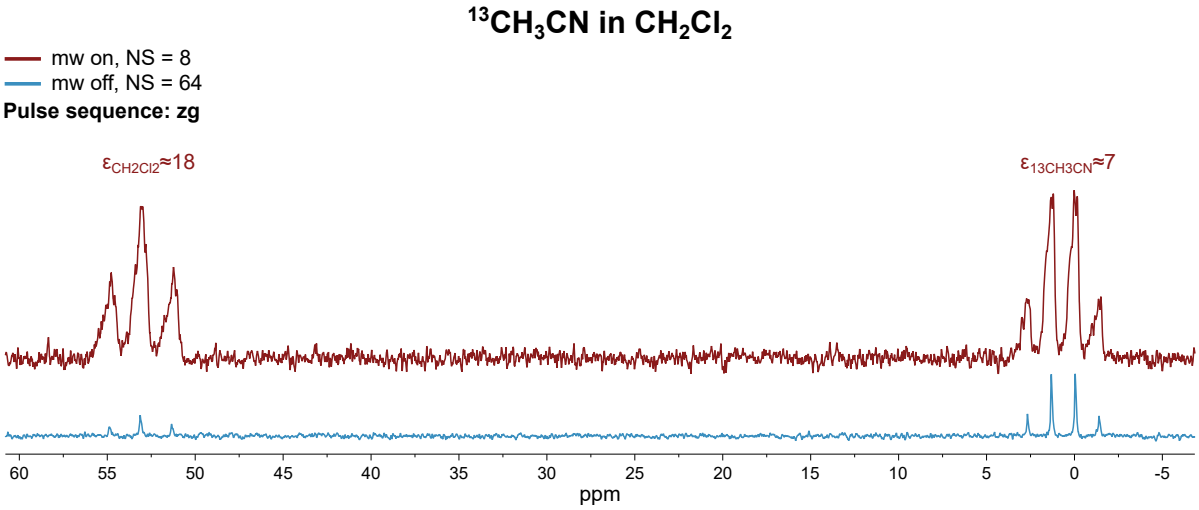

Figure C.17: ^{13}C NMR spectra of $^{13}CH_3CN$ in CH_2Cl_2 with (red) and without (blue) mw irradiation. Experimental parameters are listed in tab. C.5 and tab. C.4. Boltzmann and DNP spectra were acquired with the same pulse sequence.

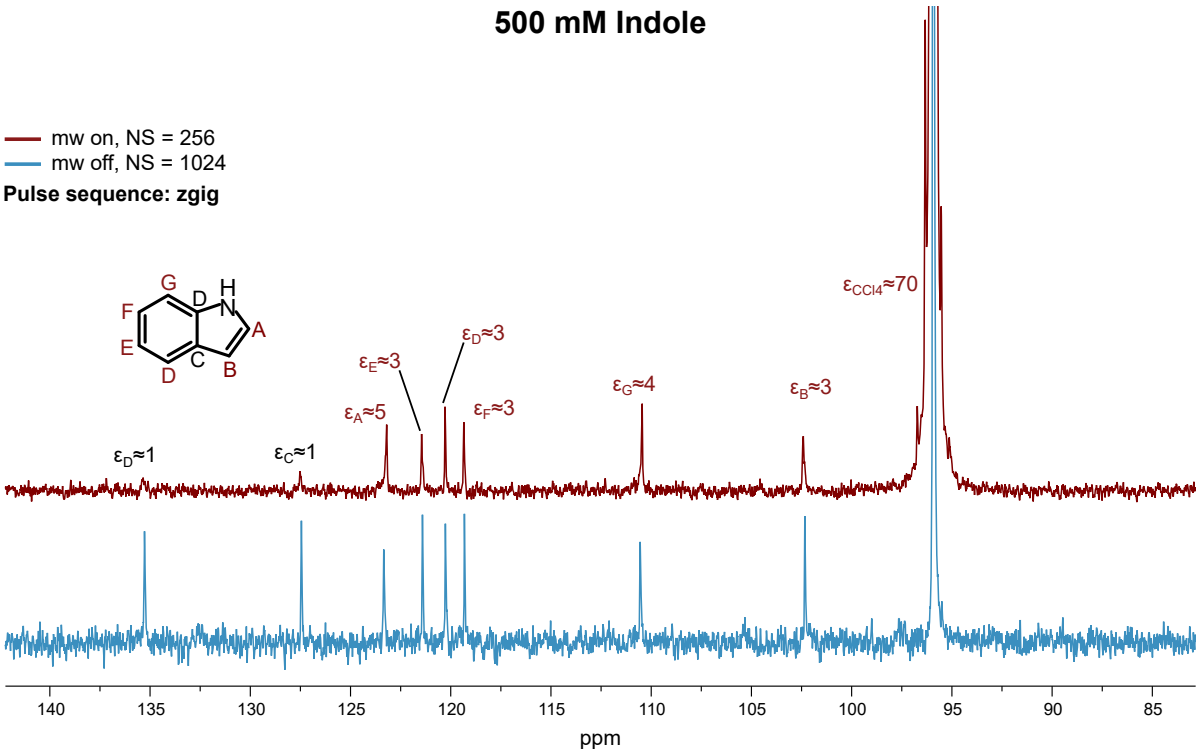

Figure C.18: ^{13}C NMR spectra of 500 mM indole doped with 25 mM ^{15}N-TN-d_{16} with (red) and without (blue) mw irradiation. Experimental parameters are listed in tab. C.5 and tab. C.4. Boltzmann and DNP spectra were acquired with the same pulse sequence.

D Nuclear Spin Longitudinal Relaxation Time

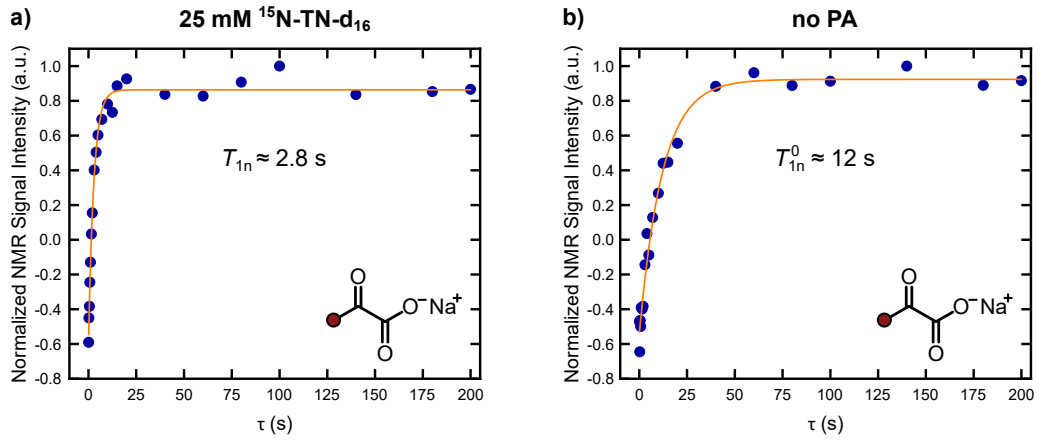

Figure D.1: Inversion recovery experiments to obtain the nuclear spin-lattice relaxation time of 3-$^{13}C_1$-pyruvate in presence T_{1n} and absence T_{1n}^0 of PA. Measurements were performed on a degassed solution of 500 mM 3-$^{13}C_1$-pyruvate in a mixture of 9/1 H_2O/glycerol (w/w). T_{1n} was obtained in presence of 25 mM ^{15}N-TN-d_{16}. a): NMR parameters: NS = 64, DS = 2, RD = 20 s, $P(\pi/2)$ = 41 W, $t_p\,(\pi/2)$ = 9.5 µs, LB = 0.3 Hz. b) NMR parameters: NS = 64, DS = 0, RD = 30 s, $P(\pi/2)$ = 41 W, $t_p\,(\pi/2)$ = 9.8 µs, LB = 0.3 Hz. Experimental errors are estimated to be 10 – 20 %

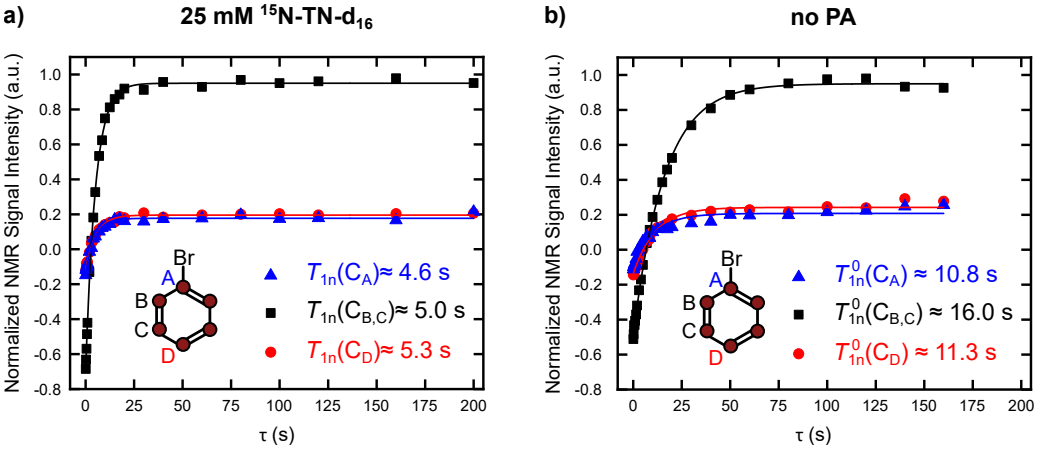

Figure D.2: Inversion recovery experiments to obtain the nuclear spin-lattice relaxation time of a degassed solution of 200 mM $^{13}C_6$-C_6-C_6H_5Br in CCl_4 in presence T_{1n} and absence T_{1n}^0 of PA. T_{1n} was obtained with of 25 mM ^{15}N-TN-d_{16}. NMR parameters: NS = 32, DS = 4, RD = 20 s, $P(\pi/2)$ = 41 W, $t_p\,(\pi/2)$ = 9.5 µs, LB = 0.3 Hz.

E Temperature Calibration at 9.4 Tesla

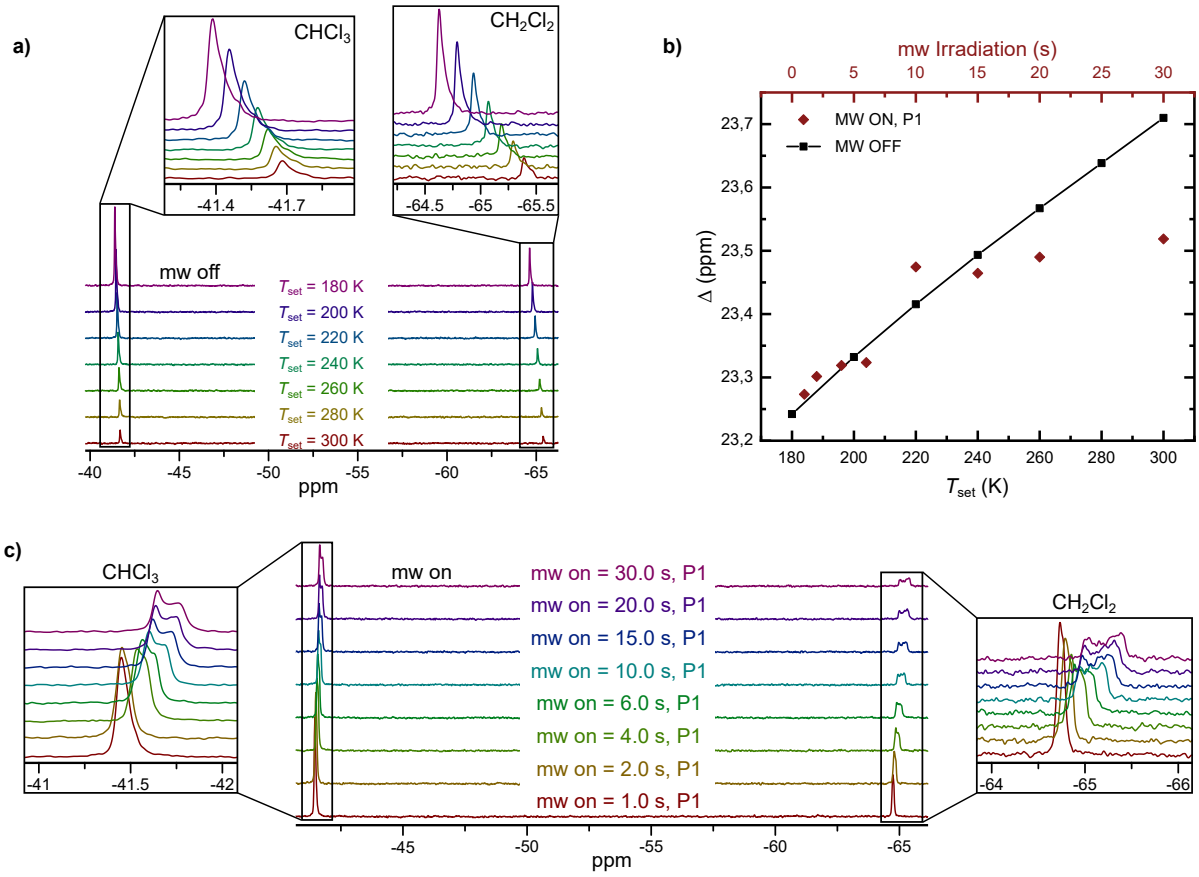

Figure E.1: Temperature calibration of dichloromethane. a) ^{13}C NMR spectra of 200 mM $^{13}CHCl_3$ in CH_2Cl_2 as a function of the temperature. b) Plot of the chemical shift difference of the reference compounds against the set sample temperature under Boltzmann conditions (black) and the duration of mw irradiation (red). The line is a guide for the eye. c) The same spectra as in a) but for different mw irradiation times ($T_{set} = 180$ K). Microwave power was $P \approx 22$ W. NMR parameters: NS = 8, DS = 2, LB = 2, D1(mw on) = 31 s, D1(mw off) = 16 s, $P(\pi/2) = 48$ W, $\pi/2 = 10$ µs, waltz64, 0.58 W. The used pulse sequence is shown in fig. 3.4b.

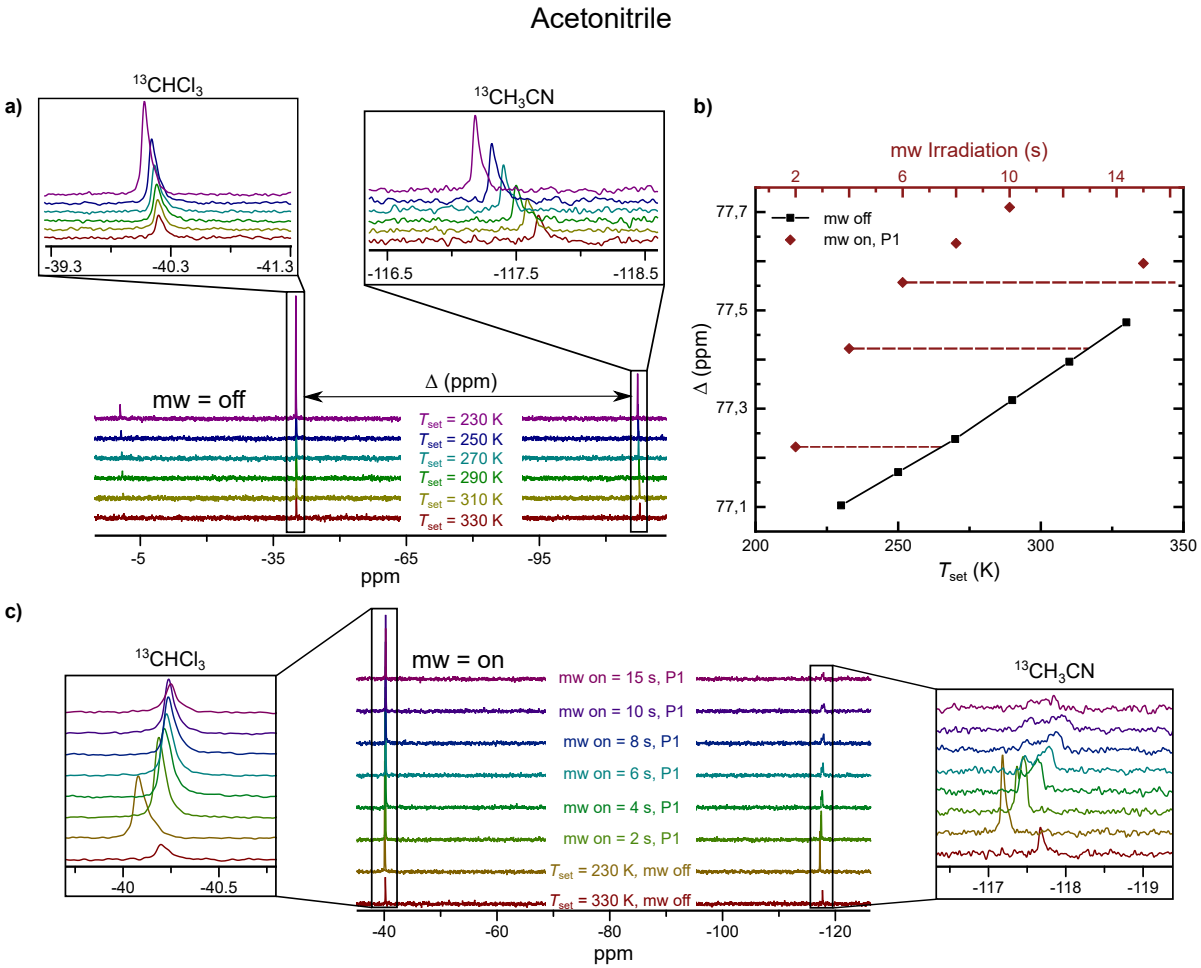

Figure E.2: Temperature calibration of acetonitrile. a) ^{13}C NMR spectra of 200 mM $^{13}CHCl_3$ in acetonitrile as a function of the temperature. b) Plot of the chemical shift difference of the reference compounds against the set sample temperature under Boltzmann conditions (black) and the duration of mw irradiation (red). The line is only a guide for the eye. c) The same spectra as in a) but for different mw irradiation times ($T_{set} = 230\,K$). Microwave power was $P \approx 22\,W$. NMR parameters: NS = 8, DS = 2, LB = 2, D1(mw on) = 31 s, D1(mw off) = 16 s, $P(\pi/2) = 48\,W$, $\pi/2 = 10\,\mu s$, waltz64, 0.58 W. The used pulse sequence is shown in fig. 3.4b.

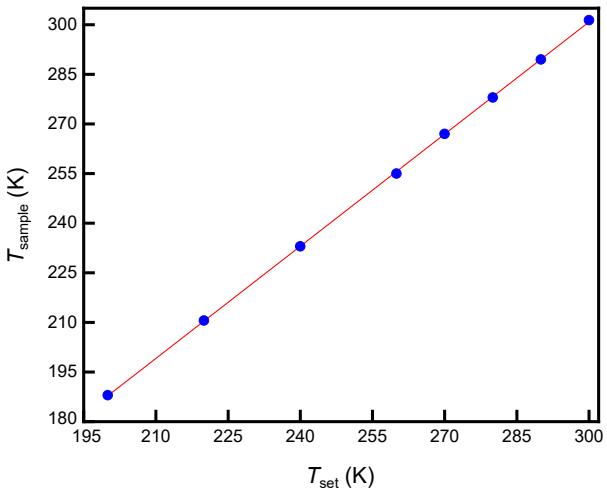

Figure E.3: Calibration of T_{set} to obtain T_{sample} by comparison of the chemical shift of the ^{1}H signals of methanol (Bruker standard calibration procedure). The sample consisted of neat methanol (full 5 mm standard glass NMR tube).

Acknowledgment

First, I would like to acknowledge my PhD supervisor Prof. Dr. Marina Bennati for her guidance and support throughout the past four years. It is my hope that I can retain at least part of the excitement for science that she, after quite a few years in the business, still has. I would also like to express my gratitude for my co-examinder Prof. Dr. Christian Griesinger and the third member of my thesis advisory board Dr. Aljaz Godec for very helpful discussions and their support during my time as a PhD student.
Next, I would like to thank my colleague Dr. Tomas Orlando. It was a pleasure to have him as a "sub" mentor. I will never forget my first big scientific conference in Warsaw including a 150 h train ride (at least it felt like it), crazy security checks due to a visit of Donald Trump in Warsaw, and an artist preparing an ice sculpture with a chainsaw at the Bruker night. Thanks for all of this and much more.
I would also like to thank Dr. Igor Tkach for sharing some of his microwave wisdom with me and for being such a patient teacher. Dr. Luming Yang is greatly acknowledged for a very productive collaboration and for being a very kind office mate. I would like to thank my former master student Maik Reinhard for the nice work during his master thesis and very fun basketball conversations. I am also grateful to Dr. Michael John and Dr. Alex van der Ham for sharing their NMR knowledge with me.
Furthermore, I would like to express my gratitude to Dr. (!) Fabian Hecker for an awesome time at work together, be it teaching, renovating the lab, or organizing events. An amazing example for me is always the trip to the Harry Potter theatre, which had the largest legroom imaginable. Monika Frömel and Gitta Angerstein are acknowledged for keeping the engine of our lab running, thereby being kind and supportive to everyone. I would like to thank all the other members of our group (and former members) Dr. Andreas Meyer, Anni Kehl, Dr. Deepshikha Verma, Marvin Lenjer, Lisa Fries, Dr. Isabell Bejenke, Dr. Markus Hiller, and Dr. Guoquan Liu for creating such a wonderful working atmosphere with many dinners, barbecues, and other activities together.
Finally, I would like to thank my friends for all the support, laughs and fun together. LAN parties are also fun when you are above 30! I would like to thank Dr. (!) Marco Eckhoff for spending an insane amount of time together and not being annoyed by each other. There are quite a few mountains (or boulders) that

still need to be climbed.
Most importantly I would like to thank my loving family for their support and kindness. Particularly, I would like thank my two grandfathers from whom I inherited my stubbornness. I would also like to express my gratitude to my mother, Monika Levien, for being a wonderful, supporting, kind, smart, and caring person. She taught me almost everything about life. Finally, I would like to thank my girlfriend, Dr. (!) Lena Aperdannier, simply for making my life wonderful by being the perfect person you are to me.
Even though I feel a lot of joy and satisfaction for finishing my PhD, it fills me with almost as much pain that I am not able to share all this with my father, Roland Levien. I wish, I could have him by my side. I hope, he is proud.

Publications

J. Altnöder, K. Krüger, D. Borodin, L. Reuter, D. Rohleder, F. Hecker, R. A. Schulz, X. Nguyen, H. Preiß, M. Eckhoff, M. Levien, M. A. Suhm, "The Guinness Molecules for the Carbohydrate Formula," *Chem. Rec.* **2014**, *6*, 1116 – 1133.

G. Liu, M. Levien, N. Karschin, G. Parigi, C. Luchinat, M. Bennati, "One-thousand-fold enhancement of high field liquid nuclear magnetic resonance signals at room temperature," *Nat. Chem.* **2017**, *9*, (7), 676-680.

T. Orlando, R. Dervisoglu, M. Levien, I. Tkach, T. F. Prisner, L. B. Andreas, V. P. Denysenkov, M. Bennati, "Dynamic Nuclear Polarization of ^{13}C Nuclei in the Liquid State over a 10 Tesla Field Range," *Angew. Chem. Int. Ed.* **2019**, *58*, (5), 1402 – 1406.

M. Levien, M. Hiller, I. Tkach, M. Bennati, T. Orlando, "Nitroxide derivatives for dynamic nuclear polarization in liquids: the role of rotational diffusion," *J. Phys. Chem. Lett.* **2020**, *11*, (5), 1629 – 1635.

M. Levien, M. Reinhard, M. Hiller, I. Tkach, M. Bennati, T. Orlando, "Spin density localization and accessibility of organic radicals affect liquid-state DNP efficiency," *Phys. Chem. Chem. Phys.* **2021**, *23*, (8), 4480 – 4485.

M. Reinhard, M. Levien, M. Bennati, T. Orlando, "Large ^{31}P-NMR enhancements in liquid state dynamic nuclear polarization through radical/target molecule non-covalent interaction," *Phys. Chem. Chem. Phys.* **2023**, *25*, 822 – 828.

M. Levien, L. Yang, A. van der Ham, M. Reinhard, M. John, R. Wylde, A. Leavesley, T. Marquardsen, A. Purea, I. Tkach, T. Orlando, M. Bennati, "Liquid state nuclear magnetic resonance spectroscopy enhanced by dynamic nuclear polarization at 9.4 Tesla and μL sample volume," *to be submitted*.